RL927

MICROWAVE REMOTE SENSING OF SNOW: AN EMPIRICAL/THEORETICAL SCATTERING MODEL FOR DENSE RANDOM MEDIA

John R. Kendra

September, 1995

Microwave Remote Sensing of Snow: An Empirical / Theoretical Scattering Model for Dense Random Media

by

John Robert Kendra

A dissertation submitted in partial fulfillment
of the requirements for the degree of
Doctor of Philosophy
(Electrical Engineering)
in The University of Michigan
1995

Doctoral Committee:

Assistant Professor Kamal Sarabandi, Chair
Professor Fawwaz T. Ulaby, Chair
Professor Anthony W. England
Assistant Professor Brian E. Gilchrist
Professor William R. Kuhn

To doubt everything or to believe everything are two equally convenient solutions; both dispense with the necessity of reflection.

—Jules Henri Poincaré

To my wife, Mayda Sylvia, and our sons, Joseph Aaron and Gabriel John—two good boys.

ACKNOWLEDGEMENTS

I gratefully acknowledge the support and direction furnished by my two advisors, Professors Fawwaz T. Ulaby and Kamal Sarabandi. Dr. Ulaby was my principal advisor during the first half of my tenure here, during which time we collaborated on a number of different projects, including a radiometer technique for the detection of ice on the surface of the external fuel tank of the space shuttle. Dr. Ulaby also provided major direction in the development of the Snow Probe, and the execution of both of the major field experiments I led involving radar measurements of snowpacks. In all of these cases, Dr. Ulaby made sure that things proceeded forward in a direct and timely fashion, that obstacles were squarely met and overcome. Dr. Sarabandi first conceived of the hybrid model concept as applied to dense media, and provided guidance during the course of its development. I thank Kamal for his insightful advice throughout the project and for the confidence he showed in me in allowing me, to an increasingly greater degree, to assume authority regarding the direction of the project.

I thank my committee for their helpful comments and suggestions regarding this dissertation. In particular I thank Prof. Anthony England for many conversations, both technical and personal, over the last six years.

I thank those individuals who rendered invaluable assistance during two very difficult

but also very memorable snow field experiments. In particular Mr. Jim Stiles, who selflessly acted as my principal counsel during both of the missions, Mr. Jim Ahne, and Mr. Steve Ciccarelli for their participation in the Cadillac experiment; for their assistance during the Brighton experiment, I gratefully acknowledge Mr. Paul Siqueira, Ms. Jasmeet Judge, Mr. Neil Peplinski and Mr. Ruben de la Sierra. Special thanks are due to Mr. Ron Hartikka for his guidance and assistance in many of the experimental and, especially, hardware issues faced during these missions and generally.

The majority of the benefit which I have received during my graduate career is associated with those individuals with whom I have closely interacted. I sincerely thank, for their friendship and technical assistance: Dr. Adib Nashashibi, Mr. Paul Siqueira, Mr. Jim Stiles, Dr. John Galantowicz, Ms. Jasmeet Judge, Dr. Joe Landry, Dr. Richard Austin, Mr. Ron Hartikka, Mr. Roger DeRoo, and Dr. Leland Pierce.

I wish to acknowledge my parents: my mother Nancy Kendra, who has given me unlimited love and support, during this experience and always, and the memory of my father, Joseph Anthony Kendra — the inspiration of his character I carry with me always.

Finally, I thank my wife, Mayda Sylvia, for her love, understanding, and encouragement, and our sons, Joseph and Gabriel, for together providing the best of all possible home lives.

TABLE OF CONTENTS

LIST OF TABLES

Table

LIST OF FIGURES

Figure

LIST OF APPENDICES

CHAPTER I

INTRODUCTION

This dissertation describes activities that were conducted to facilitate the use of microwave remote sensing for monitoring snow parameters. The primary goal of this work has been to assess and further the state of modeling of radar scattering by snow in particular and, dense media in general. The following sections, which discuss the global importance of snow and give a summary of work done to date in the area of microwave remote sensing of snow, will serve to motivate a detailed discussion of the present research.

1.1 Background

There are various aims associated with snow investigations. Large areas of the world are covered, at least part of the time, with snow of varying amounts. In certain areas of the world, California being a good example, melting snow represents a very large fraction of the total water resource available for all uses. For many areas of the world, the majority of the total electric power is generated through hydroelectric means. Many of the streams and tributaries which contribute to this process are fed from water runoff from the mountains generated by melting snow. Water management practices and strategies in these last two examples can be greatly enhanced by estimates of total water content contained in snow packs occupying very large areas.

Snow-covered ground is also an important parameter in global climate studies. It has a

much higher solar albedo than other types of terrain, thereby decreasing the absorption of incident solar radiation, and it has unique energy exchange and storage mechanisms which are related to the physical composition of the snowpack. For agricultural concerns, the amount of snow is not only related to ground moisture replenishment, but also, since snow acts as an insulating layer against extreme sub-zero temperatures, it is related to the amount of winterkill of various crops (NASA, Goddard Space Flight Center 1982). It is known that avalanche hazards are associated with snow wetness and snowpack stratigraphy (Colbeck 1991). There is a large snow recreation industry which could also benefit from retrieval of snow parameters over a large area.

Apart from examining snow for its own sake, an understanding of microwave scattering from snow is necessary because without it, the analysis of a host of other remote sensing problems may be confounded. This is due to the fact that snow is often present and influences the radar response even when it is not the principal target of an investigation. This often applies in problems involving ice sheets, presently a very active area in remote sensing because of its importance for ship navigation. Another example is forest studies, wherein the volume scattering present in snow may become a significant additional source term, and where any interaction involving the ground will be modified, perhaps significantly. Another example, which is presently receiving wide interest at millimeter-wave frequencies, is the military interest in understanding the clutter characteristics of snow for detection and signal-to-clutter analysis of point targets over a snow-covered background.

In all of the examples cited above, the desired information is basically the snow physical parameters. These parameters will then serve as inputs into formulas or models designed to yield predictions pertaining to particular interests: How much runoff can be expected from snow present in a certain mountain basin? What is the EM response of a particular snowpack and which polarization will afford maximum clutter reduction? What is the projected degree of winterkill of a particular crop? It has already been mentioned that snow tends to interfere with microwave remote sensing activities where it is not the principal target. It

is the degree to which it "interferes" that makes it a suitable candidate for investigation by microwave remote sensing means. The greater its "visibility" to remote sensing radars and radiometers, the more likely it is that specific attributes of the snowpack may be inferred from measurements made by these types of sensors.

1.2 Microwave Remote Sensing of Snow

The use of microwaves for remote sensing of snowpacks, as with the remote sensing of any other natural target, is motivated by the all-weather, day/night, target-penetrating attributes of such a system. Though optical and infrared sensors can be used (in the absence of cloud cover) to map the areal extent of snowcover, the single most important parameter associated with a snowpack, a measure of its stored water content known as *snow water equivalent* (SWE), can not be determined by such sensors. The SWE of a snowpack is the height of the column of water which would be produced if a column of standard diameter taken from the snowpack was completely melted. To arrive at such information suggests the use of a sensor capable of extracting information down to the bottom of a snowpack. The use of radar seems eminently well-suited to such a task.

In practice, however, initial optimism has not led to systems, procedures, and algorithms for the retrieval of snow parameters which can be used with any degree of certainty. This is due to the extreme complexity and highly varied forms of typical snowpacks. The average snowpack contains a number of discrete layers having properties dissimilar from one another; properties such as effective crystal size, density, and liquid water content. For wavelengths long enough to allow penetration all the way through to the bottom of the snowpack, the scattering properties of the underlying ground may have a large, even dominant influence on the scattered wave. The surface roughness of the snowpack may exert an influence of varying degrees, depending on the radar frequency, and effective dielectric constant of the snow top surface.

There have been ambitious attempts to employ microwave snow mapping systems on an experimental basis, such as in Finland, where an attempt was made (Hallikainen 1984) to correlate the difference of brightness temperatures associated with two radiometer channels with SWE over a large area of the country. In general though, the models sorely lack the sophistication necessary to adequately account for the diversity and wide dynamic range of wave scattering that can result from a snowpack due to its composition.

Perhaps the most noteworthy advances in the technology have been in characterizing the fundamental electrical properties of snow and its constituent elements. The dielectric constant of ice, for example, has been examined by many researchers (Cumming 1952; Nyfors 1982; Mätzler and Wegmüller 1987) and fairly reliable models have been formulated for that parameter as a function of frequency, temperature, and (to a much lesser degree) impurities. Investigation into the dielectric constant of snow, both dry and wet, has also seen a lot of attention (Nyfors 1982; Mätzler et al. 1984; Tiuri et al. 1984; Hallikainen et al. 1986) and here too fairly reliable models have been formulated. Regarding the snowpack as a whole, important large-scale experiments have been performed (Stiles and Ulaby 1980a; Ulaby and Stiles 1980; Mätzler and Schanda 1984) illustrating the *general* behavior of the radar response of snowpacks with respect to surface roughness, water content, water equivalent, and crystal size. However, due to the extreme diversity of the snowpack system, within and especially *between* such investigations, and the incomplete descriptions which generally exist, despite the most conscientious ground-truth efforts, there still remains considerable uncertainty regarding the effect of certain snowpack elements on radar backscatter. One exception to this is the significant decrease exhibited by the backscattering coefficient, noted (almost) universally, when liquid water is present in the snowpack. Recently, however, even this has become a point of some contention with some researchers (Shi and Dozier 1992) advocating that increased surface scatter in wet snow conditions may often lead to an increase in the backscatter[1].

[1] This question is examined in Chapter IV.

On the purely theoretical side, there has been a great deal of activity during the last fifteen years. Theoretical work which has direct application to snowpack systems include investigations into volume scattering and extinction, scattering by random surfaces, and the scattering behavior of combinations of these elements, as in the case of layered structures. With respect to volume scatter and extinction, snow is a perfect example of a dense medium, that is a medium having an appreciable volume fraction of scatterers. It has been recognized that such a medium does not conform to the assumptions inherent in conventional radiative transfer theory, namely that (1) the scatterers are independent of one another, (2) no phase relations are preserved between particles, and (3) the particles are in the far-field of one another so that far-field phase functions may be employed. Efforts to comprehend scattering from dense media in a theoretical sense have produced a great many papers in the literature, pertaining to a number of different theories (Zuniga and Kong 1980; Fung and Eom 1985; Zhu et al. 1987; Tsang and Ishimaru 1987). In general, these theories, in their attempt to deal as rigorously as possible with the problem, become quite complex and computationally intensive. As such, they do not lend themselves easily to inversion nor in many cases can the inputs required for the models be adequately obtained by any practical ground-truth effort. A limited number of controlled laboratory experiments have been performed to test these theories, some with conflicting results (Ishimaru and Kuga 1982; Gibbs and Fung 1990; Mandt 1987). The issue of modeling options for describing EM scattering from snowpacks is a central issue of this dissertation and will be elaborated on in the following chapters.

1.3 Format of This Dissertation

After reviewing in Chapter II some basic concepts central to the overall thrust of the research, the development of the Snow Probe, an electromagnetic device for the *in situ* measurement of snow liquid water content and snow density, is discussed in Chapter III. The development of this device is a prerequisite to the large scale experiments discussed in Chapter

IV involving radar measurements of artificial snowpacks. In these experiments an approach is taken which specifically seeks to address the failings, in terms of total target characterization, which have existed in virtually all such efforts to date, and which have hindered to a large degree unambiguous analysis. Chapter IV also presents an analysis of diurnal measurements which are accompanied by detailed records of snow wetness obtained *via* the Snow Probe.

Chapter V introduces a hybrid experimental/theoretical modeling approach which is intended for complex media or media which otherwise are not describable by other means. In Chapter VI, the validity of the approach is evaluated through its application to two different dense materials.

CHAPTER II

BASIC CONCEPTS

The material which will be covered in Chapters IV and (especially) V and VI of this dissertation pertains to modeling the *polarimetric* response of random media. Polarimetry refers to the measurement of a target's scattering response to an arbitrary polarization. Such target information, which can be obtained by either coherent dual (orthogonally) polarized radars or non-coherent radars with the aid of various polarizers, offers potentially much greater power of target characterization than the non-coherent co-pol (VV and HH) and cross-pol (VH) response afforded by conventional non-polarimetric radars.

In this chapter, we first briefly review the fundamentals of wave polarization, and then show how this information is preserved in non-coherent power or intensity quantities in the form of Stokes parameters. After a discussion of alignment conventions used in describing polarized scattering, we outline how Stokes parameters, in the form of a Stokes vector, can be used in the framework of vector radiative transfer to theoretically model the polarimetric response of random media.

As a rule, throughout this dissertation, vectors will be represented by boldface letters (e.g. $\mathbf{x}$) and matrices by boldface script letters (e.g. $\boldsymbol{\mathcal{X}}$).

2.1 Wave Polarization and Stokes Parameters

The discussion that follows on wave polarization and Stokes parameters follows the treatment given in Ishimaru (1978)[Chap. 2].

An electromagnetic plane wave propagating along a certain direction is specified by three parameters: (1) frequency, (2) amplitude, and (3) polarization state. Consider a plane wave propagating in the $\hat{\mathbf{z}}$ direction. The electric field vector is $\mathbf{E} = E_x\hat{\mathbf{x}} + E_y\hat{\mathbf{y}}$, with the components given by,

$$E_x = \mathrm{Re}(E_1 e^{j\omega t}) = \mathrm{Re}[a_1 \exp(j\delta_1 - jkz + j\omega t)] = a_1 \cos(\tau + \delta_1) \tag{2.1}$$
$$E_y = \mathrm{Re}(E_2 e^{j\omega t}) = \mathrm{Re}[a_2 \exp(j\delta_2 - jkz + j\omega t)] = a_2 \cos(\tau + \delta_2),$$

where $\tau = \omega t - kz$. If τ is eliminated from the above pair of equations, the equation for an ellipse is obtained, which describes the path that the tip of the electric field vector traces in the xy-plane:

$$\left[\frac{E_x}{a_1}\right]^2 + \left[\frac{E_y}{a_2}\right]^2 - 2\left(\frac{E_x E_y}{a_1 a_2}\right)\cos\delta = \sin^2\delta, \tag{2.2}$$

where $\delta = \delta_2 - \delta_1$.

It is easy to show from Eq. (2.1) that the polarization is right-handed if $\delta < 0$ and left-handed if $\delta > 0$. The IEEE Standards Handbook (IEEE 1979) defines handedness based on the direction the tip of the E-vector traces at a fixed point in space, from the perspective of a viewer looking in the direction of propagation. If the tip rotates in a clockwise (counter-clockwise) fashion, the wave is said to be right (left) handed.

An alternate means of describing wave polarization is in terms of Stokes parameters,

introduced in 1852 by G. G. Stokes. They are,

$$
\begin{aligned}
I &= a_1^2 + a_2^2 = |E_1|^2 + |E_2|^2 \\
Q &= a_1^2 - a_2^2 = |E_1|^2 - |E_2|^2 \\
U &= 2a_1 a_2 \cos\delta = 2\mathrm{Re}(E_1 E_2^*) \\
V &= 2\mathrm{Im}(E_1 E_2^*)
\end{aligned}
\tag{2.3}
$$

where $E_1 = a_1 \exp(j\delta_1 - jkz)$ and $E_1 = a_2 \exp(j\delta_2 - jkz)$ are the phasor representations of the electric field components E_x and E_y respectively.

The chief utility of Stokes parameters is that through their use it is possible to completely specify the polarization state of a wave using only measurements of intensity, made with the aid of various polarizers. In optical applications the four Stokes parameters may be constructed from a series of measurements involving (1) no polarizer, (2)–(3) $\pm 45°$ linear polarizers, and (4) left- and (5) right-hand circular polarizers (Bohren and Huffman 1983). In the case of microwaves, the "no polarizer" measurement is actually accomplished *via* separate measurements of the vertically- and horizontally-polarized components of the incident intensity

An alternative representation of the Stokes parameters is obtained by describing the polarization ellipse in terms of the semimajor (a) and semiminor (b) axes of the ellipse an the orientation angle (ψ), as shown in Figure 2.1. Using I_o, b/a, and ψ, the Stokes parameters become,

$$
\begin{aligned}
I &= I_o \\
Q &= I_o \cos 2\chi \cos 2\psi \\
U &= I_o \cos 2\chi \sin 2\psi \\
V &= I_o \sin 2\psi,
\end{aligned}
\tag{2.4}
$$

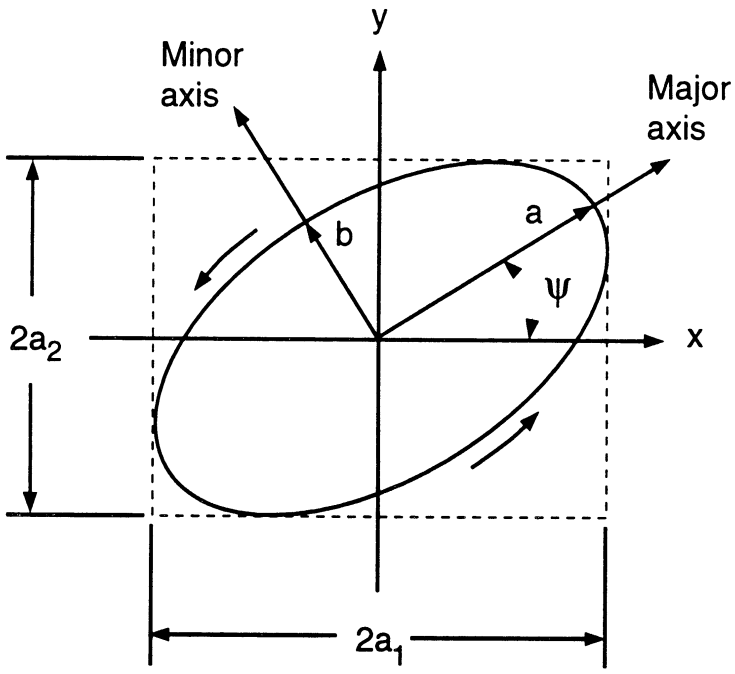

Figure 2.1: Polarization ellipse for wave traveling in the $\hat{\mathbf{z}}$ direction. Shown is right-handed elliptical polarization.

where χ is the ellipticity angle given by $\tan\chi = \pm b/a$, with the plus sign for left-handed and the minus sign for right-handed polarization. The entire range of polarizations are expressed in the range $-\pi/2 \leq \psi \leq \pi/2$ and $-\pi/4 \leq \chi \leq \pi/4$.

These ellipticity angles are related to the wave parameters of Eqs. (2.2) and (2.3) by the following expressions:

$$\tan 2\psi = (\tan 2\alpha)\cos\delta \tag{2.5}$$

$$\sin 2\chi = (\sin 2\alpha)\sin\delta \tag{2.6}$$

where,

$$\tan\alpha = \frac{a_2}{a_1} \tag{2.7}$$

In radiative transfer theory (discussed in the Section 2.3) it is most common to use the "modified" Stokes parameters, given by,

$$\mathbf{F}_m = \begin{bmatrix} I_v \\ I_h \\ U \\ V \end{bmatrix} = \frac{1}{\eta}\begin{bmatrix} |E_1|^2 \\ |E_2|^2 \\ 2\mathrm{Re}(E_1E_2^*) \\ 2\mathrm{Im}(E_1E_2^*) \end{bmatrix} = \begin{bmatrix} \frac{1}{2}(1+\cos 2\psi\cos 2\chi) \\ \frac{1}{2}(1-\cos 2\psi\cos 2\chi) \\ \sin 2\psi\cos 2\chi \\ \sin 2\chi \end{bmatrix} I_o, \tag{2.8}$$

where η is the characteristic impedance of free space.

An important property of Stokes parameters is their additivity. It has been shown (Chandrasekhar 1960)[p. 29] that when several independant or uncorrelated waves are combined, the Stokes parameters of the combined waves are equivalent to the sum of the Stokes parameters of the individual waves. This concept is what makes possible the use of Stokes parameters in the structure of vector radiative transfer in treating propagation through random media.

2.2 Scattering Alignment Conventions

There are two principal types of coordinate systems with which scattering calculations are performed. These are the forward scatter alignment (FSA) and the backscatter alignment (BSA). Since both are used in this dissertation, brief descriptions of each will be given here. The description that follows for these conventions in part reproduces, or is otherwise closely based on, the treatment given in Ulaby and Elachi (1990).

The FSA convention is a "wave-oriented" convention in that the horizontal ($\hat{\mathbf{h}}$) and vertical ($\hat{\mathbf{v}}$) directions are defined with respect to the direction of propagation, $\hat{\mathbf{k}}$. For this reason, the convention is to denote waves as "incident" and "scattered". The scattering geometry and coordinate system are shown in Figure 2.2. The coordinate system ($\hat{\mathbf{k}}, \hat{\mathbf{v}}, \hat{\mathbf{h}}$) is chosen to

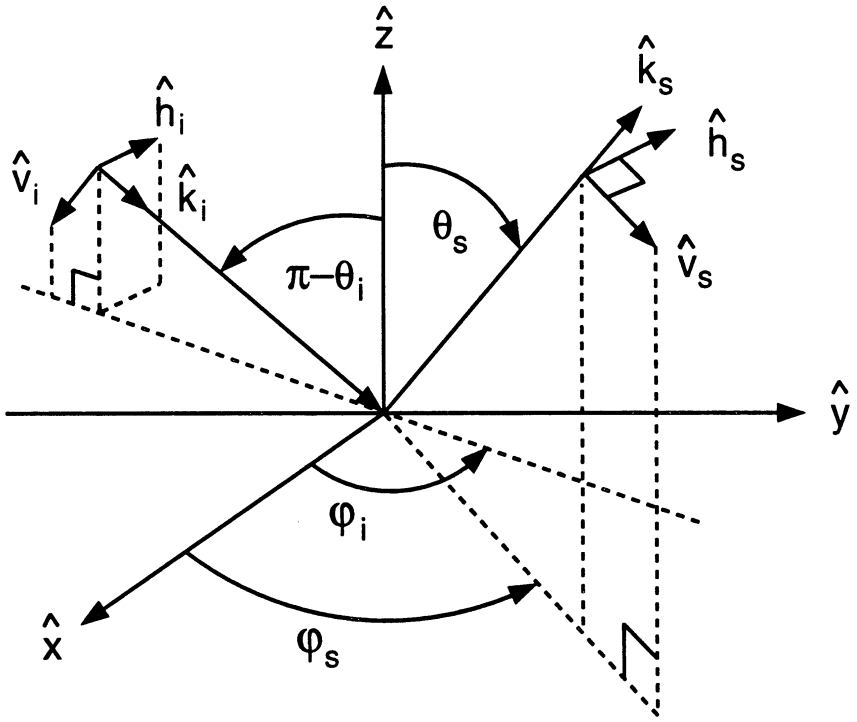

Figure 2.2: Coordinate system and scattering geometry for the forward scatter alignment (FSA) convention.

coincide with the unit vectors $(\hat{\mathbf{r}}, \hat{\theta}, \hat{\phi})$ of a standard spherical coordinate system. Thus,

$$\hat{\mathbf{k}}_i = \cos\phi_i \sin\theta_i \hat{\mathbf{x}} + \sin\phi_i \sin\theta_i \hat{\mathbf{y}} + \cos\theta_i \hat{\mathbf{z}} \tag{2.9}$$

$$\hat{\mathbf{h}}_i = \frac{\hat{\mathbf{z}} \times \hat{\mathbf{k}}_i}{|\hat{\mathbf{z}} \times \hat{\mathbf{k}}_i|} = -\sin\phi_i \hat{\mathbf{x}} + \cos\phi_i \hat{\mathbf{y}} \tag{2.10}$$

$$\hat{\mathbf{v}}_i = \hat{\mathbf{h}}_i \times \hat{\mathbf{k}}_i = \cos\phi_i \cos\theta_i \hat{\mathbf{x}} + \sin\phi_i \cos\theta_i \hat{\mathbf{y}} - \sin\theta_i \hat{\mathbf{z}}. \tag{2.11}$$

Identical expressions apply to the scattered wave upon the substitution of $(\hat{\mathbf{k}}_s, \hat{\mathbf{v}}_s, \hat{\mathbf{h}}_s)$ for $(\hat{\mathbf{k}}_i, \hat{\mathbf{v}}_i, \hat{\mathbf{h}}_i)$ and (θ_s, ϕ_s) for (θ_i, ϕ_i).

Under the BSA convention, waves are denoted as "transmitted" and "received". Whereas for the FSA convention, the polarization vectors are defined with respect to the propagating wave, in the BSA convention they are defined with respect to the antennas. The polarization state of an antenna is defined to be the polarization of the wave radiated by the antenna, even when the antenna is used in the receiving mode. Consequently, in the backscatter case, the vertical and horizontal polarization unit vectors of the local coordinate system are the same for the transmitted and received waves.

Relative to the global coordinates of $(\hat{\mathbf{x}}, \hat{\mathbf{y}}, \hat{\mathbf{z}})$, the local coordinate system unit vectors for the transmitted wave are identical to those of the incident wave in the FSA case. For the received wave however, the unit vectors are given by the following:

$$\hat{\mathbf{k}}_r = -\left[\cos\phi_r \sin\theta_r \hat{\mathbf{x}} + \sin\phi_r \sin\theta_r \hat{\mathbf{y}} + \cos\theta_r \hat{\mathbf{z}}\right] \tag{2.12}$$

$$\hat{\mathbf{h}}_r = -\sin\phi_r \hat{\mathbf{x}} - \cos\phi_r \hat{\mathbf{y}} \tag{2.13}$$

$$\hat{\mathbf{v}}_r = \cos\phi_r \cos\theta_r \hat{\mathbf{x}} + \sin\phi_r \cos\theta_r \hat{\mathbf{y}} - \sin\theta_r \hat{\mathbf{z}}. \tag{2.14}$$

The coordinate system and scattering geometry for the BSA convention are shown in Figure 2.3.

The FSA convention is the natural one for use with mathematical computations where scattering in directions other than the backscatter direction is considered. Since such mod-

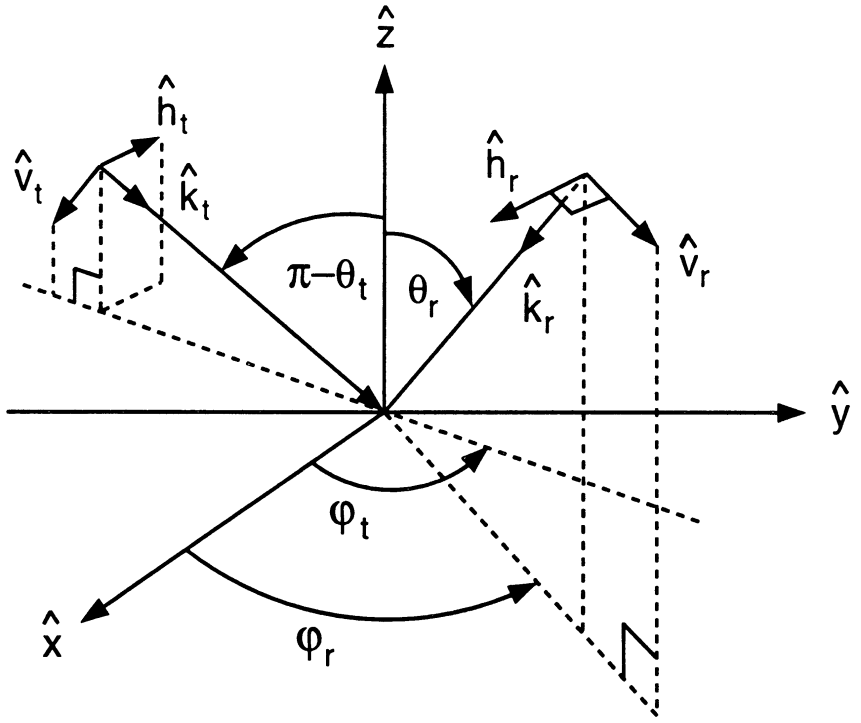

Figure 2.3: Coordinate system and scattering geometry for the backscatter alignment (BSA) convention.

eling is a primary concern of this dissertation, to avoid confusion, the FSA convention has been adopted almost exclusively.

However, there are two instances in this work where the BSA convention is employed. First, all of the radar measurements considered were calibrated following the BSA convention. This has been the preferred system in radar polarimetry because of the fact that the local coordinate systems for the transmitted and received waves are coincident in the backscatter direction. Use of the BSA convention gives the intuitive result that a polarization state at the antenna aperture is identically defined regardless of whether it is a transmitted or received wave. The matrix by which polarimetric radar data following the BSA convention is converted to the FSA convention is presented later, following a description of the constructs in which the polarimetric information is contained.

The other instance in which the BSA convention is employed is with respect to the polarization synthesis techniques described below in Section 2.4, which have been formulated following the BSA convention (Ulaby and Elachi 1990).

2.3 Vector Radiative Transfer

Two basic approaches exist for dealing with problem relating to the interaction of electromagnetic waves with random medium—field based or analytic approaches, and non-coherent, intensity based ones. The former have Maxwell's equations as a starting point, and approach the problem using rigorous electromagnetic formulations. In reality, however, it is not possible to treat all of the multiple scattering, interference, and diffraction effects in a random medium in a completely rigorous manner. Thus each of these field-based techniques must ultimately make some approximations to obtain a solution.

The second type of approach is known as transport theory, or radiative transfer. It deals directly with the transport of energy through a medium containing particles and is not based on wave theory. As this technique is used extensively in the following chapters, a descrip-

tion of the essential framework of the theory will be presented here.

The defining equation for radiative transfer (RT) is the differential equation known as the *equation of transfer*. The scalar version of the equation is given by (Ishimaru 1978)[p. 157],

$$\frac{dI(\hat{\mathbf{r}},\hat{\mathbf{s}})}{ds} = -\kappa_e I(\hat{\mathbf{r}},\hat{\mathbf{s}}) + \int_{4\pi} P(\hat{\mathbf{s}},\hat{\mathbf{s}}')I(\hat{\mathbf{r}},\hat{\mathbf{s}}')\,d\Omega + J_e. \tag{2.15}$$

This equation governs the variations of intensities in a medium that absorbs, emits, and scatters radiation. Referring to Eq. (2.15), the three terms on the right hand side comprise a loss term and two source terms. The loss depends upon the extinction parameter κ_e. It comprises the effects of energy loss due to particle scattering and absorption, and may also comprise absorption effects to propagation in a lossy background in which the particles are embedded. The first source term, expressed as an integral, accounts for contributions to the intensity propagating in direction $\hat{\mathbf{s}}$ from intensity propagating in all other directions (denoted by $\hat{\mathbf{s}}'$) scattered into direction $\hat{\mathbf{s}}$. The quantity $P(\hat{\mathbf{s}},\hat{\mathbf{s}}')$, known as the phase function, governs the amount of energy scattered from one direction to another. In conventional RT (CRT) theory, analytic wave theory is normally used to compute this phase function based on the physical properties of the particles. It is one of the principal criticisms of CRT, at least for the case when it is applied to dense media, that far-field scattering phase functions are employed even though neighboring particles in dense media will also tend to occupy the near field as well.

The final source term, denoted as J_e, pertains to the energy self-emitted by the particles as governed by Planck's radiation law ((Ulaby et al. 1986), p. 192). This term, which is of principal importance for problems involving brightness temperature computations, is negligible for active radar problems, which are the focus of the present investigation.

The scalar version of the equation of transfer is suitable for problems in which polarization properties either do not exist, (e.g. acoustic waves) or where the intensity is completely

unpolarized, and the medium in which it propagates is entirely isotropic (approximately true for unpolarized light propagating in the atmosphere). At microwave frequencies, electromagnetic waves are generally not completely unpolarized. Transmitted waves have a very distinct polarization, and the variations and distortions of this state represent information to be exploited for target characterization. The Stokes parameters described above provide a means by which the relative simplicity and flexibility of radiative transfer may be used while accounting for the polarization state of the waves as well.

The vector version of Eq. (2.15) is given by (Ishimaru 1978)[p. 164]:

$$\frac{d\mathbf{I}}{ds} = -\boldsymbol{\kappa}_e \mathbf{I}(\hat{\mathbf{r}},\hat{\mathbf{s}}) + \int_{4\pi} \boldsymbol{\mathcal{P}}(\hat{\mathbf{s}},\hat{\mathbf{s}}')\mathbf{I}(\hat{\mathbf{r}},\hat{\mathbf{s}}')\,d\Omega', \tag{2.16}$$

where now the vector intensity $\mathbf{I}$ is a 4×1 vector (having as elements the four modified Stoke's parameters), $\boldsymbol{\kappa}_e$ is the 4×4 extinction matrix, and $\boldsymbol{\mathcal{P}}$ is a 4×4 phase matrix.

2.3.1 Phase Matrix

The phase matrix is constructed for the modified Stokes parameters, as given in Eq. (2.8) by considering the scattering matrix relating the incident and scattered electric fields. We have previously considered the orthogonal components of a $\hat{\mathbf{z}}$-directed plane wave. For propagation in an arbitrary direction, we consider a new local coordinate system, comprised of three orthogonal unit vectors, $\hat{\mathbf{v}}$, $\hat{\mathbf{h}}$, and the propagation direction $\hat{\mathbf{k}}$. The electric field vector is then described as $\mathbf{E} = E_v\hat{\mathbf{v}} + E_h\hat{\mathbf{h}}$, and the relationship between incident and scattered fields is (Van de Hulst 1981),

$$\begin{pmatrix} E_v^s \\ E_h^s \end{pmatrix} = \frac{e^{-jkr}}{r} \begin{pmatrix} S_{vv} & S_{vh} \\ S_{vh} & S_{hh} \end{pmatrix} \begin{pmatrix} E_v^i \\ E_h^i \end{pmatrix} \tag{2.17}$$

or,

$$\mathbf{E}^s = \frac{e^{-jkr}}{r} \mathcal{S} \mathbf{E}^i \tag{2.18}$$

where $\mathcal{S}$ is known as the scattering matrix and its elements S_{pq} as complex scattering amplitudes. Based on the relationship between the incident and scattered electric field components given in Eq. (2.17), and the construction of the Stokes parameters shown in (2.8), a corresponding expression may be obtained for the incident and scattered Stokes parameters (see for example Ulaby et al. (1986)[p. 1087]):

$$\mathbf{F}_m^s = \frac{1}{r^2} \mathcal{L}_m^\circ \mathbf{F}_m^i \tag{2.19}$$

where $\mathbf{F}_m^s$ and $\mathbf{F}_m^i$ are the scattered and indident Stokes parameters and where $\mathcal{L}_m^\circ$ is the *Stokes matrix* for a single particle given by,

$$\mathcal{L}_m^\circ = \begin{bmatrix} |S_{vv}|^2 & |S_{hh}|^2 & \mathrm{Re}(S_{vh}^* S_{vv}) & \cdots \\ |S_{hv}|^2 & |S_{hh}|^2 & \mathrm{Re}(S_{hh}^* S_{hv}) & \cdots \\ 2\mathrm{Re}(S_{vv} S_{hv}^*) & 2\mathrm{Re}(S_{vh} S_{hh}^*) & \mathrm{Re}(S_{vv} S_{hh}^* + S_{vh} S_{hv}^*) & \cdots \\ 2\mathrm{Im}(S_{vv} S_{hv}^*) & 2\mathrm{Im}(S_{vh} S_{hh}^*) & -\mathrm{Im}(S_{vv} S_{hh}^* - S_{vh} S_{hv}^*) & \cdots \end{bmatrix}$$

$$\begin{bmatrix} -\mathrm{Im}(S_{vh}^* S_{vv}) \\ -\mathrm{Im}(S_{hv}^* S_{hh}) \\ -\mathrm{Im}(S_{vv} S_{hh}^* - S_{vh} S_{hv}^*) \\ \mathrm{Re}(S_{vv} S_{hh}^* - S_{vh} S_{hv}^*) \end{bmatrix} \tag{2.20}$$

In radiative transfer, we are interested in the transport of *intensity* (W m^{-2} sr^{-1}) which has the property of being invariant along its ray path in free space. In (2.19) the incident and scattered Stokes parameters are in units of power density (W m^{-2}), different from the

intensity Stokes parameters used in vector radiative transfer (e.g. Eq. (2.16)) We are free to consider the Stokes parameters in units of intensity providing all of the mathematical operations in which they are involved are consistant with intensity operations.

Consider an *intensity* Stokes vector,**I**, with direction unit vector $\hat{\mathbf{s}}$ incident upon a cylindrical volume with cross section da and length ds, as shown in Figure 2.4. We are interested in developing an expression for the incremental increase in the intensity, denoted by $d\mathbf{I}(\hat{\mathbf{s}})$, over the incremental length of the cylinder, ds, due to intensity from all other directions $\hat{\mathbf{s}}'$ being partially scattered by the particles in the volume into direction $\hat{\mathbf{s}}$.

The volume contains $n_o\, da\, ds$ particles, where n_o is the number density of particles in the

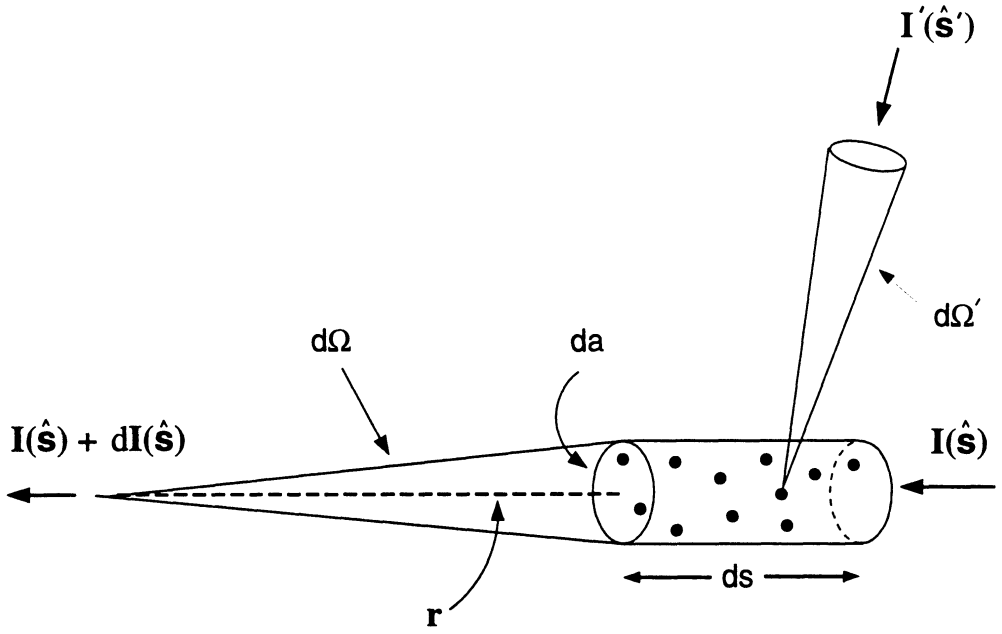

Figure 2.4: Illustration of the physical interpretion of the phase function in radiative transfer.

medium of which the cylinder is one small unit volume. The incident intensity considered for a small solid angle $d\Omega'$ represents the power density incident on one of the particles in the cylindrical volume. The single particle Stokes matrix $\mathcal{L}_m^o$ transforms this incident power density into a *scattered* power density Stokes vector. If the scattering from all of the individ-

ual particles within the volume (which number $n_o\,da\,ds$) are added up, the resulting cumulative differential increase $d\mathbf{F}_m$ to the original *power density* Stokes vector $\mathbf{F}_m$ is expressed as,

$$d\mathbf{F}_m(\hat{\mathbf{s}}) = \frac{n_o\,da\,ds}{R^2}\langle \mathcal{L}_m^\circ \rangle \mathbf{I}'(\hat{\mathbf{s}}')\,d\Omega'. \tag{2.21}$$

where $d\mathbf{F}_m(\hat{\mathbf{s}})$ and $\mathbf{I}'(\hat{\mathbf{s}}')\,d\Omega' = \mathbf{F}'_m(\hat{\mathbf{s}}')$ are both in units of W m^{-2}. The angle brackets $\langle\,\rangle$ denote ensemble averaging of the single particle Stokes matrix over distributions associated with the particles such as size and orientation, etc.. This ensemble-averaged form is typically referred to as the "Mueller" matrix, and denoted as $\mathcal{L}_m = \langle \mathcal{L}_m^\circ \rangle$. Making this substitution and noting that the small solid angle in the direction $\hat{\mathbf{s}}$ is $d\Omega = da/r^2$, Eq. (2.21) becomes,

$$d\mathbf{F}_m(\hat{\mathbf{s}}) = (n_o\,ds\,d\Omega)\,\mathcal{L}_m \mathbf{I}'(\hat{\mathbf{s}}')\,d\Omega'. \tag{2.22}$$

Dividing by the length ds of the cylindrical volume gives,

$$\frac{d\mathbf{F}_m}{ds} = (n_o\,d\Omega)\,\mathcal{L}_m \mathbf{I}'(\hat{\mathbf{s}}')\,d\Omega'. \tag{2.23}$$

Dividing both sides by the solid angle $d\Omega$ allows us to now express the left hand side as a scattered *intensity* Stokes vector:

$$\frac{d\mathbf{I}(\hat{\mathbf{s}})}{ds} = n_o\,\mathcal{L}_m \mathbf{I}'(\hat{\mathbf{s}}')\,d\Omega', \tag{2.24}$$

$$\frac{d\mathbf{I}(\hat{\mathbf{s}})}{ds} = \mathcal{P}(\hat{\mathbf{s}},\hat{\mathbf{s}}')\,\mathbf{I}'(\hat{\mathbf{s}}')\,d\Omega', \tag{2.25}$$

where the quantity,

$$\mathcal{P} = n_o\mathcal{L}_m = n_o\langle \mathcal{L}_m^\circ \rangle, \tag{2.26}$$

is the *phase matrix*, consistant with interpretation of the Stokes parameters in terms of intensities. This analysis considered scattering from only a single direction $\hat{\mathbf{s}}'$ into the direction $\hat{\mathbf{s}}$. For the total contribution to the intensity Stokes vector $I(\hat{\mathbf{s}})$ due to the incremental volume of length ds, it is necessary to integrate the contributions from all directions $\hat{\mathbf{s}}'$, giving, for the scattering contributions to the intensity *only*,

$$\frac{d\mathbf{I}(\hat{\mathbf{s}})}{ds} = \int_{4\pi} \boldsymbol{\mathcal{P}}(\hat{\mathbf{s}}, \hat{\mathbf{s}}')\,\mathbf{I}'(\hat{\mathbf{s}}')\,d\Omega', \tag{2.27}$$

which is seen to be the scattering source function appearing on the right hand side of Eq. (2.16).

2.3.2 Extinction Matrix

An additional effect of propagation of the intensity Stokes vector through the cylindrical volume of Figure 2.4 is losses due to both scattering and absorption by the particles. This effect is described in Eq. (2.16) by the term,

$$\frac{d\mathbf{I}(\hat{\mathbf{s}})}{ds} = -\boldsymbol{\kappa}_e \mathbf{I}(\hat{\mathbf{s}}) \tag{2.28}$$

where $\boldsymbol{\kappa}_e$ is the *extinction matrix*.

In radiative transfer, the extinction is defined, for a collection of uniform particles, as

$$\kappa_e = n_o \sigma_e \tag{2.29}$$

where σ_e is the extinction cross-section of a single particle, equivalent to the sum of its scattering and absorption cross-sections. The extinction cross-section may be computed using the forward scattering (or optical) theorem (see, for example Ishimaru (1978)):

$$\sigma_e = \frac{4\pi}{k} \mathrm{Im}[S_{pq}(\theta_i, \phi_i; \theta_i, \phi_i)] \tag{2.30}$$

where k is the wavenumber in the medium and S_{pq} is the complex scattering amplitude evaluated in the forward scattering direction.

The extinction may also include, when present, the effect of a lossy background as,

$$\kappa_e' = \kappa_e + \kappa_{ag} \tag{2.31}$$

where,

$$\kappa_e = 2k_o|\mathrm{Im}[\sqrt{\varepsilon}]| \tag{2.32}$$

where k_o is the free space wavenumber and ε is the dielectric constant of the background medium.

In a vector treatment, for general non-spherical particles, the extinction matrix has been shown by Ishimaru and Cheung (1980) to be,

$$\boldsymbol{\kappa_e} = \tag{2.33}$$

$$\begin{bmatrix} -2\mathrm{Re}(M_{vv}) & 0 & \mathrm{Re}(M_{vh}) & \mathrm{Im}(M_{vh}) \\ 0 & -2\mathrm{Re}(M_{hh}) & -\mathrm{Re}(M_{hv}) & \mathrm{Im}(M_{hv}) \\ -2\mathrm{Re}(M_{hv}) & -2\mathrm{Re}(M_{vh}) & -\mathrm{Re}(M_{vv}+M_{hh}) & \mathrm{Im}(M_{vv}+M_{hh}) \\ 2\mathrm{Im}(M_{hv}) & -2\mathrm{Im}(M_{vh}) & -\mathrm{Im}(M_{vv}-M_{hh}) & -\mathrm{Re}(M_{vv}+M_{hh}) \end{bmatrix}$$

where,

$$M_{mn} = \frac{-2j\pi n_o}{k_o}\langle S_{mn}(\theta_i,\phi_i;\theta_i,\phi_i)\rangle; \qquad m,n = v,h. \tag{2.34}$$

For the case of spherical particles, the extinction matrix becomes a diagonal matrix with elements κ_e as in the scalar case.

2.4 Backscatter Coefficient and Polarization Synthesis

For point targets, we are normally interested in the *radar cross section (RCS)* of a target, which has been defined, for fields, as (Ulaby and Elachi 1990)[p. 138],

$$\sigma^{\circ}_{pq} = 4\pi r^2 \frac{|E^s_p|^2}{|E^i_q|^2} \tag{2.35}$$

with $p \in [\,\hat{\mathbf{v}}_s\ \hat{\mathbf{h}}_s\,]$ and $q \in [\,\hat{\mathbf{v}}_i\ \hat{\mathbf{h}}_i\,]$. Besides the linear polarizations indicated above, a backscattering coefficient may be computed for *any* arbitrary transmitted and received polarizations, providing either the scattering matrix or the target Mueller matrix is known. In this process, known as *polarization synthesis* (van Zyl et al. 1987), the convention is to use BSA. Accordingly, when applying it, we will consider "transmitted" and "received" waves and designate the Mueller matrix with an overbar (e.g. $\overline{\mathcal{L}_m}$) to denote we are using the BSA convention. The transformation matrix which is used to convert a Mueller matrix from one scattering alignment convention to another is described below in Section 2.5.

If the polarization properties of the wave are described in terms of the ellipticity parameters ψ and χ, then, for fields (Ulaby and Elachi 1990),

$$\sigma_{rt}(\psi_r, \chi_r; \psi_t, \chi_t) = 4\pi |\mathbf{p}^r \cdot \mathcal{S}\mathbf{p}^t|^2 \tag{2.36}$$

where,

$$\mathbf{p}^m = \frac{\mathbf{E}^m}{\sqrt{\mathbf{E}^m \cdot \mathbf{E}^{m*}}} \qquad m = r,t, \tag{2.37}$$

where $\mathbf{E}^m$ denotes either the transmitted (t) or received (r) electric field vector.

In terms of the discrete target Mueller matrix where,

$$\mathbf{F}^s_m = \frac{1}{r^2} \langle \mathcal{L}^{\circ}_m \rangle \mathbf{F}^i_m, \tag{2.38}$$

the corresponding equation for the RCS is,

$$\sigma_{rt}(\psi_r, \chi_r; \psi_t, \chi_t) = 4\pi \mathbf{A}_m^r \cdot \boldsymbol{\mathcal{M}}_m \mathbf{A}_m^t \tag{2.39}$$

where $\boldsymbol{\mathcal{M}}_m$ is the modified Stokes scattering operator given by,

$$\boldsymbol{\mathcal{M}}_m = \boldsymbol{Q}\overline{\boldsymbol{\mathcal{L}}_m} \tag{2.40}$$

where,

$$\boldsymbol{Q} = \begin{bmatrix} 1 & 0 & 0 & 0 \\ 0 & 1 & 0 & 0 \\ 0 & 0 & 1/2 & 0 \\ 0 & 0 & 0 & -1/2 \end{bmatrix}, \tag{2.41}$$

and $\mathbf{A}_m^r$ and $\mathbf{A}_m^t$ are the received and transmitted *normalized* modified Stokes vectors given by $\mathbf{A}_m^r = \mathbf{F}_m(\psi_r, \chi_r)/I_o$ and $\mathbf{A}_m^t = \mathbf{F}_m(\psi_t, \chi_t)/I_o$, respectively.

For distributed targets, we normally speak of *backscatter coefficients*, $\sigma^\circ = \sigma/\Delta A$, where ΔA is a unit illuminated area of the distributed target. In terms of intensities corresponding the the principal polarizations of a wave (i.e. $\hat{\mathbf{v}}$ and $\hat{\mathbf{h}}$), we note that,

$$\frac{|E_p^s|^2}{2\eta} = I_p^s d\Omega = I_p^s \frac{A\cos\theta_i}{r^2} \tag{2.42}$$

$$\frac{|E_q^i|^2}{2\eta} = I_q^i \tag{2.43}$$

since the scattered wave is a spherical wave but the incident wave may be considered a plane wave. The angle θ_i is the incidence angle. Substituting Eqs. (2.42) and (2.43) into Eq. (2.35), and summing the contributions from all of the patches ΔA in the total illuminated

area A as,

$$\sigma^{\circ}_{pq} = \sum_{i}^{N} \frac{\sigma_i}{(\Delta A)_i}. \tag{2.44}$$

gives the definition of the backscattering coefficient in terms of incident and scattered intensities:

$$\sigma^{\circ}_{pq} = 4\pi \cos\theta_i \frac{I^s_p}{I^i_q} \tag{2.45}$$

As for the point target case, to compute the backscatter for an arbitrary polarization, a more general procedure is required. Consider (following Ulaby and Elachi (1990)[pp. 162–163]) a general transformation matrix $\mathcal{T}$, relating the intensity Stokes vector received from a distributed target to the transmitted intensity Stokes vector:

$$\mathbf{I}^s = \mathcal{T}\mathbf{I}^i. \tag{2.46}$$

Since,

$$\mathbf{F}^s_m = \mathbf{I}^s \, d\Omega^s = \mathbf{I}^s \frac{A\cos\theta_s}{r^2}, \tag{2.47}$$

$$\mathbf{F}^i_m = \mathbf{I}^i, \tag{2.48}$$

we have,

$$\mathbf{F}^s_m = \frac{A\cos\theta_s}{r^2} \mathcal{T}\mathbf{F}^i_m. \tag{2.49}$$

Comparing Eq. (2.49) with Eq. (2.38), we see that $\mathcal{T}$ is of the form,

$$\mathcal{T} = \frac{1}{A\cos\theta_s} \mathcal{L}_m. \tag{2.50}$$

We can therefore apply the polarization synthesis techniques as before, to Eq. (2.49), giving, for the backscatter coefficient for arbitrary transmitted and received polarizations,

$$\sigma^{\circ}_{rt}(\psi_r,\chi_r;\psi_t,\chi_t) = \sum_i^N \frac{[\sigma_{rt}(\psi_r,\chi_r;\psi_t,\chi_t)]_i}{(\Delta A)_i} = 4\pi\cos\theta_r \mathbf{A}^r_m \cdot \boldsymbol{\mathcal{M}}_m \mathbf{A}^t_m \tag{2.51}$$

where $\mathbf{A}^r_m$, $\mathbf{A}^t_m$, and $\boldsymbol{\mathcal{M}}_m$ are as defined for the discrete target case in Eq. (2.39).

2.5 Polarization Transformation Matrix

In comparing measured results in the form of Mueller matrices with theory it is often necessary to convert expressions formulated under the FSA convention to the BSA convention and vice versa. This is easily accomplished by considering that, for backscatter, the FSA convention defines a scattered horizontal component of a wave, $\hat{\mathbf{h}}_s$, as being 180° out of phase relative to the corresponding $\hat{\mathbf{h}}_s$ component under the BSA convention. Thus, elements in the Mueller matrix having an *uncompensated* $\hat{\mathbf{h}}_s$ undergo a sign reversal. For example, a term like $S_{vv}S_{hh}$ (recall that the first subscript denotes the scattered polarization) does require a sign reversal going between the FSA and BSA conventions but $S_{hh}S^*_{hv}$ does not because the presence of two scattered horizontal components cancel the effect. This conversion is accomplished by the operation,

$$\overline{\boldsymbol{\mathcal{L}}_m} = \boldsymbol{\mathcal{T}}_a \boldsymbol{\mathcal{L}}_m \tag{2.52}$$

where $\overline{\mathcal{L}_m}$ and $\mathcal{L}_m$ denote the Mueller matrices assembled under the BSA and FSA conventions respectively. The transformation matrix $\mathcal{T}_a$ is given by,

$$\mathcal{T}_a = \begin{bmatrix} 1 & 0 & 0 & 0 \\ 0 & 1 & 0 & 0 \\ 0 & 0 & -1 & 0 \\ 0 & 0 & 0 & -1 \end{bmatrix} \tag{2.53}$$

CHAPTER III

SNOW PROBE FOR *IN SITU* DETERMINATION OF WETNESS AND DENSITY

3.1 Introduction

In the study of microwave remote sensing of snow, it is necessary to consider the presence of liquid water in the snowpack. The dielectric constant of water is large (e.g., $\varepsilon_w = 88 - j9.8$ at 1 GHz (Sihvola and Tiuri 1986)) relative to that of ice ($\varepsilon_i \approx 3.15 - j0.001$ (Hallikainen et al. 1986)), and therefore even a very small amount of water will cause a substantial change in the overall dielectric properties of the snow medium, particularly with respect to the imaginary part. These changes will, in turn, influence the radar backscatter and microwave emission responses of the snowpack.

Among instruments available for measuring the volumetric liquid-water content of snow, m_v, under field conditions, the freezing calorimeter (Austin 1990; Jones et al. 1983; Stiles and Ulaby 1980b) offers the best accuracy ($\approx 1\%$) and has been one of the most widely used in support of quantitative snow-research investigations. In practice, however, the freezing calorimeter technique suffers from a number of drawbacks. First, the time required to perform an individual measurement of m_v is about thirty minutes. Improving the temporal resolution to a shorter interval would require the use of multiple instruments, thereby increasing the cost and necessary manpower. Second, the technique is rather involved, requiring the use of a freezing agent and the careful execution of several steps. Third, the freezing

calorimeter actually measures the mass fraction of the liquid water in the snow sample, W, not the volumetric water content m_v. To convert W to m_v, a separate measurement of snow density is required. Fourth, because a relatively large snow sample (about 250 cm^3) is needed to achieve acceptable measurement accuracy, it is difficult to obtain the sample from a thin horizontal layer, thereby rendering the technique impractical for profiling the variation of m_v with depth. Yet, the depth profile of m_v, which can exhibit rapid spatial and temporal variations (Colbeck 1991; Ellerbruch and Boyne 1980), is one of the most important parameters of a snowpack, both in terms of the snowpack hydrology and the effect that m_v has on the microwave emission and scattering behavior of the snow layer.

In experimental investigations of the radar response of snow-covered ground, it is essential to measure the depth profile of m_v with good spatial resolution (2-3 cm) and adequate temporal resolution (a few minutes), particularly during the rapid melting and freezing intervals of the diurnal cycle. There have in recent years appeared a host of instruments (Denoth 1984) which retrieve snow parameters quickly and non-destructively, by measuring the dielectric constant of snow and relating it to the physical parameters. Of these techniques, the most attractive candidate has been the "Snow Fork", a microwave instrument developed in Finland (Sihvola and Tiuri 1986). The strengths of this technique are the simplicity of the equipment and speed of the measurement, high spatial resolution, and the ability to measure both the real and imaginary parts of the dielectric constant of snow, allowing for more powerful algorithms allowing determination of snow wetness and density with a single measurement. In the process of examining the Snow Fork approach, we decided to modify the basic design to improve the sensitivity of the instrument to m_v and reduce the effective sampled volume of the snow medium, thereby improving the spatial resolution of the sensor. Our modified design, which we shall refer to as the "Snow Probe" is described in Section 2. The Snow Probe measures the real and imaginary parts of the relative dielectric constant of the snow medium, from which the liquid water content m_v and the snow density ρ_s are calculated through the use of empirical or semi-empirical relations. The degree to which such

relations are valid is established through a comparison with direct techniques. Therefore, in the process of developing a Snow Probe algorithm, it was necessary to perform independent measurements of ρ_s and m_v. Density measurements were performed with a standard tube of known volume, whose weight is measured both empty and full of snow. For a direct technique for measuring m_v we evaluated (Appendix A) two candidates: (1) the freezing calorimeter; and (2) the dilatometer (Leino et al. 1982), which measures the change in volume that occurs as a sample melts completely. The dilatometer approach was rejected because of poor measurement accuracy and long measurement time (about one hour). The form of the relations which were ultimately established as a result of these comparison studies is described in Section 3.3.

3.2 Snow Dielectric Probe

3.2.1 Snow Probe Measurement System

Figures 3.1 and 3.2 show a photograph of the Snow Probe measurement system, and a schematic diagram, respectively. The sweep oscillator, under computer control, sweeps (in discrete 10 MHz steps) over a relatively large frequency range. This serves to determine, within ± 5 MHz, the frequency at which the detected voltage is a maximum, corresponding to the resonant frequency of the probe. The RF power transmitted thru the Snow Probe is converted to video by the crystal detector, measured by the voltmeter, which in turn sends the voltage values to the computer. The frequency spectrum is generated in real-time on the monitor of the computer. In the second pass, a much narrower frequency range is centered around the peak location and swept with a finer step size (≈ 1 MHz). The center frequency and the 3-dB bandwidth around it are found, and from these, first the dielectric constant and then the snow parameters m_v and ρ_s are determined according to procedures described in detail in Section 3 of this chapter.

As it is depicted in these figures, the Snow Probe is connected to a coaxial cable ap-

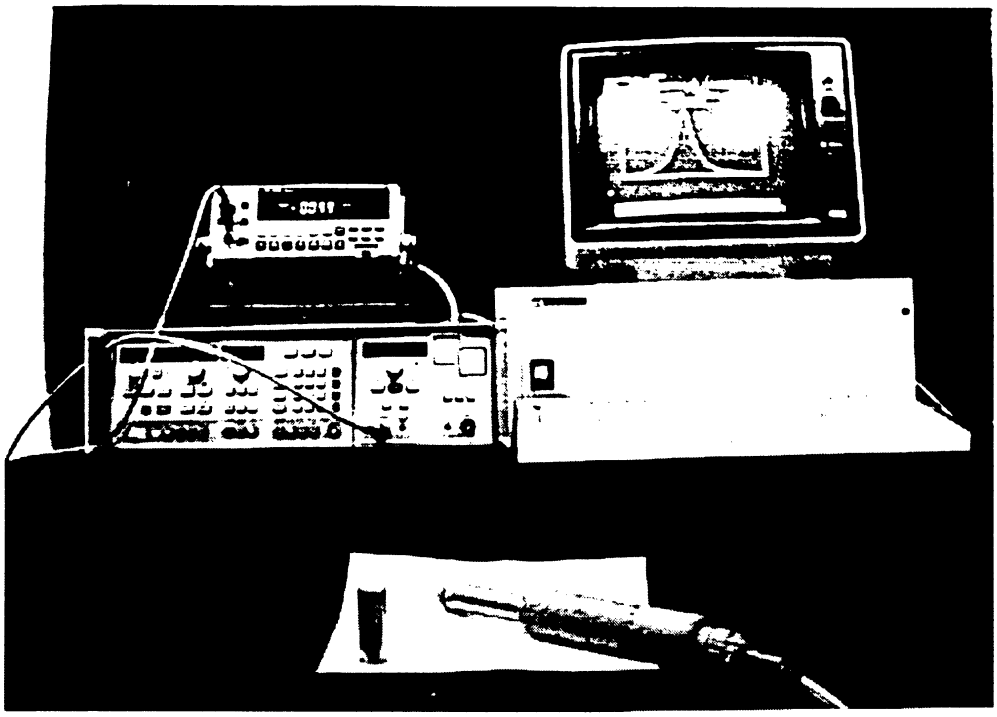

Figure 3.1: Photograph of Snow Probe system.

proximately 15 meters long. This arrangement is suitable, for example, for cases in which measurements are required in an area fairly local to truck mounted radars. For more remote field applications, the functions of the hardware shown would need to be combined into a portable unit. The technology for building a compact unit is well established.

3.2.2 Sensor Design

The Snow Probe is essentially a transmission-type electromagnetic resonator. The resonant structure used in the original design (Sihvola and Tiuri 1986) was a twin-pronged fork. This structure behaves as a two wire transmission line shorted on one end and open on the other. It is resonant at the frequency for which the length of the resonant structure is equivalent to $\lambda/4$ in the surrounding medium. The RF power is fed in and out of the structure using coupling loops.

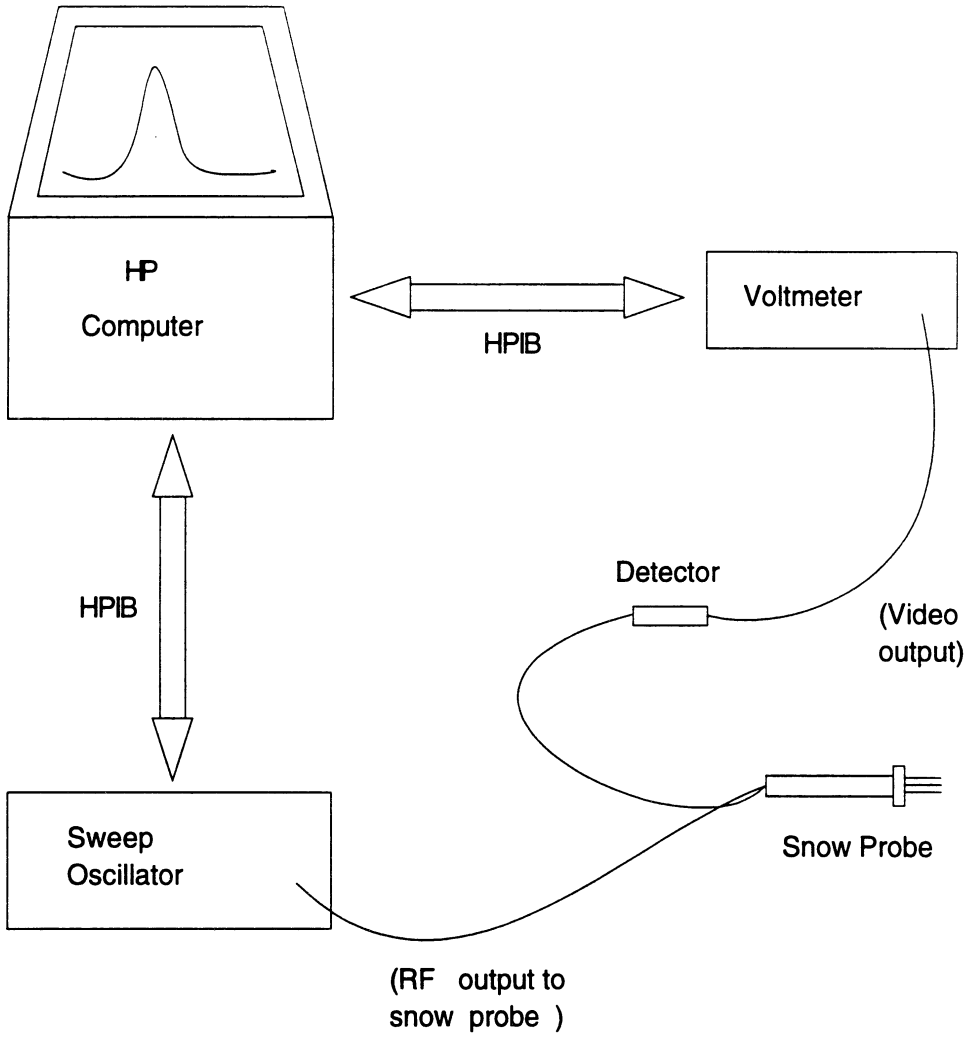

Figure 3.2: Schematic diagram of Snow Probe system.

For our design, we used a coaxial type resonator, as illustrated in Figure 3.3. The skeleton of the outer conductor is achieved using four prongs. The principle is basically the same: a quarter wavelength cavity, open on one end, shorted on the other, with power delivered in and out through coupling loops. The coaxial design was chosen for purposes of spatial resolution. Being a shielded design, the electric field is confined to the volume contained within the resonant cavity, as opposed to the original design, which used only two prongs. The coaxial design also had a much higher quality factor, (≈ 110 *vs.* $40-70$ for the original design) which, as discussed below, allows for more accurate determination of the complex dielectric constant. A photograph of the Snow Probe is shown in Figure 3.4. The stainless-steel band encircling the resonant structure near the bottom is necessary to defeat competing two-wire resonances which are otherwise excited between any given pair of the outer prongs.

The real part of the dielectric constant is determined by the resonant frequency of the transmission spectrum, or equivalently, the frequency at which maximum transmission occurs. As mentioned above, this corresponds to the frequency for which the wavelength *in the medium* is equal to four times the length of the resonator. If the measured resonant frequency is f_a in air and f_s in snow, then the real part of the dielectric constant is given by

$$\varepsilon_s' = \left(\frac{f_a}{f_s}\right)^2 . \tag{3.1}$$

The imaginary part of ε_s is determined from the change in Q_m, the measured quality factor of the resonator. The quality factor may be determined by measuring Δf, the half-power bandwidth (Collin 1966):

$$Q_m = \frac{f_r}{\Delta f} , \tag{3.2}$$

where f_r is the resonant frequency (f_a or f_s, depending on whether the medium is air or snow). For the Snow Probe, power losses exist because of radiation, finite conductivity of

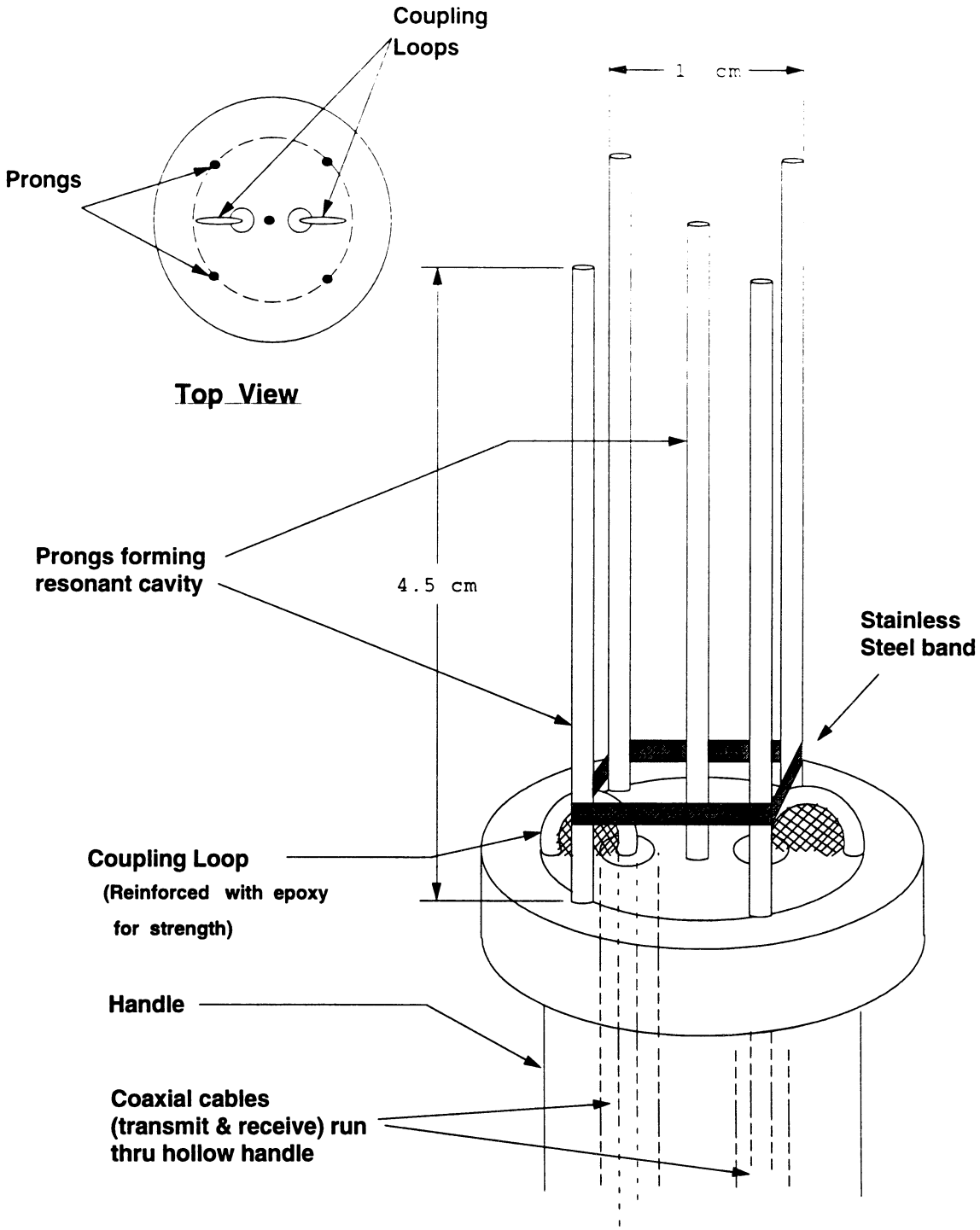

Figure 3.3: Illustration of Snow Probe. Coaxial transmission lines extend through handle. At the face of the Snow Probe, the center conductors of the coaxial lines extend beyond and curl over to form coupling loops.

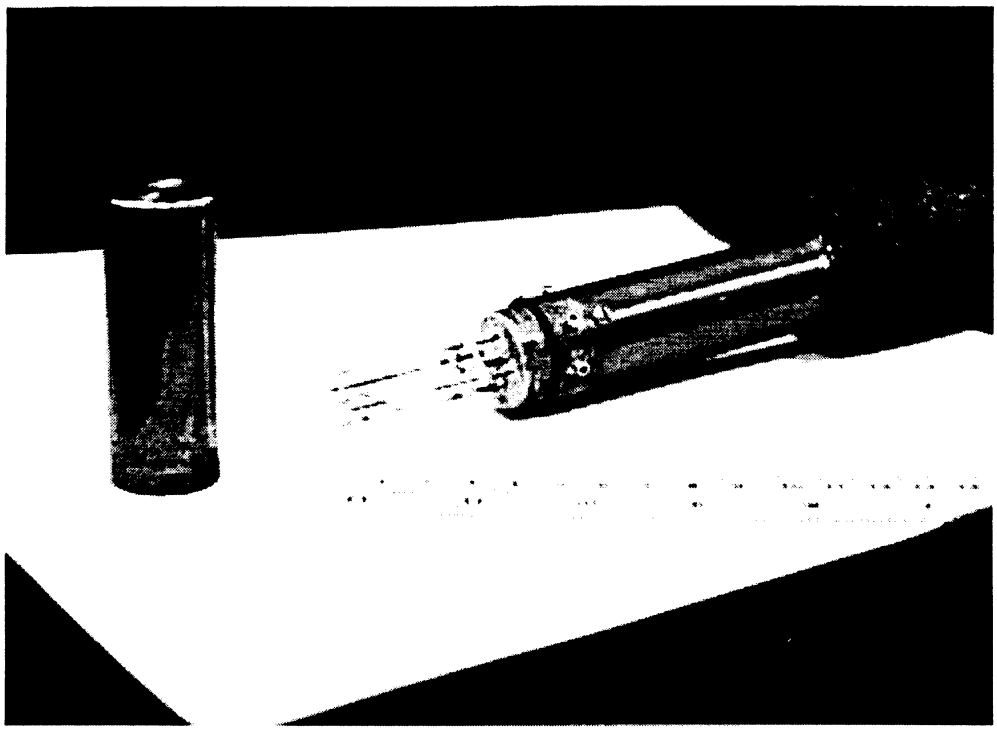

Figure 3.4: Photograph of Snow Probe with cap.

Material	$\bar{\varepsilon}$	(GHz) f_R	Q_m
Air	$1.0 - j0.0$	1.715	125
Sand	$2.78 - j3.7 \times 10^{-2}$	1.036	52
Sugar	$1.98 - j0.8 \times 10^{-2}$	1.229	89
Coffee	$1.50 - j3.3 \times 10^{-2}$	1.431	30
Wax	$2.26 - j0.3 \times 10^{-3}$	1.150	137

Table 3.1: Summary of test material properties and measurements.

the conductors, coupling mechanisms (ie. coupling loops), and dissipation in a lossy dielectric. Thus the measured Q is given by Collin (1966):

$$\frac{1}{Q_m} = \frac{1}{Q_R} + \frac{\varepsilon''}{\varepsilon'}, \tag{3.3}$$

where Q_m is the measured Q when the probe is inserted in the snow medium, and Q_R is the quality factor describing collectively radiation losses, losses due to the finite conductivity of the conductors, and the power losses due to the external coupling mechanisms for the dielectric-filled Snow Probe. To calculate ε'', from (3.3), one must not only measure Q_m and know ε', but the value of Q_R should be known also. As long as $\tan\delta = \varepsilon''/\varepsilon'$ is very small, which is the case for snow, it is reasonable to assume that Q_R is a function of ε' only. This assumption was verified experimentally by measuring Q_R for each of five materials with known dielectric properties (Table 3.2.2). For each material, Q_m was calculated by (3.2) on the basis of measurements of Δf and f_r and then it was used in (3.3) to compute Q_R. The values of ε' and ε'' of the test materials given in Table 3.2.2 were measured with an L-band cavity resonator (details of this process are given in Appendix B). This process not only validated the assumption that Q_R is dependent on ε' only, but it also produced an expression for computing it:

$$\frac{1}{Q_R} = \frac{(pf_r + b) \times 10^{-3}}{f_r}, \tag{3.4}$$

where p and b are constants and f_r is the resonant frequency associated with the material under test (which is related to ε' by $\varepsilon' = (f_a/f_r)^2$). For the probe used in this study, $p = 8.381$ and $b = 0.7426$ when f_r is in GHz. Combining (3.2),(3.3), and (3.4) and specializing the notation to snow (by adding a subscript s to ε'' and replacing the subscript r by s in f_r) we obtain the expression:

$$\varepsilon'' = \left(\frac{f_a}{f_s}\right)^2 \left[\frac{\Delta f_s}{f_s} - (p + \frac{b}{f_s})\right]. \tag{3.5}$$

Equations (3.1) and (3.5) constitute the basic relations used for determining ε'_s and ε''_s from measurements of f_a, the resonant frequency when the probe is in air, and f_s and Δf_s, the resonant frequency and associated 3-dB bandwidth measured when the probe is inserted in the snow sample.

3.2.3 Spatial Resolution / Outside Interference

As mentioned earlier, the partially shielded design of this sensor reduces its sensitivity to permittivity variations outside the sample volume. By sample volume, we refer to the volume inside the cylinder described by the four outside prongs (Figure 3.3). The coaxial design will tend to produce greater field confinement relative to a twin-prong structure.

The effective sample volume was tested in the following way: a cardboard box (30cm $\times$ 30cm) was filled with sugar to a depth of $\approx$ 16 cm. The Snow Probe was inserted into the sugar at a position in the center of the top surface, and then the dielectric constant was measured. Next, a thin metal plate (square, $\approx$ 25 cm on a side) was inserted into the sugar, parallel to and resting against one side of the box. The dielectric constant was re-measured. The metal plate was incrementally moved closer to the sensor position, with dielectric measurements recorded at each sensor-to-plate distance. The results of the experiment are shown in Figure 3.5, in which ε'' is plotted as a function of the sensor-to-plate separation.

The plate appears to have a weak influence on the measurement, even at a distance of

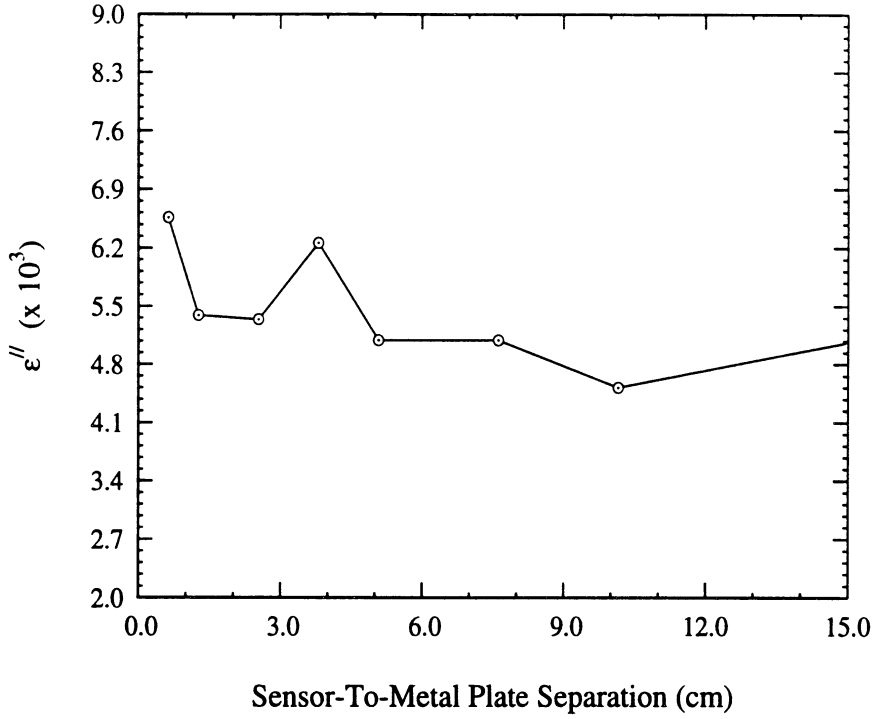

Figure 3.5: Variation in measurement of ε'' of sugar as a function of sensor proximity to metal plate. (Real part ε' stayed in the range 2.00 - 2.01.)

only 0.6 centimeters. To put this variation into perspective, had the material been snow, and using the relations given in section 3.1, the fluctuation in the estimate of liquid water would have ranged from $m_v = 0.6\%$ to $m_v = 0.8\%$. The real part of the dielectric constant (not shown in Figure 3.5) stayed within the range 2.00 - 2.01 during the experiment. The results of this experiment, which essentially confirm the expectation that the electric field is confined to the volume enclosed by the four prongs, translate into a vertical resolution of about 2 cm when the Snow Probe is inserted into the snowpack horizontally (the Snow Probe cross section is 1cm $\times$ 1cm).

There is necessarily a compromise between the ability to make high spatial resolution measurements and maximum ruggedness of design. The overall small size of the probe requires the use of small diameter prongs as well to insure that the snow volume which is being sampled is not compressed to the point of compromising the measurement. Though we used stainless steel for the prongs to afford maximum strength, it is still possible—for snow samples which are especially dense, coarse, or icy—to have some bending of the prongs occur. For some extreme cases the probe might not be a practical option for a measuring device. In these cases, it may also be the case that the simple relationships (which will be described in Section 3.3) between dielectric constant and snow parameters no longer hold.

3.3 Retrieval of Snow Density and Liquid Water Content

The preceding section described the design and operation of the Snow Probe and the procedure used for measuring ε_s' and ε_s'' of the snow medium. The next step is to use these measurements to determine the density ρ_s and liquid-water content m_v. This is accomplished by using a set of empirical or semi-empirical relationships relating the dielectric constant of wet snow to its density and liquid-water content. These relationships express the dielectric constant of wet snow ε_{ws} in terms of ε_{ds}, the dielectric constant of the snow in the absence of liquid water, plus additional terms that account for the increase in ε' and ε'' due to the

presence of liquid water:

$$\varepsilon'_{ws} = \varepsilon'_{ds} + \Delta' \tag{3.6}$$

$$\varepsilon''_{ws} = \varepsilon''_{ds} + \Delta'' \tag{3.7}$$

where Δ' and Δ'' represent the incremental increases due to m_v. The particular expressions for these quantities which we adopt for evaluation are based on the dispersion behavior of liquid water (Hallikainen et al. 1986):

$$\Delta' = 0.02 m_v^{1.015} + \frac{0.073 m_v^{1.31}}{1 + (f_s/f_w)^2} \tag{3.8}$$

$$\Delta'' = \frac{0.073 (f_s/f_w) m_v^{1.31}}{1 + (f/f_w)^2} \tag{3.9}$$

where f_s is the resonant frequency at which ε'_{ws} and ε''_{ws} are measured by the probe, $f_w = 9.07$ GHz is the relaxation frequency of water at 0° C, and m_v is expressed in percent. Thus, the quantities measured by the Snow Probe are ε'_{ws}, ε''_{ws}, and f_s, and the quantities we wish to retrieve are m_v and ρ_{ws}, the latter being the density of the wet snow medium.

3.3.1 Liquid-Water Content

In the frequency range around 1 GHz, which is the operational frequency range of the probe, the dielectric loss factor of dry snow ε''_{ds} is less than 4×10^{-4} (for a snow density ρ_{ds} less than 0.5 g/cm^3). For $m_v = 1\%$, the increment Δ'' given by (3.9) is equal to 7.5×10^{-3}, which is approximately 20 times larger than the first term. Hence, ε''_{ds} may be ignored in (3.7) and the equation can be solved to express m_v in terms of ε''_{ws}:

$$m_v = \left\{ \frac{\varepsilon''_{ws} \left[1 + (f_s/f_w)^2\right]}{0.073 (f_s/f_w)} \right\}^{\frac{1}{1.31}}. \tag{3.10}$$

The applicability of this retrieval procedure was evaluated by comparing the results obtained using (3.10) on the basis of the snow-probe measurements with those measured with a freezing calorimeter. The freezing calorimeter measures the liquid water mass fraction W, from which m_v was calculated by using the relationship

$$m_v = 100\rho_{ws}W. \tag{3.11}$$

where ρ_{ws} is the density of the wet snow sample, which was measured gravimetrically.

The results for the liquid water content comparison are shown in Figure 3.6. The error bars associated with the freezing calorimeter data points show the range of results obtained from typically two separate (and usually simultaneous) determinations. (Data points with no error bars indicate only a single measurement or that only the mean value of a set was available.) The freezing calorimeter has generally excellent precision.

The values for m_v obtained from the Snow Probe dielectric measurements are computed by equation (3.10). The data points and error bars shown for the Snow Probe are based on an average of twelve separate measurements made for each snow sample and the uncertainty of the estimate of the mean value as represented by the error bars was computed as $\pm\sigma/\sqrt{N}$ where σ is the standard deviation of the set of measurements and N is the number of measurements in that set. From the figure, the agreement between the two techniques is generally very good, and, with the exception of an outlier at the 6% level, the use of the Snow Probe and (3.9) gives results which are within $\pm 0.5\%$ of the freezing calorimeter results. This result strongly supports the validity of equation (3.9).

3.3.2 Snow Density

With m_v known, through the retrieval procedure described in the preceding section, we now turn our attention to using (3.6) and (3.8) in order to retrieve the wet snow density ρ_{ws} from ε'_{ws}, the dielectric constant of the wet snow medium measured by the Snow Probe. To

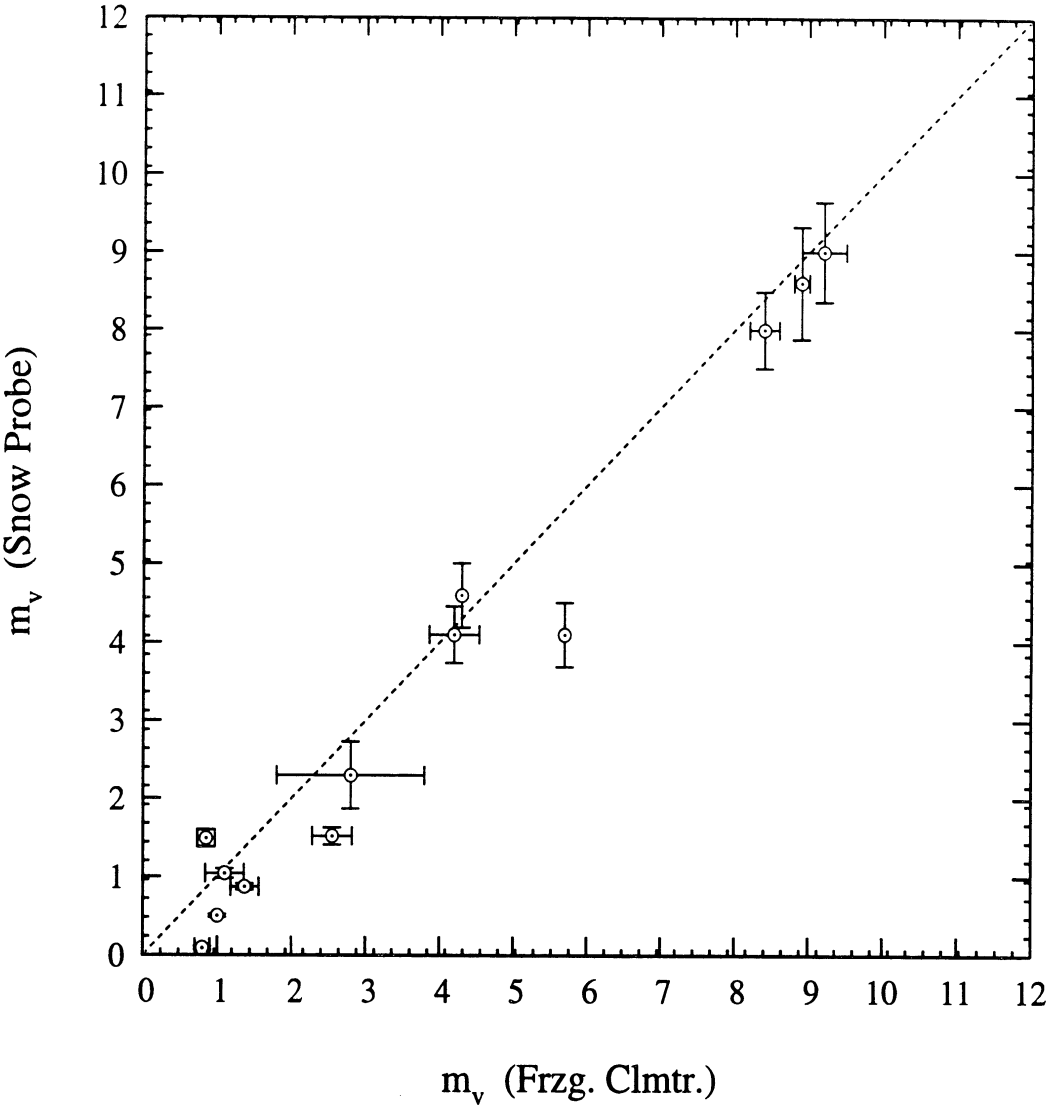

Figure 3.6: Comparison of snow wetness results obtained *via* Snow Probe and freezing calorimetry respectively. Snow Probe data points are based on an average of twelve separate measurements.

do so, we first express ρ_{ws} in terms of ρ_{ds}, the density of the snow had the liquid water been removed,

$$\rho_{ws} = \rho_{ds} + m_v/100. \tag{3.12}$$

Next, we use the expression (Tiuri et al. 1984),

$$\varepsilon'_{ds} = 1 + 1.7\rho_{ds} + 0.7\rho_{ds}^2, \tag{3.13}$$

and combine it with (3.6) to obtain the result:

$$\varepsilon'_{ws} = 1 + 1.7\rho_{ds} + 0.7\rho_{ds}^2 + \Delta', \tag{3.14}$$

where Δ' is given in (3.8). Upon combining (3.12) and (3.14) and solving for ρ_{ws}, we obtain the expression

$$\rho_{ws} = (m_v/100) - 1.214 + \sqrt{1.474 - 1.428(1 - \varepsilon'_{ws} + \Delta')}, \tag{3.15}$$

in which only the positive root is considered. To compute ρ_{ws} from (3.15), we use the value of m_v determined in the previous section through (3.10), the value of ε'_{ws} measured by the snow probe, and the value of Δ' calculated from (3.8). The values of ρ_s (for both wet and dry snow) determined through this procedure are compared with gravimetric measurements of ρ_s in Figure 3.7. The data points for which good agreement is found correspond to snow samples having low wetness levels, $< 3\%$, for which the contribution Δ' is small anyway. For the samples in which the m_v is more appreciable, there is a significant disagreement between the measurements and the model given by (3.8).

The errors in density estimates are caused by the model underestimating the incremental increase $\Delta\varepsilon'_{ws}$ for the higher wetness cases. Shown in Figure 3.8 is a plot of $\Delta\varepsilon'_{ws}$ as a

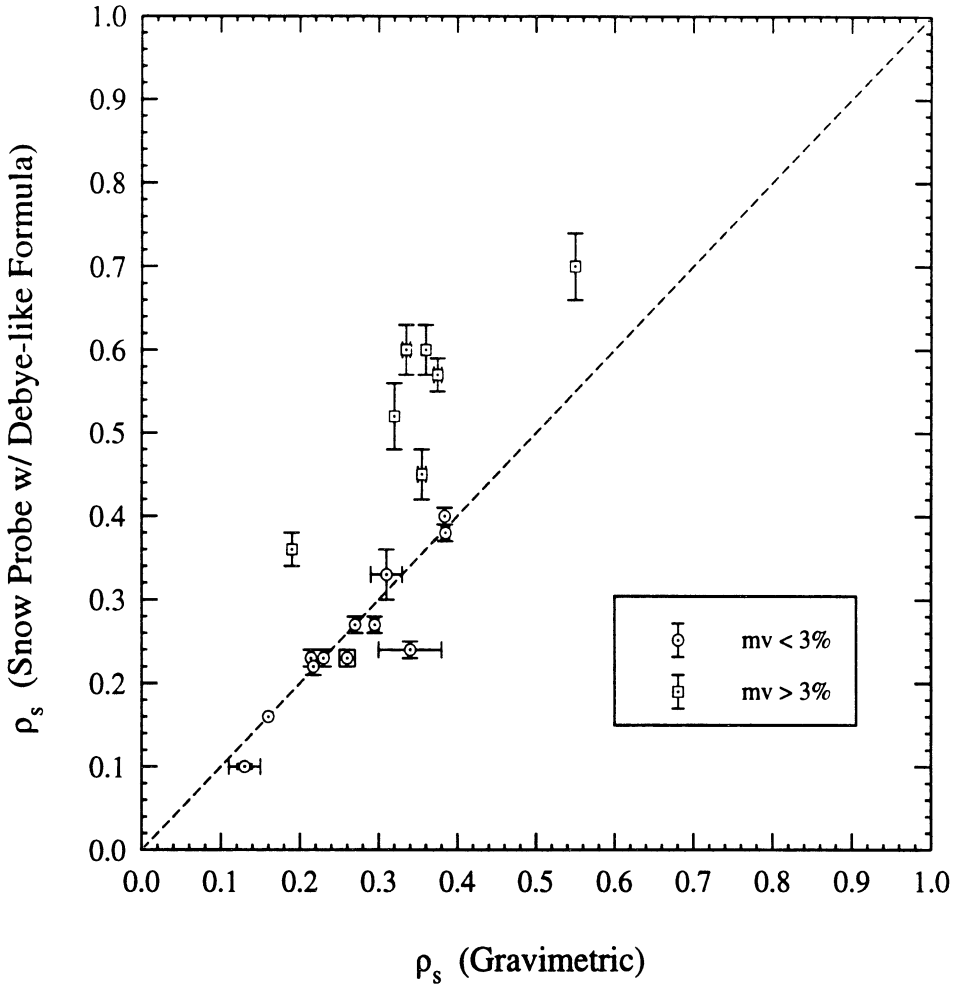

Figure 3.7: Comparison of snow density results obtained *via* Snow Probe (in conjuction with Debye-like relation) and gravimetric measurements. Data points represented with squares were from snowpacks having volumetric wetness levels of $> 3\%$; with circles, $< 3\%$.

function of m_v computed on the basis of (3.8), and the measurement points were calculated

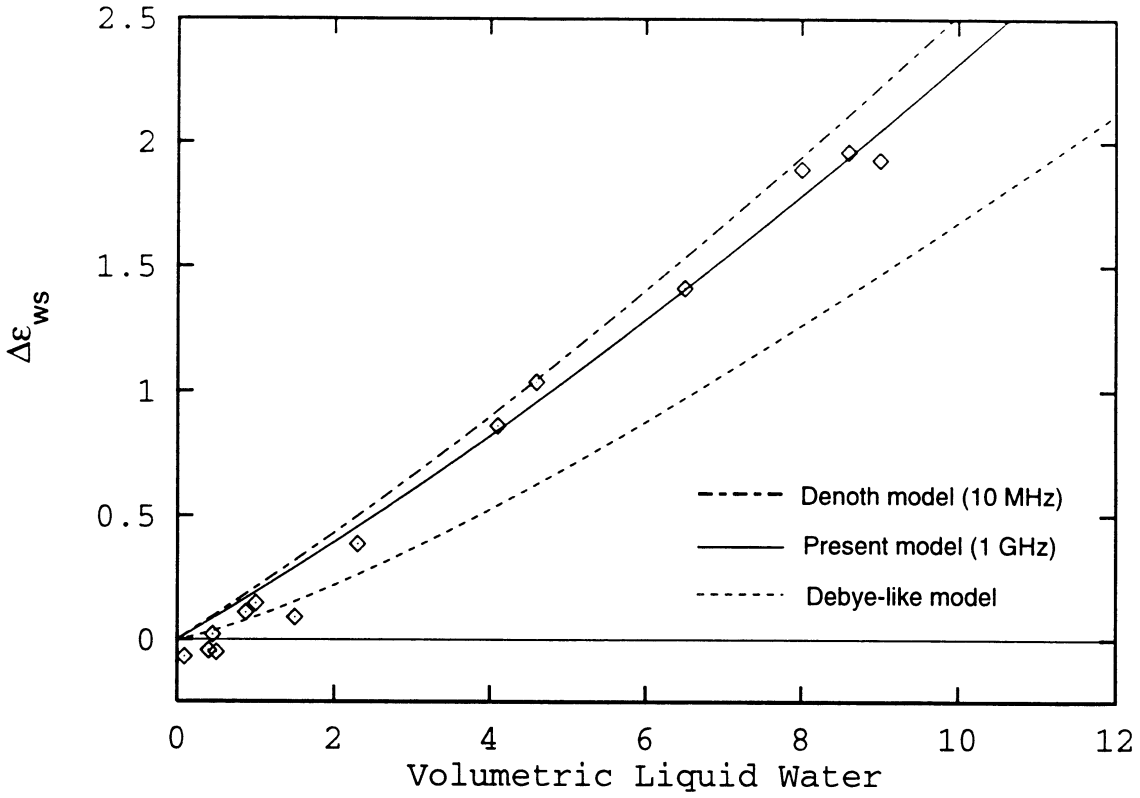

Figure 3.8: $\Delta\varepsilon'_{ws}$ *versus* m_v. Shown is data and best fit curve, plus a model obtained from a comparable study at 10 MHz, and Debye-like model.

from $\Delta\varepsilon'_{ws} = \varepsilon'_{ws} - \varepsilon'_{ds}$, with ε'_{ws} being the value measured by the probe and ε'_{ds} determined from (3.12) and (3.13). The curve drawn thru the data points is generated using a simple polynomial fit, given by:

$$\Delta\varepsilon'_{ws} = 0.187m_v + 0.0045m_v^2. \tag{3.16}$$

The agreement between the gravimetric density technique and the snow probe using (3.16) is shown in Figure 3.9. A very good fit can also be obtained via (3.8) by modifying the term $0.02m_v^{1.015}$ to $0.08m_v^{1.015}$; however, an arbitrary adjustment defeats the purpose of using a

model which is based on physical arguments. The Debye-like model of (3.8) has essentially the same frequency dependance as the real part of the dielectric constant of water, and its empirically-derived coefficients— which effectively reduce the value of this quantity from the theoretical value of the pure material—account for the water being distributed in parti-

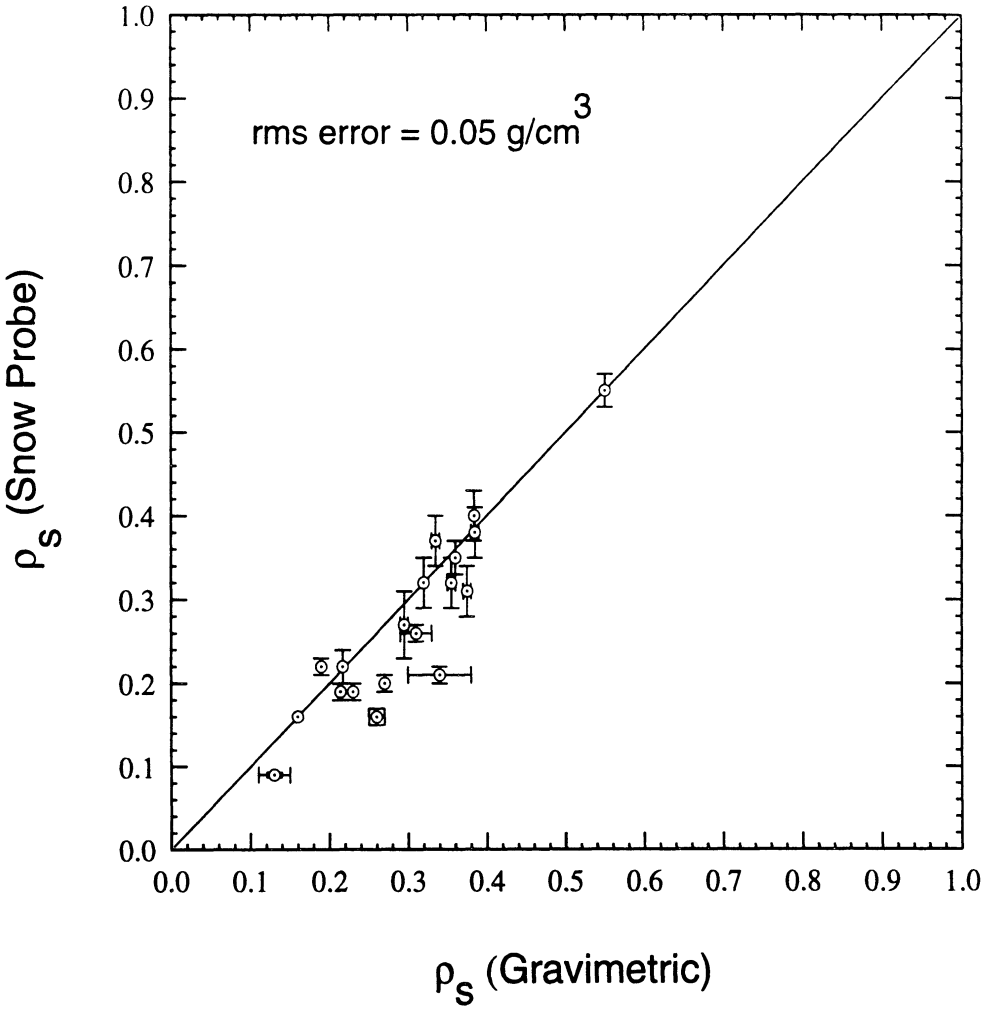

Figure 3.9: Comparison of snow density results obtained *via* Snow Probe (with associated empirical algorithm) and gravimetric measurements.

cle form within a host having a dielectric constant somewhere between those of air and ice. With this understanding, there does not appear to be any reason why a model which works

well between 3 and (at least) 15 GHz should need to be significantly modified to work at 1 GHz; physically speaking, the only difference between 3 GHz and 1 GHz is that the dielectric constant of water increases from ≈80 to ≈87.

The literature contains certain pertinent experimental results that should be considered. Tiuri et al. (1984) report measurements also at 1 GHz. In these measurements, a dilatometer technique was primarily employed for wetness measurements, but a capacitor technique was used for some of the samples corresponding to the lowest m_v levels. The dielectric measurements were made with the Snow Fork developed at the Helsinki University of Technology. The relationship they report is,

$$\Delta\varepsilon'_{ws} = 0.089m_v + 0.72m_v^2. \tag{3.17}$$

This function, when plotted, closely resembles the Debye-like model (3.8) evaluated at 1 GHz. Most recently Denoth (1989) reported measurements made at 10 MHz, in which dielectric measurements were made using a simple plate capacitor and liquid water measurements were made using a freezing calorimeter. The relation he reports is,

$$\Delta\varepsilon'_{ws} = 0.206m_v + 0.0046m_v^2. \tag{3.18}$$

Denoth observes that this relation should continue to be valid up to approximately 2 GHz, since ε' of the constituents of wet snow—ice, air, and water—are all exactly or nearly frequency-independant in this range. In particular, for water, as seen in Figure 3.10, the real part of the dielectric constant of water, ε'_w, at 1 GHz differs from that of 10 MHz by only 1.1%. Also noted on the figure is the region through which the debye-like model of Hallikainen et al. (1986) was reported to be valid (although above 15 GHz, the empirical coefficients shown in (3.8) are slightly modified as a function of frequency). The best fit function for the 10 MHz data,given by (3.18), is also shown in Figure 3.8. The close agreement between the results at 10 MHz and 1 GHz tends to bear out Denoth's prediction and suggest that at these frequen-

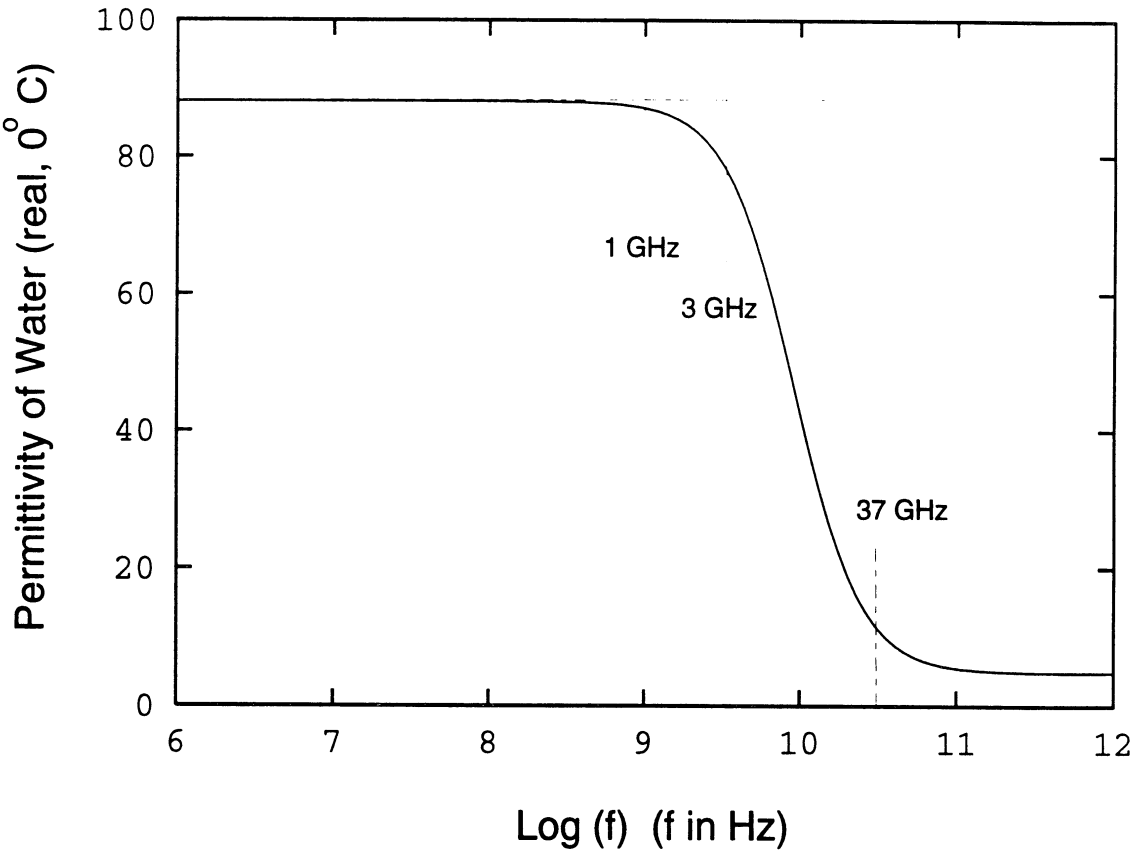

Figure 3.10: Real part of permittivity of water at 0°C.

cies, where scattering is an unimportant factor in calculating the dielectric constant, ε'_{ws} is directly relatable to ε'_w. In effect, a model like (3.8) *should* be expected to work, but, in its present form, does not appear to. Regarding the discrepancy between our results and those of Tiuri et al. (1984), a possible explanation is that they used a dilatometer to measure wetness, a technique which we found (see Appendix A) gave very unsatisfactory performance. Our standard (which was also used in Denoth (1989)) was the freezing calorimeter technique whose accuracy and precision has been demonstrated, in the above results and also in results appearing in Appendix A.

3.4 Application

Figure 3.11 is a nomogram, based on these equations which have been found to be valid in the specified ranges. It consists of contours of constant m_v and ρ_{ds} respectively, in a 2-dimensional representation bounded by the two parameters which are directly obtained by the Snow Probe: resonant frequency and bandwidth (3-dB) of the resonance spectrum. With the measurement of these two quantities, m_v and ρ_{ds} may be uniquely specified. Dry-snow density, ρ_{ds}, is related through (3.12) to wet-snow density ρ_{ws}.

As an example of the utility of the Snow Probe for elucidating snowpack character and behavior, we present in Figure 3.12 snow wetness data measured for an 0.88-m deep snowpack over a diurnal cycle. During the period shown, from 10 a.m. to 8 p.m., the temperature rose from freezing to 6° C and down to −3° C again at 8 p.m.. The lowest 16-cm of the pack was solid ice; therefore measurements start at 18-cm above ground, and were made at roughly 5-cm intervals. Among the interesting features in the figure, even at 10 a.m., after sub-freezing night temperatures, and while the surface is still completely dry, there is appreciable moisture deeper down in the snowpack. At the top surface, between the hours of 6 and 8 p.m., there was significant wetness which then quickly froze at about 8 p.m.. This data set, which was accompanied by radar measurements, is analyzed in Section 4.4 of Chapter IV.

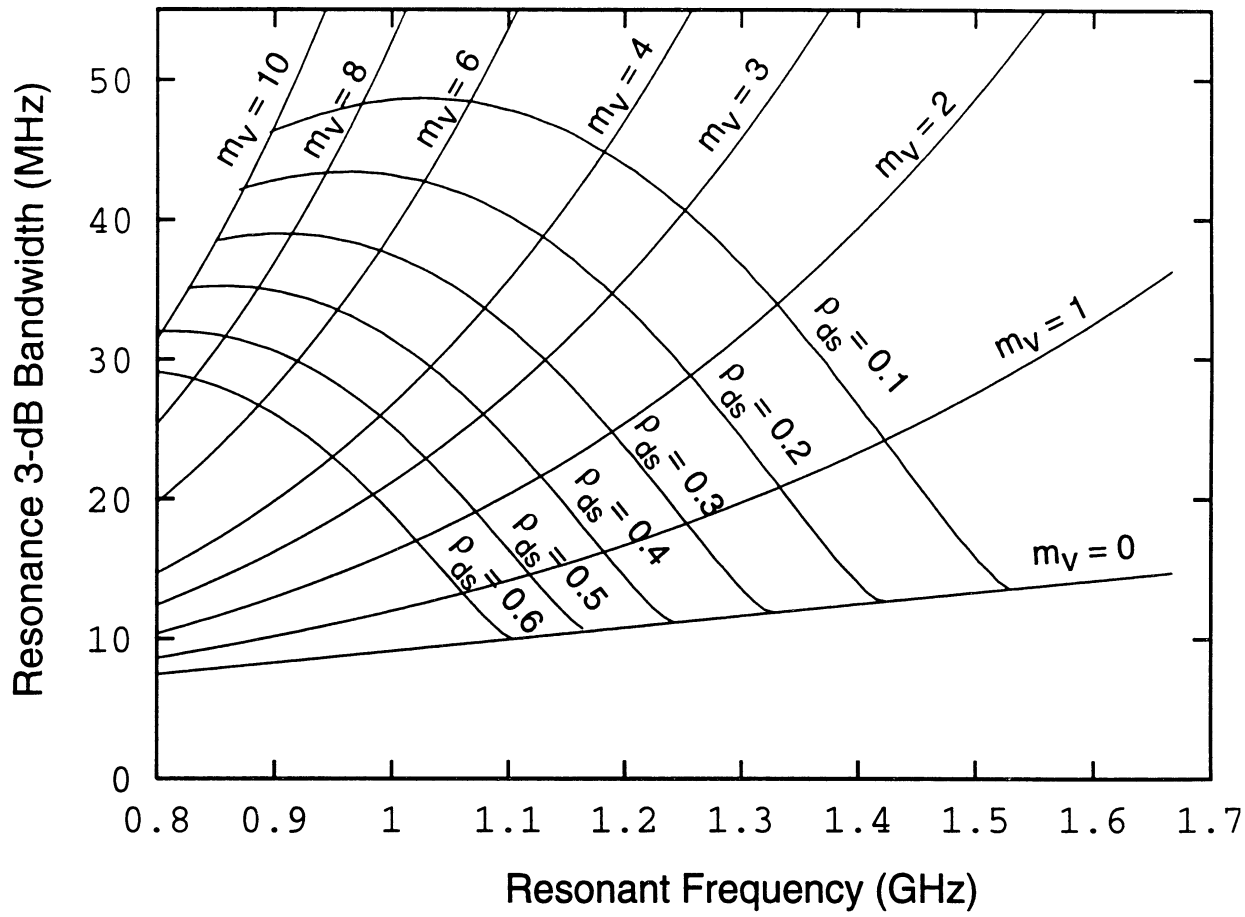

Figure 3.11: Nomogram giving snow liquid water content (m_v) and equivalent dry-snow density (ρ_{ds}) in terms of two parameters directly measured by the Snow Probe: resonant frequency (f) and resonance (3-dB) bandwidth (Δf).

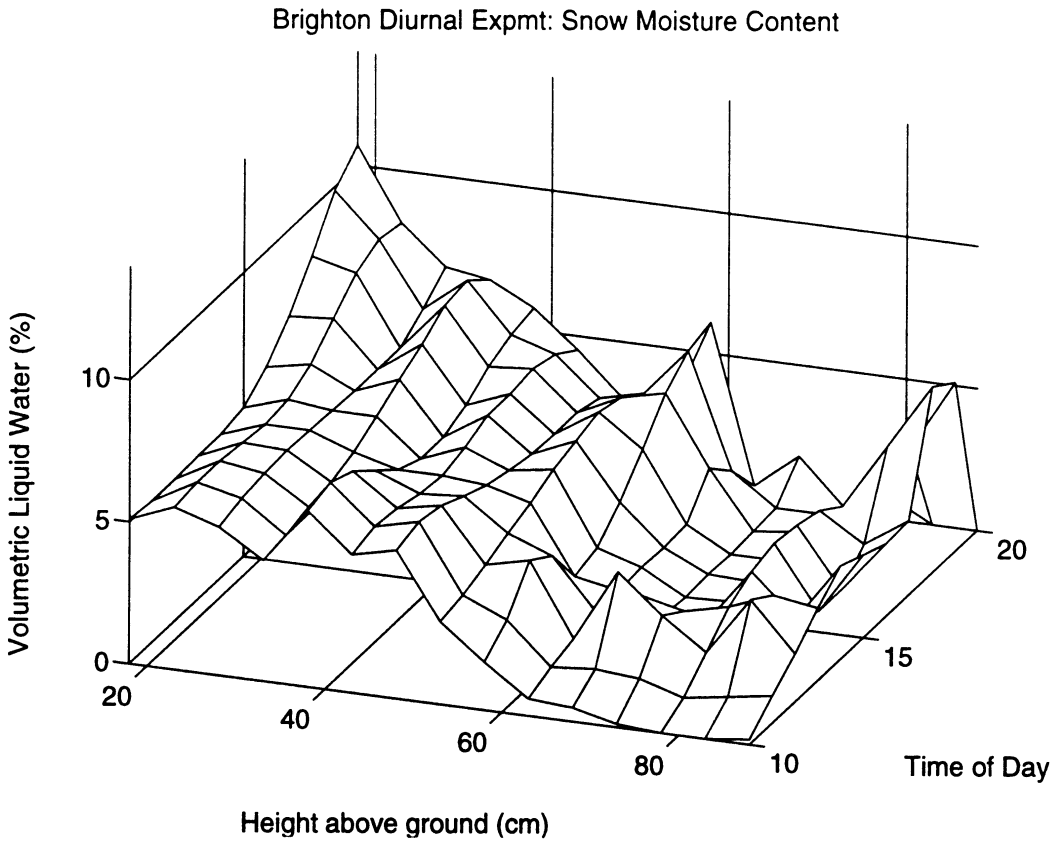

Figure 3.12: Snow moisture measured *via* the Snow Probe in a 0.88-m snowpack over a diurnal cycle, shown as a function of time and height above the ground.

3.5 Summary

This chapter has described the development and validation of an electromagnetic sensor and associated algorithm for the purpose of rapid ($\approx$ 20 seconds) and nondestructive determination of snow liquid water content and density. The sensor is similar in principle to an existing device known as a "Snow Fork", but offers additional advantages in spatial resolution and accuracy owing to a novel coaxial-cavity design. Also, the algorithm employed with that device (Sihvola and Tiuri 1986) for relating complex dielectric constant to snow parameters does not agree with the results of the present study. We have consequently developed new relations for that purpose.

Direct methods of snow wetness determination were evaluated for their suitability as standards against which the Snow Probe could be tested. The dilatometer, though simple in principle, was found to give very unfavorable performance. The freezing calorimeter, which has, as a system, been brought to a high degree of sophistication in our lab, was found capable of delivering accuracy better than $\pm 1\%$, and excellent precision.

The Snow Probe determines the dielectric constant directly. Empirical and semi-empirical models are used with this information to compute liquid water volume fraction and density. To test the suitability of existing models and/or allow the development of new models, the Snow Probe was tested against the freezing calorimeter and gravimetric density determinations. Originally, The relations set forth by Hallikainen et al. (1986) were employed to translate measured dielectric constant to snow parameters. The equation relating ε''_{ws} to m_v and frequency was found to be entirely valid. However, the equation predicting $\Delta\varepsilon'$ in terms of m_v and frequency was found to underestimate this quantity, leading to substantial errors in the estimates of ρ_{ds}. A purely empirical relation, given in (3.16) was obtained instead, and will be used in our parameter retrieval algorithm for the Snow Probe. Through the use of these functions, in association with the complex dielectric measurements of the Snow Probe, the following specifications are established: liquid water content measurement accuracy ± 0.66 % in the wetness range from 0 to 10% by volume; wet snow density measure-

ment accuracy ± 0.05 g/cm^3 in the density range from 0.1 to 0.6 g/cm^3.

Two examples of pertinent experimental results were compared against ours: Denoth's measurements (Denoth 1989) at 10 MHz are very similar to ours; those reported by Tiuri et al. (1984) at 1 GHz differ considerably from ours but agree well with the model given by (3.8), our own starting point. Denoth (1989), noting the diversity of empirical relations for the dielectric constant of wet snow suggests that because of the influence of the shape of the water component, and the stage of metamorphism of the snow sample, "a valid simple relation between $\Delta\varepsilon'$ or ε'' and liquid water content W may not exist." This may be the case, but the results of the present study are very consistant with results presented in Denoth (1989) for the case of $\Delta\varepsilon'$, and in Hallikainen et al. (1986) for the case of ε''. Accurate snow measurements of dielectric constant and liquid water content are notoriously difficult to make. This has doubtlessly been a factor in the diversity of results, and is motivation for the development of instruments such as has been the focus of this present investigation.

CHAPTER IV

RADAR MEASUREMENTS ON ARTIFICIAL SNOW OF VARYING DEPTHS

4.1 Introduction

A great deal of experimental and theoretical work has been done pertaining to the radar response of snow or,by extension, *dense random media* in the theoretical realm, for which snow is perhaps the most representative natural example. The aim of all of this work, and, what is true of any remote sensing research, is to develop the capability to characterize in some way, to a greater or lesser degree, the remote target from the sensor response(s) alone. We may identify three levels of such characterization, which we list in order of increasing power of characterization but decreasing level of reliability.

- Level 1: Empirical models are used to infer or predict information about the target characteristics. Recent examples include radar and radiometer algorithms for discriminating wet snow covered terrain from other types of terrain (Koskinen et al. 1994), a hybrid empirical/theoretical approach for estimating radar clutter at millimeter wave due to certain types of terrain (Ulaby et al. 1993), and an approach for classifying snow cover states (dry/wet/refrozen) (Narayanan and Jackson 1994).

- Level 2: Classification is performed based on the apparent scattering mechanisms inherent in the target as identified through analysis of the character of the target Mueller

matrix (van Zyl et al. 1987; van Zyl 1989). Such techniques have reportedly been successful in demarcating areas consisting of primarily urban targets, slightly rough targets like oceans and lava flows, and parks and vegetated areas. It has also been shown that such a method may allow discrimination between relatively younger and older lava flows (Evans et al. 1988). These techniques have also lately been suggested as a means for determining wetness levels in snow (Shi and Dozier 1992; Shi and Dozier 1995).

- Level 3: At this level, tools from the previous two may be used, but the central characteristic is the use of a theoretical model which is assumed to generate reasonably high fidelity predictions of sensor responses for a given set of physical parameters which is assumed to constitute an accurate description of the target. An example of this type of approach is a neural-net-driven inversion algorithm intended to allow retrieval of snow parameters, from radar and radiometer sensor responses, and which is trained using a dense medium radiative transfer model (Davis et al. 1993).

It is obvious from the descriptions that, where greater understanding of the electromagnetic interaction with a material is present, the potential for information retrieval through remotely sensed data is greater. The critical issue becomes then testing the validity of theoretical models through careful experiments.

In the present study, an attempt is made to address this issue with respect to the radar response of snow. There exists already numerous experimental studies of snow in the literature, both at microwave frequencies (Stiles and Ulaby 1980a; Ulaby and Stiles 1980; Mätzler et al. 1982; Mätzler and Schanda 1984; Chang et al. 1985), and at millimeter-wave frequencies (Ulaby et al. 1991; Mead et al. 1993). Using such experimental data for the purpose of evaluation of models is very difficult because of the need to carefully characterize the target. Even with precise characterization, substantial obstacles remain. A complex target can be described down to the finest details, but this still leaves the problem of correctly modeling the behavior of all these features, electromagnetically speaking, and all of

their interactions with each other.

Consider a typical target of snow-covered ground. Parameters which must be potentially considered are:

- Parameters associated with the top surface of the snow (rough surface)
- The snow itself: density, particle size distribution; vertical distributions of these properties within the snowpack.
- Snow wetness, when present, may well be a very complex function of time and depth. Examples of this are presented in later sections of this paper.
- The ground beneath: its dielectric constant, roughness parameters, local slope.

For experiments at millimeter-wave frequencies, the number of parameters may be somewhat reduced since it is generally accepted, and has been demonstrated by careful experiments (Hallikainen et al. 1987), that the total penetration depth is relatively shallow. Thus, at mm-wave frequencies, the snow may be treated as a half-space. The price for this, however, is that sensitivity to snow microstructure and other smaller scale features is heightened, for which accurate characterization may be very difficult.

Microwave frequencies offer the most potential for the retrieval of gross snow properties such as depth or water equivalent, parameters which are especially important for hydrological applications. For microwave frequencies, generally most of the parameters mentioned above need to be considered. Thus it is in practice difficult to address theoretical predictions in an unambiguous fashion with field experiments.

The present study describes radar backscatter experiments at L-,C- and X-band on snow. In these experiments, the use of artificially produced snow allowed an unusually high degree of confidence in the exact character of the target snowpack. Two different kinds of experiments were conducted: experiments of the angular response of dry snow at various depths, and experiments at a single angle over a partial diurnal cycle during which complete profiles of water content as a function of depth and time were recorded, using the Snow Probe

(Kendra et al. 1994). A complete description of the experiment is presented in Section 4.2. In Section 4.3 the results of the backscatter experiments are presented and analyzed with respect to certain models. In Section 4.4, the results of this diurnal experiment and another previous diurnal experiment are presented and discussed with respect to a proposed inversion algorithm for snow wetness.

4.2 Experiment Description

This section describes scatterometer experiments which were performed at L-,C-, and X-band (1.25, 5.3, and 9.5 GHz) on snowpacks comprised of artificial snow. The experimental site was the Mt. Brighton Ski Area, in Brighton, Michigan, during February and March of 1993. The radars used were truck-mounted, fully polarimetric network-analyzer-based systems, using horn antennas. The boom-mounted, truck-based systems are shown in Figure 4.1. Detailed descriptions of the systems are available elsewhere (Tassoudji et al. 1989; Oh et al. 1992). The target was an area of ground covering approximately 18m x 30m. On the average, sixty independent spatial measurements were taken with each angular measurement to reduce the variance due to fading in the estimate of the mean backscatter. Additional frequency averaging was available from the bandwidths used in the respective channels, 300, 400, and 500 MHz in the L-,C-, and X-band channels respectively. Calibration was performed using a fourteen-inch sphere and a differential Mueller matrix algorithm suitable for measurements of distributed targets (Sarabandi et al. 1990).

Two types of experiments were performed. The first consisted of backscatter measurements at incidence angles of 20° through 60° on bare ground, which were then repeated for three progressively deeper layers of artificial snow over the ground. This sequence was performed over a six day period, from February 24th to March 1. A major goal of the experiment was to simplify, insofar as was possible, the nature of the target to allow as unambiguous comparison with theory as possible. One goal we had was insuring that there

Figure 4.1: University of Michigan truck-mounted radars.

would be no wetness present in the target snowpacks, so that we would not have to deal with this complicating factor in our interpretation. We therefore conducted all of the experiments during the night. As may be seen from the daily temperatures plotted in Figure 4.2, the temperature during the data-takes averaged -15° C and was always below -10° C. Snow probe measurements verified that there was, to the accuracy of the measurement, essentially no liquid water present in the snowpack. An additional fortuitous circumstance, which may also be observed in Figure 4.2, was that the temperture was very low in the week preceeding

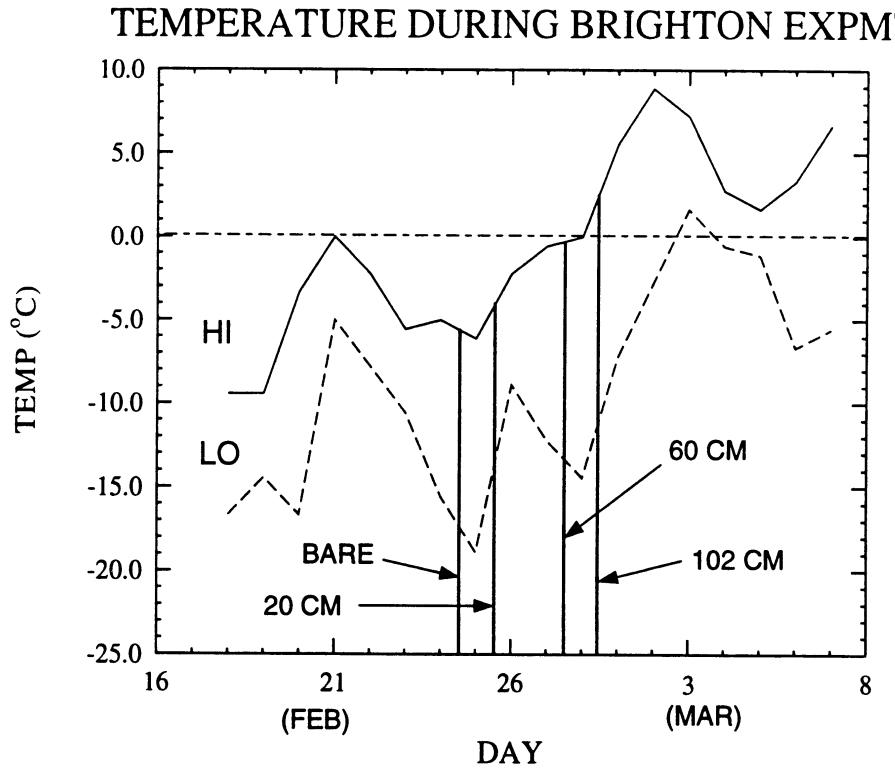

Figure 4.2: Temperature variations during the course of the radar experiments on artificial snow

the experiment, leading to a generally frozen environment which was unrelieved during the entire experiment as even the temperature highs did not go above the freezing mark until the day following the final experiment.

The bare ground target was prepared by using earth moving equipment to remove all of the existing snow, natural and artificial, and then to scrape away any grass or other vegetation on the target plot. The dielectric constant of the ground was measured using a mi-

crowave field-portable dielectric probe (Brunfeldt 1987) operating at C-band. The average dielectric was found, from twenty-five separate measurements to be 4.6 ± 1.1 (the imaginary part is not estimated accurately through this technique). The bare ground roughness was measured using a laser profilometer. Seven 95-cm linear transects were measured; the step size was 3mm. The average rms height of the surface was found to be, $s = 0.32 \pm 0.08$ cm; and for the correlation length, $l = 2.09 \pm 1.6$ cm.

The artifical snow was added in three progressively deeper layers. No chemical additives were used in the production of the snow, as is commonly done to increase production, which might have caused the dielectric constant of the particles to depart from that of water ice. The snow, once produced, was spread into a uniform layer using a grooming machine (piston bully) with extra wide treads to reduce the pressure exerted by the weight of the machine on the snowpack. A consequence of this process, was that a characteristic groove pattern was imparted to the top of the snow, having a period of 3.2 cm and a peak-to-peak amplitude of 1.3 cm, corresponding to an rms height of 0.449 cm. The correlation length of such a surface is dependent on the direction with which it is computed relative to the grooves.

The three different depths of snow deposited were 20,60, and 102 cm, with the standard deviations shown in Table 4.1. The nature of artificial snow is that it consists of very small particles and has a very high density. The average density of the snow was 0.48 g/cm^3, and the average particle diameter was found to be 0.27 mm. This combination of particle size and density are at the extreme ends of what would be found in nature, but not to the point of being unreasonable. We note, for example that the density is very comparable to that reported for Alpine snowpacks in Shi and Dozier (1992); neither are these particle sizes outside of reported ranges (Chang et al. 1994; Hallikainen et al. 1987). All of the target physical properties for the dry snow backscatter experiments are summarized in Table 4.1.

It deserves to be emphasized that there were a number of elements present in this experimental effort which make it unusually well—and simply—characterized. The snow

Ground	Snow Volume	Snow Surface	Snow Depths
$s = 0.32$ cm	$\bar{d} = 0.27 \pm 0.11$ mm	$s = 0.45$ cm	$d_1 = 20 \pm 6$ cm
$l = 2.09$	$\tilde{\varepsilon} = 1.9 - j0.015$	$\varepsilon_r' = 1.97$	$d_2 = 60 \pm 10$ cm
$\varepsilon_r' = 4.7$ (C-band)	$\rho_s = 0.48$ g/cm^3	Period: 0.32 cm	$d_3 = 102 \pm 9$ cm
		Amplitude (p-p): 1.27 cm	

Table 4.1: Dry Snow Physical Properties

machines produced very uniform "snow" over the course of the experiment, and this was recorded and photographed. From Figure 4.3, it is evident that the snowpack was in fact

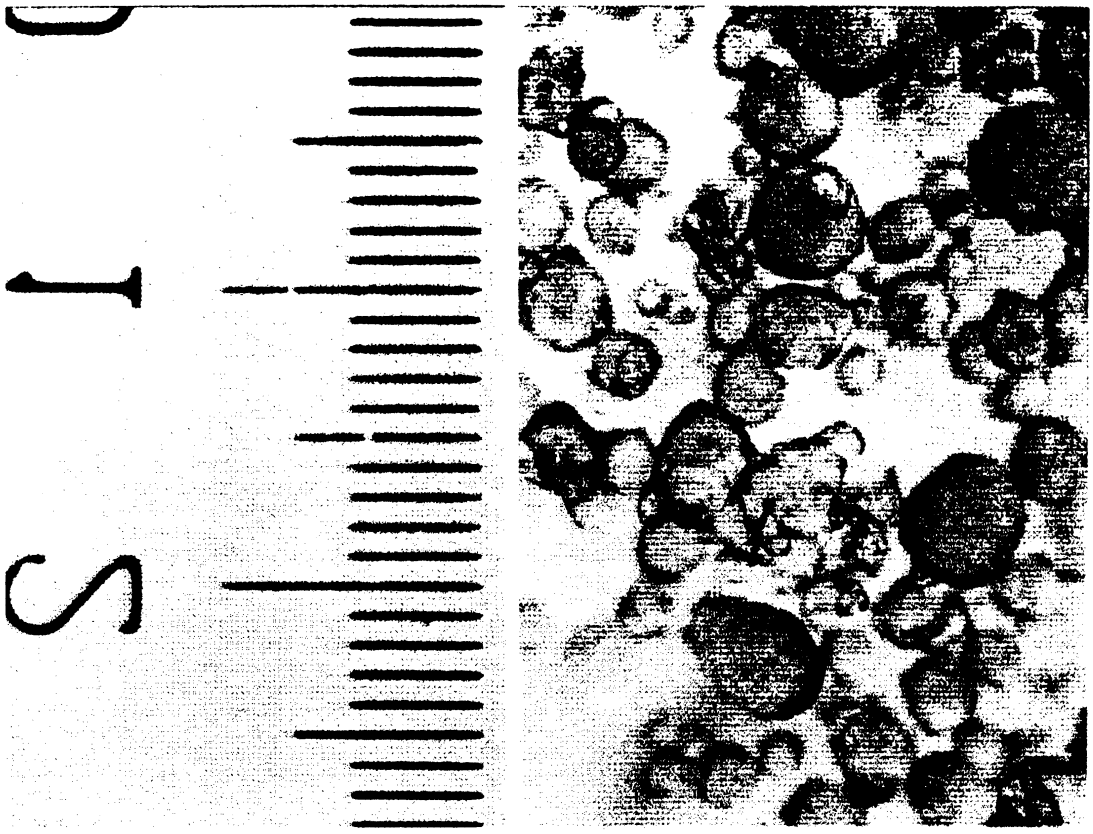

Figure 4.3: Photograph of artificial snow particles. Major divisions of ruler shown are millimeters.

composed of discrete particles having a high degree of sphericity. For comparison, we show in Figure 4.4 a photograph of the surrounding natural snow, which is on the same scale as in Figure 4.3. Furthermore, there was little or no variation from this snow composition as a function of vertical position within the snowpack. This last point is owing not only to the

Figure 4.4: Photograph of real snow particles taken from snowpacks adjacent to the artificial snowpack. Scale is the same as shown in Figure 4.3.

uniform way in which the particles were produced but also to the unbroken cold conditions which persisted throughout this experimental phase and therefore prevented any metamorphic activity associated with melting and re-freezing within the earliest deposited snow. Finally, the action of the grooming machine on the top surface of the snow guaranteed that virtually identical roughness was present for all target realizations. That the surface was not isotropic is not a desirable characteristic, but, as we will show, the surface, having such a small dielectric constant, does not make an especially large contribution to the backscatter anyway. What is most important is that it cannot be invoked to explain differences in the responses of the various target configurations.

The second type of experiment performed was of a partial diurnal cycle. This experiment took place on March 6, five days after the last experiment in the dry snowpack sequence. In this intervening period, the daily high temperatures had been consistantly above freezing, getting as high as 9° C. As a result the snow pack had experienced considerable metamorphosis. In addition, there had been deposited about 15 cm of new snow. Thus, the snowpack had begun to resemble a natural one, complex and difficult to characterize, and mainly unsuitable for comparison with rigorous modeling approaches. However, since copious data on wetness, as a function of both vertical position and time were recorded, along with the polarimetric backscatter at 40° incidence, it provides an excellent opportunity for direct evaluation of a recent algorithm (Shi and Dozier 1992; Shi and Dozier 1995) for inversion of snow wetness levels from target Mueller matrices. A second data set which was recorded on March 1, 1993, in Cadillac, Michigan, also at 40° incidence and with complete wetness data, will also be considered.

4.3 Dry Snow Backscatter Results & Discussion

4.3.1 Bare Ground

To model the backscatter from the dry (artificial) snow, it will first be necessary to account for the contributions of the soil surface below the snowpack as well as the top surface of the snowpack. In Oh et al. (1992) it is shown, as the result of an extensive experimental effort, that classical models such as the small perturbation model and the physical optics and geometric optics solutions of the Kirchhoff approximation do not accurately predict the co- and cross-polarized backscatter from bare soil surfaces. The result of that study is a simple semi-empirical model (and inversion algorithm) which uses two parameters: ks, the surface roughness, and m_v, the soil moisture content.

The co- and cross-polarized backscattering coefficients are given by:

$$\sigma^{\circ}_{vv}(\theta, \varepsilon_r, ks) = \frac{g\cos^3\theta}{\sqrt{p}} \cdot [\Gamma_v(\theta) + \Gamma_h(\theta)] \tag{4.1}$$

$$\sigma^{\circ}_{hh}(\theta, \varepsilon_r, ks) = g\sqrt{p}\cos^3\theta[\Gamma_v(\theta) + \Gamma_h(\theta)] \tag{4.2}$$

$$\sigma^{\circ}_{vh}(\theta, \varepsilon_r, ks) = q\sigma^{\circ}_{vv}(\theta, \varepsilon_r, ks) \tag{4.3}$$

where,

$$\sqrt{p} = \sqrt{\frac{\sigma^{\circ}_{hh}}{\sigma^{\circ}_{vv}}} = 1 - \left(\frac{2\theta}{\pi}\right)^{[1/3\Gamma_o]} \cdot \exp(-ks) \tag{4.4}$$

$$q = \frac{\sigma^{\circ}_{vh}}{\sigma^{\circ}_{vv}} = 0.23\sqrt{\Gamma_o}[1 - \exp(-ks)] \tag{4.5}$$

$$g = 0.7[1 - \exp(-0.65(ks)^{1.8})] \tag{4.6}$$

where Γ_o is the Fresnel reflectivity computed at nadir and θ is the incidence angle in radians. The dielectric constant of the soil, required for the computation of Γ_o, may be obtained from m_v at the desired frequency using expressions given in Hallikainen et al. (1985).

The value of m_v corresponding to our measured soil dielectric at C-band is 0.085. Using this value, along with the soil rms height s (Table 1), we may compute predictions of the soil backscatter using (4.1)–(4.3). Using these exact values, the X-band response is somewhat underestimated; however, a small adjustment of the rms height from the measured value of 0.32 cm to 0.37 cm, gives close simultaneous agreement for both frequencies for both co- and cross-polarized responses, as shown in Figure 4.5. These values, $m_v = 0.085$ and $s = 0.37$ cm will be used to compute the backscatter for the snow-covered ground.

The L-band agreement with this model prediction , also shown in the figure, is very poor. The measured backscatter is considerably higher—on the order of 5 dB for the co-polarized responses and more than 10 dB for the cross pol—relative to what is expected given these surface parameters. This suggests that the L-band is penetrating into the ground and encountering a sharper, and perhaps rougher dielectric interface. Since this condition generally persisted throughout the experiment, and having no reliable model for the L-band response for the bare ground scattering beneath a snow layer, the remainder of this analysis will be confined to the C- and X-band channels. The model given by (4.1)–(4.3) will also be used to compute the backscatter contribution from the top surface of the snow.

4.3.2 Dry Snow Backscatter

The results from the angular measurements made on three different depths of artificial snow are shown in Figure 4.6. Also shown, to better illustrate the snow *volume* contribution, are simulations (computed with (4.1)–(4.3)) of the *surface* backscatter from (1) the snow-covered ground alone and (2) the snow-covered ground plus the contribution from the top snow surface. These are shown separately to illustrate the relative importance of the top-surface term.

One obvious characteristic of the data is the relatively small dynamic range of the co-polarized responses corresponding to different depths. Indeed the co-polarized response for the shallowest (20 cm) depth can be attributed to the effects of the two rough surfaces alone.

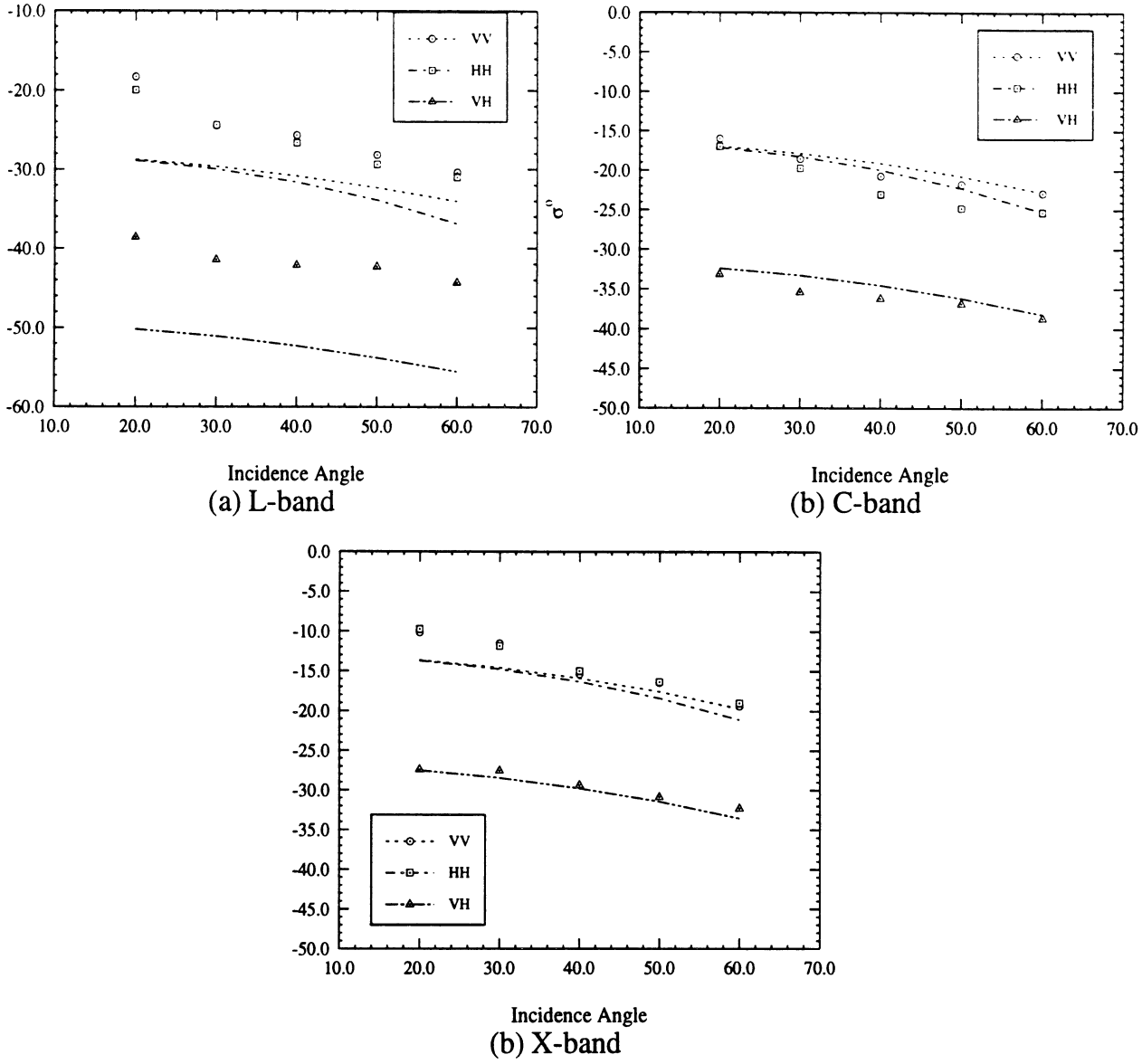

Figure 4.5: Measured (discrete marks) and predicted (lines) backscatter from bare ground.

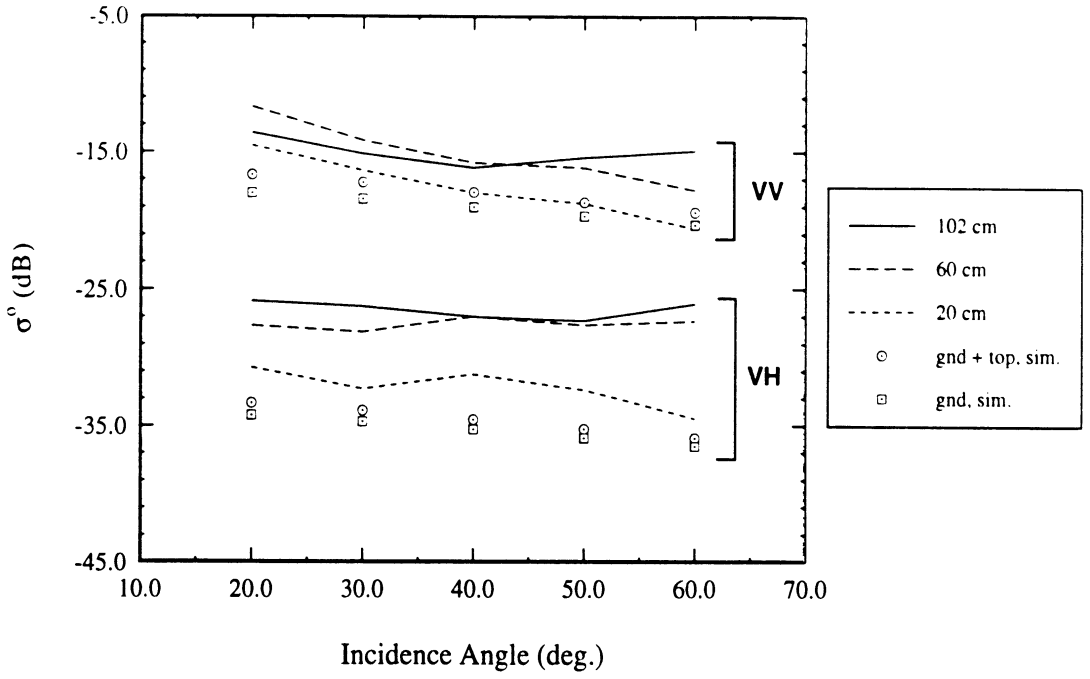

(a) C-band

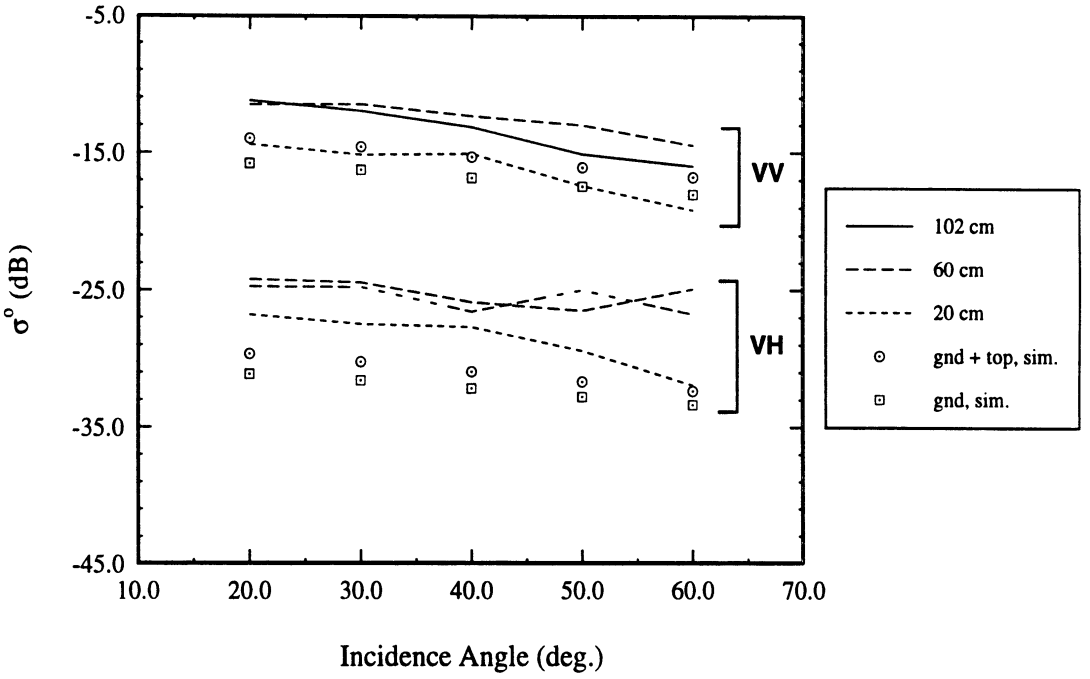

(b) X-band

Figure 4.6: Backscatter measurements (VV and VH) made of three different snow (artificial) depths at C-band and X-band. Also shown for reference are simulations of the pure ground scattering expected and also the contributions from the ground and the snow top surface.

Still, there is an upward trend apparent, as the 60 cm and 102 cm depths are on the order of 3 dB higher than the 20 cm case. There appears to be saturation occurring, as the responses from the two deeper layers appear to be essentially the same, within the apparent noise level of the measurements. The level of noise within the measurements appears to be appreciable; this is attributed to the relatively difficult conditions (cold, darkness, finite boundaries of the target area) under which they were made.

It is worth comparing these results qualitatively with what has been experimentally observed before for snow in this frequency range. One issue which has been debated in the literature is that of whether snow is observable at all at X-band. Several investigators have claimed that it is not, based on their measurement campaigns (Mätzler et al. 1982; Mätzler and Schanda 1984), whereas, in another case, Ulaby and Stiles (1980), evidence to the contrary is reported. A critical element which must be taken into account in considering this question is the magnitude of the ground scattering. For example, in Mätzler et al. (1982) and Mätzler and Schanda (1984), the reported rms roughness of the bare ground was 2 cm. Accordingly, the average bare ground scattering level is as high or higher than the maximum levels measured in our present experiments. In the dry snow-pile experiments of Ulaby and Stiles (1980), the bare ground characteristics are not reported, but σ° levels for the shallowest snow depths (from Fig. 4 in Ulaby and Stiles (1980)), are suggestive of a relatively smooth surface, probably similar to that of the present study. It is worth noting that a similar high density snow (0.42 g/cm^3) was examined in that case.

The dynamic range of the cross-pol is seen to be considerably greater than the co-pol, and is unquestionably increased with snow depth, exhibiting an increase on the order of 7 dB. Here too is observed an apparent saturation as in the case of the co-pol, for the two deepest layers.

Comparison with Discrete-Particle-Based Theories

The well-defined nature of the artificial snowpack allows direct comparison with theories which are based on discrete particles. Since intuition suggests that for particles of this size ($d = 0.27$ mm) the scattering will be small, we will start by considering an independent scatterer formulation, since it is simpler. Since it has been found both experimentally (Ishimaru and Kuga 1982) and theoretically (Tsang and Kong 1992) that correlated dense medium scattering is less than independent scattering at low frequencies, the solution will represent an upper bound on what dense medium radiative transfer (DMRT) solution techniques may predict.

For a comparison with theory, the complex dielectric constant of the ice particles $\tilde{\varepsilon}_{ice}$, must also be known. For the real part, ε'_{ice}, we use 3.15. The imaginary part is computed using the following formula (Nyfors 1982) which compares very favorably with published data and also accounts for temperature dependance:

$$\varepsilon''_{ice} = 57.34(\frac{1}{f} + 2.48 \times 10^{-14}\sqrt{f})\exp(3.62 \times 10^{-2}T) \tag{4.7}$$

where f is in Hz and T is in degrees Kelvin. For particles of this size, the scattering albedo, ω_o, as computed using the Mie solution, is only 5.2×10^{-3} for C-band and 2.3×10^{-2} for X-band. The scattering albedo is the ratio of the scattering cross-section to the total extinction cross-section (κ_s/κ_e). That it is so small in this case indicates that volume scattering may be treated as a perturbation on the reduced (by extinction) coherent wave in the medium. Thus a first-order radiative transfer solution is appropriate for the solution of a layer of these particles. If this solution is computed for a layer of particles (having a smooth surface) over a smooth dielectric half-space having the same dielectric constant as the soil in the present study, an estimate of the contribution of the snow volume is obtained. When we performed this calculation, as a function of depth and angle for the two frequencies, we found that the maximum co-polarized σ° produced was -48 dB at C-band and -32 dB at X-band. The

contribution to the total scattering represented by these levels does not appear as a visible increase relative to the curve in Figure 4.6 which corresponds to the backscattering contributions of the two rough surfaces, top and bottom, alone. The cross-polarized response corresponding the first-order solution for spherical particles is identically zero. Use of a more sophisticated radiative transfer solution (Kuga et al. 1991) which uses the discrete ordinate method and so accounts for all orders of scattering gives, not surprisingly, essentially the identical results for the co-polarized cases; the cross-pol estimate is on the order of -80 dB for C-band and -70 dB for X-band.

It is obvious that the behavior of the target cannot be explained in terms of the particles of which the snowpack was observed to be comprised. There has appeared in the literature recently work which considers "sticky" particles (Zurk et al. 1994), that is, particles which come together to form an aggregate particle, effectively much larger than the individual particles. Obviously, this could have a profound effect upon the scattering behavior of a medium, recalling that in the Rayleigh regime, scattering increases (on a per unit volume basis) as r^3. If the particle size is treated as a free parameter in the conventional RT formulation, a value can be obtained which gives the optimal agreement with the measured results. The results of such a process are shown in Figure 4.7. As shown, reasonable agreement—for the co-polarized responses—can be obtained if an effective particle diameter of 1.7 mm (more than six times larger than the measured average diameter of 0.27 mm) is used for C-band and a diameter of 0.9 mm (more than three times larger than the measured value) is used at X-band. Even in this case however, the RT formulation fails completely to predict the substantial cross-polarized response observed in the measurements.

Faced with the failure of existing particle-based theories to explain the experimental observations, we turn to the question of what useful information *can* be be extracted from this data. A record of the snowpack target that was measured adds, in itself, very little to the study and practice of remote sensing of snow. There is a low probability that the same combination of physical features, including the characteristics on top of the snowpack and be-

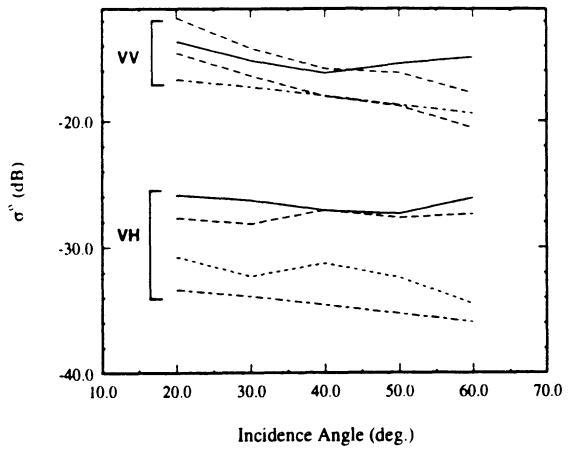

(a) C-band measured.

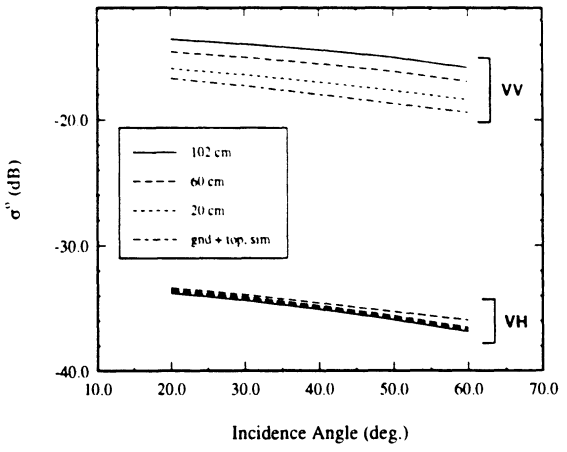

(b) C-band optimal RT simulation.

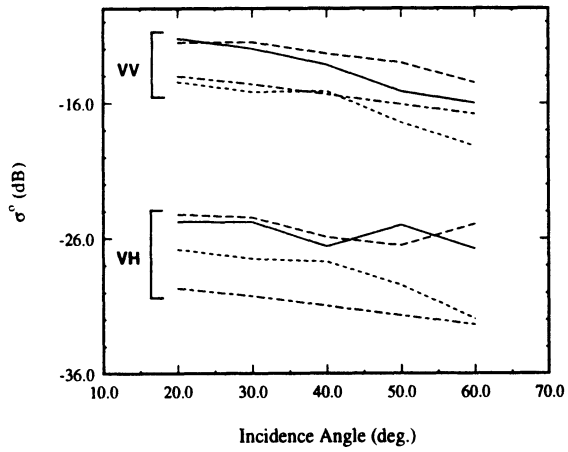

(c) X-band measured.

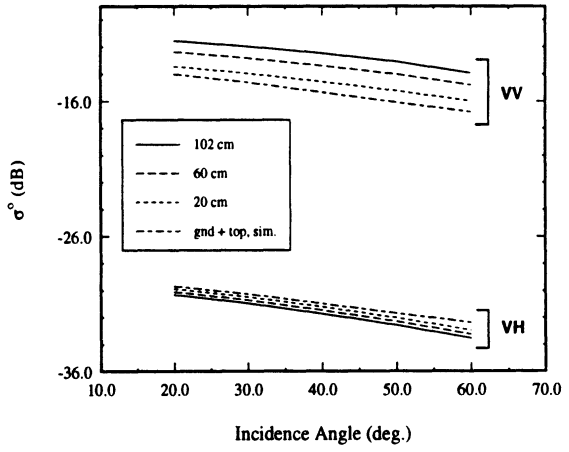

(d) X-band optimal RT simulation.

Figure 4.7: Comparison of measured backscatter results for dry (artifical) snow at C- and X-band with optimal RT predictions obtained by treating the particle size as a free parameter. Optimal snow particle diameters are (1) C-band: 1.7 mm, and (2) X-band: 0.9 mm. Measured snow particle diameter is 0.27 ± 0.11 mm.

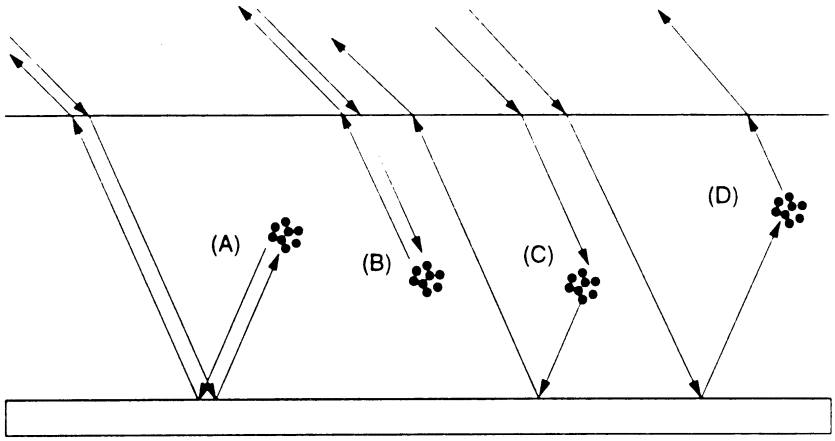

Figure 4.8: First-order volume scattering mechanisms in a layer of scatterers.

neath it, will be duplicated elsewhere.

A potentially very useful result may be obtained, however, if the intrinsic quantities which specify the extinction and scattering characteristics of this snow material can be retrieved. This concept is illustrated in the following section.

Direct Characterization of the Snow Medium

This section describes an approach for retrieving extinction and scattering parameters for the snow used in this study. A major assumption which is made is that dense media scattering *behavior* can be described by a first-order radiative transfer formulation. The familiar four terms of this formulation (derived in Chapter V) are depicted in Figure 4.8. We have intentionally represented the scattering elements as clusters to underscore the point that we are considering "effective" particles in this treatment, which may comprise correlated groups of individual physical particles and/or multiple scattering effects. The validity of such an assumption, that is, that dense media scattering can be understood in terms of a first-order radiative transfer model, will be examined in detail in Chapters V and VI. For the present, we assume that the assumption is valid.

A second assumption which will be made, which will greatly simplify the analysis, is that only the direct backscatter term (term (A) in Fig. 4.8) in the volume scattering formu-

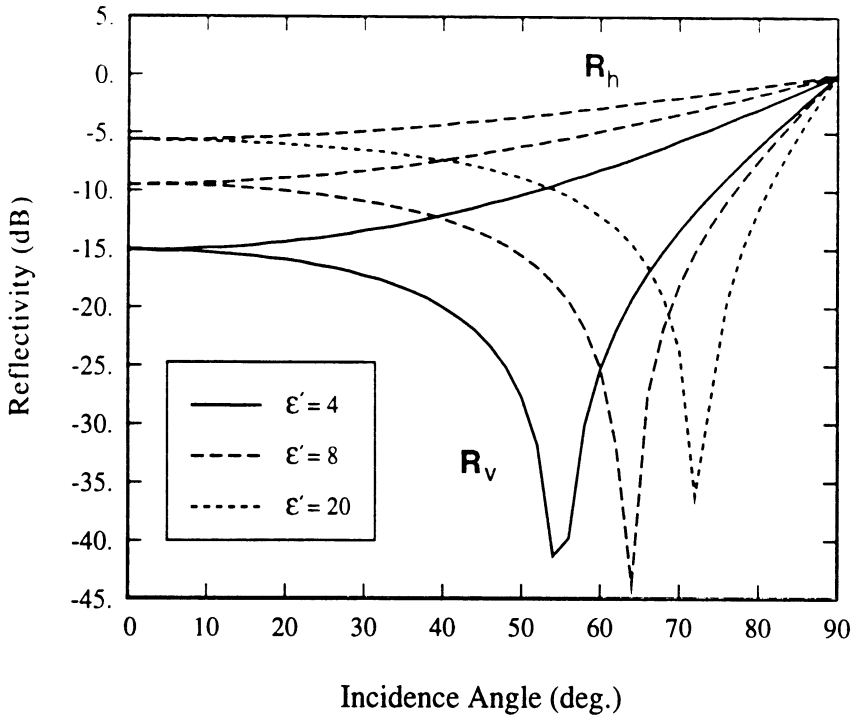

Figure 4.9: Fresnel reflectivity computed as a function of angle and polarization corresponding to the scenario of intensity inside a snow medium ($\varepsilon_s = 1.97$) specularly reflected off of terrains having the permittivities shown.

lation is important. Justification for this assumption is provided in Figure 4.9 which shows the magnitude of the Fresnel reflectivity as a function of angle for selected soil/ground permittivities beneath a snow layer having a dielectric constant of 1.97. For $\varepsilon' = 4$, which corresponds approximately to the dielectric constant of the ground in the present experiment (4.7 at C-band and 4.1 at X-band), the magnitude of this quantity is always less then -12 dB for h-polarized intensity (considering the refracted angle in the snow medium: 60° incidence in air corresponds to about 38° in the snow medium), and less then -15 dB for v-polarized intensity. Furthermore, the reflectivity will be further reduced by the roughness of the snow/soil interface (Choudbury et al. 1979). With respect to the expected magnitude of the bistatic scattering components ((C) and (D) in Fig. 4.8), some insight may be gained by a consideration of Rayleigh spheres, for which the phase function takes on its maximum

value[1], for both h- and v-polarizations, in the forward and back-scattering directions (Tsang et al. 1985)[p. 157].

Also shown in Figure 4.9 are cases of higher permittivity terrains beneath a snow layer. The two cases shown may be considered as representative of rock ($\varepsilon' = 8$ (Ulaby et al. 1990)) and wet soil ($\varepsilon' = 20$ (Hallikainen et al. 1985)). It is seen from these cases, especially at low incidence angles, it is harder to justify a formulation which considers only the direct backscatter term. This will be a particularly bad approximation for cases where the phase function takes on higher values for bistatic scattering directions relative to the backscatter direction.

In a case (such as the present one) where all but the direct backscatter term may be neglected, the first-order solution of the radiative transfer equation reduces (derived in Chapter V) to the form,

$$\mathcal{L}_m = \mathcal{L}_{ts} + \frac{1}{\mu_o'} \boldsymbol{\mathcal{T}}_{21} \left[\gamma \mathcal{P}_{bs} + \frac{\mathcal{L}_{gnd}}{L^2} \right] \boldsymbol{\mathcal{T}}_{12} \tag{4.8}$$

where, $\mathcal{L}_{ts}$ is the Mueller matrix corresponding to the top surface scattering, $\boldsymbol{\mathcal{T}}_{pq}$ is the surface transmissivity matrix[2] for transmission from p to q, where 1 corresponds to the air and 2 to the snow medium, μ_o' is the cosine of the refracted angle, $\mathcal{P}_{bs}$ is the unknown backscatter component of the phase matrix for the effective volume scattering element, $\mathcal{L}_{gnd}$ corresponds to the rough surface below, and,

$$\gamma = \frac{1 - \exp(-2\kappa_e d/\mu_o')}{2\kappa_e/\mu_o'}$$

$$L = \exp(2\kappa_e d/\mu_o'),$$

where κ_e is the extinction and d is the layer depth. This model has in the past been applied in a scalar sense to both snow (Ulaby and Stiles 1980) and vegetation (Attema et al. 1978).

[1] In the plane of incidence, scattering is uniform for an h-polarized wave for a Rayleigh sphere.
[2] The explicit form for this matrix is given in Chapter V, Eq. (5.11).

In order to apply (4.8) in a vector sense, it is necessary to construct Mueller matrices corresponding to the top and bottom rough surfaces. In the preceeding analysis, we had used an empirical model (4.1) – (4.3) for rough surface scattering because of its greater reliability. The model as it has been presented is a scalar one; in Oh et al. (1993), however, Oh extends this approach to include an empirical model for α, the degree of correlation between S_{vv} and S_{hh}. This parameter governs (Sarabandi 1992) the width of the probability density function which describes the distribution $\phi_{hh} - \phi_{vv}$, the phase difference of the co-polarized complex scattering amplitudes. Oh's formula is given as:

$$\alpha = \frac{1}{2}\left[1 - 0.2(\sin\theta)^{A(k_s,\Gamma_o)}\right](\cos\theta)^{B(k_s,\Gamma_o)} \tag{4.9}$$

where,

$$A(k_s,\Gamma_o) = (16.5\Gamma_o + 5.6)\exp[-41.6k_s\Gamma_o^2] \tag{4.10}$$

$$B(k_s,\Gamma_o) = 8.1\Gamma_o k_s \exp[-1.8k_s] \tag{4.11}$$

where, again, Γ_o is the Fresnel reflectivity at nadir. The importance of knowing α for the present purpose is that it is expressible in terms of the elements of the Mueller matrix, and thus can aid us in constructing these matrices for the ground and the snow surface. The quantity α is formally given by Sarabandi (1992) as,

$$\alpha = \frac{1}{2}\left[\frac{(M_{33}+M_{44})^2 + (M_{34}-M_{43})^2}{M_{11}M_{22}}\right]^{1/2} \tag{4.12}$$

where M_{mn} are elements of the modified Mueller matrix, $\mathcal{L}_m$:

$$\mathcal{L}_m = \begin{bmatrix} < |S_{vv}|^2 > & < |S_{hh}|^2 > & < \mathrm{Re}(S^*_{vh}S_{vv}) > \\ < |S_{hv}|^2 > & < |S_{hh}|^2 > & < \mathrm{Re}(S^*_{hh}S_{hv}) > \\ < 2\mathrm{Re}(S_{vv}S^*_{hv}) > & < 2\mathrm{Re}(S_{vh}S^*_{hh}) > & < \mathrm{Re}(S_{vv}S^*_{hh} + S_{vh}S^*_{hv}) > \\ < 2\mathrm{Im}(S_{vv}S^*_{hv}) > & < 2\mathrm{Im}(S_{vh}S^*_{hh}) > & < -\mathrm{Im}(S_{vv}S^*_{hh} - S_{vh}S^*_{hv}) > \end{bmatrix}$$

$$\begin{bmatrix} < -\mathrm{Im}(S^*_{vh}S_{vv}) > \\ < -\mathrm{Im}(S^*_{hv}S_{hh}) > \\ < -\mathrm{Im}(S_{vv}S^*_{hh} - S_{vh}S^*_{hv}) > \\ < \mathrm{Re}(S_{vv}S^*_{hh} - S_{vh}S^*_{hv}) > \end{bmatrix} \quad (4.13)$$

From Eq. (4.12), if we make the assumption that M_{43}, which corresponds (for backscatter) to the term $- < \mathrm{Im}(S_{vv}S^*_{hh} >$, is much smaller than $< \mathrm{Re}(S_{vv}S^*_{hh}) >$, then

$$< S_{vv}S^*_{hh} > \approx \pm\alpha\sqrt{M_{11}M_{22}} \quad (4.14)$$

From comparison with the bare ground backscatter data, the selection of the negative root is indicated, (following the FSA convention), which is also in agreement with polarimetric predictions for rough surfaces (van Zyl et al. 1987) in which it has been found that the statistical phase difference between S_{vv} and S_{hh} is near 180° (0° in the BSA convention). For the bare ground under the snow layer, α was found, using (4.9) to be essentially unity for both C-band and X-band for all angles between 20° and 60° degrees. For the top snow surface, α varied from unity at 20° to 0.89 at 60° for both frequencies. A further assumption that was made in constructing the Mueller matrices for the top and bottom surfaces—and one which is reasonable given the above discussion regarding the co-polarized phase difference for rough surfaces—is that the elements M_{34} and M_{43} corresponding to $\pm\mathrm{Im} < S_{vv}S^*_{hh} >$ are zero.

The polarimetric character of the two rough interfaces, above and below the snow layer are thus characterized by a target Mueller matrix having the following form:

$$\mathcal{L}_{surf} = \begin{bmatrix} g_{vv} & g_{vh} & 0 & 0 \\ g_{vh} & g_{hh} & 0 & 0 \\ 0 & 0 & -\alpha\sqrt{g_{vv}g_{hh}} - g_{vh} & 0 \\ 0 & 0 & 0 & -\alpha\sqrt{g_{vv}g_{hh}} + g_{vh} \end{bmatrix} \tag{4.15}$$

where,

$$g_{pq} = \frac{\sigma^{\circ}_{pq}}{4\pi\cos\theta_{im}} \tag{4.16}$$

with σ°_{pq} as given by the semi-empirical model of Eqs. (4.1)–(4.3), and θ_{im} the angle of incidence onto the surface in the appropriate medium (air for the top surface, snow for the underlying soil surface). The correlation coefficient α is as calculated in Eq. (4.9).

The parameters to be specified through an optimization of the measured polarimatric data with the model given in (4.8) are the scalar extinction and the backscatter component of the phase matrix $\mathcal{P}_{bs}$. Since the snow is assumed to be an isotropic medium we use the form:

$$\mathcal{P}_{bs} = \begin{bmatrix} P1 & P2 & 0 & 0 \\ P2 & P1 & 0 & 0 \\ 0 & 0 & P3-P2 & -P4 \\ 0 & 0 & P4 & P3+P2 \end{bmatrix} \tag{4.17}$$

which requires the volume backscattering for the two co-polarized channels to be identical. The nature of the other elements is set by considerations of reciprocity ($|S_{vh}|^2 = |S_{hv}|^2$) and zero correlation between the co- and cross-polarized complex scattering amplitudes. With the unknown scalar extinction there are therefore five unknown quantities to be determined

Parameter	C-band	X-band
κ_e	0.513	1.28
P_1	0.316×10^{-2}	0.128×10^{-1}
P_2	0.330×10^{-3}	0.740×10^{-3}
P_3	-0.169×10^{-3}	-0.976×10^{-3}
P_4	0.531×10^{-3}	0.220×10^{-2}

Table 4.2: Artificial snow: Empirical parameters for RT-model

Source	C-band	X-band
"Meas."	0.513	1.28
EFA	0.020	0.047
QCA-CP	0.042	0.096

Table 4.3: Estimates of the extinction of the artificial snow

in order to characterize the snow polarimetrically. The estimation of these parameters is done using an optimization package suitable for non-linear problems (Zhou and Tits 1993). The optimization is performed using only the 40° data, considering all three depths, for both C-band and X-band, and then the results applied to generate predictions for the other cases (depths and angles) not used in the optimization process.

In Figures 4.10 thru 4.12, we show the measured data along with predictions generated using the estimated parameters κ_e and $P_1, \ldots, P_4$ in (4.8). The angular variation predicted by (4.8) (in which the angular variation is contained in the transmissivity matrices) appears reasonable, as does the behavior with respect to depth at angles which were not involved in the optimization process. The estimated values for the parameters κ_e and $P_1, \ldots, P_4$ for both C- and X-band are summarized in Table 4.2. A comparison of the values for extinction obtained by this empirical and two theoretical methods is given in Table 4.3. One of the two methods, EFA or the Effective Field Approximation, is associated with conventional radiative transfer (CRT) and the other, QCA-CP or, Quasi-Crystalline Approximation–Coherent Potential, is used in dense medium radiative transfer (DMRT). These techniques are described (briefly) in Chapter VI. It is seen from Table 4.3, as for the scattering computations mentioned earlier, the predicted effects of the snowpack are practically negligible.

Since the analysis was a complete polarimetric one, we can examine the results with

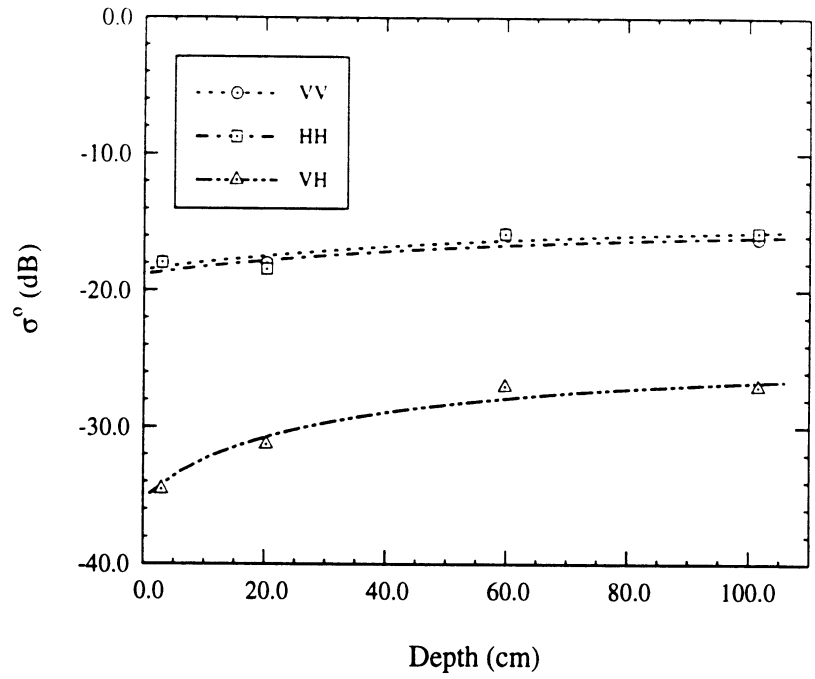

(a) C-band, 40°

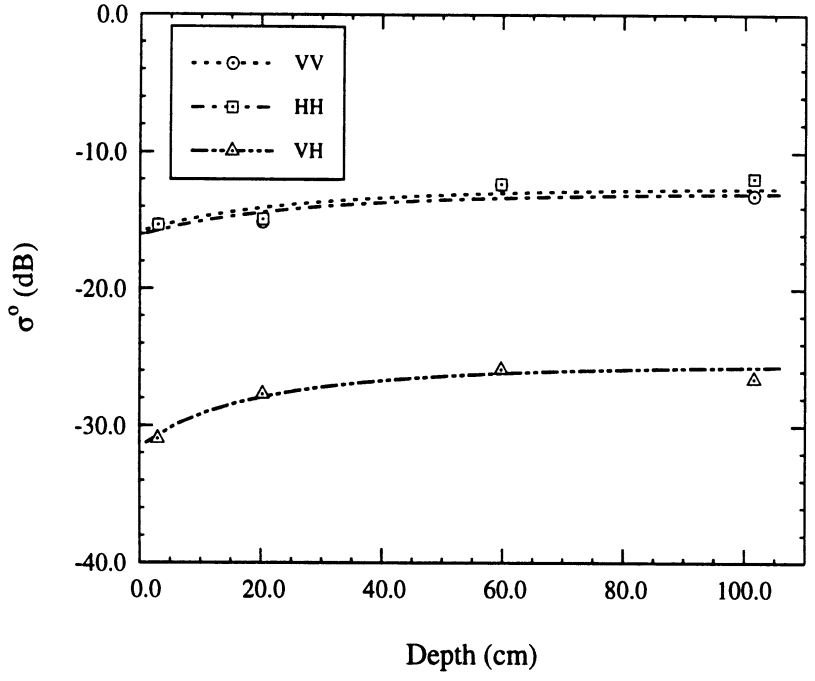

(b) X-band, 40°

Figure 4.10: Comparison of snow data to radiative transfer-type model computations. Parameters for model are obtained through an optimization process which uses this data.

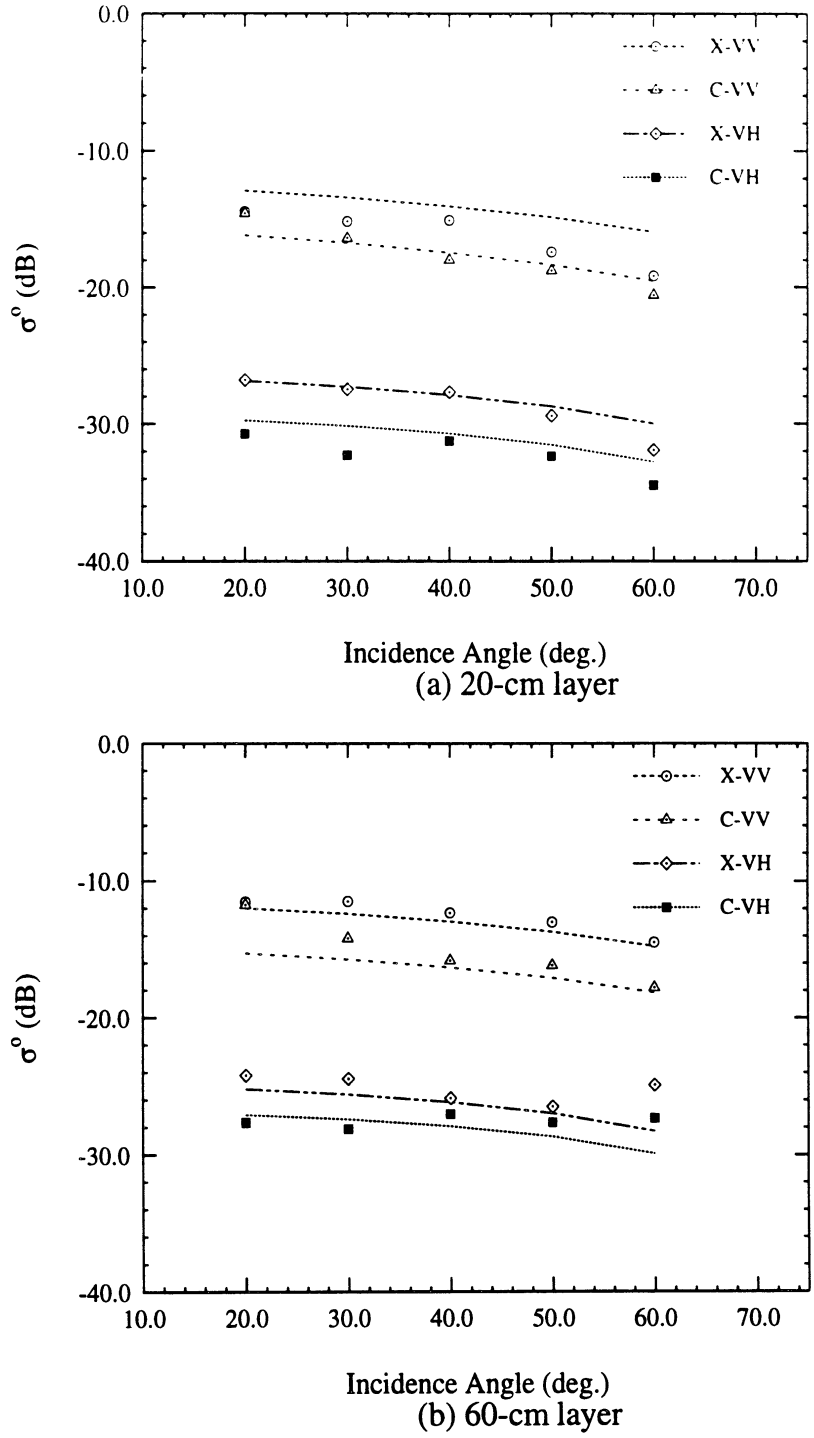

Figure 4.11: Comparison of C- and X-band snow data to radiative transfer-type model predictions. Model is parameterized though analysis of 40° data.

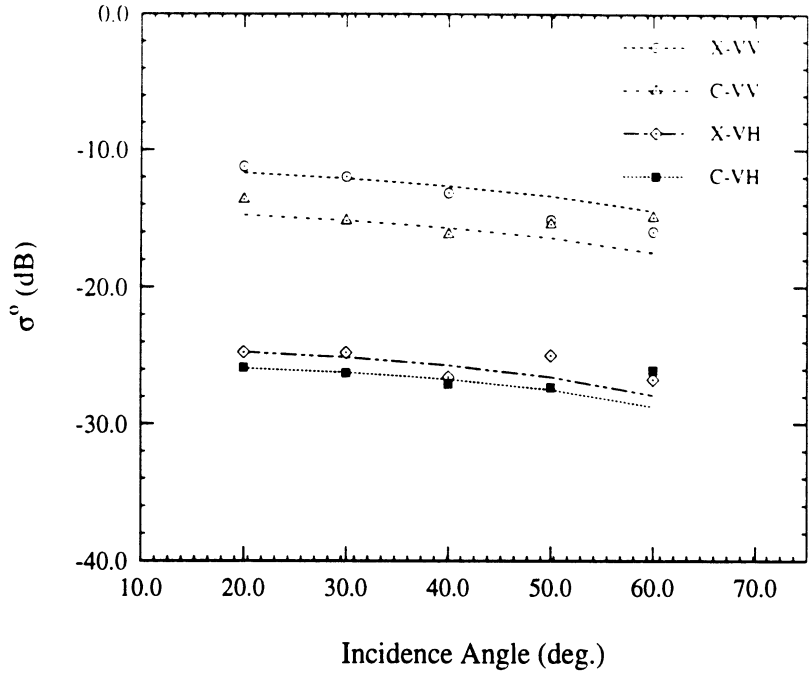

Figure 4.12: Comparison of C- and X-band snow data to radiative transfer-type model predictions, for a 102-cm layer. Model is parameterized though analysis of 40° data.

respect to the two remaining (given the two co-polarized responses and the cross-polarized response already examined) independent quantities associated with a measured Mueller matrix in the backscatter direction. These quantities are the Degree of Correlation, α, which was introduced earlier, and another quantity which pertains to the position of the maximum of the pdf (Sarabandi 1992) describing the distribution of the phase difference between S_{vv} and S_{hh}^{*}. This quantity is known as the Co-polarized Phase Difference and is denoted by the symbol ζ.

Figure 4.13 compares the measured values of these quantities and the estimates generated throught the use of the RT model with parameters given in Table 4.2, for the case of the 60 cm artificial snow layer. The agreement is not exceptionally good. This is attributed to (1) the need to specify the polarimetric character of both rough surface (above and below the snow) and (2) the generally noisy character of the data.

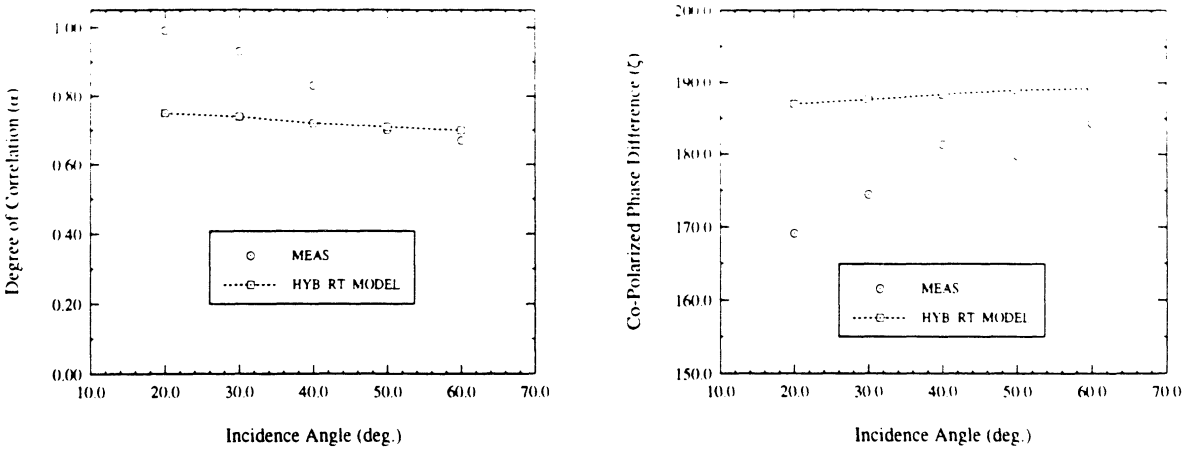

(a) Degree of Correlation (b) Co-polarized Phase Difference

Figure 4.13: Phase statistics for the 60 cm artifical snow layer. Shown are the measured values and those calculated using an RT model with associated parameters given in Table 4.2.

4.3.3 Discussion of Dry Snow Results

The most important result from the dry snow experiments was the observation that the most widely used models describing the electromagnetic scattering characteristics of dense media failed to give reasonable predictions in comparison to measured data. While one experiment is not sufficient for evaluating the valdity of a theory, the present experiment carries significant weight because of the relatively simple and well-characterized nature of the target snowpack.

In the subsequent analysis, a simple method for retrieving electromagnetic parameters intrinsic to the snow medium itself was described. It is noteworthy—in the face of the very large body of research which has been done on snow and pertaining directly to snow—that this marks the first time an attempt has been made to characterize the effect of a snow medium considered in isolation from other effects, in a polarimetric way. The only other comparable example is the snow-pile experiments and subsequent scalar analysis described in Ulaby and Stiles (1980), in which the radar response of a snow-pile of varying depths was collected. That effort was hampered by a number of departures from ideal experimental cir-

cumstances. For example, only one spatial sample was available, the snow was artificially heaped up by mechanical means, and efforts to characterize the upper or lower surfaces or even the general uniformity of the snow pile were absent.

If, as the present results seem to indicate, theoretical means are not presently (or practically) capable of accurately representing the character of complex snow media, a direct measurement campaign could be beneficial in providing the basis for *realistic* modeling of snow, and to drive model development as well. Since a given snow type is an extensible medium, i.e. its character is independent of depth, a hybrid modeling approach is possible. Such an approach would use experimentally derived extinction and scattering parameters intrinsic to the snow material and a simple radiative transfer model such as (4.8) to generate predictions with respect to depth. Integrated in a first-order, non-coherent way with the effects of rough surfaces above and below, the approach allows considerable versatility with respect to realistic modeling of snow, and enhances the potential for practical estimation of highly desirable hydrological quantities such as depth and water equivalent.

Of course, for direct characterization of snow, it is not feasible to use the approach employed in this study. A practical scheme should borrow from the spirit of the snow-pile experiments alluded to above, in terms of having a target of a fairly manageable size—except that a turntable could be employed to allow realization of independent samples and steps taken to control the character of the surfaces above and below. The material representing the underlying half-space could be chosen to best facillitate the retrieval of information. Feasibility studies on this technique, using not snow but stable materials like sand and gravel, have in fact been carried out by the author and the results, including an analysis of the validity of a vector radiative transfer model with empirically-derived parameters for describing very dense media are presented in Chapters V and VI.

4.4 Diurnal Results and Discussion

This section present the results from measurements of partial diurnal cycles which were collected on two separate occasions, as described in the Section 4.2. The snow probe was used on both occasions to record vertical profiles of the liquid water content as a function of time. The two snowpacks examined had very different physical descriptions as will be shown. This allows some insight into the generation and spatial behavior of liquid water in a snowpack. Additionally, we will examine the degree to which features in the polarimetric response can be tied to the detailed characteristics of a wet snowpack. Finally, we will use the diurnal results and associated wetness data to evaluate a particular algorithm which has been proposed for the retrieval of snow liquid water content.

4.4.1 Brighton Diurnal Results

In the Brighton diurnal experiment, the measurements were made continuously from 10 a.m. until 7 p.m.. Overnite temperatures prior to the experiment were well below freezing; the temperatures during the day ranged from -6°C at 8 a.m. to more than 6°C at 3 p.m. It was a very sunny day, and heavy melting was evident. By 6 p.m. the temperature dropped abruptly below freezing again. The target snowpack was 0.88-m deep, with about 15-cm of relatively fresh snow on top, however, the bottom 16 cm consisted of solid ice. The density of the snowpack was about 0.25 g/cm^3 at the top, increasing linearly to 0.45 by 30 cm into the pack, where it remained essentially constant to the bottom of the snowpack.

The co- and cross-polarized results for C- and X-band are shown in Figure 4.14. Both frequencies show a significant reduction in the backscatter at midday, very typical of a diurnal response, in this case 8–10 dB for C-band, and $\approx$14 dB for X-band. By the end of the measurements however, the radar response at both frequencies appears to be headed back up towards the original morning levels. The results of the snow probe measurements made concurrently with the radar measurements are shown in Figure 4.15. The wetness

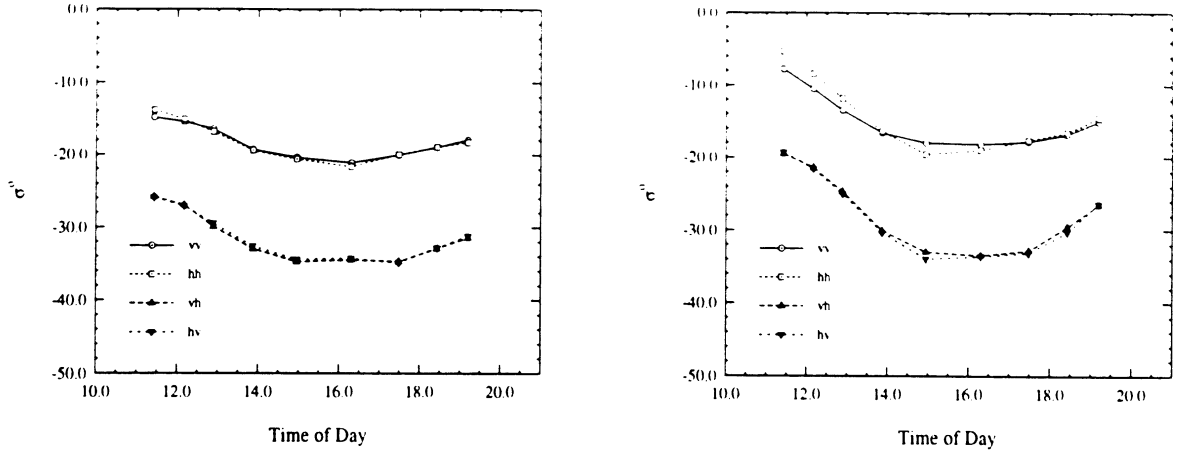

(a) C-band (b) X-band

Figure 4.14: Co- and cross-polarized backscatter results from Brighton (partial) diurnal experiment. Incidence angle is 40°.

measurements begin at 18-cm, due to the presence of the ice layer below this, and are made at roughly 5-cm intervals. The temporal spacing between measurements of the vertical profile was ≈1 hour. What is most striking about the wetness map is the presence of very significant wetness levels in the lower 35–40 cm of the snowpack, even at the earliest point measured in the morning, while the top surface is completely dry. The wetness level of the top surface remains fairly moderate through the day, staying below 5% except, curiously, at the very end of the day, just before the temperature fell very swiftly below freezing again. It would appear that the top of the snowpack was freely draining throughout the day as the wetness levels towards the bottom were observed to increase to maximal snow wetness levels, >12%.

4.4.2 Cadillac Diurnal Results

In the Cadillac diurnal experiment, the snowpack was only 22 cm deep. The measurements were made from 10 a.m. to about 4 p.m. As in the Brighton case, the overnite temperatures had been sub-freezing but the experiment day itself became very warm, reaching 12°C for a high, and very sunny. Extensive melting was clearly evident around the entire

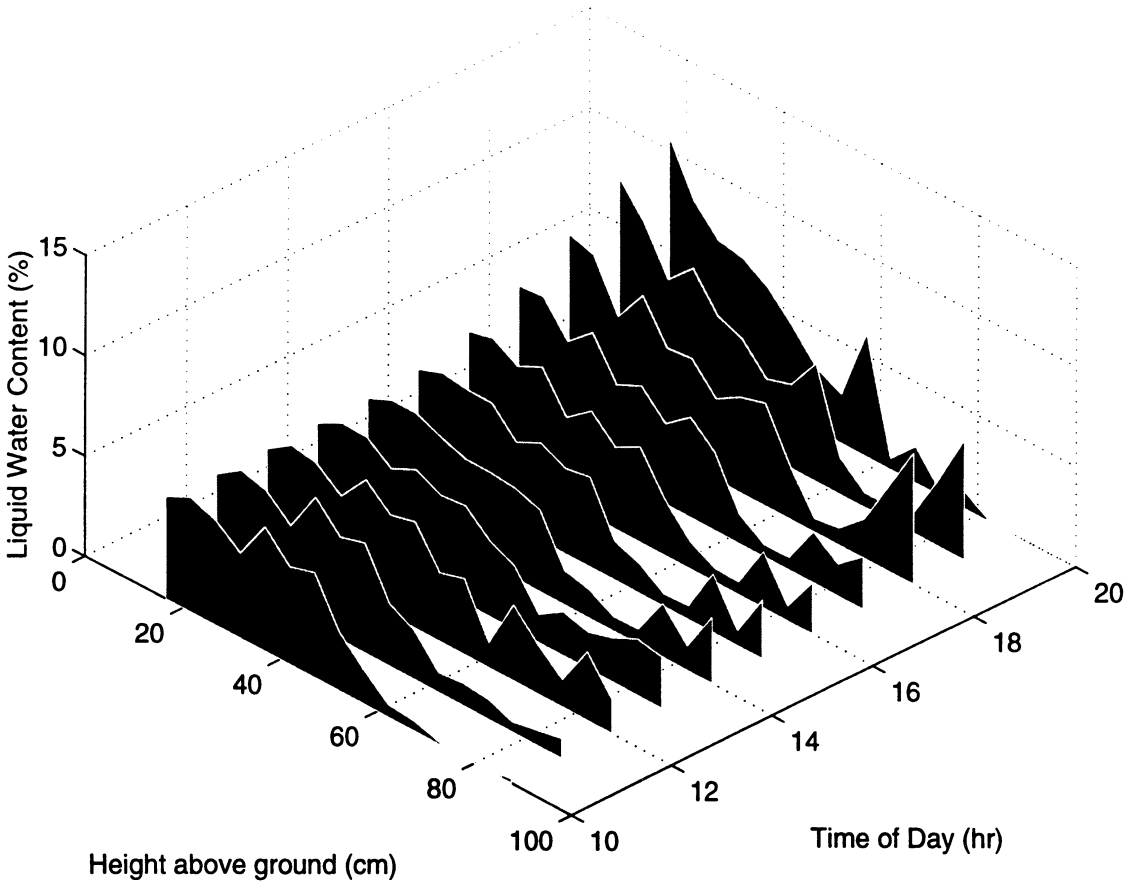

Figure 4.15: Vertical profiles of snow wetness measured as a function of time. Measurements were taken with the snow probe during the Brighton diurnal experiment.

experimental area.

The co- and cross-polarized results are shown in Figure 4.16, and the associated wetness map in Figure 4.17. The apparent higher frequency of collection of radar measurements relative to the Brighton data pertains to the number of measurements which were combined

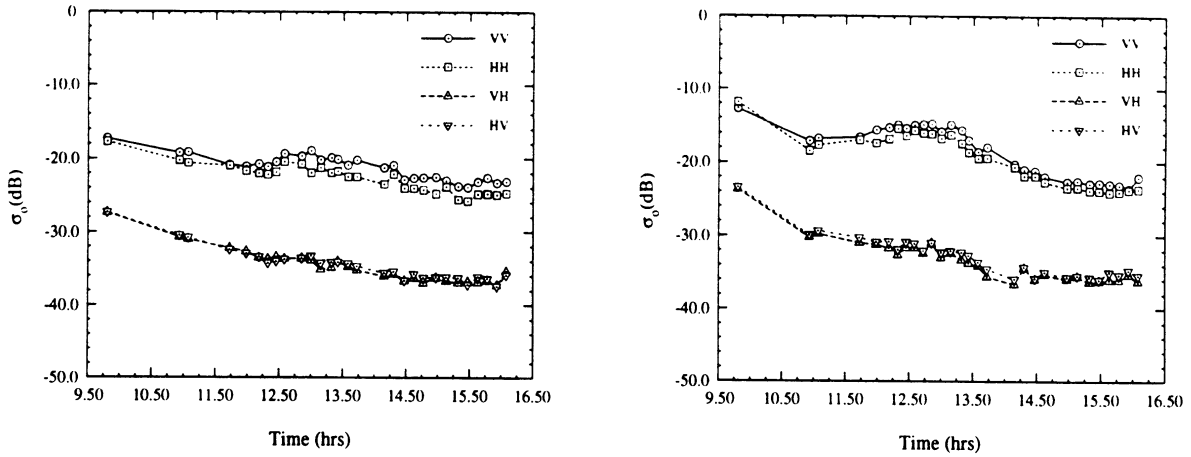

(a) C-band (b) X-band

Figure 4.16: Co- and cross-polarized backscatter results from Cadillac (partial) diurnal experiment. Incidence angle is 40°.

as a single data point in each case. These results are seen to have a very different character than that observed in the Brighton case. An important feature of the Cadillac snowpack was the presence, at least during the initial few hours of the experiment, of a very prominant ice lens, starting approximately 2.5 cm below the top surface and having a thickness of about 2 cm. A result which is attributable to both this feature and the relatively much warmer temperatures which occurred compared to the Brighton case, is the presence of very high wetness levels in the uppermost levels of the snowpack. Though the high wetness levels are not strictly confined to the 2.5 cm above the ice lens, it is apparent that the ice lens, particularly early on and to a lesser extent as it became softer and more permeable, impeded the drainage of the liquid water through the snowpack. Indeed there appears to be some evidence from an examination of Figure 4.17 that the ice lens rapidly evolved, as it softened, into a region supporting very high wetness levels.

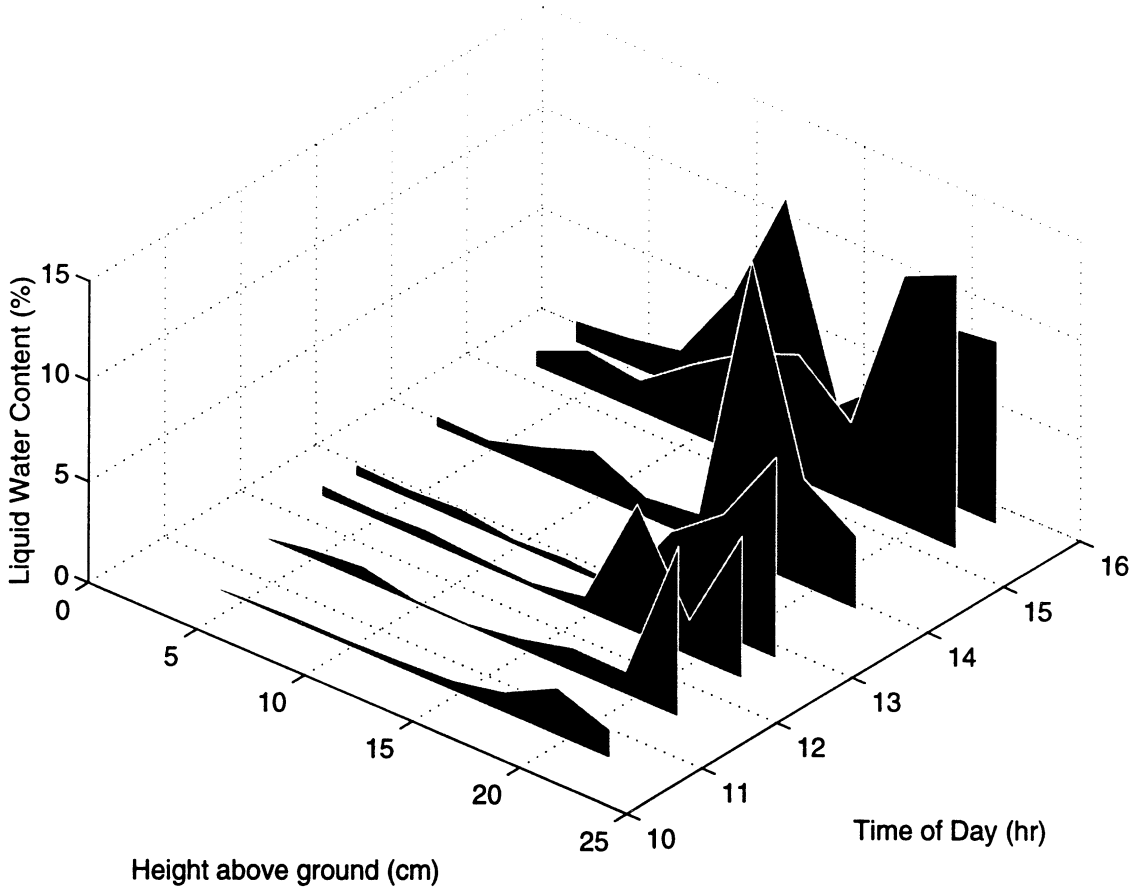

Figure 4.17: Vertical profiles of snow wetness measured as a function of time. Measurements were taken with the snow probe during the Cadillac diurnal experiment.

One implication of this situation (high wetness levels near the surface) evident in the backscatter (Fig. 4.16) is a "hump", or at least a temporary departure from the downward trend of σ°, for both co- and cross-polarized channels. This feature, occurring between the 11:30 a.m. and about 2 p.m., is apparently tied to the increase in surface scattering, due to a higher dielectric contrast, balancing the reduction in volume scattering. Additional interpretation of the polarimetric scattering response is given, for both diurnal cases, in the following section.

4.4.3 Polarization Features of Diurnal Responses

It has been suggested (van Zyl et al. 1987; Evans et al. 1988; van Zyl 1989; Shi and Dozier 1992) that certain polarimetric features contain information pertaining to the nature of the scattering mechanisms present in a given target cell. In particular, it has been suggested that these features can be used to discern the degree to which volume and surface scattering contribute, respectively, to the scattering response for a given target. It will be instructive, and also relevant to the wetness inversion algorithm which is evaluated in the next section, to examine the implications of such assertions with respect to the present diurnal data sets. Three such polarimetric features are the *correlation coefficient*, which has been discussed in Section 4.3.2, the *depolarization ratio*, and the *coefficient of variation*.

The correlation coefficient, α, pertains to the correlation between the two quantities S_{vv} and S_{hh}^*. This correlation is expected to be reduced in the presence of multiple scattering due to the rapidly varying phase differences between HH and VV polarizations.

The depolarization ratio, χ_d, is defined as

$$\chi_d = \frac{\sigma_{vh}^\circ + \sigma_{hv}^\circ}{\sigma_{vv}^\circ + \sigma_{hh}^\circ}. \tag{4.18}$$

The production of cross-pol in a random medium is another attribute associated with volume scattering.

The coefficient of variation (van Zyl et al. 1987), ν, is the ratio of the minumum value to the maximum value of a polarization signature. It is thought to be a measure of the diversity of scattering mechanisms which are present in a target. It is formally expressed by

$$\nu = \frac{\text{minimum power received}}{\text{maximum power received}}. \tag{4.19}$$

Moderately rough surfaces, like the ocean at L-band, have a very small coefficient of variation, meaning that the radar response is highly polarized and hence sensitive to changes in polarization. Diffuse scattering has a very high coefficient of variation, meaning that the target response is mainly unpolarized and hence insensitive to changes in the transmit and receive polarizations.

The values of parameters α, χ_d, and ν are shown for the Brighton and Cadillac diurnals in Figures 4.18–4.20. Figure 4.18 compares α for the two different experiments. For the Brighton case, (a), α is essentially constant, though the X-band results appear somewhat

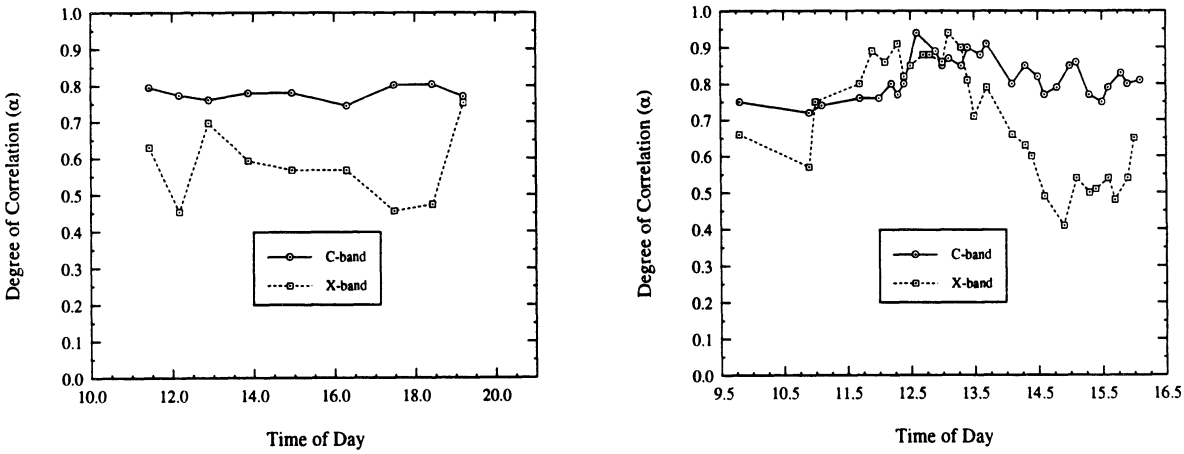

(a) Brighton Expmt. (b) Cadillac Expmt.

Figure 4.18: Degree of Correlation compared for the two diurnal experiments.

noisy. The Cadillac results show a clear increase in the degree of correlation, in a time range consistant with the "hump" described above for the σ° results. These higher values of α may be attributed to an increased surface scattering component in the total backscatter. In general, the phases of S_{vv} and S_{hh} will be more highly correlated, leading to a higher value

of α, for pure surface scattering than for volume scattering where multiple scattering events will tend to randomize the phase relationship between these two quantities.

The comparisons with respect to χ_d and ν between the two diurnal experiments show essentially the same effect. An interesting byproduct of this analysis is the observation that the information provided by the coefficient of variation, ν, appears to be essentially equiva-

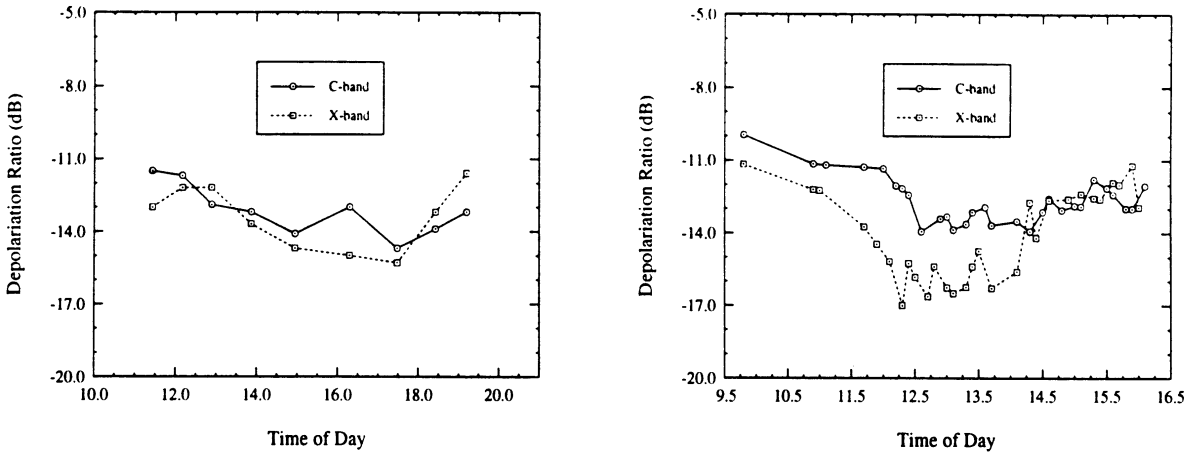

(a) Brighton Expmt. (b) Cadillac Expmt.

Figure 4.19: Depolarization Ratio compared for the two diurnal experiments.

lent to that provided by the degree of correlation α. The depolarization ratio for the Brighton case (Figure 4.19(a)) does show a reduction consistant with a reduction of volume scattering; indicating that even as the backscatter is reduced with increasing wetness, the cross-pol is reduced to a greater degree than the co-pol.

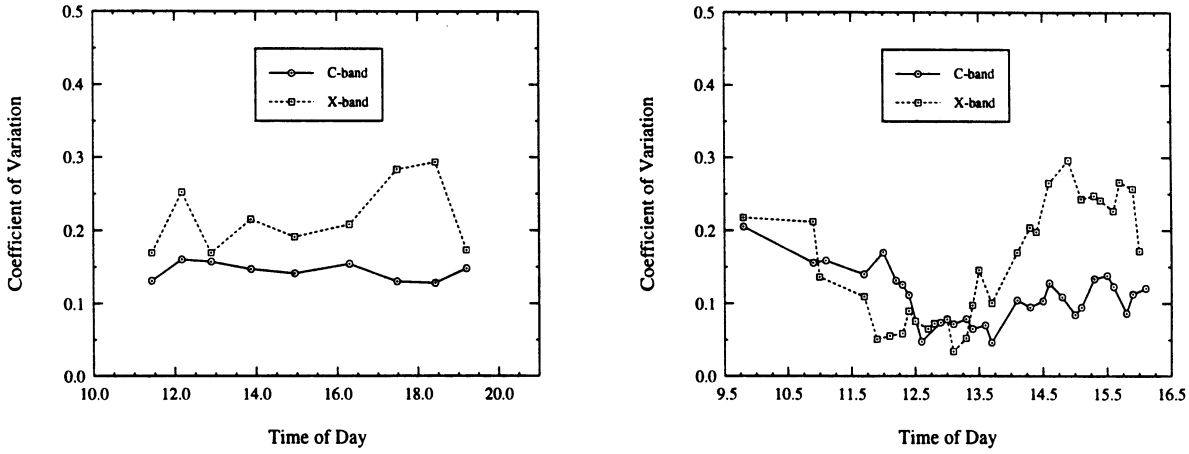

(a) Brighton Expmt. (b) Cadillac Expmt.

Figure 4.20: Coefficient of Variation compared for the two diurnal experiments.

4.4.4 Evaluation of Wetness Retrieval Algorithm

The availability of detailed snow wetness information along with polarimetric backscatter data allows comparison with an algorithm which has recently been developed (Shi and Dozier 1992; Shi and Dozier 1995), for the retrieval of snow liquid water estimates from polarimetric data at C-band. The ability to detect, quantitatively, from remotely-sensed data, a parameter such as liquid-water content in snow would constitute a very important achievement and a major step forward in supplying hydrologists and other earth scientists with data products critical for various applications. It is all the more impressive given the difficulties associated even with *direct* measurements of liquid water content. Given the potential value of such an algorithm, it is highly desirable that its validity be supported by careful ground-based measurement efforts. The present diurnal experiment appears to be an excellent candidate for this evaluation.

The algorithm was originally motivated by an AIRSAR data set which was collected over glaciers in the Öztal Alps, Austria. Prior to these measurements, physical characteristics such as snow depth, density, wetness and surface roughness were measured. The final version of the algorithm, as appears in Shi and Dozier (1995) was developed in conjunction with data from a recent (Apr. 1994) SIR-C/X-SAR mission, taken over Mammoth Mountain on the eastern slope of the Sierra Nevadas. A similar ground truth campaign was employed in this effort as well.

Model Details

The following reproduces the essential features of the wetness retrieval algorithm which are explicity described in Shi and Dozier (1995):

- Snow volume scattering is assumed to be first order and isotropic. In this case, for a halfspace (which is an assumption of the model, which the authors deem justifiable

when liquid water is present), the following relationship holds for the volume scatter:

$$D_T(\theta_i, \varepsilon_s) = \frac{\sigma^v_{vv}}{\sigma^v_{hh}} = \left[\frac{\mathcal{T}_{vv}(\theta_i, \varepsilon_s)}{\mathcal{T}_{hh}(\theta_i, \varepsilon_s)}\right]^2 \tag{4.20}$$

where T_{pp} are the Fresnel power transmissivities.

- Non-coherent addition of the surface and volume contributions are assumed:

$$\sigma^v + \sigma^s = \sigma^t. \tag{4.21}$$

- The correlation coeffient is assumed to be unity (in seeming contradiction to their own observations with respect to the AIRSAR data). Thus, can define,

$$D_{TV} = \frac{\sigma^v_{vvhh}}{\sigma_{vv}} = \frac{\mathcal{T}_{vv}\mathcal{T}_{hh}}{\mathcal{T}^2_{vv}} \tag{4.22}$$

$$D_{TH} = \frac{\sigma^v_{vvhh}}{\sigma_{hh}} = \frac{\mathcal{T}_{vv}\mathcal{T}_{hh}}{\mathcal{T}^2_{hh}} \tag{4.23}$$

where

$$\sigma^v_{vvhh} = \mathrm{Re}[S^v_{vv}S^{v*}_{hh}]$$

and also, as in the case of the co-polarized responses,

$$\sigma^t_{vvhh} = \mathrm{Re}[S^t_{vv}S^{t*}_{hh}] = \sigma^v_{vvhh} + \sigma^s_{vvhh}.$$

Eqs. (4.22) – (4.23) also implicitly assume that the value of the co-polarized phase difference is zero, that is, the quantities S_{vv} and S_{hh} have the same phase.

- They used a statistical treatment of the results from the IEM (Integral Equation Method) rough surface scattering model (Fung and Chen 1991) computed over the range of

surface parameters (ε, s, l) expected for snow to produce an empirical model given by:

$$\sigma^s_{pp} = |\alpha_{pp}|^2 \left[\frac{S_R}{a(\theta_i) + b(\theta_i) S_R} \right]. \tag{4.24}$$

where α_{vv} and α_{hh} are the same as found for the small perturbation model in (Ulaby et al. 1986)[Chap. 12, pp. 961 & 965], expressed in terms of the dielectric constant of the medium and the angle of incidence. The constants a and b are provided in the appendix of Shi and Dozier (1995), in the form of third- degree polynomials in θ. The quantity S_R is the surface roughness parameter, given by,

$$S_R = (ks)^2 W \tag{4.25}$$

where s is the rms height of the surface roughness and W is the power spectrum of the correlation function of the surface roughness.

- From equations (4.20)–(4.24), two relations may be derived which contain only two unknowns: (1) ε_{ws}, the permittivity of the wet snow and (2) S_R, the surface roughness parameter. These two relations are:

$$\sigma^t_{vvhh} - D_{TV}\sigma^t_{vv} = \sigma^s_{vvhh} - D_{TV}\sigma^s_{vv} \tag{4.26}$$

$$\sigma^t_{vv} + \sigma^t_{hh} - \frac{D_{TV} + D_{TH}}{D_{TV} D_{TH}} \sigma^t_{vvhh} = \sigma^s_{vv} + \sigma^s_{hh} - \frac{D_{TV} + D_{TH}}{D_{TV} D_{TH}} \sigma^s_{vvhh}. \tag{4.27}$$

- The unknown S_R in the above equations can be eliminated altogether by developing numerical relationships, using Eq. (4.24), between the pairs $[\sigma^s_{vv}, \sigma^s_{vvhh}]$ and $[\sigma^s_{vv} + \sigma^s_{hh}, \sigma^s_{vvhh}.]$ These are:

$$\frac{|\alpha_{vv}|^2}{\sigma^s_{vv}} = a_{vx}(\theta_i) \frac{\mathrm{Re}[\alpha_{vv}\alpha^*_{hh}]}{\sigma^s_{vvhh}} + b_{vx}(\theta_i) \tag{4.28}$$

and,

$$\frac{\sigma^s_{vv}+\sigma^s_{hh}}{|\alpha_{vv}|^2+|\alpha_{hh}|^2}=a_{vhx}(\theta_i)\frac{\sigma^s_{vvhh}}{\mathrm{Re}[\alpha_{vv}\alpha^*_{hh}]}. \tag{4.29}$$

where the coefficients a_{vx}, b_{vx}, and a_{vhx} are provided in the appendix of Shi and Dozier (1995).

- Eqs. (4.26)–(4.29) can be used to produce an equation which is only a function of ε_s, the permittivity of the snow:

$$M_1[a_{vx}\mathrm{Re}[\alpha_{vv}\alpha^*_{hh}](a_{vhx}D_{RS}-D_{TS})+b_{vx}M_2] = M_2\left[a_{vx}\mathrm{Re}[\alpha_{vv}\alpha^*_{hh}]+\frac{b_{vx}M_2}{a_{vhx}D_{RS}-D_{TS}}-D_{TV}|\alpha_{vv}|^2\right], \tag{4.30}$$

where,

$$M_1=\sigma^t_{vvhh}-D_{TV}\sigma^t_{vv} \tag{4.31}$$

$$M_2=\sigma^t_{vv}+\sigma^t_{hh}-D_{TS}\sigma^t_{vvhh} \tag{4.32}$$

$$D_{TS}=\frac{D_{TV}+D_{TH}}{D_{TV}D_{TH}} \tag{4.33}$$

$$D_{RS}=\frac{|\alpha_{vv}|^2+|\alpha_{hh}|^2}{\mathrm{Re}[\alpha_{vv}\alpha^*_{hh}]}. \tag{4.34}$$

The inversion algorithm amounts to finding the value of ε_s which most nearly satisfies Eq. (4.30).

Application to Measured Diurnal Data

We first attempted to treat the Cadillac data set with this algorithm. The physical description of the snowpack in the Cadillac experiment seemed to agree generally with the inherent assumptions of the model, namely m_v effects manifesting themselves primarily in the upper regions of the snowpack. Only the C-band data was used in the algorithm evalua-

tion, which consisted of testing a range of values of ε_s to find the value most nearly satisfying Eq. (4.30). We used a range which corresponded to values of this parameter which might reasonably be associated with snow: $1.1 \leq \varepsilon_s \leq 5.0$.

The values of ε_s which were the outputs of the algorithm with respect to the cadillac data are shown in Figure 4.21. As seen, most of the twenty-nine separate sets of polarimetric

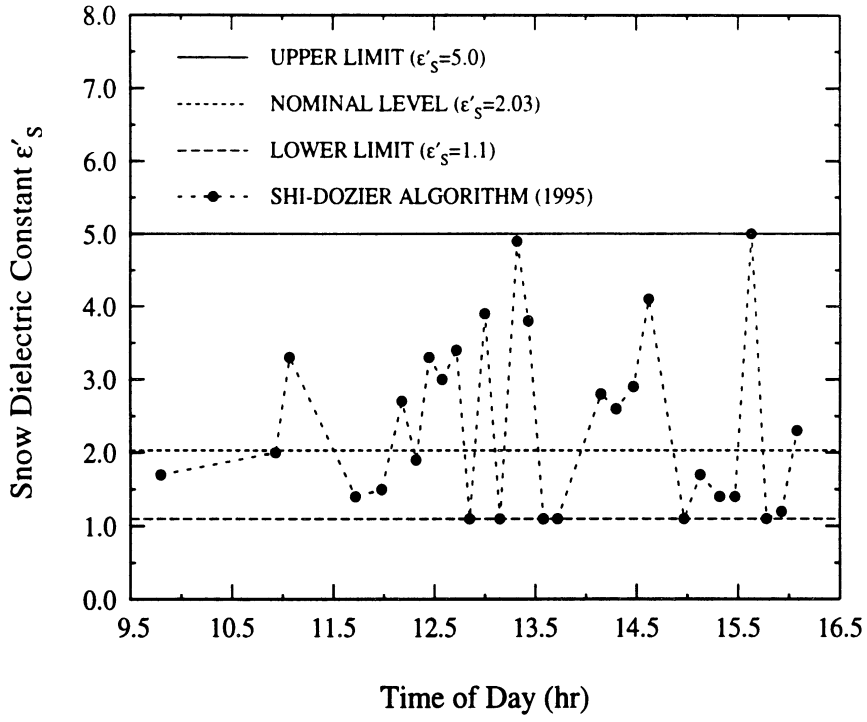

Figure 4.21: Application of inversion algorithm for snow wetness applied to Cadillac diurnal data set. Shown is the actual output from the algorithm, snow permittivity ε_s. The "nominal level" shown is based on the expected *dry* snow permittivity based on ground truth measurements of density.

radar measurements resulted in estimates of ε_s which are within the bounds of "reasonable" results which we set. Only one data set produced a value pegged at the top of the range ($\varepsilon_s = 5.0$) and six were pegged at the bottom ($\varepsilon_s = 5.0$). Also shown in the figure is the nominal value of the permittivity of the top layer of the snowpack, based on ground truth measurements. The average measured density of the top layer was found to be about 0.5 g cm^{-3}; such a density would correspond to a *dry snow dielectric constant* of 2.03, which is

the nominal value shown in the figure.

As described in Chapter III, the permittivity of wet snow is modeled as a dry snow value (given by Eq. (3.13)) which depends on density alone *plus* an incremental increase (given by Eq. (3.6)) which depends on snow wetness (m_v) alone. If the incremental increase is known, an accurate estimate of m_v may be obtained. The incremental increase itself may really only be known if the density of the snow is known also, so that the base contribution to ε_s represented by the dry snow component ε_{ds} may be accounted for. Then the incremental increase is given by,

$$\Delta\varepsilon_s(m_v) = \varepsilon_s(m_v, \rho) - \varepsilon_{ds}(\rho). \tag{4.35}$$

This is one shortcoming of the algorithm by Shi and Dozier (1995), and one which is not addressed by the authors, namely, the relatively large errors which result in trying to estimate m_v of snow from a measurement of ε_s alone, with no knowledge of the snow density. We will examine this question further below.

For the purpose of evaluating the present algorithm however, we will compute estimates of m_v for the Cadillac data set by subtracting the value of 2.03 (based on the measured density of 0.5 g cm^{-3}) from each of the algorithm-estimated permittivities shown in Figure 4.21. The remainder of this operation is the incremental increase in the permitivity due to water, and this quantity can be inverted using Eq. (3.6) to obtain an estimate of m_v. These estimates are shown in Figure 4.22, along with the values of m_v which were measured in the upper most layer as a function of time using the Snow Probe. All cases where the algorithm estimated value of ε_s are *less* than the nominal dry-snow value of 2.03 are considered as having $m_v = 0$. It is seen that the algorithm gives a reasonable performance in terms of its predictions that there were very high snow wetness levels present. About half of the cases examined result in estimates of $m_v = 0$. Of the cases which give non-zero estimates of m_v, very high wetness levels are indicated—similar to but in general exceeding the actual

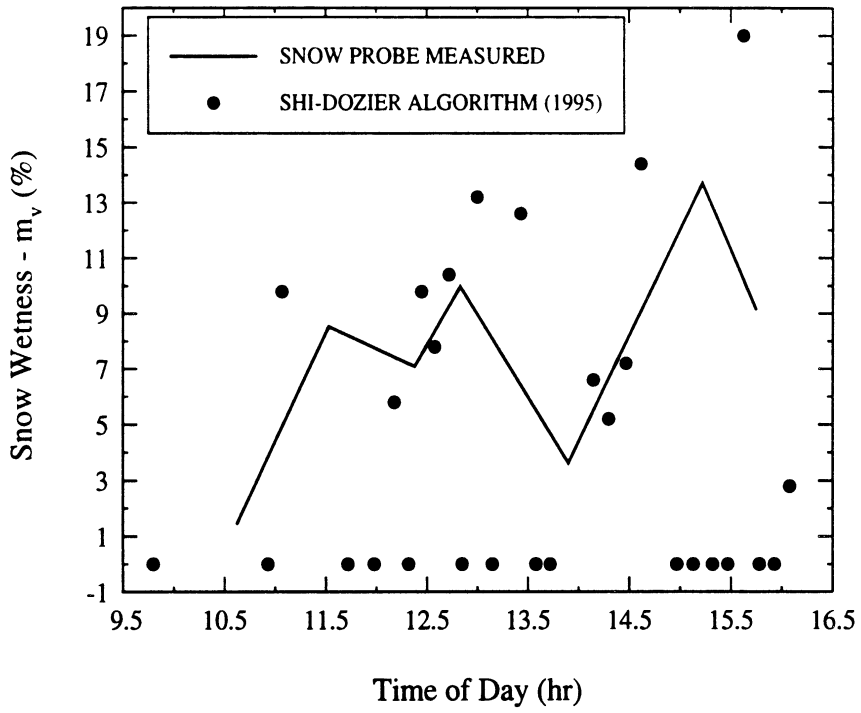

Figure 4.22: Snow wetness inversion algorithm results from Cadillac diurnal data set compared with actual measured values of m_v in the uppermost layer of the snowpack.

measurements—which may be seen to—very roughly—follow the trends, as a function of time, which were observed in the measurements.

As an additional test, we applied the algorithm to the Brighton diurnal data set, for which, as was seen in Figure 4.24, the top layer of the snowpack had relatively low levels of liquid water content. The values of ε_s which we obtained from the application of the inversion algorithm to this data set are shown in Figure 4.23. The "nominal value" of ε_s indicated in

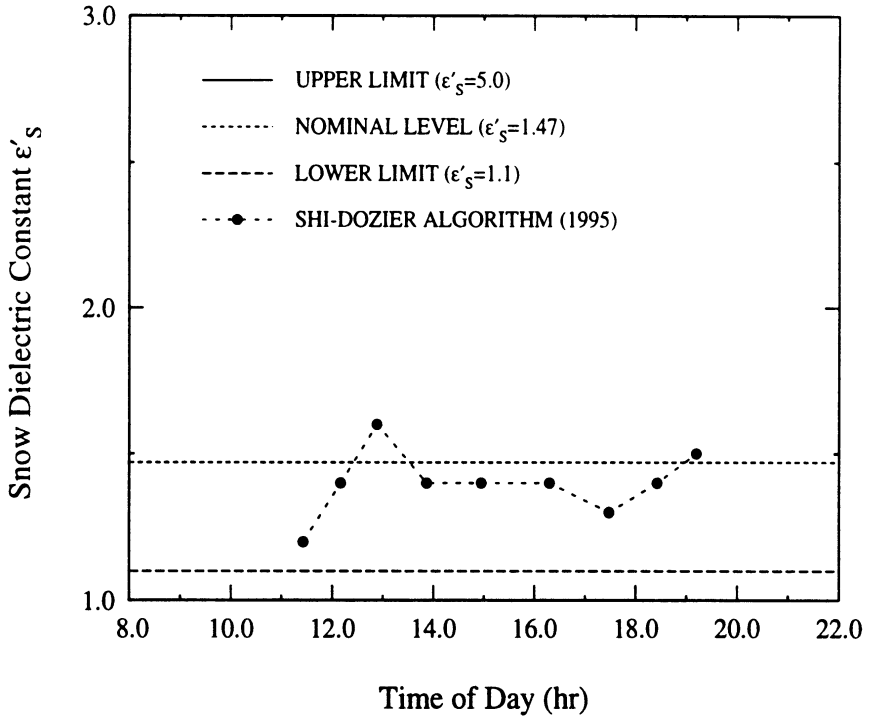

Figure 4.23: Application of inversion algorithm for snow wetness applied to Brighton diurnal data set. Shown is the actual output from the algorithm, snow permittivity ε_s. The "nominal level" shown is based on the expected *dry* snow permittivity based on ground truth measurements of density.

this figure is based on the measured density of about 0.25 g cm^{-3} in the uppermost layer of the snowpack. As can be seen, most of the estimated values are lower than this nominal level, but not by much. In particular, none of the nine separate cases treated resulted in permittivity estimates outside of the range ($1.1 \leq \varepsilon_s \leq 5.0$) which are "reasonable". Also, the relatively very low estimates relative to those shown for the Cadillac case in Figure 4.21

demonstrate the algorithm is genuinely sensitive to this parameter.

The associated estimates of m_v, generated in the same manner as was described for the Cadillac case above, that is, using our knowledge of the actual snow density in the topmost layer of the snowpack, are shown in Figure 4.24. Only two of the nine cases examined give

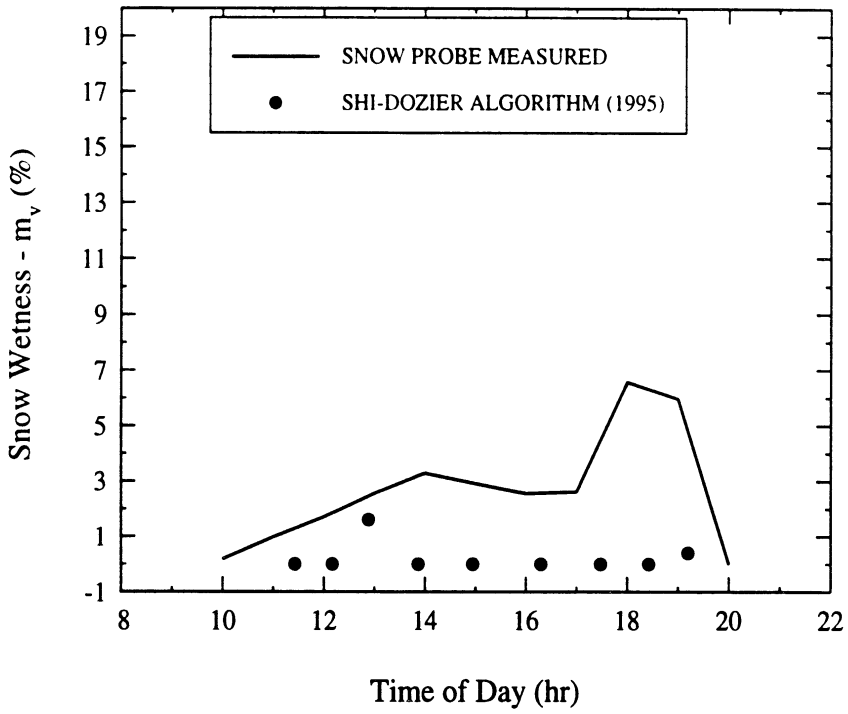

Figure 4.24: Snow wetness inversion algorithm results from *Brighton* diurnal data set compared with actual measured values of m_v in the uppermost layer of the snowpack.

non-zero estimates of the snow liquid water content. The actual measured values however are relatively low, with the possible exception of the values measured at about 6 p.m. (18.00 hours) which are seen to be above 5% liquid water content. This condition itself was a rather anomalous one, occurring as it did just prior due the refreezing of the snowpack top surface.

General Comments on the Wetness Retrieval Algorithm

The central concept behind this algorithm appears to be that the relationships among the quantities σ_{vv}, σ_{hh}, and σ_{vvhh} (the latter of which is related to the correlation between the

co-polarized responses as shown in Eq. (4.23)) for *volume* scattering can be distinguished from the corresponding relationships of these quantities associated with *surface* scattering. That this should be the case is not obvious. With respect to the co-polarized responses, for both *surface* and *volume* scattering it is generally the case that the vv-polarized response exceeds the hh- response increasingly more as incidence angle increases. With respect to the quantity σ_{vvhh}, it has previously been noted by both Shi and Dozier (1992) (the authors of the inversion algorithm) and others (van Zyl et al. 1987) [3] that the correlation coefficient for rough surface scattering is approximately unity. In addition, in the wetness inversion algorithm, the authors implicitly (in Eqs. (4.22) and (4.23)) use a correlation coefficient of unity for the volume scattering as well. Thus it is difficult to see how the polarization relationships between the polarimetric quantities in *volume* and *surface* scattering respectively could allow discrimination between these two scattering mechanisms.

Despite these questions about the fundamental concepts upon which the algorithm is constructed, it must be said that its performance with respect to the two quite different data sets of this present study — the Cadillac and Brighton diurnal experiments — is fairly impressive. Using only polarimetric radar data, the algorithm gave estimates of dielectric constant which were fairly comparable to those directly measured. In addition, when provided with density values for the two respective snowpacks, the algorithm was able to produce estimates of liquid water content reasonably close to those found to be present by direct measurements.

On the Question of the Behavior of σ° with Increasing m_v

The authors of this wetness inversion algorithm make a case for the increase in the backscatter levels for wet snow. While it is true that such a phenomenon is readily predicted theoretically, it has only been observed experimentally in some exceptional cases. The Cadillac

[3] Specifically addresses the coefficient of variation for rough surfaces which, as we have indicated, carries essentially identical information as the correlation coefficient.

scenario might be considered such a case, where a combination of circumstances (ice lens near the surface and exceptionally warm weather) produced, to a small degree, a surface scattering effect. In general however, the depression of the radar backscatter level has been almost universally observed in practice (Mätzler et al. 1982; Mätzler and Schanda 1984; Stiles and Ulaby 1980a; Ulaby et al. 1991; Chang et al. 1994) at both microwave (including the present study) and millimeter wave frequencies. In Mätzler et al. (1982) examples are given of the opposite case, of increasing σ°, but these cases were brought on by the presence of rain in a time frame very close to the measurements in one case, the presence of hail in another case, and in one other case, wet snow which was roughened with a shovel. The rain scenario, in fact, mirrors the circumstances under which the experiment in the Öztal Alps was conducted—an experiment which produced the data in which the inversion algorithm was originally based.

The preponderance of evidence with respect to a decreased backscatter suggests that models of wet snow may not be realistic. Possible explanations for the departure from theoretical predictions may be that (1) liquid water drains from the upper levels of the snowpack before it becomes abundant enough to increase the dielectric constant significantly or, as may well be the case with the Cadillac data (2) drainage from the immediate top of the layer helps to create a sort of matching layer leading to small surface scattering even for high wetness levels *near* the top surface.

Estimation of Liquid Water Content from ε'_{ws}: General Comments

One final issue which should be considered is with what *accuracy* can liquid water content, m_v, be estimated, if the dielectric content ε'_{ws} could be successfully estimated?

The vertical profiles of m_v are seen, from the two examples presented, to be fairly complex functions of time and vertical position. In the case of the Brighton data in particular, it would be virtually impossible to infer the state of the liquid water content of the snowpack from the surface properties alone. Let us consider however a simple case where the

permittivity of the surface is related to the liquid water content present.

It is true that m_v may be estimated from knowledge of ε'_{ws}, *if* the density is also known. It has been found (Kendra et al. 1994; Denoth 1989) that the real part of the dielectric constant of wet snow may be understood as an incremental quantity associated with the liquid water added to a quantity based on the dry snow density[4] alone. The dry snow density in this case is calculated by removing the contribution of the mass of the liquid water in a given volume. That is,

$$\rho_{ds} = \rho_{ws} - m_v/100. \tag{4.36}$$

Expressions for computing the dielectric of dry snow from the dry snow density as well as the incremental increase due to liquid water content are given in Equations (3.13) and (3.16) in chapter III.

From the above, it is seen that even if the density is known along with ε'_{ws}, there are still uncertainties associated with determining m_v, since for the incremental increase to be known (from which m_v will be found) it is first necessary to compute the dielectric constant of the effective dry snow. As shown, this is done using the dry snow density. From (4.36) we see that, strictly speaking, m_v must be known to obtain the dry snow density from the wet snow density. It becomes a circular argument: m_v will be computed from the incremental increase $\Delta\varepsilon'_{ws}$ which is obtained from subtracting the effective dry snow dielectric from the measured (or estimated) wet snow dielectric; to compute the dry snow dielectric the dry snow density must be known which may be obtained from the wet snow density if m_v is known. Thus the entire process may only go forward providing the desired output is known from the very beginning. This situation illustrates the value of determining m_v from the imaginary part of the dielectric constant, ε''_{ws}, a quantity for which, unfortunately, there is no hope of specification by remote means.

[4]Denoth (1989) uses dry snow ice volume fraction, ϕ, which is equal to ρ_{ds}/ρ_i, where ρ_i is the density of ice equal to 0.917 g/cm^3.

Practically speaking, the scenario described above is only a problem if the snow wetness is quite high. For 10% liquid water, for example, a wet snow density of 0.4 g/cm^3 corresponds to an effective dry snow density of 0.3 g/cm^3. If this is not taken into account the resulting error in the estimate of m_v is about 2.4% by volume.

Compared with the uncertainties associated with estimates of m_v given ε'_{ws} and ρ_{ws}, the situation for the case where only ε'_{ws} is known is much worse. The uncertainty in the estimate of m_v which results in such a case is shown graphically in Figure 4.25. In the figure, it is assumed that the dry snow density is confined to the range of 0.2–0.53 g/cm^3, for which the corresponding range of dielectric constant is 1.3 to 2.1. It is also assumed that the maximum wetness level that can be attained by the snowpack is m_v = 10%, for which the incremental permittivity at C-band is computed using Eq. (3.6). As shown, the uncertainty in the estimate of m_v is based on considering which dry snow conditions, with a particular incremental permittivity increase due to liquid water, could give rise to the value of ε'_{ws} which is known. The range of increments determines the error. The smallest error is incurred when the value of ε'_{ws} is so high that it can only correspond to a narrow range of dense snow types having a high liquid water content as in Figure 4.25(a) and (b).

4.5 Summary

This chapter has described the results of two types of polarimetric radar experiments which were carried out on snowpacks.

In Section 4.3 we presented results and analysis for measurements which were made at L-, C-, and X-band on the bare ground and then three successively deeper (20,60, and 102 cm) layers of artificial dry snow. The details of the physical character of the snowpack and the environmental conditions associated with the experiments made these results especially amenable to comparison with discrete -particle -based theoretical modeling techniques. It was shown, however, that these techniques did not give reasonable agreement with the ex-

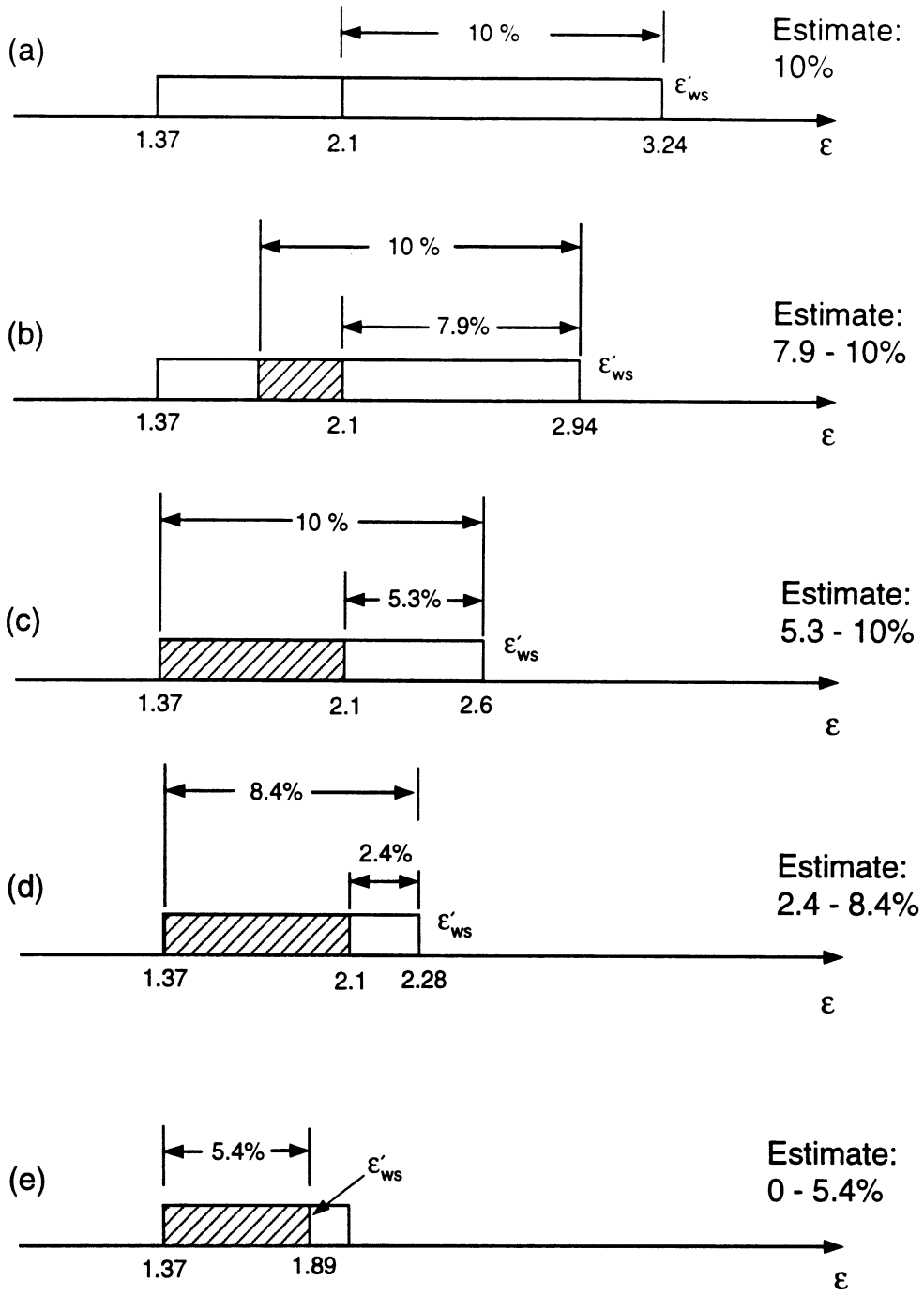

Figure 4.25: Graphical demonstration of the uncertainty associated with inferring m_v from a measurement of ε'_{ws}, the dielctric constant of the wet snow, alone. Range of 1.37–2.1 is dry snow dielectric range for ρ_{ds} from 0.2–0.53 g/cm^3.

perimental observations. A subsequent analysis of the data was presented by which polarimetric scattering and extinction quantities intrinsic to the snow medium were retrieved.

In Section 4.4, results for backscatter collected during partial diurnal cycles were presented, along with the results of extensive measurements of snow liquid water content which were made concurrently. This data was used in an attempt to confirm the validity of an algorithm which has recently been developed by Shi and Dozier (1995) for the retrieval of snow liquid water content from polarimetric C-band measurements. Although an examination of the *conceptual* framework of the algorithm reveals certain basic assumptions which seem difficult to justify, its performance with respect to the two separate diurnal data sets is fairly impressive. The algorithm was able to correctly characterize the Cadillac and Brighton snowpacks (top layer) as very wet and reasonably dry, respectively.

CHAPTER V

A HYBRID EXPERIMENTAL / THEORETICAL SCATTERING MODEL FOR DENSE RANDOM MEDIA

5.1 Motivation

In the previous chapter evidence was presented which strongly suggested that existing particle-based theories are inadequate for modeling very dense random media. This raises the very fundamental question of what recourse exists for simulating the effects of a dense medium, for example, for the case of a layer of snow over sea ice, or a deep layer of dense snow on a forest floor. The ability to generate realistic predictions is an essential prerequisite to any scheme for retrieving physical characteristics about a target from remotely sensed data.

Given the inability to explain the behavior of densely packed discrete particles, it is evident that the issue is only exacerbated when dealing with materials of a very complex physical character, for example the amorphous interconnected form which snowpacks can often—or even usually—take. There are of course theoretical techniques which are appropriate for treating such cases; these are field-based techniques in which the medium is described as a fluctuating dielectric constant. To obtain a solution, the Born approximation or the Distorted Born approximation is usually applied. In practice however, although some studies have investigated this technique (Vallese and Kong 1981) the particular material characteristic which is required as an input, the *correlation function* of the medium, is

exceedingly difficult to obtain. The standard technique for its measurement is the "thin sections" technique. In this technique (Vallese and Kong 1981; Koh and Davis 1994) a supercooled liquid is allowed to fill the pore spaces of a snow sample. After freezing the samples, they are shaved on a microtome and polished, treated with a contrast enhancer, and digitized. Not only is this a very arduous process, but it has been recently shown (Siqueira et al. 1995) that the correlation function must be known with high accuracy, including its tail region, to obtain accurate prediction of scattering; that is, it is not sufficient to know that the function approximates, say, a gaussian or exponential function. In additon to these obstacles, it is also true that the distorted Born approximation does not account for multiple scattering of the incoherent wave (Tsang and Ishimaru 1987).

Apart from the theoretical approaches addressed above, we have previously considered in Chapters I and III the limitations of a purely empirical approach; namely that the entire parameter space of the target cannot be sufficiently well known to allow estimation of more specific target properties.

To circumvent the difficulties associated with the techniques above, and to offer some means by which realistic modeling of dense media might be accomplished, a new hybrid experimental / theoretical modeling scheme is introduced in this chapter.

5.2 Hybrid Model Concept

The hybrid model involves two major assumptions. The first is that radiative transfer is applicable. That is, that the flow of electromagnetic energy through any dense medium obeys the fundamental equation of transfer,

$$\frac{d\mathbf{I}(\hat{\mathbf{s}},\mathbf{r})}{ds} = -\boldsymbol{\kappa}_e(\hat{\mathbf{s}})\mathbf{I}(\hat{\mathbf{s}},\mathbf{r}) + \int_{\theta=0}^{\pi}\int_{\phi=0}^{2\pi} \boldsymbol{\mathcal{P}}(\hat{\mathbf{s}},\hat{\mathbf{s}}')\mathbf{I}(\hat{\mathbf{s}}',\mathbf{r})\,d\Omega' \tag{5.1}$$

where $\mathbf{I}$ is the 4×1 Stokes vector, $\boldsymbol{\kappa}_e$ is the 4×4 extinction matrix, and $\boldsymbol{\mathcal{P}}$ is the 4×4 phase matrix, which were introduced in Chapter II. In Chapter II it was shown that phase

and extinction matrices for the medium may be formulated in terms of the characteristics of a single particle if the medium consists of uniform particles or a weighted average of the individual characteristics of various particles if the medium is heterogeneous. This type of formulation, known as *conventional* radiative transfer (CRT), contains two simplifying assumptions: (1) that all particles are in the far-field of one another and (2) that the particle positions are completely uncorrelated with one another, thereby eliminating any coherence effects.

It has also been shown (Wen et al. 1990) that for Rayleigh particles, a rigorous field-based approach to scattering in a dense medium, where particle correlations are considerd and exact wave transformations from one particle to another are employed, yields a solution which may be couched in exactly the same form as (5.1). It was found from this analysis that the phase function is the Rayleigh phase function, similar to CRT. However, the scale of the phase function, which is provided by the scattering albedo, and the extinction differ from CRT[1]. Thus the assumption that such an equation describes the mechanism is reasonable, although it has not been shown to hold for the case of a rigorous field-based analysis of *non*-Rayleigh particles (Tsang and Kong 1992).

It has already been established in the previous chapter that the available techniques by which κ_e and $\mathcal{P}$ are computed do not appear to be adequate. In addition, for complex or amorphous materials, where a "particle" cannot be unambiguously identified, it is not possible to formulate these quantities. Therefore, in the present hybrid model, no attempt is made to specify them based on the physical characteristics of the medium. Instead, a direct measurement process will be carried out, effectively interrogating the medium, and from these measurements an inversion process will be used to retrieve κ_e and $\mathcal{P}$.

In order to make this approach tractable, a second major assumption is required. This is that, not only does radiative transfer apply, but that the *first-order* evaluation of it is suf-

[1]Simple expressions for computation of the extinction and the scattering albedo for DMRT are provided in Wen et al. (1990).

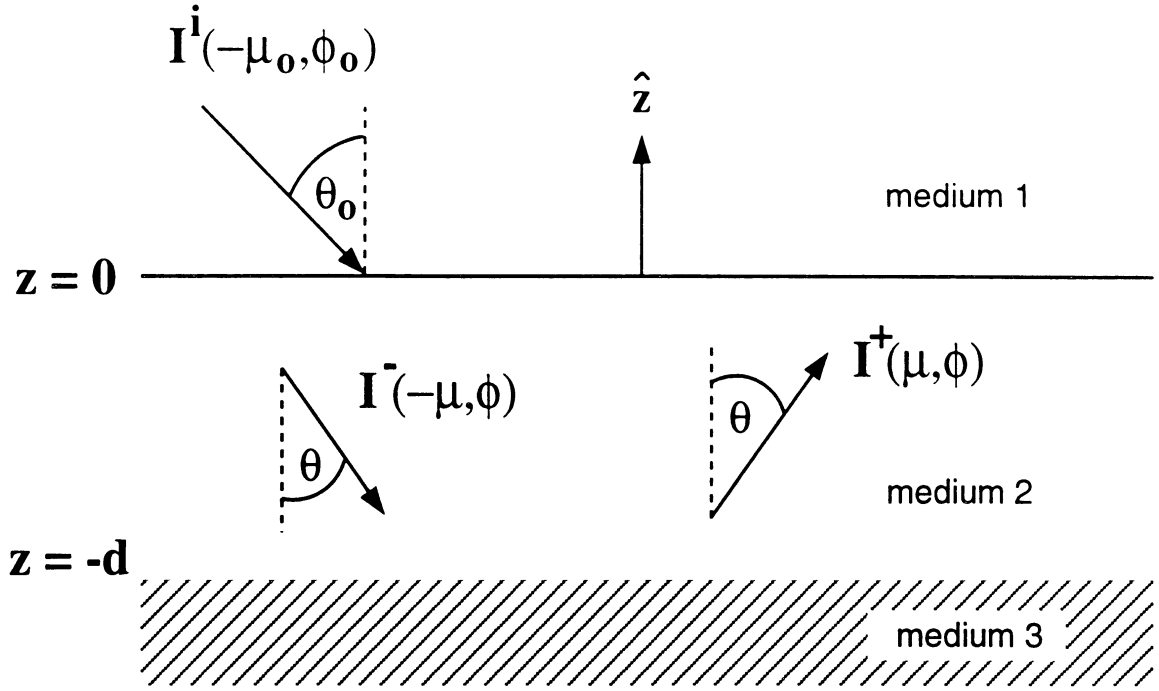

Figure 5.1: Geometry of scattering layer for radiative transfer analysis

ficient. In the following section we derive the first order solution to the radiative transfer equation for the case of a layer with smooth surfaces above and below.

5.3 First-Order Radiative Transfer Formulation

The formulation outlined in this section follows that given in various textbooks (Ulaby and Elachi 1990; Ulaby et al. 1986; Ishimaru 1978; Tsang et al. 1985) to which the reader is referred for additional details.

The layer geometry is illustrated in Figure 5.1. Azimuthal symmetry is assumed, but it is considered that the constituent particles of the layer can be in general non-spherical and have orientation distributions which are not completely uniform in elevation. In this case, the extinction matrix, κ_e, is only a function of the elevation angle θ, in the layer, or equivalently, $\mu = \cos\theta$. For the case of invariance in the *xy* or horizontal plane, the problem of solving equation (5.1) may be divided into upwelling intensity, $\mathbf{I}^{+}(\mu,\phi,z)$, and downwelling

intensity, $\mathbf{I}^-(-\mu,\phi,z)$, which may be solved through the application of boundary conditions at the top ($z=0$) and bottom ($z=-d$) of the layer respectively. For this case we have,

$$\frac{d\mathbf{I}^+(\mu,\phi,z)}{dz} = -\frac{1}{\mu}\boldsymbol{\kappa}_e(\mu)\mathbf{I}^+(\mu,\phi,z) + \frac{1}{\mu}\mathbf{F}^+(\mu,\phi,z) \tag{5.2}$$

$$\frac{d\mathbf{I}^-(-\mu,\phi,z)}{dz} = \frac{1}{\mu}\boldsymbol{\kappa}_e(-\mu)\mathbf{I}^+(\mu,\phi,z) - \frac{1}{\mu}\mathbf{F}^-(\mu,\phi,z) \tag{5.3}$$

wherein the incremental pathlength ds in (5.1) has been replaced by $dz/\cos\theta$ or dz/μ. These equations are coupled through the scattering source functions $\mathbf{F}^+$ and $\mathbf{F}^-$, which are functions of both $\mathbf{I}^+$ and $\mathbf{I}^-$ as follows:

$$\mathbf{F}^+(\mu,\phi,z) = \int_{\phi=0}^{2\pi}\int_{\mu=0}^{\pi/2}\Big[\boldsymbol{\mathcal{P}}(\mu,\phi;\mu',\phi')\mathbf{I}^+(\mu',\phi') + \boldsymbol{\mathcal{P}}(\mu,\phi;-\mu',\phi')\mathbf{I}^-(-\mu',\phi')\Big]d\mu'\,d\phi' \tag{5.4}$$

$$\mathbf{F}^-(-\mu,\phi,z) = \int_{\phi=0}^{2\pi}\int_{\mu=0}^{\pi/2}\Big[\boldsymbol{\mathcal{P}}(-\mu,\phi;\mu',\phi')\mathbf{I}^+(\mu',\phi') + \boldsymbol{\mathcal{P}}(-\mu,\phi;-\mu',\phi')\mathbf{I}^-(-\mu',\phi')\Big]d\mu'\,d\phi' \tag{5.5}$$

The differential forms given in (5.2) and (5.3) may be cast into their integral counterparts by noting that a perfect integral may be constructed from the left hand side and first term on the right hand side of each equation. For the upwelling case the integration is carried out (with respect to z') after multiplying both sides of equation (5.2) by $e^{\boldsymbol{\kappa}_e z'(\mu)/\mu}$, giving,

$$\int_{-d}^{z}\left[\frac{d\mathbf{I}^+(\mu,\phi,z')}{dz'} + \frac{1}{\mu}\boldsymbol{\kappa}_e(\mu)\mathbf{I}^+(\mu,\phi,z')\right]e^{\boldsymbol{\kappa}_e(\mu)z'/\mu}dz' = \mathbf{I}^+(\mu,\phi,z')e^{\boldsymbol{\kappa}_e(\mu)z'/\mu}\Big|_{-d}^{z} \tag{5.6}$$

$$= \mathbf{I}^+(\mu,\phi,z)e^{\boldsymbol{\kappa}_e(\mu)z/\mu} - \mathbf{I}^+(\mu,\phi,-d)e^{-\boldsymbol{\kappa}_e(\mu)d/\mu}.$$

Together with a similar treatment for the downwelling case, the integral forms are given as,

$$\mathbf{I}^+(\mu,\phi,z) = e^{-\kappa_e(\mu)(d+z)/\mu}\mathbf{I}^+(\mu,\phi,-d) + \frac{1}{\mu}\int_{-d}^{z} e^{\kappa_e(\mu)(z'-z)/\mu}\mathbf{F}^+(\mu,\phi,z')dz' \tag{5.7}$$

$$\mathbf{I}^-(-\mu,\phi,z) = e^{\kappa_e(-\mu)z/\mu}\mathbf{I}^-(-\mu,\phi,-d) + \frac{1}{\mu}\int_{z}^{0} e^{-\kappa_e(-\mu)(z'-z)/\mu}\mathbf{F}^-(-\mu,\phi,z')dz' \tag{5.8}$$

The boundary conditions at the top and bottom of the layer are

$$\mathbf{I}^-(-\mu,\phi,0^-) = \mathbf{I}^i(-\mu_o',\phi_o,0^+)\boldsymbol{\mathcal{T}}_{12}(-\mu_o)\delta(\mu-\mu_o')\delta(\phi-\phi_o) + \boldsymbol{\mathcal{R}}_{21}(\mu)\mathbf{I}^+(\mu,\phi,0_-) \tag{5.9}$$

$$\mathbf{I}^+(\mu,\phi,-d) = \boldsymbol{\mathcal{R}}_{23}(-\mu)\mathbf{I}^-(-\mu,\phi,-d) \tag{5.10}$$

where μ_o refers to the cosine of the incidence angle in medium 1 (air) and μ_o' to the corresponding refracted quantity, and where $\boldsymbol{\mathcal{T}}_{pq}$ and $\boldsymbol{\mathcal{R}}_{pq}$ are the transmissivity and reflectivity matrices for intensity propagating in medium p towards medium q. For intensity vectors constructed from Stokes parameters, these matrices are

$$\boldsymbol{\mathcal{T}}_{12} = \frac{n_2^3\cos\theta_2}{n_1^3\cos\theta_1}\begin{bmatrix} |t_{v12}|^2 & 0 & 0 & 0 \\ 0 & |t_{h12}|^2 & 0 & 0 \\ 0 & 0 & \mathrm{Re}(t_{v12}t_{h12}^*) & -\mathrm{Im}(t_{v12}t_{h12}^*) \\ 0 & 0 & \mathrm{Im}(t_{v12}t_{h12}^*) & \mathrm{Re}(t_{v12}t_{h12}^*) \end{bmatrix} \tag{5.11}$$

$$\boldsymbol{\mathcal{R}}_{23} = \begin{bmatrix} |r_{v23}|^2 & 0 & 0 & 0 \\ 0 & |r_{h23}|^2 & 0 & 0 \\ 0 & 0 & \mathrm{Re}(r_{v23}r_{h23}^*) & -\mathrm{Im}(r_{v23}r_{h23}^*) \\ 0 & 0 & \mathrm{Im}(r_{v23}r_{h23}^*) & \mathrm{Re}(r_{v23}r_{h23}^*) \end{bmatrix} \tag{5.12}$$

where r_{v23} and r_{h23} are the vertical and horizontal polarization Fresnel reflection coefficients

and t_{v12} and t_{h12} the Fresnel transmission coefficients:

$$r_{v23} = \frac{n_2 \cos\theta_3 - n_3 \cos\theta_2}{n_2 \cos\theta_3 + n_3 \cos\theta_2} \tag{5.13}$$

$$r_{h23} = \frac{n_2 \cos\theta_2 - n_3 \cos\theta_3}{n_2 \cos\theta_3 + n_3 \cos\theta_2} \tag{5.14}$$

$$t_{v12} = \frac{2n_1 \cos\theta_1}{n_2 \cos\theta_1 + n_1 \cos\theta_2} \tag{5.15}$$

$$t_{h12} = \frac{2n_1 \cos\theta_1}{n_1 \cos\theta_1 + n_2 \cos\theta_2} \tag{5.16}$$

Although the top boundary of the layer is not diffuse in the general case, the scattering mechanisms which include a reflection off this interface represent a product of at least two small scattering events in the formulation. This effect will be re-visited at the completion of this derivation. The inclusion of this feature in the first boundary condition (equ. (5.9)) in the form of the $\mathcal{R}_{21}$ term, greatly complicates the analysis and obfuscates the final result so that separation and examination of the major scattering mechanisms is very difficult. Therefore, in this derivation, we will not consider the second term in boundary condition #1 and, deferring justification until the end, will instead just use the following truncated version of it:

$$\mathbf{I}^-(-\mu,\phi,0^-) = \mathbf{I}^i(-\mu_o',\phi_o,0^+)\mathcal{T}_{12}(-\mu_o)\delta(\mu-\mu_o')\delta(\phi-\phi_o) \tag{5.17}$$

An iterative solution to the coupled equations given in (5.7) and (5.8) is constructed by considering that the contribution of the scattering source function to the intensity propagating in a direction $\hat{\mathbf{s}}$ is much smaller than the coherent wave at any point in the medium. Setting the scattering source functions $\mathbf{F}^+$ and $\mathbf{F}^-$ to zero and applying boundary conditions

(5.17) and (5.10) gives the *zeroth-order* solution for the up- and downwelling intensities:

$$\mathbf{I}^{+}(\mu,\phi,z) = e^{-\kappa_e(\mu)(d+z)/\mu}\boldsymbol{\mathcal{R}}_{23}(-\mu)e^{\kappa_e(-\mu)d/\mu}\boldsymbol{\mathcal{T}}_{12}(-\mu_o)\mathbf{I}^{i}(-\mu_o',\phi_o,0^{+})\delta(\mu-\mu_o')\delta(\phi-\phi_o) \tag{5.18}$$

$$\mathbf{I}^{-}(-\mu,\phi,z) = e^{\kappa_e(-\mu)z/\mu}\boldsymbol{\mathcal{T}}_{12}(-\mu_o)\mathbf{I}^{i}(-\mu_o',\phi_o,0^{+})\delta(\mu-\mu_o')\delta(\phi-\phi_o) \tag{5.19}$$

The *first-order* solution is obtained by using these zeroth-order intensities in the integral of the scattering source functions (5.4) and (5.5). These integrals can be immediately reduced, due to the presence of the Kronecker delta functions in (5.18) and (5.19), to the following forms:

$$\begin{aligned}\mathbf{F}^{+}(\mu,\phi,z) = \Big[&\boldsymbol{\mathcal{P}}(\mu,\phi;\mu_o',\phi_o)e^{-\kappa_e(\mu_o')(d+z)/\mu_o'}\boldsymbol{\mathcal{R}}_{23}(-\mu_o')e^{\kappa_e(-\mu_o')d/\mu_o'} \\ &+\boldsymbol{\mathcal{P}}(\mu,\phi;-\mu_o',\phi_o)e^{\kappa_e(-\mu_o')z/\mu_o'}\Big]\boldsymbol{\mathcal{T}}_{12}(-\mu_o)\mathbf{I}^{i}(-\mu_o',\phi_o,0^{+})\end{aligned} \tag{5.20}$$

$$\begin{aligned}\mathbf{F}^{-}(-\mu,\phi,z) = \Big[&\boldsymbol{\mathcal{P}}(-\mu,\phi;\mu_o',\phi_o)e^{-\kappa_e(\mu_o')(d+z)/\mu_o'}\boldsymbol{\mathcal{R}}_{23}(-\mu_o')e^{\kappa_e(-\mu_o')d/\mu_o'} \\ &+\boldsymbol{\mathcal{P}}(-\mu,\phi;-\mu_o',\phi_o)e^{\kappa_e(-\mu_o')z/\mu_o'}\Big]\boldsymbol{\mathcal{T}}_{12}(-\mu_o)\mathbf{I}^{i}(-\mu_o',\phi_o,0^{+})\end{aligned} \tag{5.21}$$

These source functions are then substituted into the original integral expressions for the up- and downwelling intensities, given in (5.7) and (5.8). As done in the zeroth-order case, the boundary conditions are applied to generate the first-order solutions for $\mathbf{I}^{+}$ and $\mathbf{I}^{-}$. It is only necessary to specify the upwelling intensity here, since it alone, evaluated at the top boundary, will be used in determining the intensity scattered from the layer in the direction

of the receiver. The general first-order upwelling intensity is given by,

$$\begin{aligned}\mathbf{I}^{+}(\mu,\phi,z) = {} & e^{-\kappa_e(\mu)(z+d)/\mu}\boldsymbol{\mathcal{R}}_{23}(-\mu)e^{-\kappa_e(\mu)d/\mu}\boldsymbol{\mathcal{T}}_{12}(-\mu_o)\mathbf{I}^{i}(-\mu_o',\phi_o,0^{+})\delta(\mu-\mu_o')\delta(\phi-\phi_o) \\ & + \frac{1}{\mu}\Bigg\{ e^{-\kappa_e(\mu)(z+d)/\mu}\Bigg[\boldsymbol{\mathcal{R}}_{23}(-\mu)\boldsymbol{\mathcal{A}}_1(\mu,\phi;\mu_o',\phi_o)\boldsymbol{\mathcal{R}}_{23}(-\mu_o')e^{\kappa_e(-\mu_o')d/\mu_o'} \\ & + \boldsymbol{\mathcal{R}}_{23}(-\mu)\boldsymbol{\mathcal{A}}_2(\mu,\phi;\mu_o',\phi_o)\Bigg] \\ & + \boldsymbol{\mathcal{A}}_3(z,\mu,\phi;\mu_o',\phi_o)\boldsymbol{\mathcal{R}}_{23}(-\mu_o')e^{\kappa_e(-\mu_o')d/\mu} \\ & + \boldsymbol{\mathcal{A}}_4(z,\mu,\phi;\mu_o',\phi_o)\Bigg\}\boldsymbol{\mathcal{T}}_{12}(-\mu_o)\mathbf{I}^{i}(-\mu_o',\phi_o,0^{+}) \end{aligned} \tag{5.22}$$

where the matrix quantities $\boldsymbol{\mathcal{A}}_1$–$\boldsymbol{\mathcal{A}}_4$ are given by,

$$\boldsymbol{\mathcal{A}}_1(\mu,\phi;\mu_o',\phi_o) = \int_{-d}^{0} e^{-\kappa_e(-\mu)(z'+d)/\mu}\boldsymbol{\mathcal{P}}(-\mu,\phi;\mu_o',\phi_o)e^{-\kappa_e(\mu_o')(z'+d)/\mu_o'}\,dz' \tag{5.23}$$

$$\boldsymbol{\mathcal{A}}_2(\mu,\phi;\mu_o',\phi_o) = \int_{-d}^{0} e^{-\kappa_e(-\mu)(z'+d)/\mu}\boldsymbol{\mathcal{P}}(-\mu,\phi;-\mu_o',\phi_o)e^{\kappa_e(-\mu_o')z'/\mu_o'}\,dz' \tag{5.24}$$

$$\boldsymbol{\mathcal{A}}_3(z,\mu,\phi;\mu_o',\phi_o) = \int_{-d}^{z} e^{\kappa_e(\mu)(z'-z)/\mu}\boldsymbol{\mathcal{P}}(\mu,\phi;\mu_o',\phi_o)e^{-\kappa_e(\mu_o')(d+z')/\mu_o'}\,dz' \tag{5.25}$$

$$\boldsymbol{\mathcal{A}}_4(z,\mu,\phi;\mu_o',\phi_o) = \int_{-d}^{z} e^{\kappa_e(\mu)(z'-z)/\mu}\boldsymbol{\mathcal{P}}(\mu,\phi;-\mu_o',\phi_o)e^{\kappa_e(-\mu_o')z'/\mu_o'}\,dz' \tag{5.26}$$

For backscatter, $\mu = \mu_o$ and $\phi = \phi_o + \pi$, and the intensity at the receiver is given by,

$$\begin{aligned}
\mathbf{I}^+(\mu_o, \phi_o + \pi, 0^+) &= \boldsymbol{\mathcal{T}}_{21}(\mu_o')\mathbf{I}^+(\mu_o', \phi_o + \pi, 0^-) \\
&= \frac{1}{\mu_o'}\boldsymbol{\mathcal{T}}_{21}(\mu_o')\Big\{ e^{\boldsymbol{\kappa}_e(\mu_o')d/\mu_o'}\Big[\boldsymbol{\mathcal{R}}_{23}(-\mu_o')\boldsymbol{\mathcal{A}}_1(\mu_o', \phi_o + \pi; \mu_o', \phi_o) \\
&\qquad \cdot \boldsymbol{\mathcal{R}}_{23}(-\mu_o')e^{\boldsymbol{\kappa}_e d/\mu_o'} \\
&\quad + \boldsymbol{\mathcal{R}}_{23}(-\mu_o')\boldsymbol{\mathcal{A}}_2(\mu_o', \phi_o + \pi; \mu_o', \phi_o)\Big] \\
&\quad + \boldsymbol{\mathcal{A}}_3(0, \mu_o', \phi_o + \pi; \mu_o', \phi_o)\boldsymbol{\mathcal{R}}_{23}(-\mu_o')e^{\boldsymbol{\kappa}_e(-\mu_o')d/\mu_o'} \\
&\qquad + \boldsymbol{\mathcal{A}}_4(0, \mu_o', \phi_o + \pi; \mu_o', \phi_o)\Big\}\boldsymbol{\mathcal{T}}_{21}(\mu_o)\mathbf{I}^i(-\mu_o', \phi_o, 0^+)
\end{aligned} \tag{5.27}$$

The evaluation of the quantities $\boldsymbol{\mathcal{A}}_1$–$\boldsymbol{\mathcal{A}}_4$ involves the exponential of $\boldsymbol{\kappa}_e$, which as shown in Eq. (2.33), is a non-diagonal matrix in the general case. The evaluation of this exponential is done in the standard way by diagonalizing $\boldsymbol{\kappa}_e$ and applying the exponential function to the eigenvalues of that matrix:

$$e^{\xi\boldsymbol{\kappa}_e} = \boldsymbol{Q}(\mu)\Lambda(\xi;\mu,\phi)\boldsymbol{Q}(\mu)^{-1} \tag{5.28}$$

where $\boldsymbol{Q}$ is a 4×4 matrix whose columns are the eigenvectors of $\boldsymbol{\kappa}_e$ and $\Lambda(\xi)$ is a diagonal matrix whose elements are

$$[\Lambda(\xi;\mu)]_{mm} = e^{\lambda_m \xi}$$

where λ_m is the *mth* eigenvalue of $\boldsymbol{\kappa}_e$. For $\boldsymbol{\kappa}_e$ as given in Eq. (2.33), the eigenmatrix $\boldsymbol{Q}$ has

been found to be (Tsang et al. 1985)[p. 243]:

$$Q(\mu) = \begin{bmatrix} 1 & b_2^* & b_2 & |b_2|^2 \\ |b_1|^2 & b_1 & b_1^* & 1 \\ 2\mathrm{Re}(b_1) & 1+b_1 b_2^* & 1+b_1^* b_2 & 2\mathrm{Re}(b_2) \\ -2\mathrm{Im}(b_1) & -i(1-b_1 b_2^*) & i(1+b_1^* b_2) & 2\mathrm{Im}(b_2) \end{bmatrix} \tag{5.29}$$

where,

$$b_1 = \frac{2M_{hv}}{M_{vv} - M_{hh} + r}, \tag{5.30}$$

$$b_2 = \frac{2M_{vh}}{-M_{vv} + M_{hh} - r}, \tag{5.31}$$

$$r = \sqrt{(M_{vv} - M_{hh})^2 + 4M_{hv}M_{vh}}, \tag{5.32}$$

and where the quantities of the form M_{pq} are those comprising the elements of $\mathbf{K}_e$, as given in Eq. (2.34). The corresponding eigenvalues are,

$$\begin{bmatrix} \lambda_1(\mu) \\ \lambda_2(\mu) \\ \lambda_3(\mu) \\ \lambda_4(\mu) \end{bmatrix} = -[\mathrm{Re}(M_{vv}) + \mathrm{Re}(M_{hh})] + \frac{1}{2}\begin{bmatrix} -r - r^* \\ -r + r^* \\ r - r^* \\ r + r^* \end{bmatrix}$$

$$= \begin{bmatrix} 2\mathrm{Im}(K_1) \\ iK_2^* - iK_1 \\ iK_1^* - iK_2 \\ 2\mathrm{Im}(K_2) \end{bmatrix} \tag{5.33}$$

where,

$$K_1 = k - \frac{i}{2}[M_{vv} + M_{hh} + r] \tag{5.34}$$

$$K_2 = k - \frac{i}{2}[M_{vv} + M_{hh} - r]. \tag{5.35}$$

Applying (5.28) to (5.23)–(5.26) gives, in the backscatter case,

$$\begin{aligned}\mathcal{A}_1(\mu_o', \phi_o + \pi, \mu_o', \phi_o) = \\ \int_{-d}^{0} \mathbf{Q}(-\mu_o')\Lambda(-\mu_o'; -(d+z')/\mu_o')\mathbf{Q}^{-1}(-\mu_o') \\ \cdot \mathcal{P}(-\mu_o', \phi_o + \pi, \mu_o', \phi_o)\mathbf{Q}(\mu_o')\Lambda(\mu_o'; -(d+z')/\mu_o')\mathbf{Q}^{-1}(\mu_o')\, dz'\end{aligned} \tag{5.36}$$

$$\begin{aligned}\mathcal{A}_2(\mu_o', \phi_o + \pi, \mu_o', \phi_o) = \\ \int_{-d}^{0} \mathbf{Q}(-\mu_o')\Lambda(-\mu_o'; -(d+z')/\mu_o')\mathbf{Q}^{-1}(-\mu_o') \\ \cdot \mathcal{P}(\mu_o', \phi_o + \pi, -\mu_o', \phi_o)\mathbf{Q}(-\mu_o')\Lambda(-\mu_o'; z'/\mu_o')\mathbf{Q}^{-1}(-\mu_o')\, dz'\end{aligned} \tag{5.37}$$

$$\begin{aligned}\mathcal{A}_3(0, \mu_o', \phi_o + \pi, \mu_o', \phi_o) = \\ \int_{-d}^{0} \mathbf{Q}(\mu_o')\Lambda(\mu_o'; z'/\mu_o')\mathbf{Q}^{-1}(\mu_o') \\ \cdot \mathcal{P}(\mu_o', \phi_o + \pi, \mu_o', \phi_o)\mathbf{Q}(\mu_o')\Lambda(\mu_o'; -(z'+d)/\mu_o')\mathbf{Q}^{-1}(\mu_o')\, dz'\end{aligned} \tag{5.38}$$

$$\begin{aligned}\mathcal{A}_4(0, \mu_o', \phi_o + \pi, \mu_o', \phi_o) = \\ \int_{-d}^{0} \mathbf{Q}(\mu_o')\Lambda(\mu_o'; z'/\mu_o')\mathbf{Q}^{-1}(\mu_o') \\ \cdot \mathcal{P}(\mu_o', \phi_o + \pi, -\mu_o', \phi_o)\mathbf{Q}(-\mu_o')\Lambda(-\mu_o'; -z'/\mu_o')\mathbf{Q}^{-1}(-\mu_o')\, dz'\end{aligned} \tag{5.39}$$

Equations (5.36)–(5.39) may be evaluated to give,

$$\mathcal{A}_1(\mu'_o.\phi_o+\pi.\mu'_o.\phi_o)=\mathcal{Q}(-\mu'_o)\mathcal{U}_1(\mu'_o.\phi_o+\pi;\mu'_o.\phi_o)\mathcal{Q}^{-1}(\mu'_o)$$

$$[\mathcal{U}_1(\mu'_o.\phi_o+\pi;\mu'_o.\phi_o)]_{ij}=\frac{1-\exp[-(\lambda_i(-\mu'_o)+\lambda_j(\mu'_o))d/\mu'_o 1]}{(\lambda_i(-\mu'_o)+\lambda_j(\mu'_o))/\mu'_o}$$

$$\cdot[\mathcal{Q}^{-1}(-\mu'_o)\mathcal{P}(-\mu'_o.\phi_o+\pi.\mu'_o.\phi_o)\mathcal{Q}(\mu'_o)]_{ij} \quad (5.40)$$

$$\mathcal{A}_2(\mu'_o,\phi_o+\pi,\mu'_o,\phi_o)=\mathcal{Q}(-\mu'_o)\mathcal{U}_2(\mu'_o,\phi_o+\pi;\mu'_o,\phi_o)\mathcal{Q}^{-1}(-\mu'_o)$$

$$[\mathcal{U}_2(\mu'_o,\phi_o+\pi;\mu'_o,\phi_o)]_{ij}=$$

$$\begin{cases} de^{-\lambda_i(\mu'_o)d/\mu'_o}\cdot[\mathcal{Q}(-\mu'_o)\mathcal{P}(-\mu'_o,\phi_o+\pi,-\mu'_o,\phi_o)\mathcal{Q}(-\mu'_o)]_{ij} & i=j, \\ \dfrac{\exp[-(\lambda_i(-\mu'_o)d/\mu'_o]-\exp[-\lambda_j(\mu'_o))d/\mu'_o]}{(-\lambda_i(-\mu'_o)+\lambda_j(-\mu'_o))/\mu'_o} & \\ \cdot[\mathcal{Q}^{-1}(-\mu'_o)\mathcal{P}(-\mu'_o,\phi_o+\pi,-\mu'_o,\phi_o)\mathcal{Q}(-\mu'_o)]_{ij} & i\neq j. \end{cases} \quad (5.41)$$

$$\mathcal{A}_3(0,\mu'_o,\phi_o+\pi,\mu'_o,\phi_o)=\mathcal{Q}(\mu'_o)\mathcal{U}_3(\mu'_o,\phi_o+\pi;\mu'_o,\phi_o)\mathcal{Q}^{-1}(\mu'_o)$$

$$[\mathcal{U}_3(\mu'_o,\phi_o+\pi;\mu'_o,\phi_o)]_{ij}=$$

$$\begin{cases} de^{-\lambda_i(\mu'_o)d/\mu'_o}\cdot[\mathcal{Q}(\mu'_o)\mathcal{P}(\mu'_o,\phi_o+\pi,\mu'_o,\phi_o)\mathcal{Q}(\mu'_o)]_{ij} & i=j, \\ \dfrac{\exp[-(\lambda_i(\mu'_o)d/\mu'_o]-\exp[-\lambda_j(\mu'_o))d/\mu'_o]}{(\lambda_i(\mu'_o)-\lambda_j(\mu'_o))/\mu'_o} & \\ \cdot[\mathcal{Q}^{-1}(\mu'_o)\mathcal{P}(\mu'_o,\phi_o+\pi,\mu'_o,\phi_o)\mathcal{Q}(\mu'_o)]_{ij} & i\neq j. \end{cases} \quad (5.42)$$

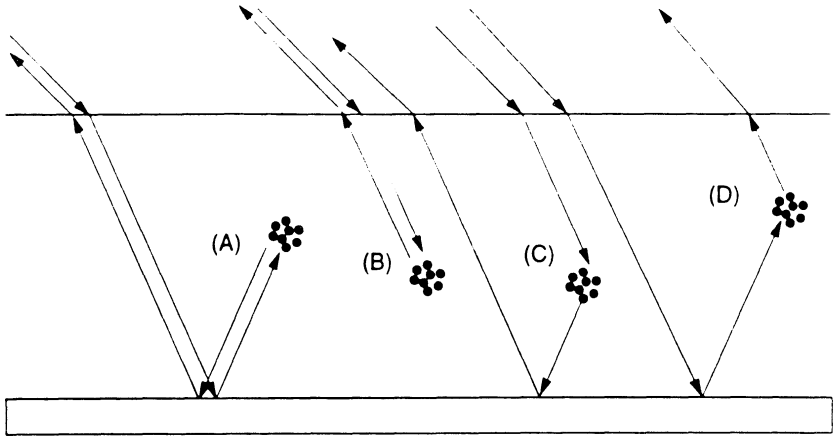

Figure 5.2: First-order volume scattering mechanisms in a layer of scatterers.

$$\mathcal{A}_4(0,\mu_o',\phi_o+\pi,\mu_o',\phi_o) = \mathcal{Q}(\mu_o')\mathcal{U}_4(\mu_o',\phi_o+\pi;\mu_o',\phi_o)\mathcal{Q}^{-1}(-\mu_o')$$

$$[\mathcal{U}_4(\mu_o',\phi_o+\pi;\mu_o',\phi_o)]_{ij} = \frac{1-\exp[-(\lambda_i(\mu_o')+\lambda_j(-\mu_o'))d/\mu_o' 1]}{(\lambda_i(\mu_o')+\lambda_j(-\mu_o'))/\mu_o'}$$

$$\cdot[\mathcal{Q}^{-1}(\mu_o')\mathcal{P}(\mu_o',\phi_o+\pi,-\mu_o',\phi_o)\mathcal{Q}(-\mu_o')]_{ij} \quad (5.43)$$

Substituting (5.40)—(5.43) into (5.27) gives the general first-order solution for backscattered intensity from a layer.

It can be seen from an examination of this formulation that the first-order solution consists of four separate scattering mechanisms, which are shown in Figure 5.2. As mentioned at the beginning of this derivation, the interfaces have been considered to be smooth so that there are no contributions to the backscattered intensity from rough surface effects. The original boundary condition for the top of the layer, equation (5.9), accounted for upwelling intensity internally reflected off the top interface. Retaining that feature would have generated additional expressions for the infinite series associated with repeated reflections of these four terms between the top and bottom interfaces of the layer as shown in Figure 5.3. Since the primary scattering events from the effective particle of the medium are considered small, even one internal reflection from a surface having a generally high transmissivity is a product of two small numbers. Combined with the additional attenuation these

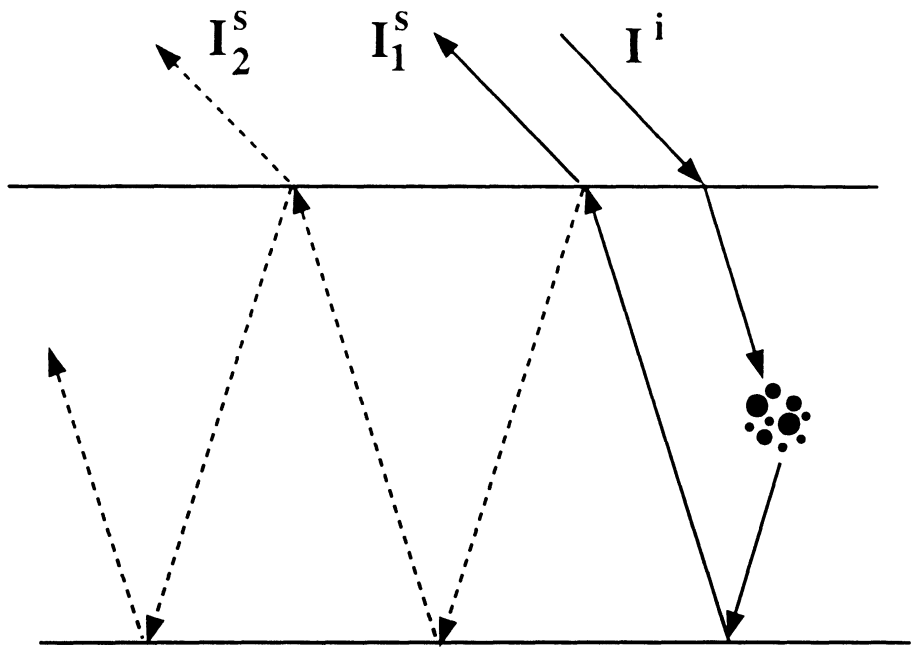

Figure 5.3: Additional contributions to scattering due to internal reflections from the top interface.

terms undergo due to an additional round trip propagation through the layer, it is reasonable to assume that the solution is negligibly affected by their omission.

5.4 Inversion Considerations

As indicated above, κ_e is in general a function of the direction of propagation in the medium, only restricted by an assumption of azimuthal symmetry. Thus for every incidence angle μ_o considered, there are two unknown extinction matrices, $\kappa_e(\mu_o')$ and $\kappa_e(-\mu_o')$, which, as seen from (5.29) and (5.33) above, are characterized by four independant scalar quantities, M_{vv}, M_{hh}, M_{hv}, and M_{vh}. In addition, for this general case there are four distinct components of the phase matrix $\mathcal{P}$ corresponding to the four scattering mechanisms depicted in Figure 5.2. The scattering elements in this figure are depicted as clusters to underscore the point that we are considering "effective" particles in this treatment, which may comprise correlated groups of individual physical particles and/or multiple scattering effects.

Success of an inversion process, based upon a relatively few number of backscatter measurements, depends largely upon keeping the mathematical model as simple as possible. The large number of unknown parameters in the general case described above reduces the potential for a successful inversion, especially to a unique solution. This runs counter to the goal of the Hybrid Model concept which aims to find a simple but mathematically flexible macroscopic description of the polarimetric scattering behavior of a medium.

Accordingly, we consider two simplified versions of the general case:

Isotropic Layer: In this case, the layer is considered a collection of non-spherical particles with a completely uniform orientation distribution. The assumption of non-spherical particles is necessary to allow modeling of the cross-polarized backscatter, since first-order radiative transfer gives zero cross-polarization for spherical particles. For completely uniform orientation, $\boldsymbol{\kappa}_e$ and $\boldsymbol{\mathcal{P}}$ are independant of the direction of propagation; $\boldsymbol{\mathcal{P}}$ therefore depends only on the *difference* between the incident and scattered directions. The total unknown matrices consist of a single extinction matrix, $\boldsymbol{\kappa}_e$, (in which $M_{vv} = M_{hh}$); and two components of the phase matrix: a backscatter component, corresponding to mechanisms (A) and (B) in Figure 5.2, which is *not* a function of the angle of propagation, and a bistatic component, corresponding to (C) and (D) in the figure, which *is* a function of the particular incidence angle, since the scattering angle changes. Furthermore, for $\boldsymbol{\mathcal{P}}_{bs}$, because of the totally uniform orientation, $|S_{vv}S_{vv}^*| = |S_{hh}S_{hh}^*|$. This isotropic layer case is examined further in a theoretical way for the case of Rayleigh particles in the following section.

Non-Isotropic Layer: In this more general case, the layer consists of non-spherical particles having some prescribed, non-uniform orientation distribution. It resembles the general case in that the quantities $\boldsymbol{\kappa}_e$, $\boldsymbol{\mathcal{P}}_{bs}$, and $\boldsymbol{\mathcal{P}}_{bi}$ are functions of the direction of propagation; however, an additonal assumption is made that the orientation of the particles, while having some prescribed distribution in the Eulerian angle β, is completely uniform in α and γ, as shown in Figure 5.4(a). The justification for such a

model is the partial ordering which might possibly be produced for particles arranged in the presence of a vertical force, for example,gravity. There is no such force in the horizontal directions. For such a scenario, the expectation would be as stated above: azimuthal symmetry but some prescribed orientation with respect to the vertical. A result of this situation, which is also indicated in part (b) of the figure, is that the matrix quantities in question are unchanged for reflections about the $\hat{\mathbf{x}}$ and $\hat{\mathbf{y}}$ axes. This feature corresponds to a great simplification in the parameterization of the first-order RT model.

In this case, there are three unknown matrix quantities as in the isotropic case, except now they are in general distinct for *each* direction μ_o (or refracted direction μ_o') considered. In addition, there is no longer the requirement that $M_{vv} = M_{hh}$ for the extinction matrix $\boldsymbol{\kappa}_e$, or that $|S_{vv}S_{vv}^*| = |S_{hh}S_{hh}^*|$ for the backscatter component of the phase matrix $\boldsymbol{\mathcal{P}}_{bs}$

We have intentionally referred to *non*-isotropic instead of *an*isotropic, the latter being a term with very specific connotations in electromagnetic theory. Though the material descriptions are essentially the same, (i.e., our partially ordered description corresponds to a uniaxial tensor relative dielectric constant) a strict wave treatment necessitates consideration of such concepts as double refraction, ordinary and extraordinary waves, and birefringence (Kong 1975). In the heuristic framework of radiative transfer, these issues are mainly not considered. One aspect in RT which is suggestive of the results of the wave treatment is the existence of distinct eigenvalues of coherent propagation, as is seen in equation (5.33).

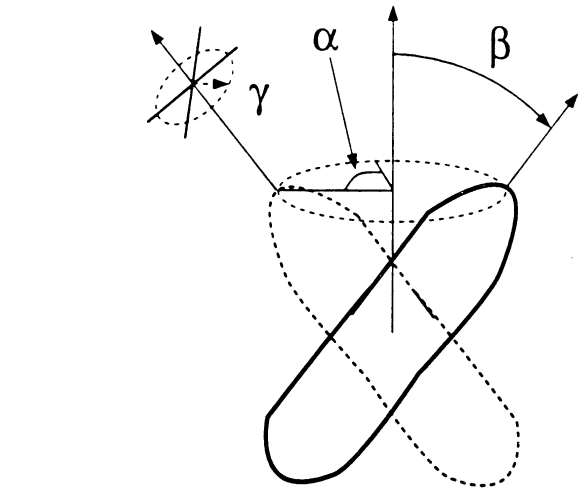

(a)

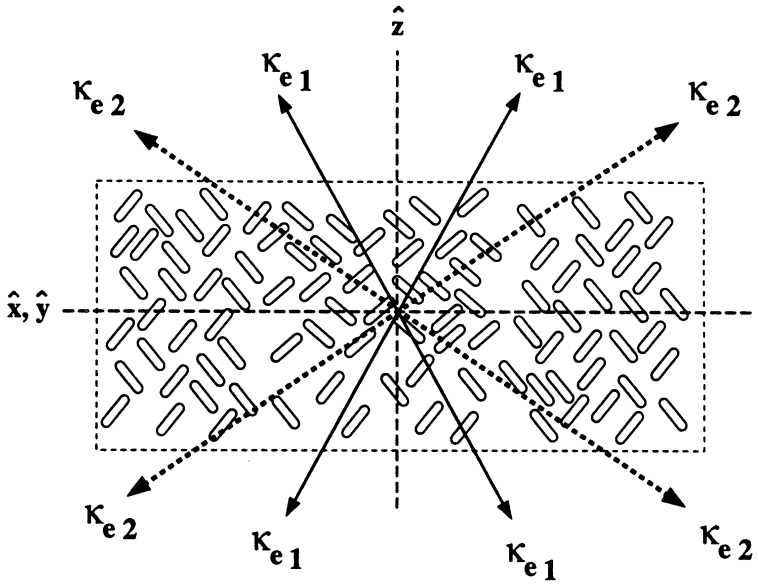

(b)

Figure 5.4: Non-isotropic layer: (a) Non-spherical particles have prescribed orientation with respect to β, but are completely uniform in Eulerian angles α and γ; (b) extinction and scattering quantities are a function of angle, but are invariant for reflections about the $\hat{\mathbf{x}}$, $\hat{\mathbf{y}}$, and $\hat{\mathbf{z}}$ axes.

Both of these cases lead to the same simplified versions of (5.40)–(5.43).

$$\mathcal{A}_1 = Q\,\mathcal{U}_1 Q^{-1}$$

$$[\mathcal{U}_1]_{ij} = \frac{1-\exp[-(\lambda_i+\lambda_j)d/\mu_o']}{(\lambda_i+\lambda_j)/\mu_o'} \cdot \left[Q^{-1}\mathcal{P}_{bs}Q\right]_{ij} \tag{5.44}$$

$$\mathcal{A}_2 = Q\,\mathcal{U}_2 Q^{-1}$$

$$[\mathcal{U}_2]_{ij} = \begin{cases} de^{-\lambda_i d/\mu_o'}\left[Q^{-1}\mathcal{P}_{bi}Q\right]_{ij} & (i=j) \\ \dfrac{\exp[-\lambda_j d/\mu_o'] - \exp[-\lambda_i d/\mu_o']}{(\lambda_i-\lambda_j)/\mu_o'} \cdot \left[Q^{-1}\mathcal{P}_{bi}Q\right]_{ij} & (i\neq j) \end{cases} \tag{5.45}$$

where, $\mathcal{A}_3 = \mathcal{A}_2$ and $\mathcal{A}_4 = \mathcal{A}_1$. These quantities, inserted into equation (5.27) give the first-order model which will be the basis for the inversion algorithm associated with the hybrid model concept. As mentioned, for the isotropic case, only the quantity $\mathcal{P}_{bi}$ is a function of μ_o; for the non-isotropic case, *all* quantities are functions of μ_o.

5.5 Rayleigh Model for Phase and Extinction Matrices

In this section, we examine, as an aid to inversion of the hybrid model, the essential character of the extinction matrix $\mathcal{K}_e$, and the two components of the phase matrix $\mathcal{P}_{bs}$ and $\mathcal{P}_{bi}$, for the special case of scattering by a layer of Rayleigh particles. This scenario corresponds to the isotropic case mentioned above, where $\mathcal{K}_e$ and $\mathcal{P}_{bs}$ are constant matrices, but $\mathcal{P}_{bi}$ is a function of angle.

The motivation for this analysis is that it is intuitive that the number of measurements required and the complexity of the ensuing inversion operation could be reduced through knowledge of the general form of the unknown matrices. That is, knowledge of which elements are non-zero, which are independent, and the nature of the dependences between

elements.

As a starting point, we consider the effective particles of the layer (as depicted in Figure 5.2) to be Rayleigh particles. As we will show in the following sections, this will allow us to derive symbolically the form the desired quantities, the extinction matrix, and certain components of the phase matrix consistant with a first-order approach, in terms of the elements of the polarizability tensor of the particles. This derivation follows closely that found in Whitt (1991), except that in that case only axisymmetric particles were considered, whereas, in the present case, no assumptions are made about the particle's symmetry properties.

5.5.1 Rayleigh Theory: Scattering Matrix Element Representation

For particles with dimensions small relative to the wavelength, scattering may be described in terms of a polarizability tensor. A scattered electric field vector is given by Kleinman and Senior (1986):

$$\mathbf{E}^s = \frac{-\omega^2\mu}{4\pi r} e^{ik_o r} \hat{\mathbf{k}}_s \times \hat{\mathbf{k}}_s \times \mathbf{p} \tag{5.46}$$

where $\hat{\mathbf{k}}_s$ is the unit vector in the direction of propagation of the scattered wave, and $\mathbf{p}$ is the induced dipole moment determined from the solution of the Laplace equation. If the induced dipole moments $(\mathbf{p}_x, \mathbf{p}_y, \mathbf{p}_z)$ are derived for $(\hat{\mathbf{x}}, \hat{\mathbf{y}}, \hat{\mathbf{z}})$ polarized incident fields, then The scattered field may be expressed as

$$\mathbf{E}^s = \frac{-\omega^2\mu}{4\pi r} e^{ik_o r} \hat{\mathbf{k}}_s \times \hat{\mathbf{k}}_s \times (\mathcal{D} \cdot \mathbf{E}^i) \tag{5.47}$$

where, $\mathcal{D}$ is the 3×3 polarizability tensor having as its columns the vectors $\mathbf{p}_x, \mathbf{p}_y$, and $\mathbf{p}_z$, and $\mathbf{E}^i$ is the incident field vector, $[E_x, E_y, E_z]^T$. The polarizability tensor $\mathcal{D}$ is a function of the geometry and dielectric constant of the Rayleigh particle. In general, $\mathcal{D}$ will be a function of the orientation of the particle.

Since,

$$\mathbf{E}^s = \frac{e^{ik_o r}}{r}\mathbf{S}\cdot\mathbf{E}^i \tag{5.48}$$

where,

$$\mathbf{S} = \begin{pmatrix} S_{vv} & S_{vh} \\ S_{hv} & S_{hh} \end{pmatrix} \tag{5.49}$$

the scattering matrix elements corresponding to the scattered polarization $\hat{\mathbf{p}}_s$ and the incident polarization $\hat{\mathbf{q}}_i$ such that $\hat{\mathbf{p}}_s \in \{\hat{\mathbf{v}}_s, \hat{\mathbf{h}}_s\}$ and $\hat{\mathbf{q}}_i \in \{\hat{\mathbf{v}}_i, \hat{\mathbf{h}}_i\}$, is given by

$$S_{pq} = \hat{\mathbf{p}}_s \cdot \mathbf{S} \cdot \hat{\mathbf{q}}_i. \tag{5.50}$$

Then from Eqs. (5.47) and (5.48),

$$S_{pq} = \frac{-k_o^2}{4\pi}\hat{\mathbf{p}}_s \cdot [\hat{\mathbf{k}}_s \times \hat{\mathbf{k}}_s \times (\boldsymbol{\mathcal{D}} \cdot \hat{\mathbf{q}}_i)] \tag{5.51}$$

which, upon invoking the vector identity

$$\hat{\mathbf{k}}_s \times \hat{\mathbf{k}}_s \times (\boldsymbol{\mathcal{D}} \cdot \hat{\mathbf{q}}_i) = (\hat{\mathbf{k}}_s \cdot (\boldsymbol{\mathcal{D}} \cdot \hat{\mathbf{q}}_i))\hat{\mathbf{k}}_s - (\hat{\mathbf{k}}_s \cdot \hat{\mathbf{k}}_s)(\boldsymbol{\mathcal{D}} \cdot \hat{\mathbf{q}}_i) \tag{5.52}$$

becomes

$$S_{pq} = \frac{-k_o^2}{4\pi}\hat{\mathbf{p}}_s \cdot [\hat{\mathbf{k}}_s \cdot (\boldsymbol{\mathcal{D}} \cdot \hat{\mathbf{q}}_i))\hat{\mathbf{k}}_s - (\boldsymbol{\mathcal{D}} \cdot \hat{\mathbf{q}}_i)]. \tag{5.53}$$

Since the polarization vector corresponding to the receiver is perpendicular to the direction

of the wave, $\hat{\mathbf{k}}_s$, (5.53) reduces to

$$S_{pq} = \frac{k_o^2}{4\pi} \hat{\mathbf{p}}_s \cdot (\mathcal{D} \cdot \hat{\mathbf{q}}_i). \tag{5.54}$$

5.5.2 Derivation of Extinction and Phase Matrix Elements

The extinction and phase matrix elements are expressed in terms of the ensemble-averaged quantities $\langle S_{pq} \rangle$ (Eqs. (2.33) and (2.34)) and $\langle S_{pq} S_{mn}^* \rangle$ (Eqs. (2.20) and (2.26)), respectively. In this section, we present the derivation of the forms of these elements in terms of the elements of the polarizability tensor in global coordinates.

Extinction Matrix Elements

We consider first terms of the form $\langle S_{pq} \rangle$. From (5.54),

$$\langle S_{pq} \rangle = \frac{k_o^2}{4\pi} \langle \hat{\mathbf{p}}_s \cdot (\mathcal{D} \cdot \hat{\mathbf{q}}_i) \rangle. \tag{5.55}$$

Since the polarization vectors themselves are not a function of the particle orientation, the averaging process is performed only on $\mathcal{D}$ itself:

$$\langle S_{pq} \rangle = \frac{k_o^2}{4\pi} \hat{\mathbf{p}}_s \cdot (\langle \mathcal{D} \rangle \cdot \hat{\mathbf{q}}_i). \tag{5.56}$$

The form of $\mathcal{D}$ in local coordinates is transformed from that in global coordinates ($\mathcal{D}'$) through the application of transformation matrices involving the Eulerian rotation angles α, β, and γ (see, for example, Tsang et al. (1985), pp. 158–160):

$$\mathcal{D} = \mathcal{A}^T \cdot \mathcal{D}' \cdot \mathcal{A} \tag{5.57}$$

where the elements of the $3 \cdot 3$ transformation matrix $\mathcal{A}$ are trigonometric functions of α, β, and γ, e.g.,

$$\begin{aligned} a_{11} &= \cos\gamma\cos\beta\cos\alpha - \sin\gamma\sin\alpha \\ a_{12} &= \cos\gamma\cos\beta\sin\alpha + \sin\gamma\cos\alpha \\ a_{12} &= -\cos\gamma\sin\beta \\ &\vdots \end{aligned} \tag{5.58}$$

Therefore for each element of $\mathcal{D}$, the polarizability tensor in local coordinates is:

$$d_{ij} = (\mathcal{A}^T \cdot \mathcal{D}' \cdot \mathcal{A})_{ij} = \sum_{m,n=1}^{3} (a_{mi}a_{nj})d'_{mn}. \tag{5.59}$$

It is seen from (5.59) that the symmetry property of $\mathcal{D}$ is preserved across a coordinate transformation.

For extinction, the quantity $\langle S_{pq} \rangle$ is computed in the forward direction only. Because of the assumption of classical radiative transfer that the positions of particles are uncorrelated, $\langle S_{pq} \rangle$ will be zero for every direction but forward scattering.

Since we have assumed there is no orientation dependence, we can assign the simplest possible forms to the vertical and horizontal polarization vectors, incident and scattered, and compute $\langle S_{pq} \rangle$ from (5.56). Considering an incident direction along the positive x-axis, using the Forward Scattering Convention (FSA), we have,

$$\begin{aligned} \hat{\mathbf{h}}_i &= [0\ 1\ 0]^T = \hat{\mathbf{h}}_s \\ \hat{\mathbf{v}}_i &= [0\ 0\ \text{-}1]^T = \hat{\mathbf{v}}_s. \end{aligned} \tag{5.60}$$

Ignoring the factor $\frac{k_0^2}{4\pi}$, and applying (5.56),

$$\begin{aligned}
\langle S_{vv} \rangle &= \langle d'_{33} \rangle \\
\langle S_{hh} \rangle &= \langle d'_{22} \rangle \\
\langle S_{hv} \rangle &= -\langle d'_{23} \rangle \\
\langle S_{vh} \rangle &= -\langle d'_{32} \rangle = -\langle d'_{23} \rangle
\end{aligned} \tag{5.61}$$

From (5.59),

$$\langle d_{ij} \rangle = \int_{\alpha=0}^{2\pi} \int_{\beta=0}^{\pi} \int_{\gamma=0}^{2\pi} \sum_{m,n=1}^{3} (a_{mi} a_{nj}) d'_{mn} \, p(\alpha) \, p(\beta) \, p(\gamma) d\alpha \, d\beta \, d\gamma \tag{5.62}$$

where, for completely uniform orientation, the respective probability density functions are:

$$\begin{aligned}
p(\alpha) &= \frac{1}{2\pi} \\
p(\beta) &= \frac{\sin\beta}{2} \\
p(\gamma) &= \frac{1}{2\pi}
\end{aligned} \tag{5.63}$$

over the limits indicated on the integrals in (5.62). These integrals may be evaluated without difficulty and the results are:

$$\begin{aligned}
\langle d_{22} \rangle &= \frac{1}{3}(d'_{11} + d'_{22} + d'_{33}) \\
\langle d_{33} \rangle &= \langle d_{22} \rangle \\
\langle d_{23} \rangle &= 0.
\end{aligned} \tag{5.64}$$

Thus for the scenario under consideration, the extinction is found to be a scalar and—when the result above is used in the definition (given in Eq. (2.34)) for the extinction elements—

we obtain the following expression:

$$\kappa_e = -2\mathrm{Re}\left[\frac{-2j\pi n_o}{3k_o}(d'_{11}+d'_{22}+d'_{33})\right]. \tag{5.65}$$

where n_o is the particle number-density.

The presence of a scalar extinction, κ_e, reduces the first-order formulation of (5.27) and the associated equations given in (5.44) and (5.45) to a very simple form. Expressing (5.27) as,

$$\mathbf{I}^s(\mu_o) = \mathcal{L}_m(\mu_o)\mathbf{I}^i(-\mu_o) \tag{5.66}$$

we have[2],

$$\mathcal{L}_m(\mu_o) = \frac{1}{\mu'_o}\mathcal{T}_{21}\left[\gamma\mathcal{R}_{23}\mathcal{P}_{bs}\mathcal{R}_{23} + \frac{d}{L}\mathcal{R}_{23}\mathcal{P}_{bi} + \frac{d}{L}\mathcal{P}_{bi}\mathcal{R}_{23} + \gamma\mathcal{P}_{bs}\right]\mathcal{T}_{12} \tag{5.67}$$

where,

$$\gamma = \frac{1-\exp(-2\kappa_e d/\mu'_o)}{2\kappa_e/\mu'_o)} \tag{5.68}$$

$$L = \exp(2\kappa_e d/\mu'_o) \tag{5.69}$$

[2]This form is the basis for the model which was implemented for the analysis of dry snow backscatter in Section 4.3.2. As it appears there (Eq. (4.8)), all but the direct backscatter term are neglected and additional terms comprising surface contributions to the backscatter are added.

Phase Matrix Elements

The derivation of the phase matrix elements involves evaluation of quantities of the form $\langle S_{pq} S^*_{mn} \rangle$. Referring back to Eq. (5.54), we have:

$$\langle S_{pq} S^*_{mn} \rangle = \frac{k_o^4}{(4\pi)^2} \langle (\hat{\mathbf{p}}_s \cdot \boldsymbol{\mathcal{D}} \cdot \hat{\mathbf{q}}_i)(\hat{\mathbf{m}}_s \cdot \boldsymbol{\mathcal{D}}^* \cdot \hat{\mathbf{n}}_i) \rangle. \tag{5.70}$$

It can be shown that this may be expressed as,

$$\langle S_{pq} S^*_{mn} \rangle = \frac{k_o^4}{(4\pi)^2} \hat{\mathbf{p}}_s \cdot \langle \mathcal{G} \rangle \cdot \hat{\mathbf{n}}_i \tag{5.71}$$

where,

$$\langle \mathcal{G} \rangle = \langle \boldsymbol{\mathcal{D}} \cdot Q \cdot \boldsymbol{\mathcal{D}}^* \rangle \tag{5.72}$$

and,

$$Q = \hat{\mathbf{q}}_i \otimes \hat{\mathbf{m}}_s \tag{5.73}$$

where $\otimes$ denotes the Kronecker tensor product. This quantity comprises all possible products between the elements of the two matrices involved. For example, if X is 2×2, then:

$$X \otimes Y = \begin{bmatrix} X(1,1)Y & X(1,2)Y \\ X(2,1)Y & X(2,2)Y \end{bmatrix}. \tag{5.74}$$

Through another application of this tensor product rearrangement, (5.72) becomes,

$$\langle \mathbf{G} \rangle = \langle \mathcal{D} \otimes \mathcal{D}^* \rangle \mathbf{Q} \tag{5.75}$$

where $\langle \mathbf{G} \rangle$ and $\mathbf{Q}$ are the (9 x 1) vector representations of the (3 x 3) matrices $\langle \mathcal{G} \rangle$ and Q,

respectively. That is, if $\langle \mathcal{G} \rangle$ has elements g_{ij}, then

$$\mathbf{G} = [g_{11}, g_{12}, g_{13}, g_{21}, g_{22}, g_{23}, g_{31}, g_{32}, g_{33}]. \tag{5.76}$$

and similarly for **Q**. Here, as with the elements of the extinction matrix, the ensemble-averaging process over orientation has been confined to the polarizability tensor quantity alone.

The task of expressing phase matrix elements symbolically in terms of the polarizability tensor elements reduces to evaluation of the ensemble-averaged quantity on the right -hand - side of (5.75). Once this quantity is evaluated, operations upon it with matrices and vectors formed from the four polarization vectors $\hat{\mathbf{p}}_s, \hat{\mathbf{n}}_i, \hat{\mathbf{m}}_s$, and $\hat{\mathbf{n}}_i$, yield the desired phase matrix elements. The averaging process proceeds as before, using equation (5.59). The Kronecker tensor product, however, inflates the formulation greatly since each element d_{ij} in $\mathcal{D}$ is composed of approximately twelve terms (since some of the elements in the transformation matrix $\mathcal{A}$ have two terms), each element in $\langle \mathcal{D} \otimes \mathcal{D}^* \rangle$, a 9×9 matrix, has on the order of one hundred and forty-four terms, each requiring integration with respect to the three Eulerian rotation angles α, β, and γ.

For the **backscatter** component of the phase matrix, because of reciprocity, we need derive expressions for only six quantities to allow specification of the entire matrix. These quantities are:

$$\begin{array}{ll} \langle S_{hv} S_{hv}^* \rangle & \langle S_{hh} S_{hh}^* \rangle \\ \langle S_{vv} S_{hv}^* \rangle & \langle S_{vh} S_{hh}^* \rangle \\ \langle S_{vv} S_{hh}^* \rangle & \langle S_{vv} S_{vv}^* \rangle \end{array} \tag{5.77}$$

Again, for orientation independence and following the FSA convention, we invoke very simple descriptions for the incident and scattered polarization vectors, for both polarizations

respectively. (Recall, for FSA, $\hat{\mathbf{h}}_i = (\hat{\mathbf{z}} \times \hat{\mathbf{k}}_i)/|\hat{\mathbf{z}} \times \hat{\mathbf{k}}_i|$ and $\hat{\mathbf{v}}_i = \hat{\mathbf{h}}_i \times \hat{\mathbf{k}}_i$.) For incidence along the positive x-axis ($\theta_i = \pi/2, \phi_i = 0$),

$$\hat{\mathbf{h}}_i = [0\ 1\ 0]^T \qquad \hat{\mathbf{h}}_s = [0\ {-1}\ 0] \tag{5.78}$$
$$\hat{\mathbf{v}}_i = [0\ 0\ {-1}]^T \qquad \hat{\mathbf{v}}_s = [0\ 0\ {-1}]$$

It is not necessary for the first-order solution—and would indeed require a very large amount of effort—to evaluate each one of the elements of the forty-five distinct (since it is symmetric) elements of the 9×9 matrix $\langle \mathcal{D} \otimes \mathcal{D}^* \rangle$. We need only evaluate those elements which are selected out by the operations indicated in (5.71) and (5.75). For the backscatter component, the vectors $\hat{\mathbf{p}}_s, \hat{\mathbf{q}}_i, \hat{\mathbf{m}}_s$, and $\hat{\mathbf{n}}_i$ used in (5.71) and (5.75) are dictated by (5.77) and (5.78) above. Accordingly, we find that (ignoring the factor $k_o^4/(4\pi)^2$ in (5.71)):

$$\langle S_{hv} S_{hv}^* \rangle = \langle d_{23} d_{23}^* \rangle \tag{5.79}$$
$$\langle S_{vv} S_{hv}^* \rangle = \langle d_{33} d_{23}^* \rangle$$
$$\langle S_{vv} S_{hh}^* \rangle = -\langle d_{33} d_{22}^* \rangle$$
$$\langle S_{hh} S_{hh}^* \rangle = \langle d_{22} d_{22}^* \rangle$$
$$\langle S_{vh} S_{hh}^* \rangle = \langle d_{23} d_{22}^* \rangle$$
$$\langle S_{vv} S_{vv}^* \rangle = \langle d_{33} d_{33}^* \rangle$$

For the **bistatic** component of the phase matrix, there are ten distinct quantities to be

determined:

$$\begin{array}{ll} \langle S_{vv}S_{vv}^* \rangle & \langle S_{vv}S_{hh}^* \rangle \\ \langle S_{vv}S_{vh}^* \rangle & \langle S_{hh}S_{hh}^* \rangle \\ \langle S_{hv}S_{hv}^* \rangle & \langle S_{vh}S_{hv}^* \rangle \\ \langle S_{vv}S_{vv}^* \rangle & \langle S_{hh}S_{hh}^* \rangle \\ \langle S_{hv}S_{hh}^* \rangle & \langle S_{vh}S_{vh}^* \rangle \end{array} \tag{5.80}$$

Again, the elements of the matrix $\langle \mathcal{D} \otimes \mathcal{D}^* \rangle$ which are required for the specification of the quantities in (5.80) are found through applying the appropriate polarization vectors as shown in (5.71) and (5.75).

To construct these polarization vectors, we examine in Figure (5.5) the geometry of this bistatic scattering mechanism, where θ_r corresponds to the refracted angle with the layer. We refer to θ_r rather than our earlier notation θ_i' since our interest in this present treatment is in an angle magnitude as opposed to a propagation direction. The scattering event for which we are interested in determining the form of the polarization vectors occurs at point (A) in the figure. Since the medium is completely isotropic, to find the simplest form of the polarization vectors, we can consider the incidence direction to be along the positive $\hat{\mathbf{y}}$-axis ($\theta_i = \pi/2$, $\phi_i = \pi/2$) as shown in Figure 5.6. In this case, the scattered direction is given by $\theta_s = \pi/2 - 2\theta_r$ and $\phi_s = \pi/2$. Following the FSA convention, we then have,

$$\begin{array}{ll} \hat{\mathbf{h}}_i = [\text{-}1\ 0\ 0]^T & \hat{\mathbf{h}}_s = [\text{-}1\ 0\ 0]^T \\ \hat{\mathbf{v}}_i = [0\ 0\ \text{-}1]^T & \hat{\mathbf{v}}_s = [0\ \sin 2\theta_r\ -\cos 2\theta_r]^T. \end{array} \tag{5.81}$$

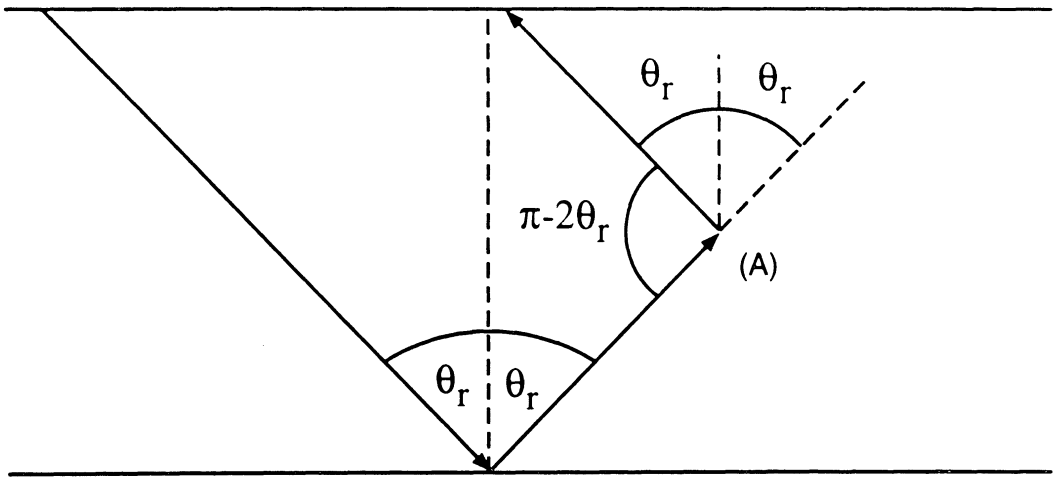

Figure 5.5: Geometry of scattering for first-order bistatic term.

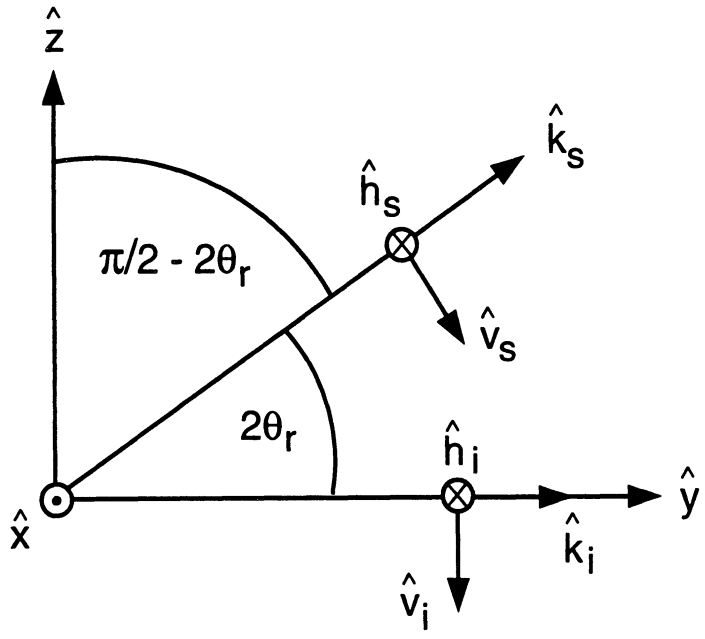

Figure 5.6: Illustration of polarization vectors for first-order bistatic term.

Applying (5.80) and (5.81) to (5.71) and (5.75) we have:

$$\begin{aligned}
\langle S_{vv}S_{vv}^{*}\rangle &= \sin^2 2\theta_r\langle d_{23}d_{23}^{*}\rangle - \sin 2\theta_r\cos 2\theta_r\left(\langle d_{23}d_{33}^{*}\rangle + \langle d_{33}d_{23}^{*}\rangle\right) \\
&\quad + \cos^2 2\theta r\cos^2 2\theta\langle d_{33}d_{33}^{*}\rangle \qquad (5.82)\\
\langle S_{vv}S_{vh}^{*}\rangle &= \sin^2 2\theta_r\langle d_{12}d_{23}^{*}\rangle - \sin 2\theta_r\cos 2\theta_r\left(\langle d_{13}d_{23}^{*}\rangle + \langle d_{12}d_{33}^{*}\rangle\right) \\
&\quad + \cos^2 2\theta r\cos^2 2\theta\langle d_{13}d_{33}^{*}\rangle \\
\langle S_{hv}S_{hv}^{*}\rangle &= \langle d_{13}d_{13}^{*}\rangle \\
\langle S_{vv}S_{hv}^{*}\rangle &= -\sin 2\theta_r\langle d_{13}d_{23}^{*}\rangle + \cos 2\theta_r\langle d_{13}d_{33}^{*} \\
\langle S_{hv}S_{hh}^{*}\rangle &= \langle d_{11}d_{13}^{*}\rangle \\
\langle S_{vv}S_{hh}^{*}\rangle &= -\sin 2\theta_r\langle d_{11}d_{23}^{*}\rangle + \cos 2\theta_r\langle d_{33}d_{11}^{*}\rangle \\
\langle S_{hh}S_{hh}^{*}\rangle &= \langle d_{11}d_{11}^{*}\rangle \\
\langle S_{vh}S_{hh}^{*}\rangle &= -\sin 2\theta_r\langle d_{11}d_{12}^{*}\rangle + \cos 2\theta_r\langle d_{11}d_{13}^{*}\rangle \\
\langle S_{vh}S_{hv}^{*}\rangle &= -\sin 2\theta_r\langle d_{12}d_{12}^{*}\rangle + \cos 2\theta_r\langle d_{13}d_{13}^{*}\rangle \\
\langle S_{vh}S_{vh}^{*}\rangle &= \sin^2 2\theta_r\langle d_{12}d_{12}^{*}\rangle - \sin 2\theta_r\cos 2\theta_r\left(\langle d_{12}d_{13}^{*}\rangle + \langle d_{13}d_{12}^{*}\rangle\right) \\
&\quad + \cos^2 2\theta r\cos^2 2\theta\langle d_{13}d_{13}^{*}\rangle
\end{aligned}$$

From (5.79) and (5.82) we find that it is necessary to evaluate eighteen distinct elements of the matrix quantity $\langle \mathcal{D}\otimes\mathcal{D}^{*}\rangle$ in order to specify the first-order vector scattering mechanisms. As mentioned earlier, each one of these elements has approximately one-hundred and forty terms each of which require integration with respect to α, β, and γ.

Fortunately, there are a limited number of integral types which occur. All are of the form,

$$I_{xmn} = \int \sin^m x\cos^n x\, p(x)\, dx \qquad x = \alpha, \beta, \gamma \qquad (5.83)$$

m	n	i	$I_{\alpha mn} = I_{\gamma mn}$	$I_{\beta mn}$
1	0	1	0	$\pi/4$
0	1	1	0	0
1	1	2	0	0
2	0	2	1/2	2/3
0	2	2	1/2	1/3
0	3	3	0	0
1	2	3	0	$\pi/16$
2	1	3	0	0
3	0	3	0	$3\pi/16$
0	4	4	3/8	1/5
1	3	4	0	0
2	2	4	1/8	2/15
3	1	4	0	0
4	0	4	3/8	8/15

Table 5.1: Values of α, β, and γ Integrals

where,

$$m+n=i, \qquad i=1,4$$

and where $p(x)$ is one of the pdf's specified in (5.63). Table 5.1 gives the values of all possible combinations of (5.83) for α, β, and γ. Apart from the need to wade through a very large number of terms, it is straightforward to evaluate the eighteen terms of the form $\langle d_{jk} d_{lm}^* \rangle$ in (5.79) and (5.82). The result of the analysis is the following extremely simple form:

$$\mathcal{P}_{bs} = \begin{bmatrix} P_1 & \frac{1}{2}(P_1 - P_2) & 0 & 0 \\ \frac{1}{2}(P_1 - P_2) & P_1 & 0 & 0 \\ 0 & 0 & -\frac{1}{2}(P_1 + P_2) & 0 \\ 0 & 0 & 0 & \frac{1}{2}(P_1 - 3P_2) \end{bmatrix} \tag{5.84}$$

and,

$$\mathcal{P}_{bi} = \begin{bmatrix} \frac{1}{2}P_1(1+\cos^2(2\theta)) - \frac{1}{2}P_2\sin^2(2\theta) & \frac{1}{2}(P_1 - P_2) & \cdots \\ \frac{1}{2}(P_1 - P_2) & P_1 & \\ 0 & 0 & \\ 0 & 0 & \end{bmatrix} \tag{5.85}$$

$$\begin{bmatrix} 0 & 0 \\ 0 & 0 \\ \frac{1}{2}\cos 2\theta(P_1 + P2) & 0 \\ 0 & -\frac{1}{2}\cos 2\theta(P_1 - 3P_2) \end{bmatrix}$$

where,

$$P_1 = \frac{1}{5}A + \frac{4}{15}B + \frac{2}{15}C \qquad A = |d'_{11}|^2 + |d'_{22}|^2 + |d'_{33}|^2$$

$$P_2 = \frac{1}{15}A - \frac{2}{15}B + \frac{4}{15}C \qquad B = |d'_{12}|^2 + |d'_{13}|^2 + |d'_{23}|^2$$

$$C = \mathrm{Re}(d'_{11}d'^{*}_{22} + d'_{11}d'^{*}_{33} + d'_{22}d'^{*}_{33}).$$

5.5.3 Summary

An analytical evaluation of the theoretical problem of backscattering from a layer of general Rayleigh particles reveals that scattering and extinction within the layer is described by just three parameters. This extremely simple form can potentially be exploited in the inversion process associated with the hybrid model concept. In Chapter VI, we will examine the validity of this model for actual dense media.

This completes the theoretical framework of the Hybrid Model concept. The remaining elements are an experimental process and a numerical inversion algorithm. These are

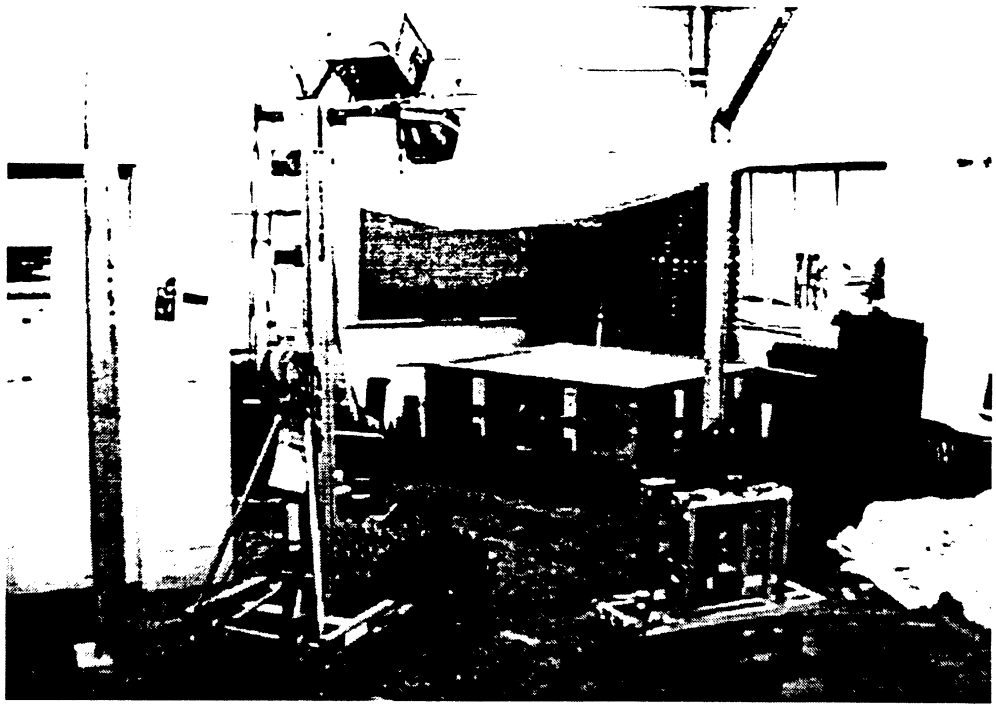

Figure 5.7: Photograph of experimental setup. Radar mounted on a mechanical lift overlooking a sandbox filled with the test material. (Additional equipment is part of an unrelated bistatic facility.)

described in the following sections.

5.6 Experimental Process

A experimental effort was carried out to test the validity of the Hybrid Model concept. A photograph and a schematic of the experimental setup are shown in Figures 5.7 and 5.6, respectively. The experimental process was straightforward. Polarimetric backscatter measurements of selected dense materials were made with a Ku-band, network-analyzer-based radar. A detailed description of the radar, which was developed by the author, is given in Appendix D. Details of the specific materials examined are given in Chapter VI. The material examined was contained inside a large 1.8 x 1.8 meter wooden "sandbox". The sandbox

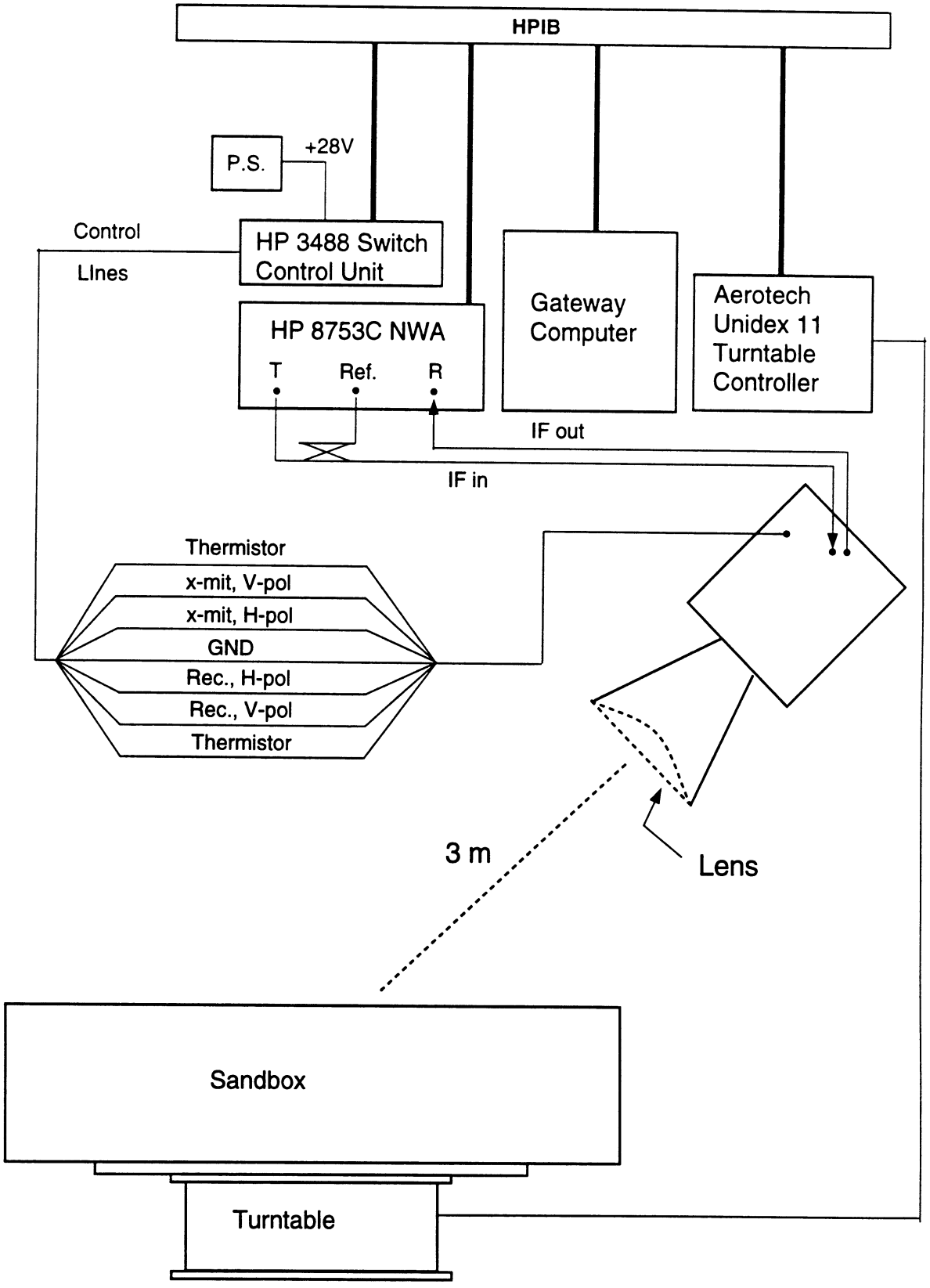

Figure 5.8: Schematic of experimental setup.

itself was mounted on top of a turntable to allow for independent spatial measurements. The sides of the sandbox were two-tiered with the first tier removable so that it could have a maximum depth of either 23 cm or 43 cm. This was useful to prevent an excessive amount of "shadowing" of the surface of the layer for shallow depths. The radar was mounted on a manually adjustable, telescoping mechanical lift (Genie Superlift, manufactured by Genie Industries of Redmond, Washington). The radar mount was such that manual adjustment of the incidence angle could be accomplished by simply tilting it and locking it into place. The range from the aperture of the radar antenna to the layer surface, along the boresite direction of the antenna was always 3 meters. This corresponds to approximately D^2/λ where D is the dimension of the square aperture of the antenna, and was sufficiently small to allow a full range of incidence angles to be observed in an indoor setting.

As is described fully in Appendix D, the radar consists of upconversion, downconversion, and polarization selection circuitry attached to a square horn antenna *via* an orthomode transducer. A coherent IF signal at 1–3 GHz is provided by the network analyzer and mixed with a local oscillator at the radar box to produce a 15–17 GHz RF. The design and operation of the radar follows closely that of the LCX POLARSCAT system described in Tassoudji et al. (1989). A compact geometry for the antenna is enabled through the use of a dielectric lens to correct the phase error at the aperture. Details are given in the appendix. The final beamwidth for the lens-corrected antenna (one-way, HPFW) was 5.3° for both E- and H-plane.

Two parameters were varied in the experimental process for each of the materials examined: (1) layer depth, (2) and the nature of the underlying "halfspace". The layer depth was varied between 2 cm and about 40 cm. For the underlying surface, either an aluminum sheet ($\tilde{\varepsilon} = 1 - j3.97 \times 10^7$ at 16 GHz) or a flat absorber was used. The flat absorber was created by cutting off, with a bandsaw, the projecting portion of seven inch high pyramidal absorber, leaving 60 × 60-centimeter slabs of 5 centimeter thick flat absorber. These slabs were then arranged to cover the bottom of the sandbox. The dielectric constant of the ab-

sorber ($\tilde{\varepsilon} = 1.64 - j0.15$) was measured by comparing the nadir-viewing reflectivity relative to the conducting sheet. The imaginary part was estimated (a lower limit) by considering the minimum amount that the reflection from a conducting sheet under the absorber had been attenuated.

As indicated in the schematic (Fig. 5.6), both the radar operation and the movement of the turntable were under computer control. To reduce the variance in the estimate of the mean backscatter, independant measurements were realized by rotating the sandbox. It was found that the signal was sufficiently decorrelated for a rotation of five degrees. Thus, for each target scenario examined (incidence angle, depth, underlying dielectric) 72 independant spatial samples were collected, one every five degrees for one complete revolution of the sandbox. Additional averaging was obtained using frequency averaging, normally using the responses from 21 frequency points equally spaced throughout the 2 GHz bandwidth. The gating capability of the network analyzer was used to isolate the backscatter response of the layer. The footprint of the antenna at 3 meters, even at 60°, the highest incidence angle examined, was sufficiently small (<0.56 m) so that scattering from the wooden sides of the sandbox constituted a negligible interference.

Since the primary goal of this investigation is to study volume scattering, great care was taken to make the surface of the layers as smooth as possible to minimize surface backscatter. The smoothing technique employed a sled whose skids rode along two opposite sides of the sandbox, and from which was suspended, spanning the entire width of the sandbox, a metal blade. The metal blade was lowered to the appropriate depth and leveled. The sled was then pulled across the box multiple times. After each pass, excess material was removed manually or additional material added where the level was perceived to be low. In this fashion, an optimally smooth and *reproducible* surface, with roughness dictated mainly by the particle size of the test material, was achieved. The roughness of the surface corresponding to each of the materials examined was accurately characterized by measurement with a laser profiler.

For calibration of the radar, the Isolated Antenna Calibration Technique (IACT) was used (Sarabandi et al. 1990), which requires the measurement of a sphere (a 6″ one in this case) and an arbitrary depolarizing target (we used a length of wire oriented at roughly 45°). This technique, as the name implies, requires a radar system with excellent polarization isolation. The K_u-band system has polarization isolation on the order of 30 dB. A calibration technique which requires *only* the measurement of a sphere (Single Target Calibration Technique (Sarabandi and Ulaby 1990)) was originally attempted. This technique is intended for systems with moderate polarization isolation, where quantitative information about the cross-polarized channels can be obtained *via* a measurement of a non-depolarizing target, like a sphere. An additional assumption is made that the cross-talk can be described in terms of a single constant. Owing to the excellent isolation of the K_u-band system, the STCT was found to give unsatisfactory results. In particular, the two cross-polarized results, required by reciprocity to be identical in the backscatter, were separated by as much as 4 dB. With the IACT technique, these terms were always within 0.5 dB of one another.

The effect of the calibration techniques mentioned above is to remove system distortions thereby correcting the measured electric fields (complex voltages). To actually convert these electric fields to backscatter coefficients (σ°) for distributed targets, a quantity based on the antenna pattern, known as an illumination integral, must be employed. This procedure is described in Appendix D.

5.7 Inversion Process

In general, the inversion process consists of two steps:

1. Assume some form of the unknown matrices $\boldsymbol{\kappa}_e$, $\boldsymbol{\mathcal{P}}_{bs}$, and $\boldsymbol{\mathcal{P}}_{bi}$. A logical starting point is for example, an isotropic model using the three parameters, κ_e, $\mathbf{P}_1$, and $\mathbf{P}_1$ from the Rayleigh derivation above.

2. Use an optimization algorithm to minimize the least-squares function given by:

$$\sum_{i=1}^{N_\theta}\sum_{j=1}^{N_d}\sum_{k=1}^{N_\varepsilon}\sum_{l=1}^{4}\sum_{m=1}^{4}\left\{\frac{\left[\mathcal{M}_{i,j,k}\right]_{l,m}-\left[\overline{\mathcal{M}}_{i,j,k}\right]_{l,m}}{\left[\mathcal{M}_{i,j,k}\right]_{l,m}}\right\}^{1/2} \tag{5.86}$$

where $\mathcal{M}$ and $\overline{\mathcal{M}}$ are the measured and predicted Mueller matrices, respectively, corresponding to all of the different experimental variables—incidence angle, depth, and dielectric of underlying surface—indexed up to N_θ, N_d, and N_ε.

The formulation of $\overline{\mathcal{M}}$ is non-linear, even for the simple case of a scalar extinction, due to the presence of the exponential functions of the extinction. Initially a conjugate gradient procedure was attempted but was found to be unsatisfactory because of the absence of a means for enforcing upper and lower limits on the parameters being estimated. It is, for example, a physical requirement that the parameters corresponding to $< S_{vv}S_{vv}^* >$, $< S_{hh}S_{hh}^* >$, and $< S_{vh}S_{vh}^* >$ be strictly postitive. We eventually settled upon a very robust algorithm written by the Institute of Systems Research at the University of Maryland (Zhou and Tits 1993) called FSQPD (**F**ortran, **S**equential **Q**uadratic **P**rogramming, **D**ouble precision). The algorithm allows upper and lower bounds to be set for the parameters and also provides for the imposition of linear and non-linear constraints, though none were used in this case.

CHAPTER VI

APPLICATION OF HYBRID MODELING APPROACH TO DENSE MEDIA

In this chapter, we test the Hybrid Model concept which was proposed in the previous chapter. Specifically we will test whether from measured backscatter data we can retrieve, through an inversion process, parameters which, when used in some form of first-order radiative transfer, provide a comprehensive and polarimetric description of scattering. After evaluating the degree to which such a concept is valid, we will examine some additional considerations, including experimental efficiency, or the minimum number of experiments necessary to sufficiently characterize a medium; the degree to which our measurements of volume scattering agree with theoretical predictions; and some insights obtainable through the application of the Hybrid model to synthetic data generated by "rigorous" scattering models.

The experimental procedure and general inversion algorithm were described in Sections (5.6) and (5.7). The specific materials which were examined are described next.

6.1 Materials Examined

The most interesting application of the Hybrid Modeling concept would be to snow. However, in this development stage, the handling requirements of snow for the purpose of a (possible lengthy) set of controlled experiments are too prohibitive. In this initial develop-

ment stage therefore, we opted to use "stable" materials, for which material characteristics are static and unchanging through the layer.

Two dense materials were examined: a construction grade of sand, henceforth referred to as "Common sand", and a sized silica gravel, henceforth referred to as "8-12 Gravel", based on its being produced in a sieving process as the material retained on Standard Sieves 8–12. Some characteristics of these materials are given in Figure 6.1 which shows the particle distributions of each material obtained from sieve analyses; also given in the figure are some pertinent physical and electrical properties of the materials. Both materials have high volume fractions which indicate a maximum packing density of particles. The particle-size distribution of the 8-12 gravel has been rendered as a probability density function to facilitate, as will be discussed below, its comparison with theoretical scattering predictions. Presentation of the Common sand particle-size distribution has been left in the form of mass fraction.

The dielectric constants of these materials were measured in two different ways: (1) a coaxial waveguide complex reflection coefficient technique at 9.5 GHz, and (2) using the Snow Probe (described in Chapter III) at about 1.5 GHz. While the 9.5 GHz result would seem to be most pertinent to the present effort which is conducted at 15-17 GHz, there are questions about the accuracy of the estimate of the imaginary part of the dielectric constant, which is frequency dependent, as measured by the waveguide technique. The issue of determining $\tilde{\varepsilon}$ for the materials is addressed further in Section 6.5. For now, we show in Figure 6.1 only the real part of the dielectric constants of the materials, ε', which is essentially the same at both of the frequencies at which it was measured.

The common sand has a particle distribution which appears Rayleigh distributed, comprising a relatively small volume fraction of fairly large particles in a host medium of predominantly very small particles. It is an example of a material which does not easily lend itself to theoretical modeling. Though composed of discrete particles, it is a heterogeneous blend, the largest particles in particular appearing to be of a different composition than the

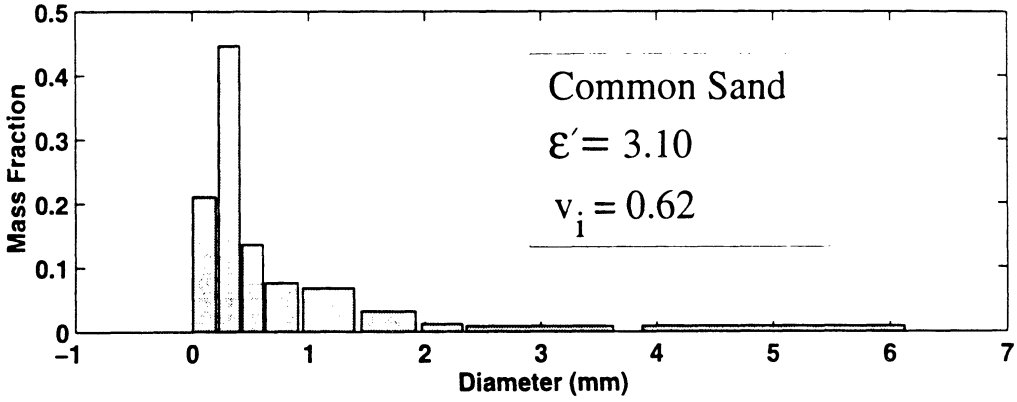

(a)

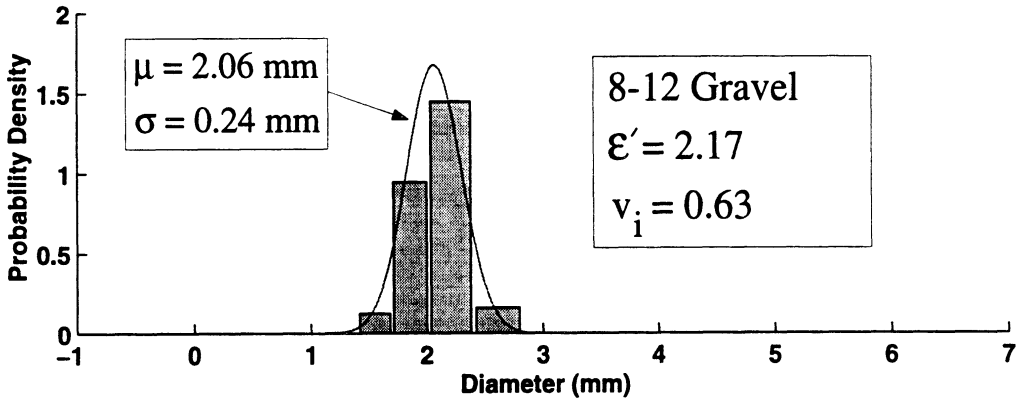

(b)

Figure 6.1: Characteristics of (a) Common sand, and (b) 8-12 Gravel: v_i denotes volume fraction. Note that distribution in (b) has been rendered as a probability density function.

Typical Physical Properties		Typical Chemical Analysis	
Fusion Point	3135 °F	Silicon dioxide	98.20%
Hardness	7 Mhos scale	Aluminum oxide	0.72%
Grain Shape	Spherical	Calcium oxide	0.56%
Specific gravity	2.65 g/cm^3	Iron oxide	0.07%
Bulk density	$\approx$1.57 g/cm^3	Magnesium oxide	0.13%
pH	6.8–7.2	Manganese oxide	0.03%
Sphericity (Krumbein)	0.6–0.7	Potassium oxide	0.10%
Roundness (Krumbein)	0.6–0.7	Sodium oxide	0.03%
		Titanium oxide	0.07%
		Loss on ignition	0.09%

Table 6.1: Material characteristics of 8-12 Gravel

main bulk of the material, which is a silica sand. In addition, the largest particles have very irregular shapes. With these complicating factors it shares some similarity to the amorphous snowpacks mentioned earlier in that neither case is amenable to straightforward modeling approaches.

A detailed description of the 8-12 Gravel, provided by the supplier (AGSCO Corp., Wheeling, Il.) is given in Table 6.1. As shown in Figure 6.1b, this material has a relatively narrow particle size distribution, which corresponds to a gaussian pdf having mean value $\mu = 2.062$ mm and variance $\sigma^2 = 0.056$ mm. The particles themselves have a high degree of sphericity. The 8-12 Gravel is seen to have a character quite different from that of the Common sand and as such can test to a certain extent the robustness of the Hybrid Modeling technique. In addition, it constitutes an excellent candidate for testing against theoretical RT models. At K_u-band ($\lambda \approx 1.875$ cm), the associated size parameter, ka, where k is the wavenumber in the particle and a is its radius, is just beyond the Rayleigh limit, for which the criterion has been given as $ka < 0.5$ (Ulaby et al. 1986) (present case: ka =0.61). Although the DMRT model (Tsang and Ishimaru 1987) is intended specifically for Rayleigh particles, applications have been demonstrated by its authors for cases having ka as high as 1.0 (West et al. 1993); thus, a meaningful comparison should be permissible with the 8-12 material. One obstacle to theoretical comparisons is the problem of precisely ascertaining

the precise complex dielectric constant of the particles themselves at K_u-band. The issue of a theoretical comparision with measurements is taken up in Section 6.5.

6.2 Surface Contributions

In Section 5.6 a means by which the top surface of the layer was made as smooth as possible was presented. In order to carefully analyze the scattering behavior of the volume, the effect of the surface must be either (1) very well understood, or (2) negligible. Since the physics of rough surface scattering is in itself a very challenging problem, and doubly so when integrated with volume scatter, we have attempted to achieve option (2).

The importance of the influence of the surface backscattter on the measurements may be gauged to some degree by the variability of the signal with different target parameters. If, for example, at a given incidence angle, backscatter changes very little with changing depth, or with changes in the underlying "halfspace" material, then it may be suspected that the dominant source of the backscatter is the surface term. As will be shown in the following sections, this was not found to be the case in our measurements. However, even for the case in which the signal is seen to be quite responsive to changes in the target configuration, it is possible that the small surface term may represent a substantial contribution for the cases involving the very lowest backscatter levels, and so introduce errors into an analysis based on volume scattering exclusively. For this reason, an attempt was made to calculate the expected backscatter based on measured parameters of the surface.

The surface parameters consist of the effective dielectric constant, given in Figure 6.1 and the roughness parameters, rms height and correlation length which can be obtained through the measurement of the surface height profile. Accordingly, the surface height profiles were measured with a laser profiler. The auto-correlation functions were seen to be essentially exponential. The roughness parameters for both of the test materials are presented in Table 6.2. A suitable theoretical solution for these parameters is given by the small per-

Description	RMS Height s (mm)	ks	Corr. Length* l (mm)	kl
Common Sand	0.45	0.015	20	9.88
8-12 Gravel	0.66	0.022	2	1.18

*Approximately exponential correlation function

Table 6.2: Surface parameters of test materials.

turbation method (SPM) (see, for example, Ulaby et al. (1986)). The estimated backscatter as a function of angle is presented in Figure 6.2(a). Also shown are predictions obtained by using the semi-empirical model given by Eqs. (4.1) and (4.2), which was described in Chapter IV. As anticipated, the backscattering level predicted by both of these techniques is quite low for these smooth surfaces and the two separate techniques produce very comparable results. The relative contribution of this surface scattering component may be evaluated with respect to the measurements which are presented next.

6.3 Interpretation of Results

In the following sections we present the results of our controlled experiments and analyze them in the context of the hybrid modeling approach outlined in Chapter V. It is our intent to investigate whether one of the three approaches described in Chapter V constitute an appropriate polarimetric model, at least for the test materials being considered. The three approaches were, in order of increasing generality: an isotropic model consisting of Rayleigh particles, a general isotropic model, and a particular non-isotropic model.

Before proceeding further, however, it will first be instructive to state explicitly what consitutes a comprehensive comparison between a polarimetric model and measurements. For an azimuthally symmetric medium, there are normally considered to be five independent quantities contained in the measured Mueller matrix in the backscatter direction. These are the co-pol responses, $|S_{vv}|^2$ and $|S_{hh}|^2$, the cross-pol response, $|S_{vh}|^2$ ($= |S_{hv}|^2$ for backscat-

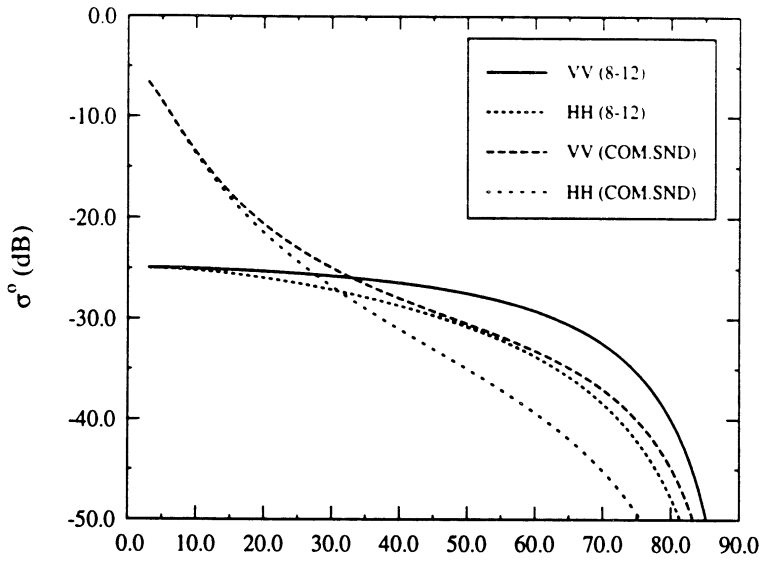

(a) Small Perturbation Method

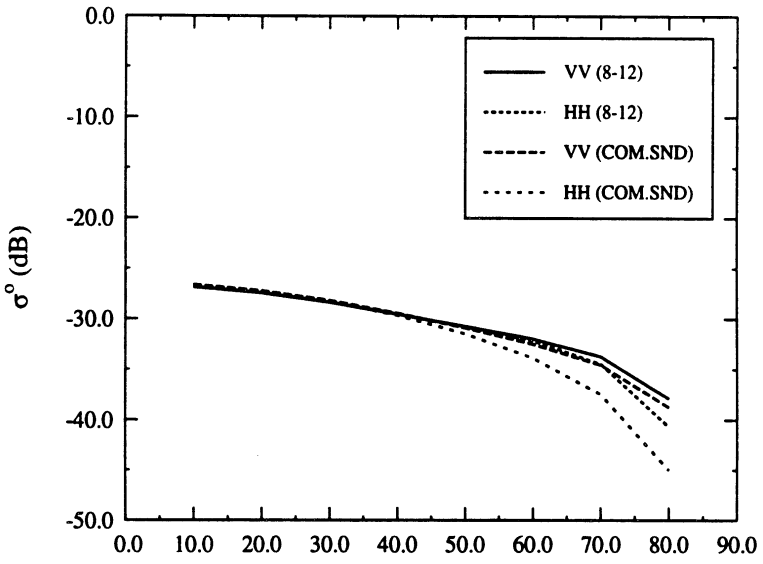

(b) Semi-empirical scattering model.

Figure 6.2: Predictions of surface scattering for Common sand and 8-12 Gravel, generated using (a) the Small Perturbation Method, and (b) the semi-empirical model by Oh et al. (1992).

ter) and two parameters which together specify the statistics of the co-polarized phase difference $\phi_{hh} - \phi_{vv}$. The pdf governing this random variable has been shown to be (Sarabandi 1992):

$$f_\Phi(\phi) = \frac{1-\alpha^2}{2\pi[1-\alpha^2\cos^2(\phi-\zeta)]}\left\{1+\frac{\alpha\cos(\phi-\zeta)}{\sqrt{1-\alpha^2\cos^2(\phi-\zeta)}} \times\left[\frac{\pi}{2}+\tan^{-1}\frac{\alpha\cos(\phi-\zeta)}{\sqrt{1-\alpha^2\cos^2(\phi-\zeta)}}\right]\right\}. \quad (6.1)$$

which is specified by the two parameters α—the *degree of correlation*—and ζ—the *co-polarized phase difference*. The quantities are defined in terms of the elements of the Mueller matrix as,

$$\alpha = \sqrt{\frac{\lambda_{13}^2+\lambda_{14}^2}{\lambda_{11}\lambda_{33}}}, \qquad \zeta = \tan^{-1}\frac{\lambda_{14}}{\lambda_{13}} \quad (6.2)$$

where,

$$\lambda_{11} = \frac{\mathcal{M}_{11}}{2}, \qquad \lambda_{33} = \frac{\mathcal{M}_{22}}{2} \quad (6.3)$$

$$\lambda_{13} = \frac{\mathcal{M}_{33}+\mathcal{M}_{44}}{4}, \qquad \lambda_{14} = \frac{\mathcal{M}_{34}-\mathcal{M}_{43}}{4}, \quad (6.4)$$

where $\mathcal{M}_{pq}$ are elements of the Mueller matrix. Therefore, a comprehensive comparison will examine the agreement between the model and the data with respect to these five elements.

Extensive data was collected for the two materials introduced above, Common sand and 8-12 gravel, using the experimental procedure described in Section 5.6. The Common sand was examined for fifteen different layer depths—five over an absorbing layer, and ten over a conducting surface—for incidence angles ranging from 20° to 60°. In the inversion analyses performed, generally all of the data corresponding to angles 20°, 40°, and 60° were utilized. A somewhat more limited amount of data was collected for the 8-12 Gravel: ten total layer

depths—four over a conductor and six over an absorbing layer (except at 30°, for which it was only two depths over an absorbing layer and five over a conductor)—were examined also at incidence angles ranging from 20° to 60°. In the 8-12 Gravel case however, there was some indication in the results, not predicted by the surface scattering analysis done in the previous section, that at 20° there was some surface contribution to the backscatter which was not negligible. Therefore the 8-12 Gravel is analyzed using only the data corresponding to 30°, 40°, and 60°.

6.3.1 Isotropic Approach

Rayleigh Model

The Rayleigh model derived in Section 5.5 utilized a scalar extinction, and phase matrix components $\mathcal{P}_{bs}$ and $\mathcal{P}_{bi}$ given by equations (5.84) and (5.85). As mentioned, these phase matrix components were entirely specified by just two parameters, which are themselves functions of the elements of the polarizability tensor of the arbitrary Rayleigh particles. This theoretical framework was used along with the results from the measurements in the inversion algorithm described in Section 5.7. Some selected results of this analysis are shown in Figures 6.3 and 6.4. These results are representative of the degree of success which was achieved generally in comparing the Rayleigh model to the measured data. Figure 6.3 shows the angular variation of the co- and cross-pol responses for both materials, examined over both a conductor and an absorber at the depths specified in the figures. In general, the angular variation built into the Rayleigh model does not agree with the observed behavior very well. This is most evident for the case ((c)) of a layer of Common sand over a conductor.

Figure 6.4 presents the results with respect to the phase statistics. Only the degree of correlation (α) is shown for both materials at specific layer depths over both absorber and conductor. It is clear that the Rayleigh model is inadequate for explaining the observed behavior for these materials. The lack of success of this model is not too surprising. As mentioned,

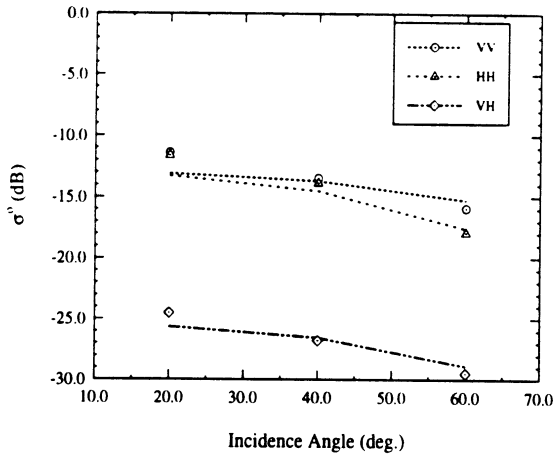

(a) Common sand, 22.9 cm absorber.

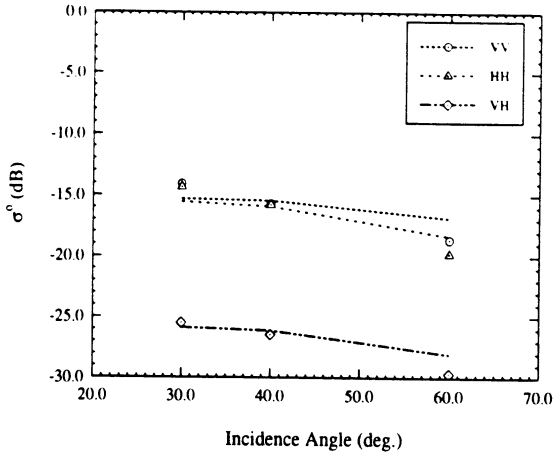

(b) 8-12 gravel, 14.3 cm over absorber.

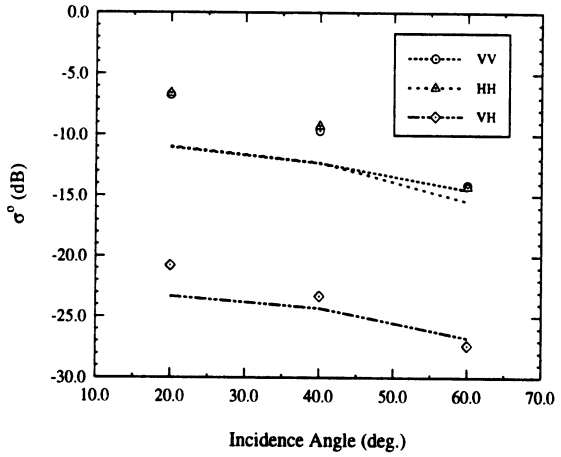

(c) Common sand, 12.4 cm over conductor.

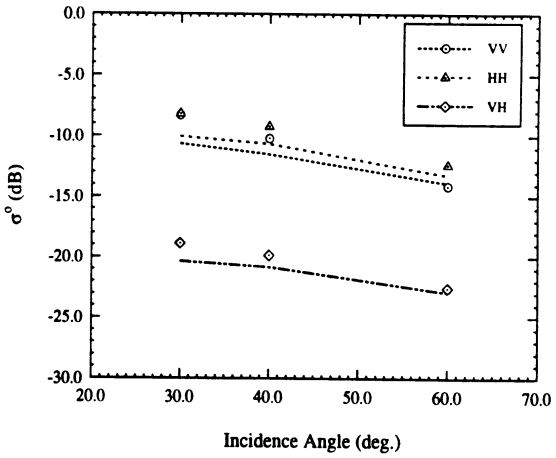

(d) 8-12 gravel, 16.5 cm over conductor.

Figure 6.3: Application of Rayleigh model to measured data. Comparison for co- and cross-polarized response, over both absorber and conductor, for both materials, common sand and 8-12 gravel.

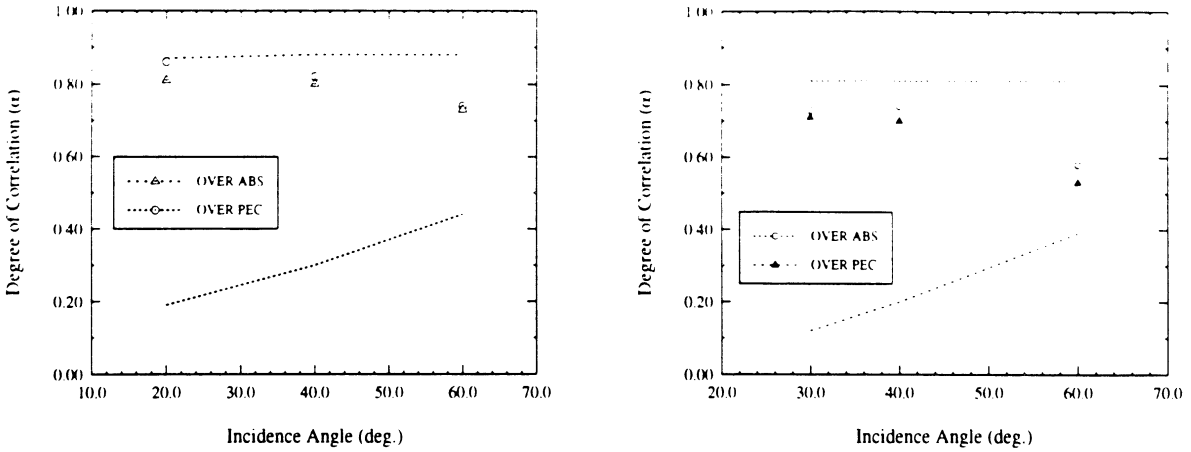

(a) Common sand (b) 8-12 gravel

Figure 6.4: Application of Rayleigh model to measured data. Comparison for degree of correlation (α). For **Common sand** (a), layers over absorber and conductor are 12.4 and 22.9 cm respectively; for **8-12 gravel** (b), 14.3 and 16.5 cm.

the individual particles of either medium are for the most part not Rayleigh particles for the wavelength being used. When consideration is made of some "effective" aggregate particle, which might comprise many individual particles, the hypothesis becomes even more doubtful. Still it is possible that such a model might be valid for smaller particles and where the volume fraction is not quite so high.

The angular variation in the Rayleigh model is controlled by two factors: (1) the Fresnel transmissivity of the surface, and (2) the explicit dependence shown in equation (5.85). It is possible that a general isotropic model could work if the explicit constraints of the Rayleigh model are relaxed.

General Isotropic Model

For the general isotropic model, the quantities of interest take the following forms:

- The diagonal elements of the exinction matrix are required to be identical. This is easily understood from the very definition of isotropic media. The propagation characteristics of the medium are insensitive to the polarization of the intensity. Thus the

extinction for vertical polarization must be the same as for horizontal. For the non-diagonal elements of the extinction matrix, which for general non-spherical particles is given in equation (2.33), we assume the cross-coupling between **v** and **h** polarizations is zero for forward scattering, making these off-diagonal elements zero. Thus, for the general isotropic model we are considering, the extinction κ_e becomes a scalar, κ_e, as in the Rayleigh model.

- The form of $\mathcal{P}_{bs}$ also resembles that of the Rayleigh model. The isotropic constraint requires that $< S_{vv}S_{vv}^* >=< S_{hh}S_{hh}^* >$. Reciprocity requires that $S_{vh} = S_{hv}$ (in the Backscattering Alignment (BSA); in the Forward Scattering Alignment, $S_{vh} = -S_{hv}$). From arguments of azimuthal symmetry and experimental evidence, the co-pol terms and the cross-pol terms have been found to be statistically uncorrelated; thus all terms of the form $< S_{pp}S_{pq}^* >$ are zero. The resulting form of the matrix, which is independent of incidence angle, is:

$$\mathcal{P}_{bs} = \begin{bmatrix} P_2 & P_3 & 0 & 0 \\ P_3 & P_2 & 0 & 0 \\ 0 & 0 & P_4 - P_3 & P_5 \\ 0 & 0 & -P_5 & P_4 + P_3 \end{bmatrix} \tag{6.5}$$

- For the $\mathcal{P}_{bi}$ matrix, there is less that can be specified in advance. Reciprocity does not require the S_{vh} and S_{hv} terms to be identical, and the like- and cross-pol terms are not necessarily uncorrelated. For the latter point, we will borrow from the findings of the Rayleigh analysis, which showed these covariance terms to be zero, but relieve generally the other constraints which that analysis placed upon the elements of this matrix. In particular, we will allow the matrix as a whole to be a function of the incidence

angle as specified by μ_o ($\mu_o = \cos\theta_o$). The structure is,

$$\boldsymbol{\mathcal{P}}_{bi} = \begin{bmatrix} P_6 & P_7 & 0 & 0 \\ P_8 & P_9 & 0 & 0 \\ 0 & 0 & P_{10} & P_{11} \\ 0 & 0 & P_{12} & P_{13} \end{bmatrix} \tag{6.6}$$

The resulting model is identical to that given in equation (5.67), using $\boldsymbol{\mathcal{P}}_{bs}$ and $\boldsymbol{\mathcal{P}}_{bi}$ as given above. There are thirteen parameters to be specified for a complete polarimetric description for a single angle. Of these, the extinction κ_e and the matrix $\boldsymbol{\mathcal{P}}_{bs}$ will be common to all angles. A separate bistatic matrix $\boldsymbol{\mathcal{P}}_{bi}$ must be determined for each angle.

Thirteen parameters is a considerable space to explore for an algorithm for non-linear optimization. Given the task of optimizing all thirteen parameters at once the algorithm will generally not produce a very satisfactory result, and will tend to arrive at different solutions depending on the initial guess. Fortunately, it is not necessary to optimize all parameters simultaneously. Two options exist for a much more limited optimization process.

For the first, it is recognized that, if a "quadrant" is defined by a 2×2 submatrix, then proceeding clockwise from the top left of the 4×4 matrices in this formulation, the first and third quadrants are decoupled from one another, since the second and fourth quadrants are identically zero. The zero status of these latter two quadrants holds for all of the matrices involved in the first-order solution, including, from (5.11) and (5.12), the transmissivity and reflectivity matrices. Thus, it is possible to optimize initially only the seven parameters affecting the co- and cross-pol responses. After these have been found, the remaining six may be found, using the value for κ_e obtained in the initial process. Additional iterations may be performed to improve the overall result. In general, it is found that, due to a model which is only an approximation and data which contains errors, no absolute convergence is observed from an iterative process, and degradation of the perceived "goodness" of the solution occurs with many iterations.

An alternate (second) option is to initially optimize only the co-pol responses, treating them as scalars since they are generally at least 10 dB greater than the cross-pol terms. In this case, it is only necessary to treat four parameters, and then use these to "seed" the solution space so that the remaining nine parameters may be found. As in option 1, additional iterations may be performed to improve the appearance of the overall solution. A flowchart illustrating this two-part inversion process is shown in Figure 6.5. The figure expressly refers to the submatrix approach of option 1, with the submatrices designated as "Q_1", "Q_2", etc. For the scalar optimization process (option 2 above), the sequence is essentially unchanged.

A complete comparison of the isotropic modeling approach with the measured data is shown in Figures 6.6–6.8 for the 8-12 Gravel, for incidence angles 30°, 40°, and 60°, respectively, and Figures 6.9–6.11 for the Common sand for incidence angles 20°, 40°, and 60°, respectively. Each figure constitutes a comprehensive comparison of the five aforementioned independent elements of the measured Mueller matrix with the model predictions for the angle specified.

The agreement with the 8-12 Gravel is seen to be generally very good. There is some disagreement for the case of the co-pol response over an absorber layer, at all three angles. The response is somewhat underpredicted (by 1-2 dB) at 30°, and over predicted by about this amount at 60°. This is an interesting case to examine, since the bistatic component of the phase function, $\mathcal{P}_{bi}$, which can be individually tailored for each incidence angle in the inversion process, is not involved. Since the backscatter component, $\mathcal{P}_{bs}$, is a constant quantity, the angular variation is governed solely by the Fresnel transmissivity of the surface. Angular behavior which is in agreement with this Fresnel variation, for a "halfspace", which our layers over absorber approximate, is a necessary requirement for scattering which is truly first-order and isotropic.

The behavior of the phase statistics of the measurements appears to be a very simple function of all of the parameters varied (angle, depth, underlying "halfspace"), which is

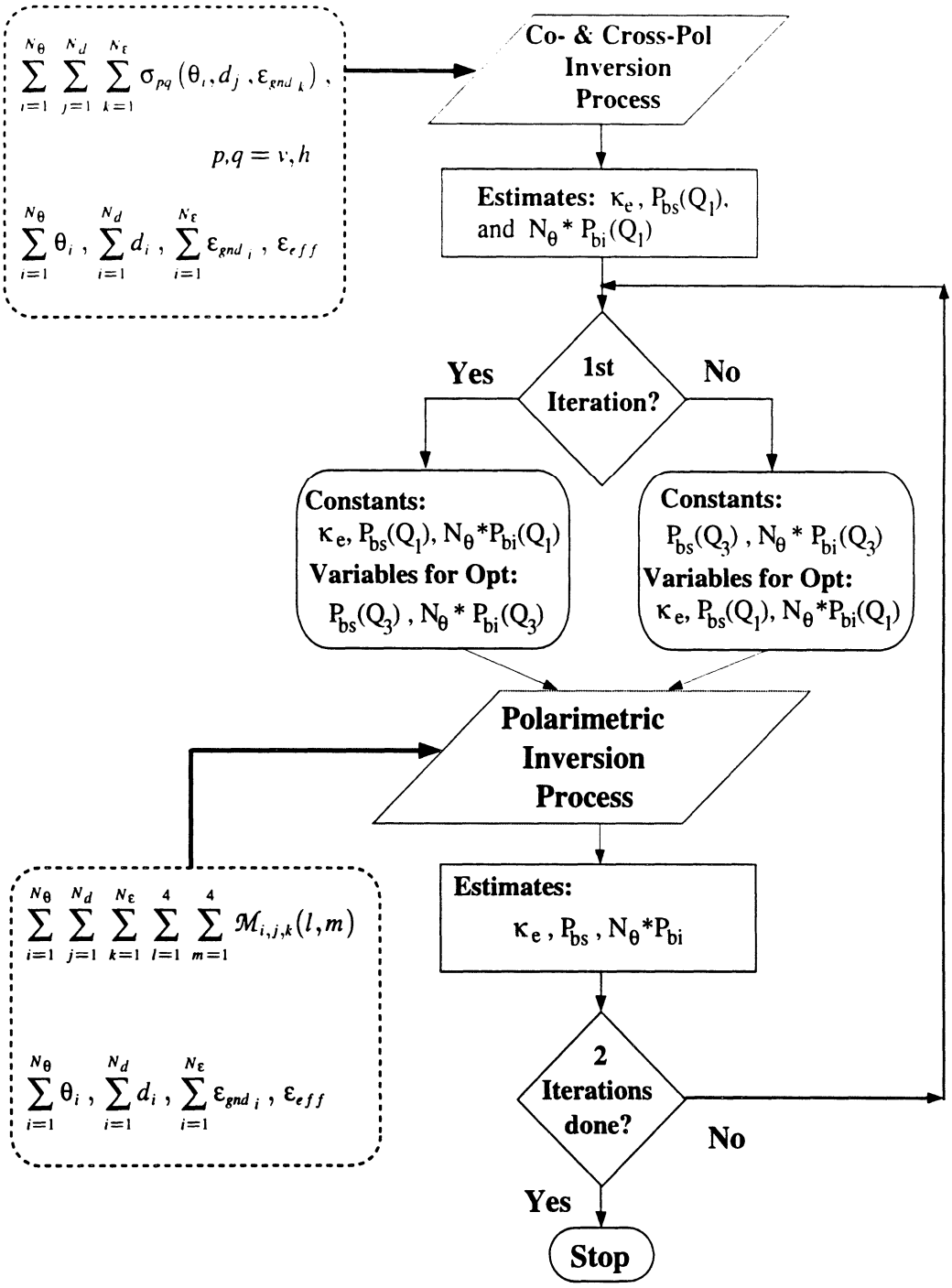

Figure 6.5: Iterative, two-part, numerical inversion process for the retrieval of first-order RT parameters from measured polarimetric data.

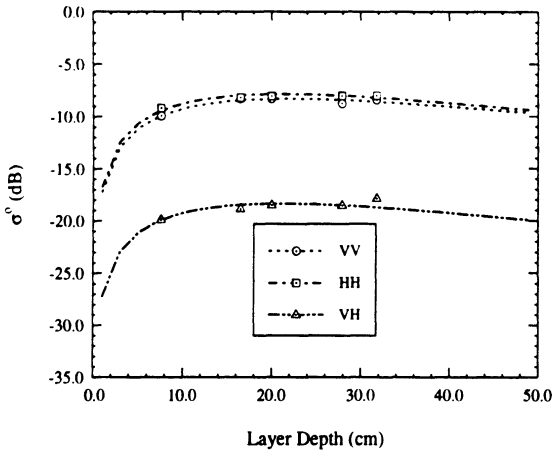

(a) Co- and Cross over conductor.

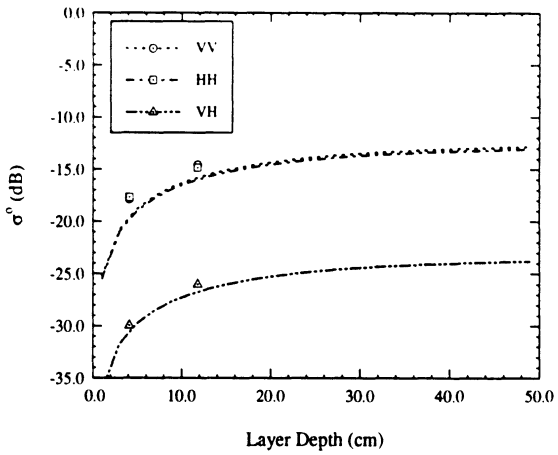

(b) Co- and Cross over absorber.

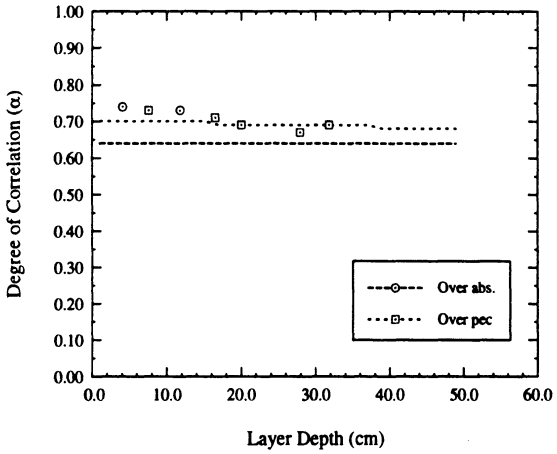

(c) Degree of Correlation.

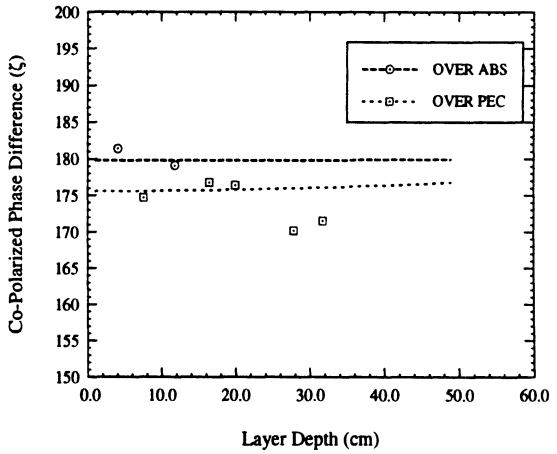

(d) Co-Polarized Phase Difference.

Figure 6.6: Results of application of Isotropic RT model to measured data: 8-12 Gravel, 30° incidence.

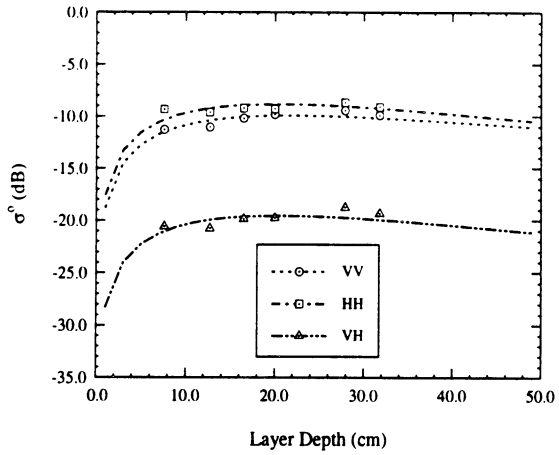

(a) Co- and Cross over conductor.

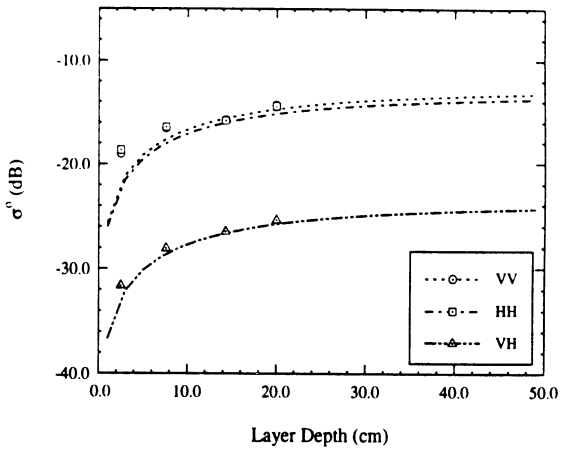

(b) Co- and Cross over absorber.

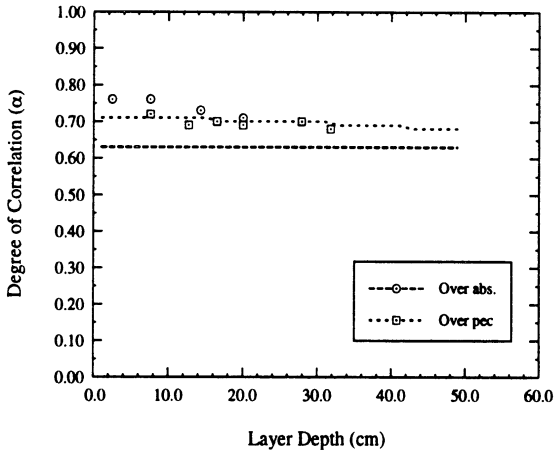

(c) Degree of Correlation.

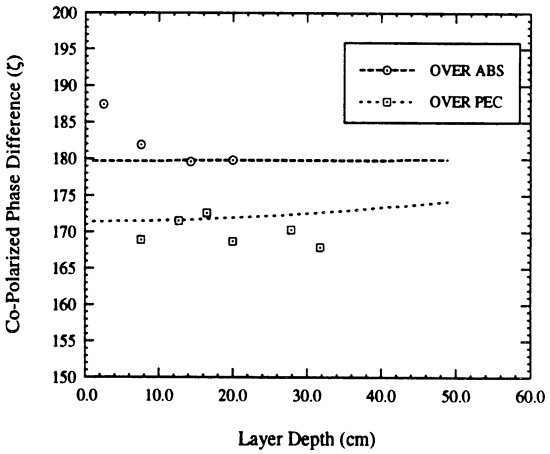

(d) Co-Polarized Phase Difference.

Figure 6.7: Results of application of Isotropic RT model to measured data: 8-12 Gravel, 40° incidence.

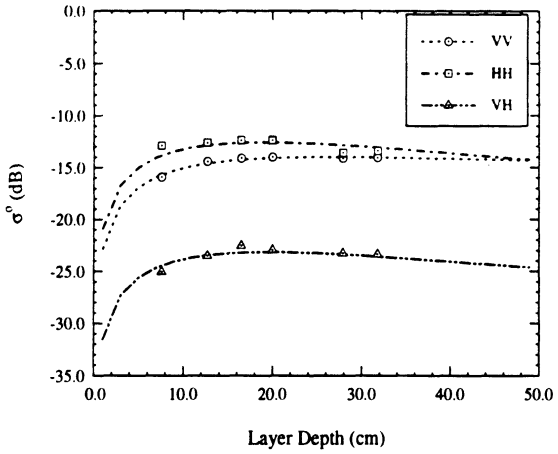

(a) Co- and Cross over conductor.

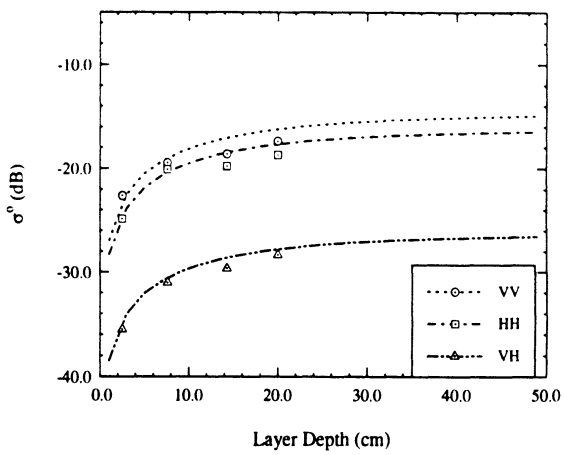

(b) Co- and Cross over absorber.

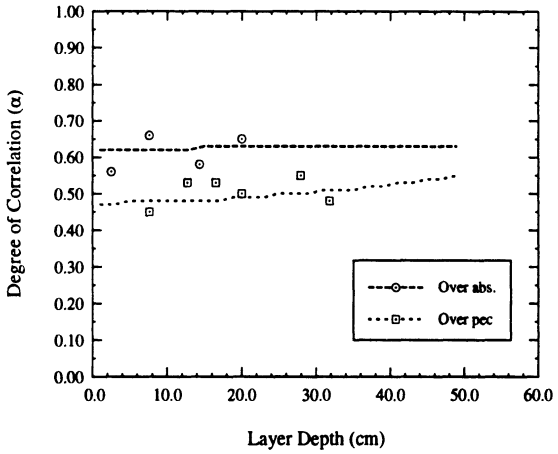

(c) Degree of Correlation.

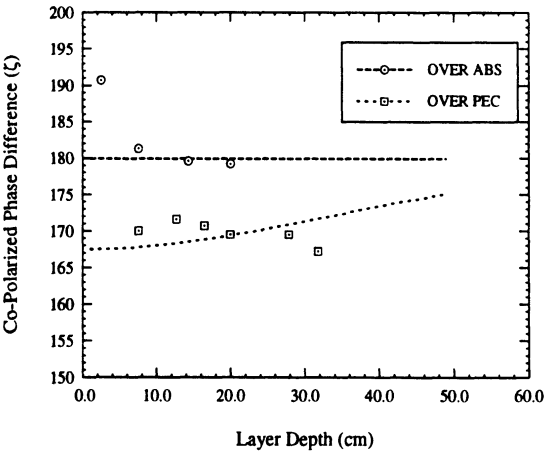

(d) Co-Polarized Phase Difference.

Figure 6.8: Results of application of Isotropic RT model to measured data: 8-12 Gravel, 60° incidence.

modeled fairly well. The degree of correlation is underpredicted ($\approx$0.65 vs. $\approx$0.75) at both 30° and 40°, and the model shows the wrong trend with respect to the character of the underlying "halfspace" (decreases with the case of the absorber layer whereas the measurements show α increasing.) This parameter is modelled well at 60°. Except for the shallowest layer depth over absorber, the co-polarized phase difference, ζ, is modeled quite well at all three angles.

For the Common sand (Figures 6.9–6.11), the agreement is somewhat worse. As in the case of the 8-12 Gravel, the co-pol response over an absorber layer shows a discrepancy of typically 3-dB for the 20° case; nor is the cross-pol response for this case (Fig. 6.9(b)) especially well characterized. The situation is somewhat improved at 40°, and fits well by 60°. This means that the angular variation for this scenario, where only the direct backscatter mechanism is contributing, is at least 3-dB greater for the measured data than what is provided by the Fresnel transmissivity of the surface.

For the (a) case, that is, co- and cross-pols over a conductor, there is observed, starting with the 40° case but becoming especially prominant by 60°, a failure to accurately model the varying behavior of the two co-polarized channels. In the 60° case (Figure 6.11(a)), the H-pol is significantly underpredicted for depths below 6 cm, and then over-predicted above 20 cm. The V-pol is also underpredicted by about 1.5 dB above 25 cm.

The phase statistics for the measured data exhibit a much noisier character than was observed for the 8-12 Gravel. The co-polarized phase difference (ζ) in particular shows a great deal of variation. The model does not follow this variation with any great accuracy though it does in general follow, for shallow depths, the trend of decreasing value with increasing incidence angle, from approximately 180° at 20° to approximately 160° at 60°. The trend of the model to approach the absorber value for deep layers, a logical development, is not clearly indicated by the data.

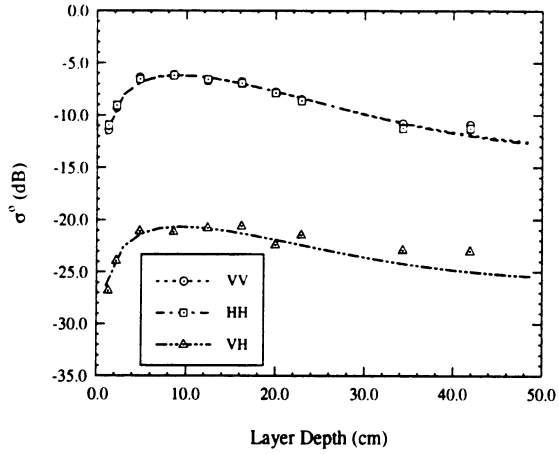

(a) Co- and Cross over conductor.

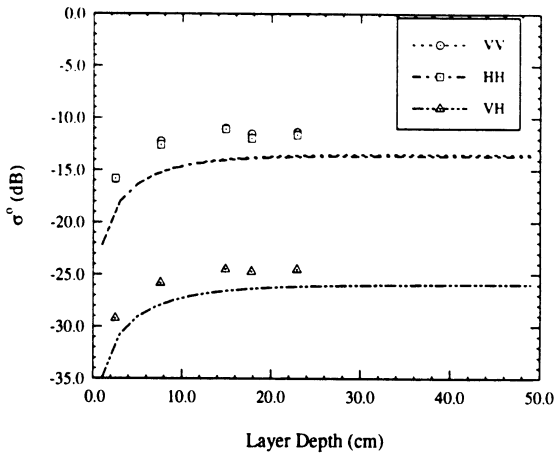

(b) Co- and Cross over absorber.

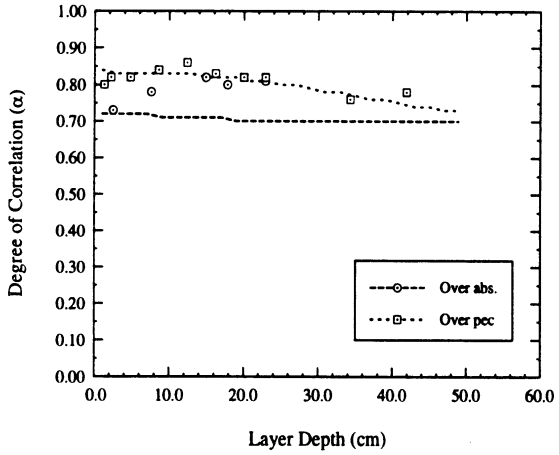

(c) Degree of Correlation.

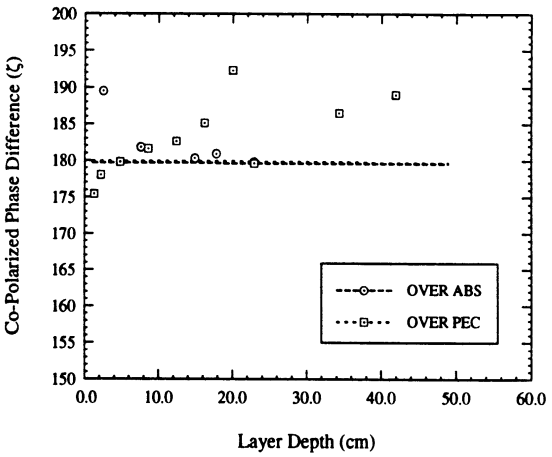

(d) Co-Polarized Phase Difference.

Figure 6.9: Results of application of Isotropic RT model to measured data: Common sand, 20° incidence.

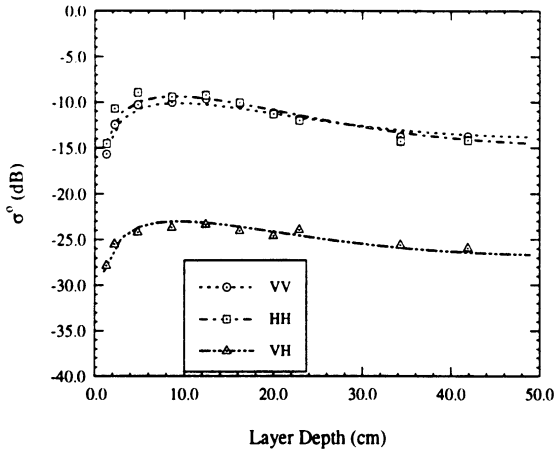

(a) Co- and Cross over conductor.

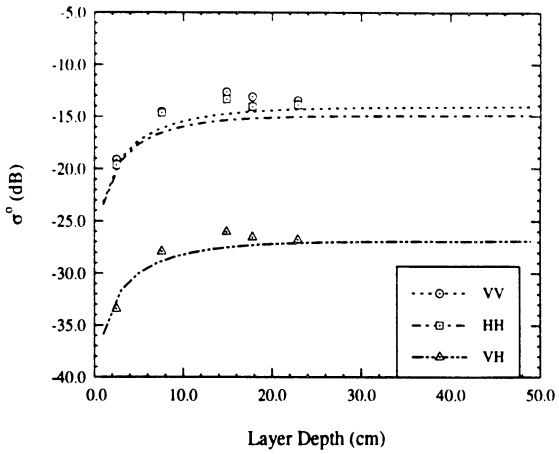

(b) Co- and Cross over absorber.

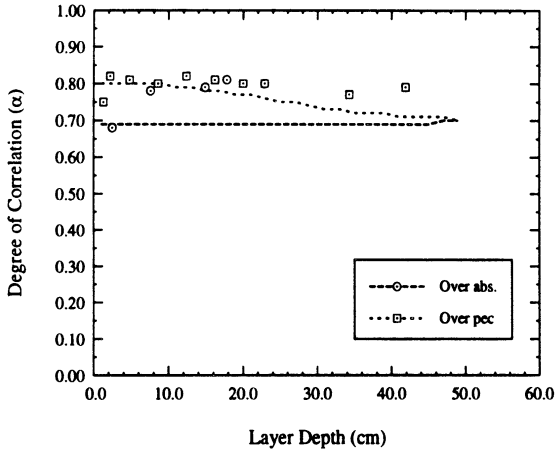

(c) Degree of Correlation.

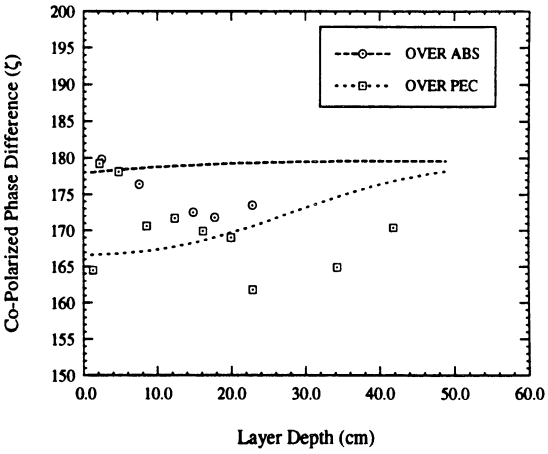

(d) Co-Polarized Phase Difference.

Figure 6.10: Results of application of Isotropic RT model to measured data: Common sand, 40° incidence.

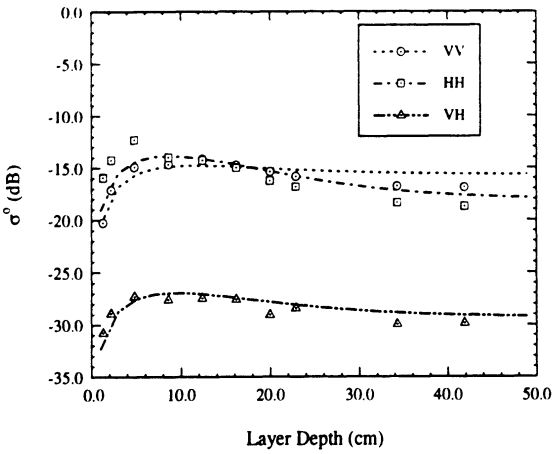

(a) Co- and Cross over conductor.

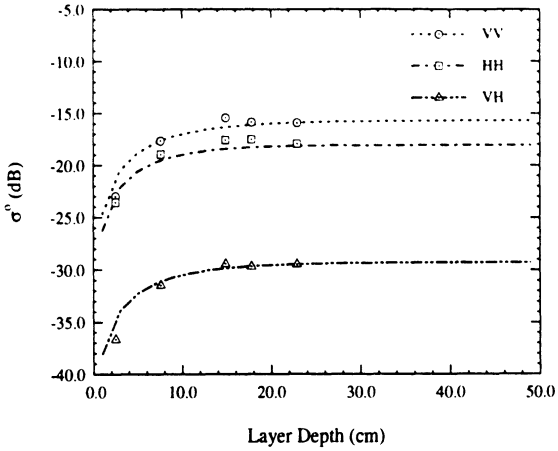

(b) Co- and Cross over absorber.

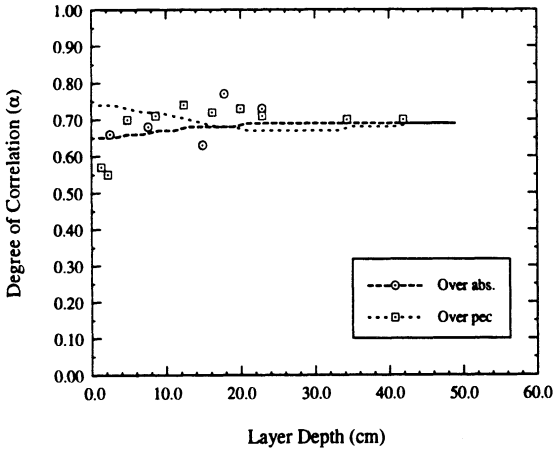

(c) Degree of Correlation.

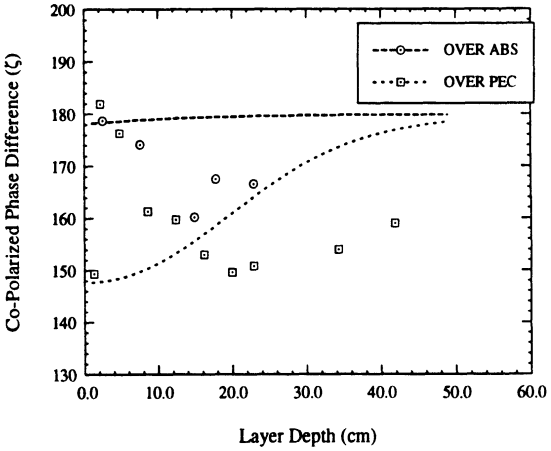

(d) Co-Polarized Phase Difference.

Figure 6.11: Results of application of Isotropic RT model to measured data: Common sand, 60° incidence.

RT Model	κ_e	$\mathcal{P}_{bs}$	$\mathcal{P}_{bi}$	Total
Isotropic	1	4	8/θ	5 + 8*N_θ
Non-Isotropic	2/θ	5/θ	8/θ	15*N_θ

Table 6.3: Number of Parameters in Isotropic and Non-Isotropic Hybrid RT Models

6.3.2 Non-isotropic Approach

The lack of perfect agreement observed between the general isotropic first-order RT hybrid model and the measured data can be addressed through allowing additional functionality in the RT formulation. Though discrepancies were much smaller in the case of the 8-12 Gravel, it is clear that, for the Common sand case, agreement for the case of a layer over an absorber can only be achieved if some variation with angle is allowed for the backscatter component of the phase matrix, $\mathcal{P}_{bs}$, which, as mentioned, is the only quantity contributing in this case. Additionally, differences were apparent, again for the Common sand case, between the two co-polarized channels, for which no mathematical description can be furnished by the isotropic model.

In Section 5.4 a non-isotropic model was proposed which would tend to address both of these apparent difficiencies of the isotropic model. Specifically, a matrix extinction, κ_e, is called for, though we continue the assumption, employed for the isotropic model, of zero coupling between the two orthogonal polarizations in the forward scattering direction, making the off-diagonal elements of the κ_e zero.

Two other important changes relative to the isotropic case are that, for the $\mathcal{P}_{bs}$ matrix, it is no longer required that $|S_{vv}|^2 = |S_{hh}|^2$, and whereas in the isotropic case, the matrix $\mathcal{P}_{bs}$ was independent of angle while the bistatic component $\mathcal{P}_{bi}$ was determined separately for each angle, in the non-isotropic case both of these components are allowed to vary with angle and therefore must be separately determined for each angle.

Table 6.3 summarizes the total parameters required for characterization of materials based on the isotropic and non-isotropic models respectively.

The agreement obtained with the non-isotropic model is shown in Figures 6.12–6.14

for the 8-12 Gravel and Figures 6.15–6.17 for Common sand. The format for comparison is identical to that used with respect to the isotropic results. For the 8-12 Gravel, the small

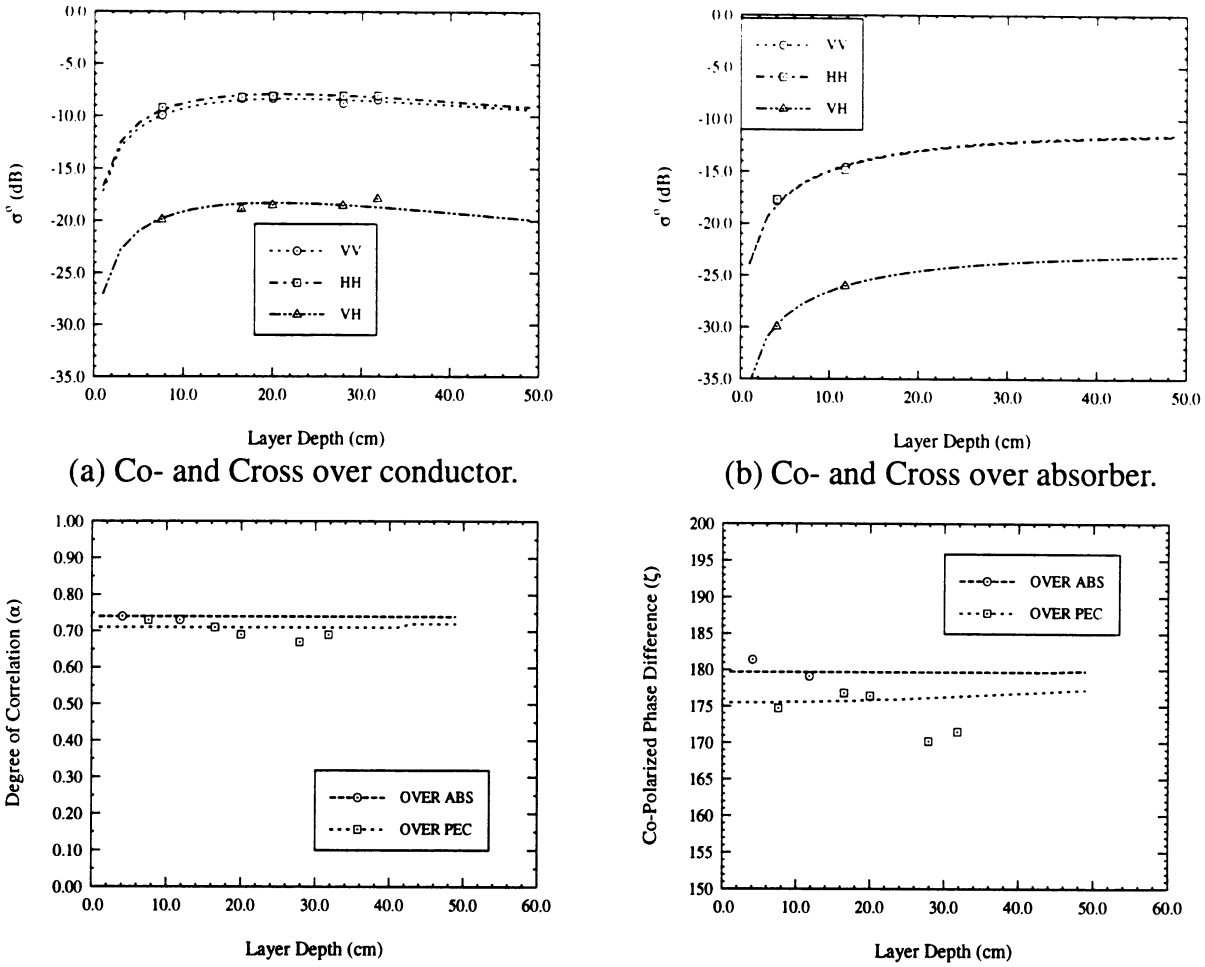

(a) Co- and Cross over conductor.

(b) Co- and Cross over absorber.

(c) Degree of Correlation.

(d) Co-Polarized Phase Difference.

Figure 6.12: Results of application of Non-Isotropic RT model to measured data: 8-12 Gravel, 30° incidence.

discrepancies observed for the isotropic case have been corrected. Specifically, the angular variation of the co-pol channels, in the case of a layer over absorber ((b) in the figures) now shows excellent agreement, and the differences in the prediction of the degree of correlation α ((c) in the figures) has been corrected, so that the value for the layer-over-absorber case is larger than that for the layer-over-conductor case and matches the data much closer. The remaining features are mainly unchanged from the generally good quality showed for the isotropic case.

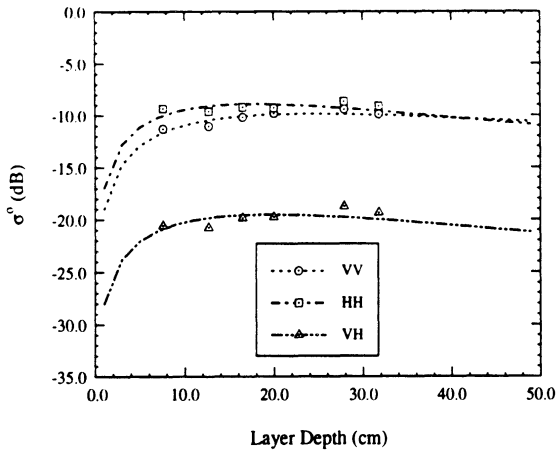

(a) Co- and Cross over conductor.

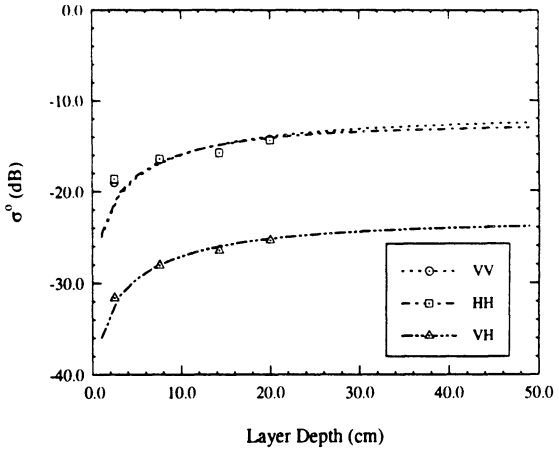

(b) Co- and Cross over absorber.

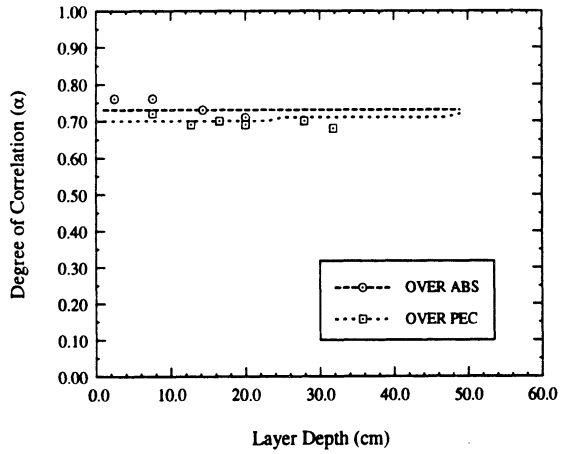

(c) Degree of Correlation.

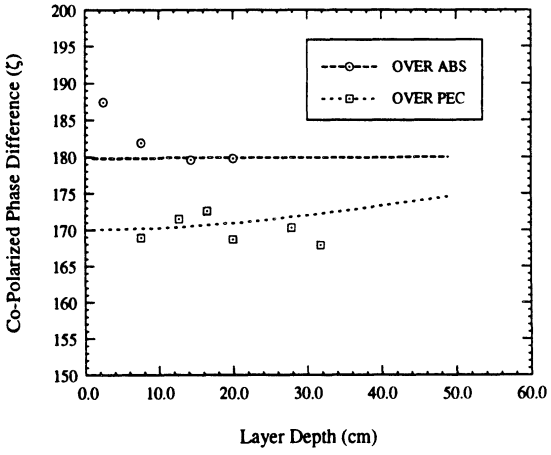

(d) Co-Polarized Phase Difference.

Figure 6.13: Results of application of Non-Isotropic RT model to measured data: 8-12 Gravel, 40° incidence.

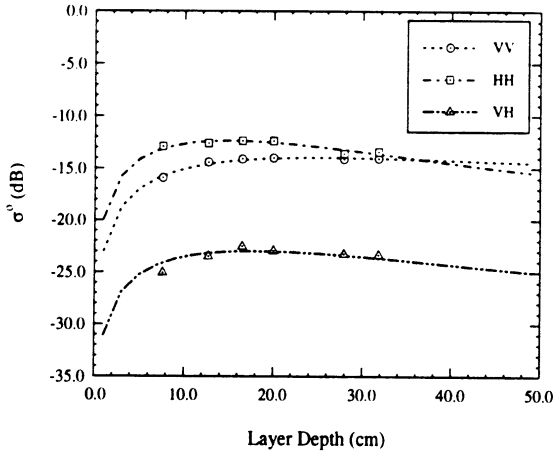

(a) Co- and Cross over conductor.

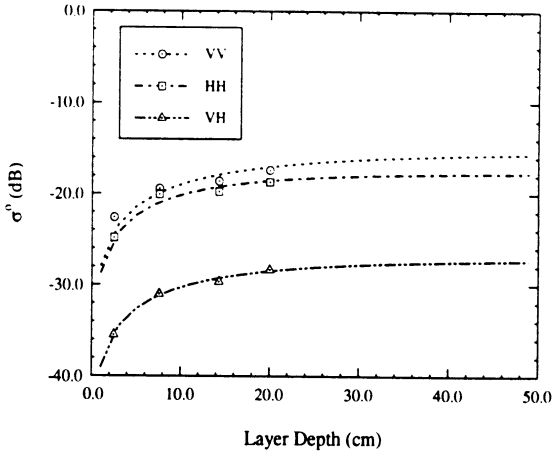

(b) Co- and Cross over absorber.

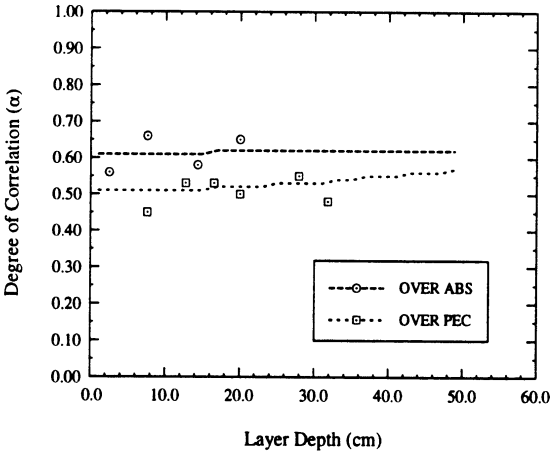

(c) Degree of Correlation.

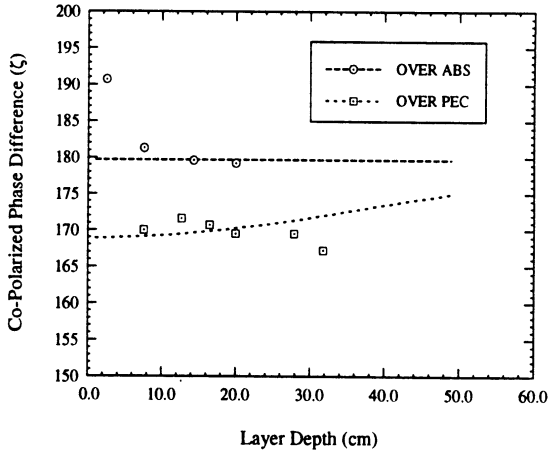

(d) Co-Polarized Phase Difference.

Figure 6.14: Results of application of Non-Isotropic RT model to measured data: 8-12 Gravel, 60° incidence.

For the Common sand, the major discrepancy observed in the isotropic case of insufficient angular variation produced by the model, for the "over absorber" case is mainly corrected ((b) in Figs. 6.15–6.17 *versus* Figs. 6.9–6.11), although the agreement for the 60° case is slightly degraded relative to the isotropic case. This is apparently due the simul-

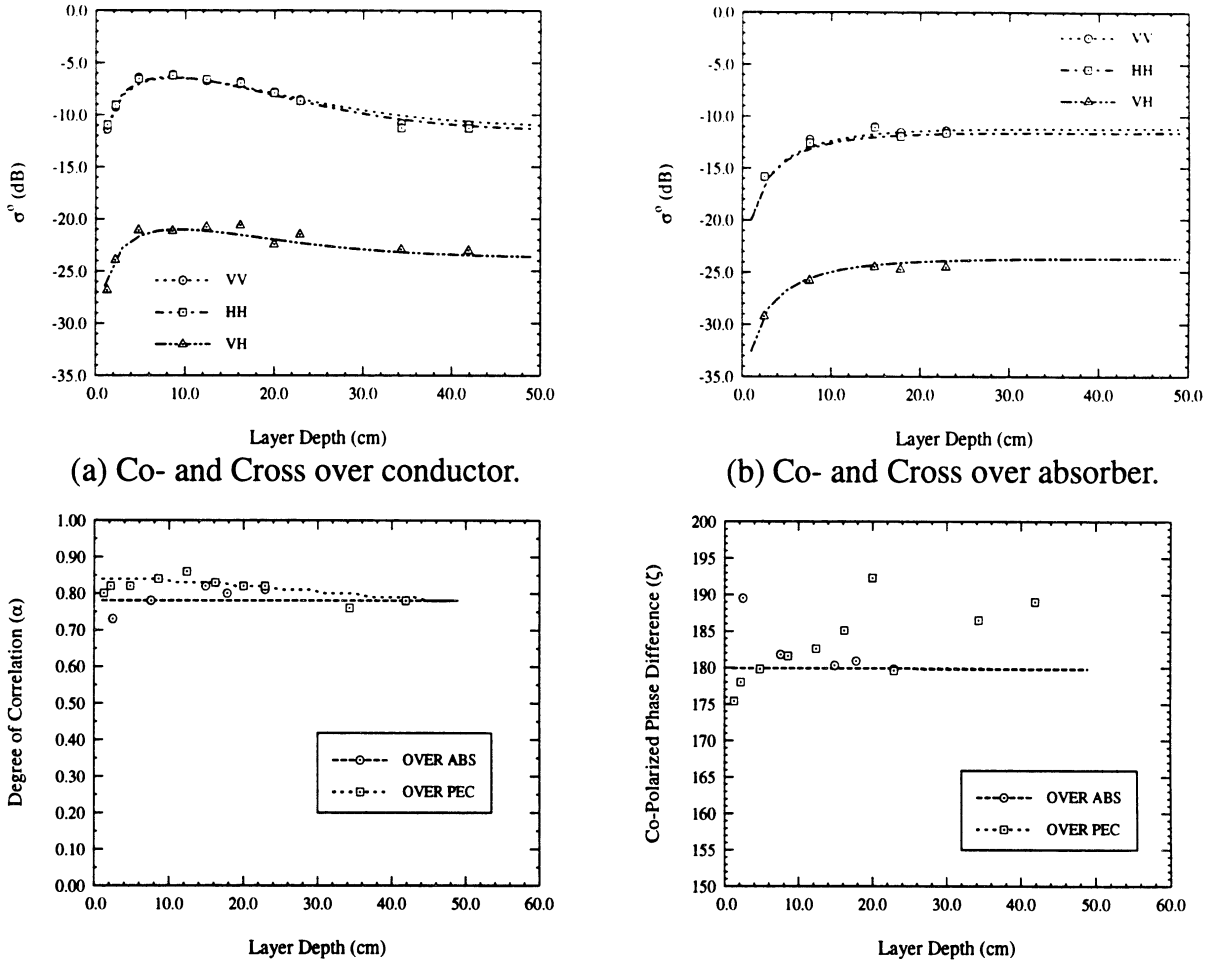

(a) Co- and Cross over conductor.

(b) Co- and Cross over absorber.

(c) Degree of Correlation.

(d) Co-Polarized Phase Difference.

Figure 6.15: Results of application of Non-Isotropic RT model to measured data: Common sand, 20° incidence.

taneous requirement for the model to comprehend the polarization differences in the "over conductor" case ((a) in Figure 6.17). The agreement in this case is seen to be very markedly improved relative to the isotropic attempt (Figure 6.11(a)). With respect to the phase statistics, considerably better agreement is obtained for both α and ζ, for the "over absorber" case. The "over conductor" case is essentially unchanged from the generally good agree-

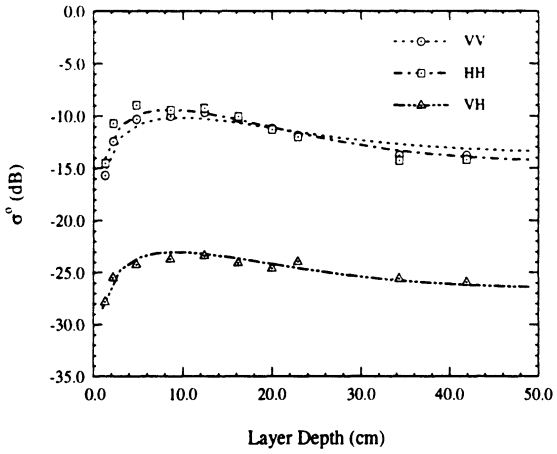

(a) Co- and Cross over conductor.

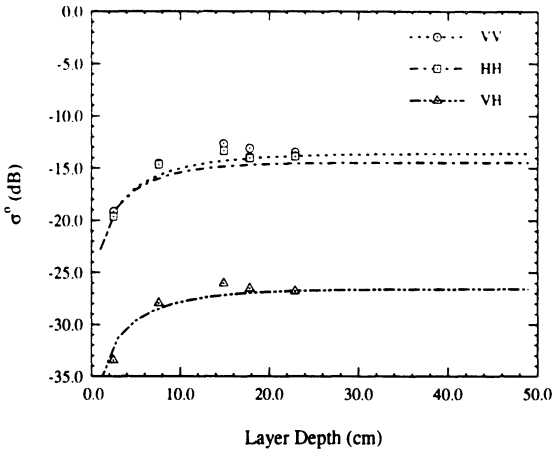

(b) Co- and Cross over absorber.

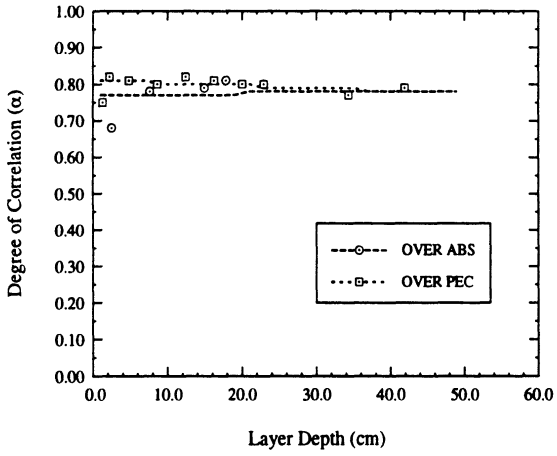

(c) Degree of Correlation.

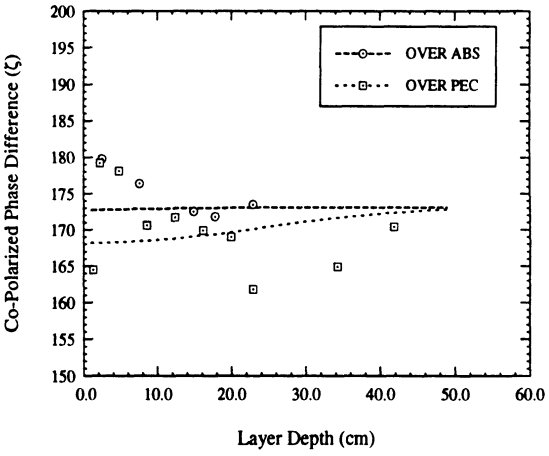

(d) Co-Polarized Phase Difference.

Figure 6.16: Results of application of Non-Isotropic RT model to measured data: Common sand, 40° incidence.

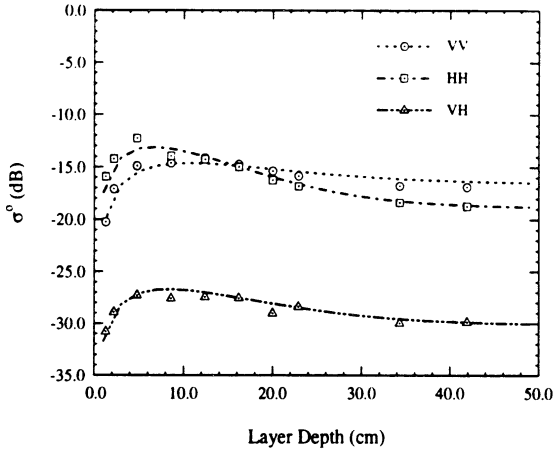

(a) Co- and Cross over conductor.

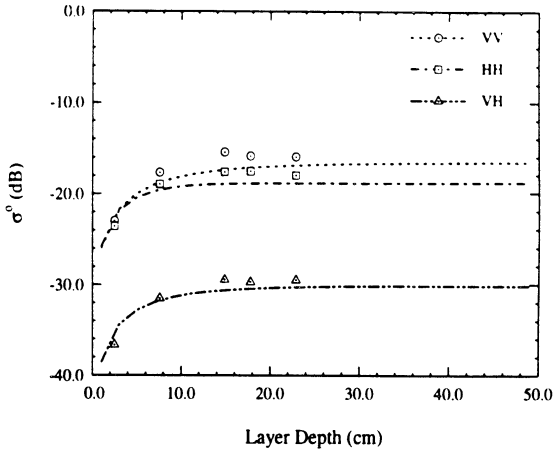

(b) Co- and Cross over absorber.

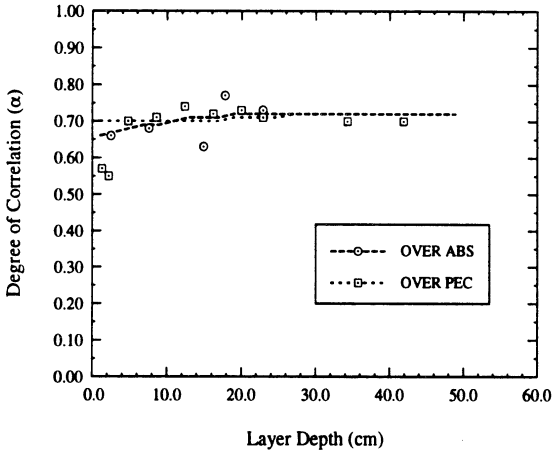

(c) Degree of Correlation.

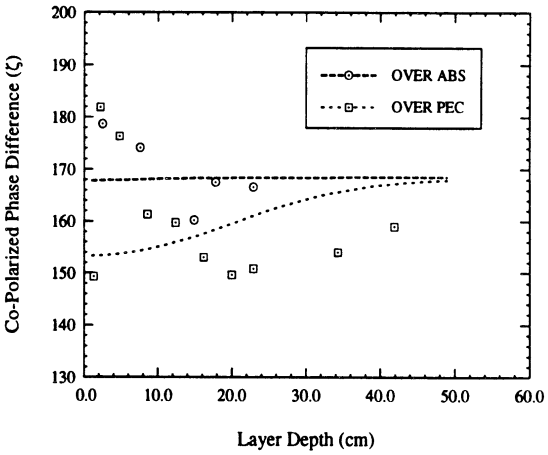

(d) Co-Polarized Phase Difference.

Figure 6.17: Results of application of Non-Isotropic RT model to measured data: Common sand, 60° incidence.

ment showed in the isotropic case for both of these parameters.

As mentioned, the improvements afforded by the non-isotropic model come from allowing polarization difference in both the extinction, κ_e, and the backscatter component of the phase function, $\mathcal{P}_{bs}$, and allowing these to be a function of angle. In Figures 6.18 and 6.19 the "distortions" of these parameters relative to the isotropic case are shown. It is seen

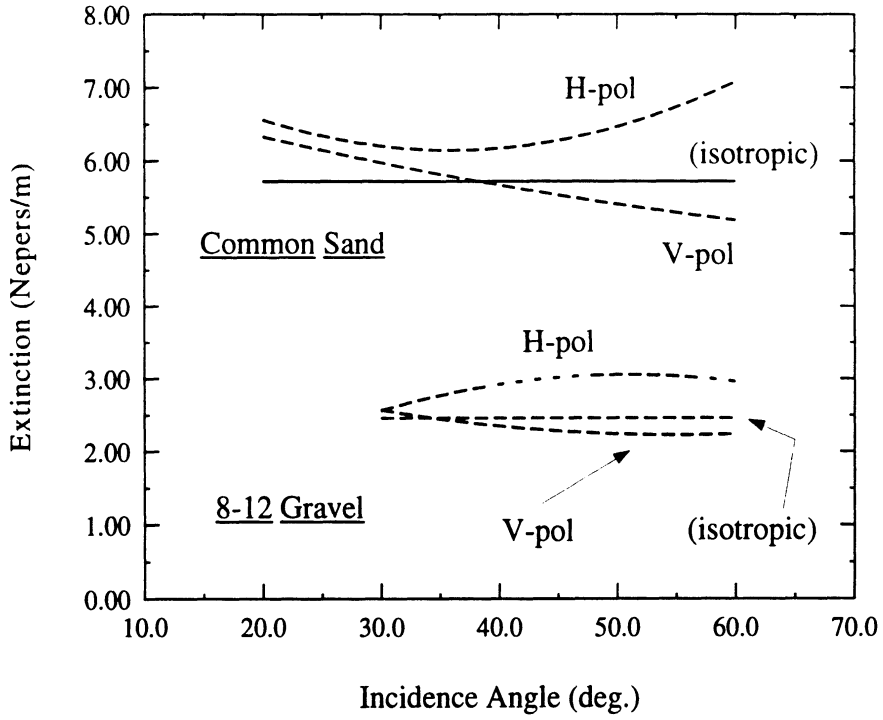

Figure 6.18: Variation with incidence angle of estimates of extinction as obtained through *non-isotropic* RT modeling. Results shown for both Common sand and 8-12 Gravel. Shown for reference are the corresponding values found from an *isotropic* RT analysis of the materials.

that for the Common sand in particular, very significant deviations from the isotropic values are required to provide agreement with the measurements. For the 8-12 Gravel, the departures from the isotropic case are much less severe, as expected given the generally very good agreement obtained applying the isotropic model to that material.

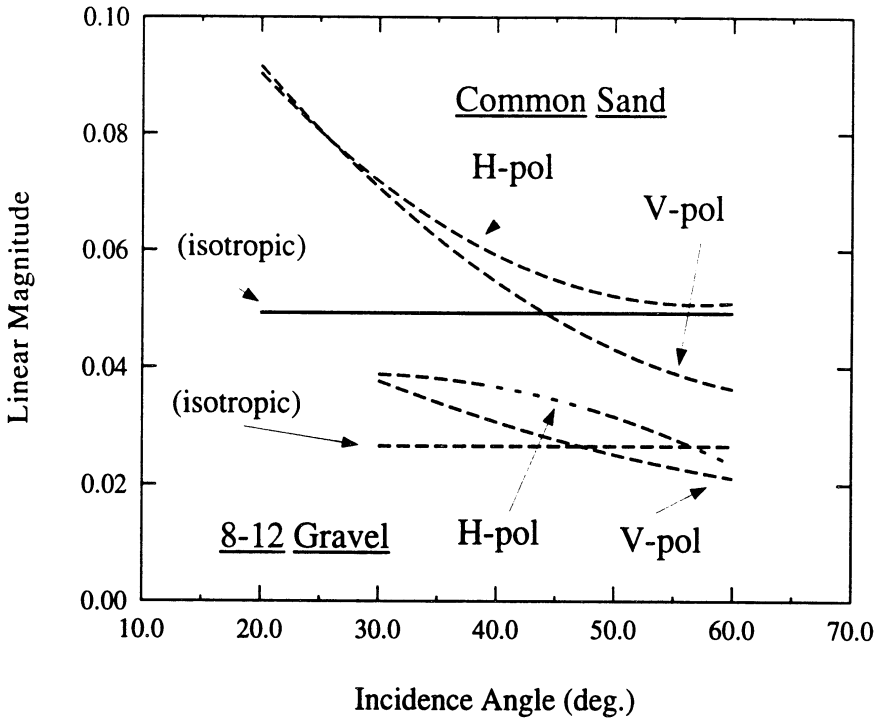

Figure 6.19: Variation with incidence angle of estimates of volume backscattering coefficient as obtained through *non-isotropic* RT modeling. Results shown for both Common sand and 8-12 Gravel. Shown for reference are the corresponding values found from an *isotropic* RT analysis of the materials.

6.4 Experimental Efficiency

One implication of the validity of the *isotropic* hybrid first-order RT model is that a material can be characterized with a relatively few number of experiments. The scalar extinction and backscatter component of the phase matrix $\mathcal{P}_{bs}$ are independent of angle. Furthermore, if these two quantities are known, then it may be a very simple task to determine the bistatic component $\mathcal{P}_{bi}$, provided a target is observed where both components have appreciable contributions. In this case the elements of $\mathcal{P}_{bi}$ must be the complement to the $\mathcal{P}_{bs}$ contribution required to make up the entire observed polarimetric response.

This concept can be illustrated for the 8-12 Gravel, which, as seen, appears to exhibit scattering behavior very comparable to that predicted by the isotropic RT model. Figures 6.20–6.22 show the results of an analysis in which the quantities κ_e and $\mathcal{P}_{bs}$ are obtained using only the measurements made at 40°. Of course, the component $\mathcal{P}_{bi}(40°)$ is obtained as well in this process. The quantities $\mathcal{P}_{bi}(30°)$ and $\mathcal{P}_{bi}(60°)$ are then obtained using polarimetric measurements made for only a single case at each of those angles. In this analysis, that case was a 16.5 cm layer over a conductor.

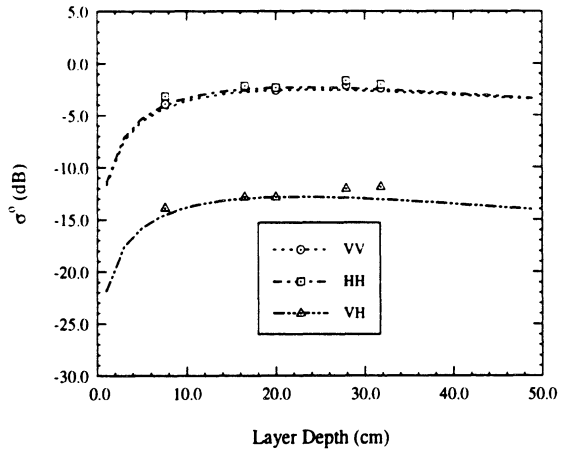

(a) Co- and Cross over conductor.

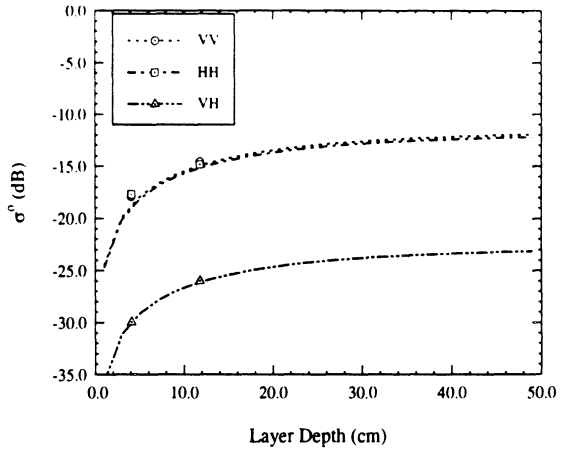

(b) Co- and Cross over absorber.

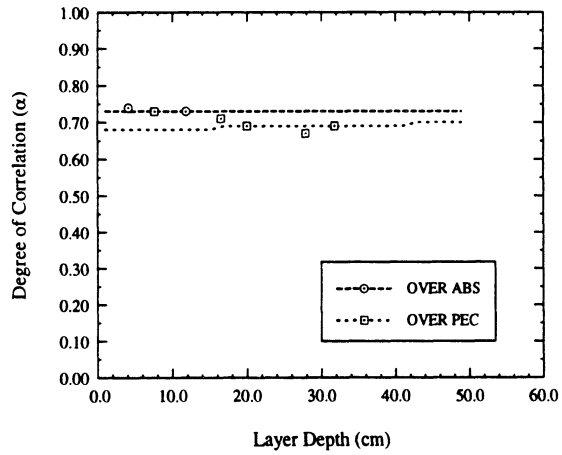

(c) Degree of Correlation.

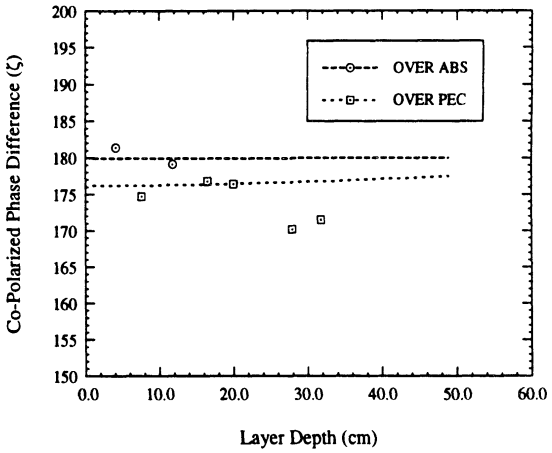

(d) Co-Polarized Phase Difference.

Figure 6.20: 8-12 Gravel, 30° incidence: Predictions generated from an Isotropic model based on measured data at 40°, except for *one* polarimetric measurement of a layer (16.5 cm) over a conductor at 30° and 60°.

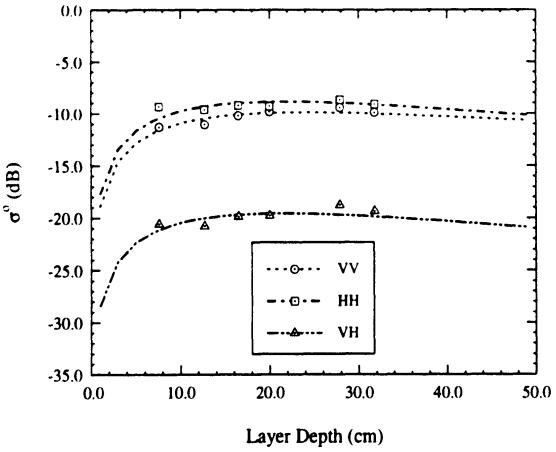

(a) Co- and Cross over conductor.

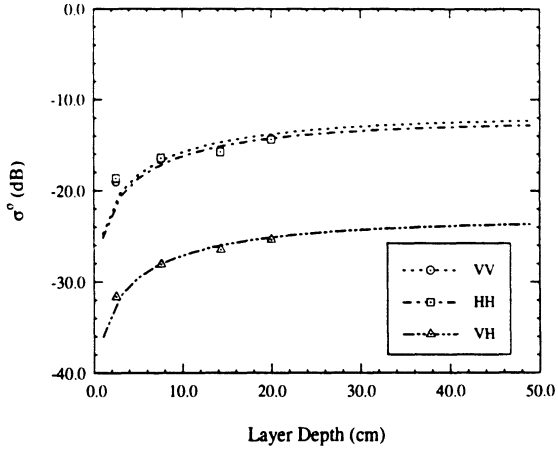

(b) Co- and Cross over absorber.

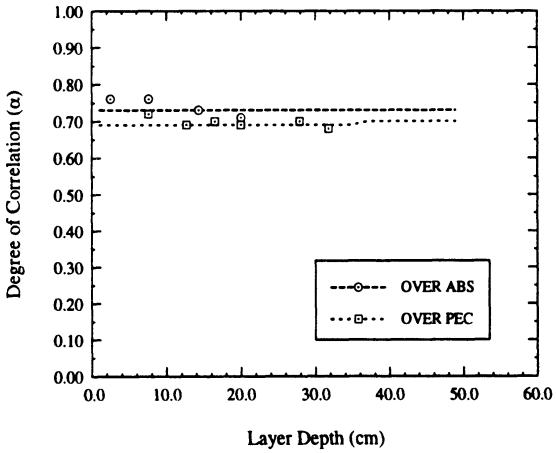

(c) Degree of Correlation.

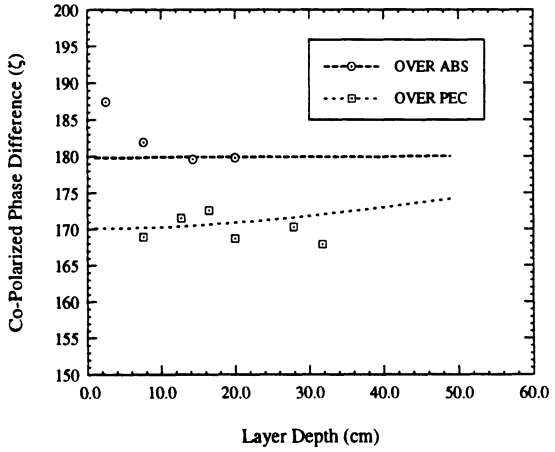

(d) Co-Polarized Phase Difference.

Figure 6.21: 8-12 Gravel, 40° incidence: Predictions generated from an Isotropic model based on measured data at 40°, except for *one* polarimetric measurement of a layer (16.5 cm) over a conductor at 30° and 60°.

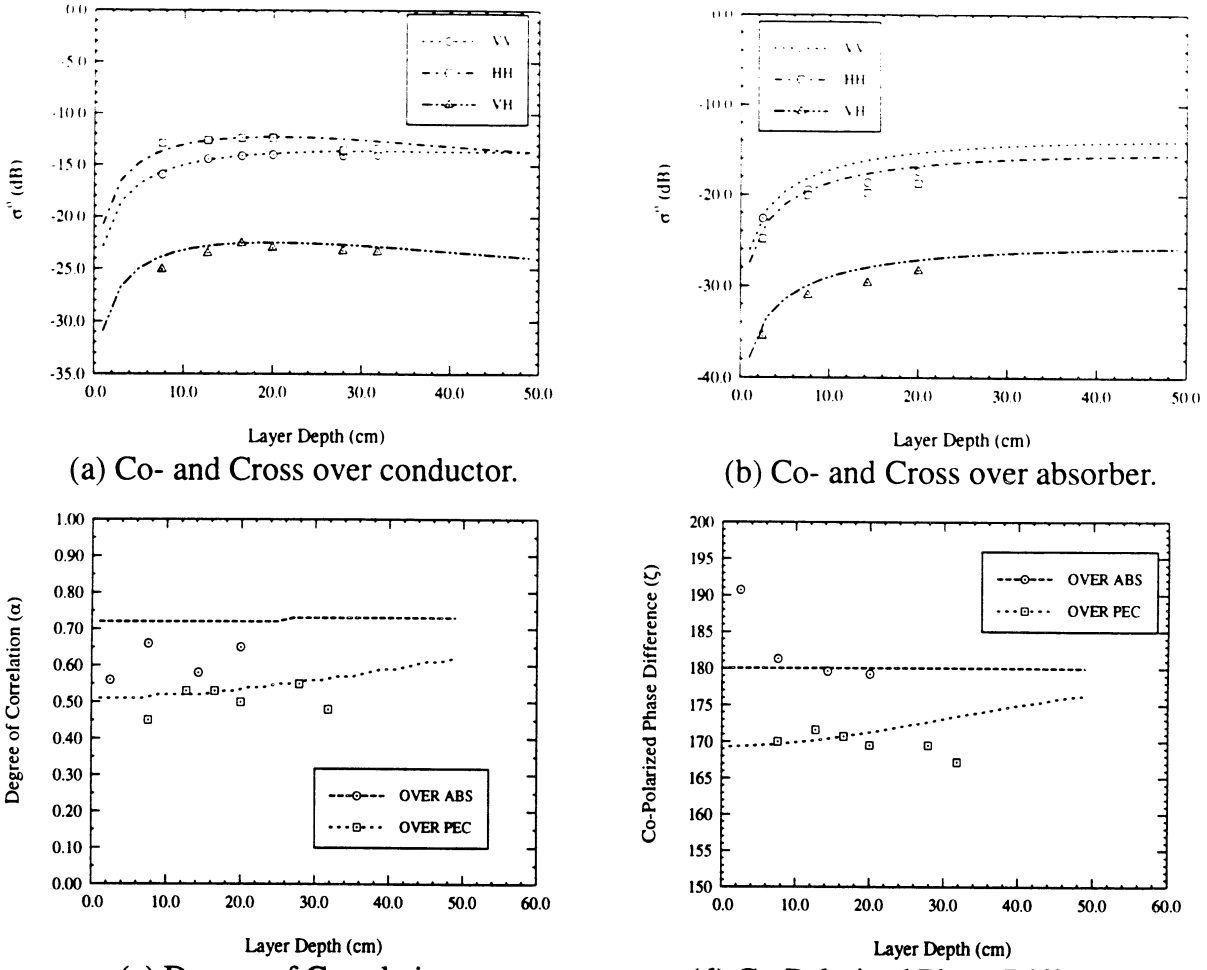

(a) Co- and Cross over conductor.

(b) Co- and Cross over absorber.

(c) Degree of Correlation.

(d) Co-Polarized Phase Difference.

Figure 6.22: 8-12 Gravel, 60° incidence: Predictions generated from an Isotropic model based on measured data at 40°, except for *one* polarimetric measurement of a layer (16.5 cm) over a conductor at 30° and 60°.

It is seen that the scattering behavior can still be modelled with a high degree of accuracy using this abbreviated characterization process. Still greater economy can doubtless be obtained by using only *some* of the data measured at 40°. An effective strategy with respect to this last point will vary according to the specific material under test. There is little information gained, for example, from measurements made after the scattering has reached a saturation level.

6.5 Comparison of Results with Theory

In Section 6.1 we stated that the characteristics of the 8-12 Gravel made it especially suitable for comparison with theory. One impediment, however, to such a comparison is the task of determining the precise dielectric constant of the particles themselves, $\tilde{\varepsilon}_p$, at the frequency of interest, in this case, our center frequency of 16 GHz.

One approach by which this might be accomplished is to measure by some means the effective dielectric constant, $\tilde{\varepsilon}_{eff}$, of the medium and then invert a dielectric mixing formula like the Polder-Van Santen mixing model (Ulaby et al. 1986) to get the dielectric of the inclusions (particles). The fact that the particles have a high degree of sphericity removes the ambiguity associated with assigning the three shape factors for that model. If, however, $\tilde{\varepsilon}_{eff}$ is measured at the test frequency (16 GHz was the center frequency), then the imaginary part, ε''_{eff}, would comprise the effects of the scattering losses as well as the dielectric conducting losses, and therefore would not lead to the proper result for the particle dielectric $\tilde{\varepsilon}_p$. A more appropriate procedure is to measure ε''_{eff} at low frequency, where scattering is negligible. The variation of the dielectric constant of dry rocks with frequency in the microwave region has been studied (Ulaby et al. 1990). The real part ε'_p is essentially constant from 1 to 16 GHz. The imaginary part ε''_p has been found to decrease with frequency, in a manner dependant on the particular rock class. The material in the 8-12 Gravel appears to be either a sedimentary, plutonic, or volcanic silicate. The frequency dependance of ε''_p for each one of these classes is given in Ulaby et al. (1990).

In this case, $\tilde{\varepsilon}_p$ for the 8-12 Gravel was measured at about 1.5 GHz using the Snow Probe, which was described in Chapter III, and found to be $\tilde{\varepsilon}_{eff} = 2.17 - j0.007$. The Polder Van Santen mixing formula for spherical particles (shape factors: $A_1 = A_2 = A_3 = 1/3$) is,

$$\varepsilon_m = \varepsilon_h + 3v_i\varepsilon_m \frac{\varepsilon_i - \varepsilon_h}{\varepsilon_i + 2\varepsilon_m},$$

where ε_m, ε_h, and ε_i are the effective dielectric constants of the medium, the host (air), and

the inclusions (or particles), respectively, and v_i is the volume fraction. This equation may be easily solved for ε_i $(= \tilde{\varepsilon}_p)$ yielding $3.11 - j1.38 \times 10^{-2}$. This value of ε_p'' is already considerably lower than the average for all of the silicate classes mentioned above (see Figure 13 in Ulaby et al. (1990)). Therefore, instead of applying the frequency dependance associated with the much higher values of the quantity ε_p'' measured for the various silicate classes in Ulaby et al., we will simply use the low frequency value of $\tilde{\varepsilon}_p$ as our estimate at the frequency of interest, 16 GHz.

This result completes the information required to examine the correspondence between the measurements of this material and the predictions of certain discrete-particle-based theories. A pertinent quantity for comparison is the effective propagation constant in the medium:

$$K = K' - jK''$$

from which may be obtained the real and imaginary parts of the effective index of refraction:

$$n' = \frac{K'}{k_o} \qquad\qquad n'' = \frac{K''}{k_o}, \tag{6.7}$$

with the extinction specified as $\kappa_e = 2K''$.

The theories we compare with are the Effective Field Approximation (EFA), the Quasi-Crystalline Approximation (QCA), and the Quasi-Crystalline Approximation with Coherent Potential (QCA-CP). We present here a very brief description of each technique.

In conventional radiative transfer (CRT) the extinction is obtained using EFA (also known as Foldy's approximation), which can be considered a special case of QCA, (Tsang et al. 1985) in that the particles are considered as acting completely independent of one another with zero correlation. The solution for the effective propagation constant is formally given by Tsang et al. (1985),

$$K = [k^2 - 4\pi n_o < S_{pq}(\theta_s, \phi_s; \theta_i, \phi_i) >]^{1/2}$$

where S_{pq} is the complex far-field scattering amplitude, k is the wavenumber of the surrounding medium and n_0 is the number density of the scatterers. The loss the wave experiences is due to the total extinction cross-section of a particle multiplied by n_0.

A detailed description of QCA theory is outside the scope of this presentation. A detailed derivation may be found in Tsang et al. (1985). In general, QCA takes into account interactions between particles, using exact wave transformations, a "T-matrix" approach, for computing this interparticle interaction rather than far-field phase functions. The particle correlation is specified by the pair-distribution function which describes the conditional probability of a particle location relative to another particle's position. The Percus-Yevick approximation is most often used to derive the pair-distribution function for a medium. This approximation assumes non-interpenetrability of particles and zero forces between the particles. This assumption, which has, in some specific experiments (Mandt 1987), been found to agree with experimental observations, removes the requirement of characterizing by more direct means the exact configuration of particles in a dense medium. In more recent studies (Siqueira and Sarabandi 1995) this assumption has been shown to break down outside of its intended domain of validity, which comprises mainly liquids or gases.

QCA-CP constitutes an improvement upon QCA in that it provides for energy conservation in the formulation. Essentially it amounts to employing the effective wavenumber K in the Green's functions of the QCA formulation instead of the background wavenumber k. The formulation is valid for Rayleigh particles only.

The results produced by each one of these methods are summarized in Table 6.4. Shown are estimates for n', the real part of the effective index of refraction and κ_e. Shown for comparison, as "Meas.", are the Snow Probe measured n' and κ_e obtained from the isotropic Hybrid model analysis of the 8-12 Gravel. The correlated particle treatments represented by QCA and QCA-CP produce estimates of n' which are in close agreement with the measured value. EFA gives a considerably lower estimate. While the QCA result for κ_e is very low, the QCA-CP and EFA estimates bracket, below and above, respectively, the experi-

Source	n'	κ_e
Meas.	1.47	2.35
EFA	1.35	3.09/3.02*
QCA	1.43	0.29
QCA-CP◇	1.47	1.69

*Background = air / Background = ε_{eff}
◇Intended for Rayleigh region.

Table 6.4: Theoretical predictions based on 8-12 Gravel characteristics.

mentally determined value for κ_e. This result resembles previous findings (Mandt 1987) for glass spheres in styrofoam at much lower volume fractions (<10%).

Figure 6.23 shows a comparison between measurements and scattering computations from a numerical CRT model which employs the EFA theory, using Mie calculations for the phase function and extinction and the discrete ordinate solution method (Kuga et al. 1991). The inputs to the model consisted of the physical characteristics of the 8-12 gravel as they have been described in the preceding sections, including particle size distribution, volume fraction, effective dielectric constant of the medium and dielectric constant of the individual particles. Though the trends with respect to polarization and depth are similar, the CRT model overestimates the scattering level by typically 3-4 dB.

A comparison between measurements and predictions from a Dense Medium radiative transfer (DMRT, described in Section 5.2) model are shown in Figure 6.24. The theoretical predictions are seen to be extremely low—on the order of 15–20 dB down—relative to the measured results. This very serious disagreement can be explained in terms of the behavior of the scattering albedo, ω_o which scales the phase matrix (as described in Section 5.2) and hence the scattering production of a collection of scatters. The value of ω_o computed (from Wen et al. (1990)) for the DMRT model is similar to the CRT computation for very low volume fractions (eg. <5%) but diminishes rapidly with increasing volume fraction. For this scenario, with a volume fraction of 0.63, the scattering albedo computed from DMRT is about 250 times smaller than that computed by CRT. Since the values of extinction given

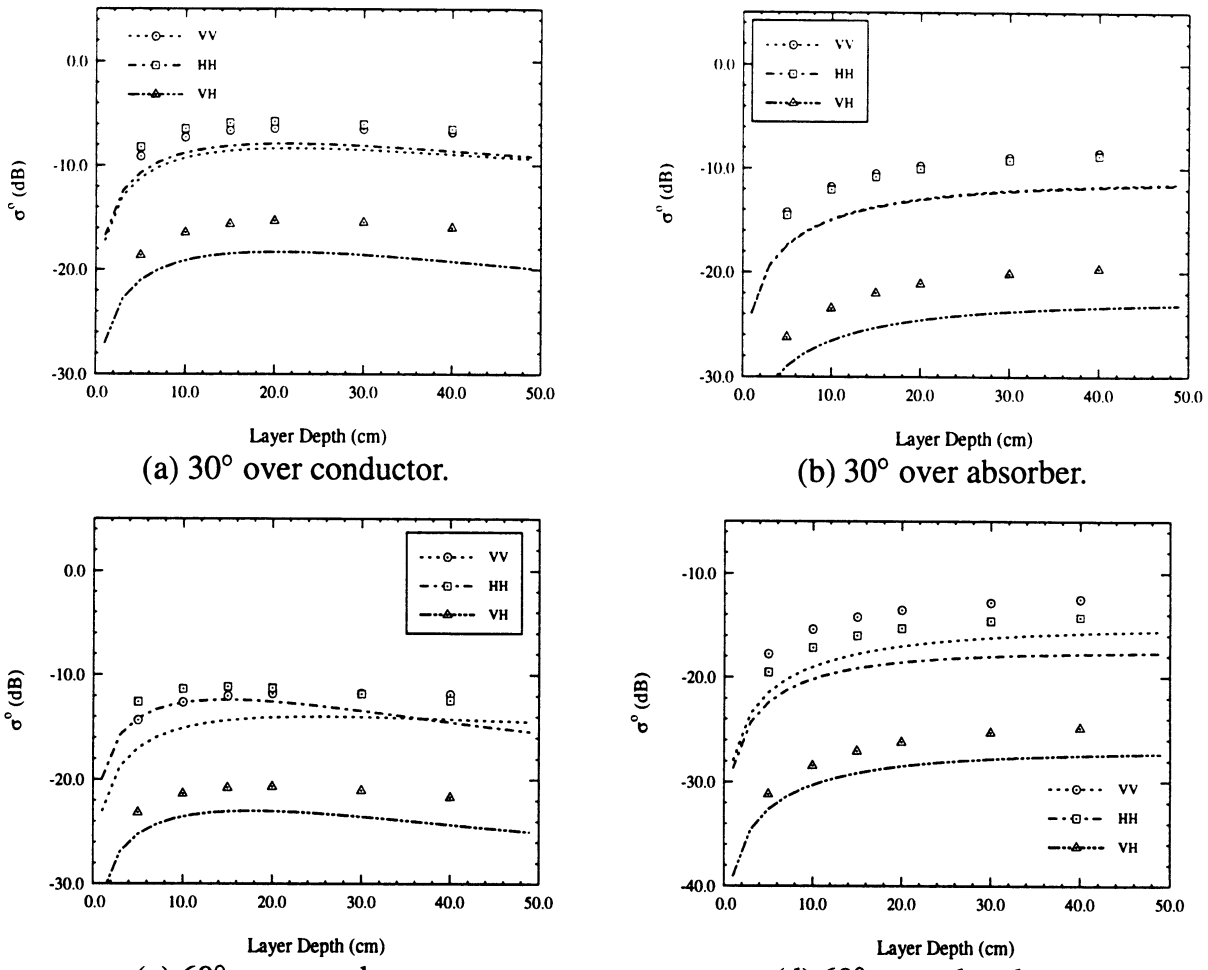

(a) 30° over conductor.

(b) 30° over absorber.

(c) 60° over conductor.

(d) 60° over absorber.

Figure 6.23: Comparison of measurements of 8-12 Gravel with CRT simulations. Discrete marks are CRT simulations; continuous lines are from non-isotropic, first-order RT analysis of measured data which very closely approximates the actual data.

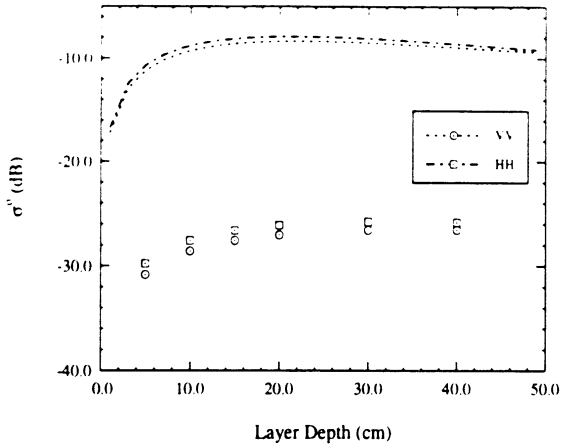

(a) 30° over conductor.

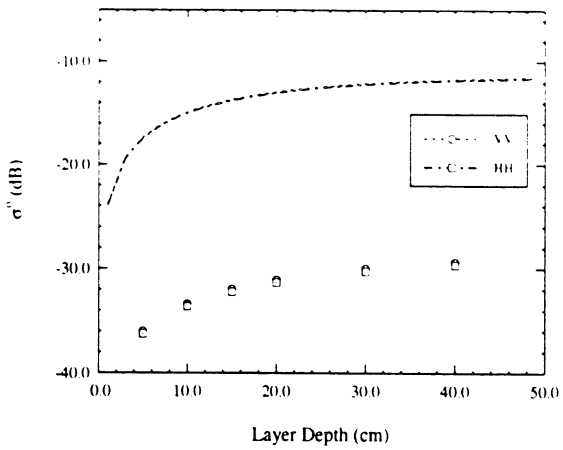

(b) 30° over absorber.

Figure 6.24: Comparison of measurements of 8-12 Gravel with DMRT simulations. Discrete marks are DMRT simulations; continuous lines are from non-isotropic, first-order RT analysis of measured data which very closely approximates the actual data.

in that table for EFA and QCA-CP are fairly similar, this means that the difference in the respective albedos pertains to the scattering (recall, $\omega_o = \kappa_s/\kappa_e$). The value for the extinction computed from QCA-CP given in Table 6.4 is based almost entirely on the absorptive losses in the particles. That the QCA result is smaller than this value is symptomatic of that technique's failure to obey energy conservation.

For a final comparison, we note that in the isotropic Hybrid model, finding $\mathcal{P}_{bi}$ independently for various incidence angles amounts to mapping out some portion of the scattering phase function of the particle (refer, for example, to Figure 5.2). Figure 6.25 shows these experimentally derived phase functions. Shown for comparison are Mie calculations made for the cases of (a) a particle having the same characteristics as the 8-12 Gravel particles, and (b) a particle having the same dielectric but three times as large. All results are normalized to the backscatter level. The obvious implication, consistent with the assumptions of the Hybrid model concept, is that multiple particles combine to form an effective scattering element which is amenable to a first-order RT approach.

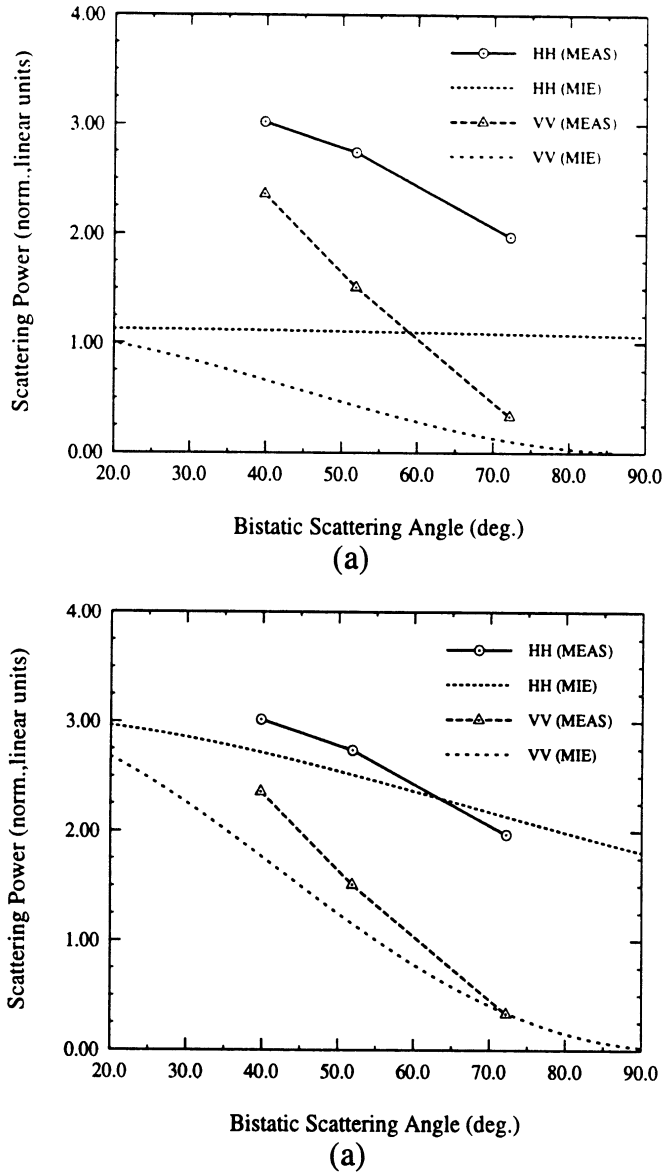

Figure 6.25: A portion of the scattering phase function obtained *via* isotropic RT analysis of 8-12 Gravel compared with Mie phase function for a particle (a) identical to an 8-12 Gravel particle, (b) three times larger than an 8-12 Gravel particle.

6.6 Application of Hybrid Model Technique to Synthetic Data

In the previous Sections, we have explored the question of whether actual scattering behavior in dense media—where it is probable that multiple scattering and correlated scattering is present—can be described by a simple first-order RT model. It may also be instructive to ask whether the scattering predictions of more rigorous theoretical models may be similarly described in such a simple way. In other words, do these theoretical models implicitly generate effective quantities which can be shown to conform to the assumptions of the Hybrid Model approach?

The results of the application of an *isotropic* hybrid model to numerical CRT-generated data are shown in Figure 6.26. This particular set of simulated data was generated using input parameters similar to the 8/12 gravel parameters except that the imaginary part of the dielectric constant of the particles was reduced from the value which was experimentally determined ($\varepsilon_p'' = 0.0138$) to 0.003. This reduced loss value translates into an increase in the backscatter level of several dB's relative to Figure 6.23, wherein the experimentally determined value for ε_p'' was used. The exact value of the backscatter is not critical in the present analysis, though a comparison of the two figures does give some indication of the sensitivity of scattering calculations to the values of the input parameters.

From 6.26(c), the angular variation in the CRT model data is shown to be greater than that produced by the first-order Hybrid model. The cross-pol level is also underpredicted for the over-absorber case. Figure 6.27 shows the results of the non-isotropic hybrid model, applied to the CRT model data. As in the case of the measured data shown earlier, permitting $\mathcal{P}_{bs}$ to be a function of angle frees the Hybrid model from the angular constraint of the Fresnel transmissivity of the surface. It is noteworthy however that the Hybrid model is still not able, despite the functionality of the non-isotropic version, to accurately comprehend the cross-pol response in the over-absorber case. This is an interesting contrast to the treatment

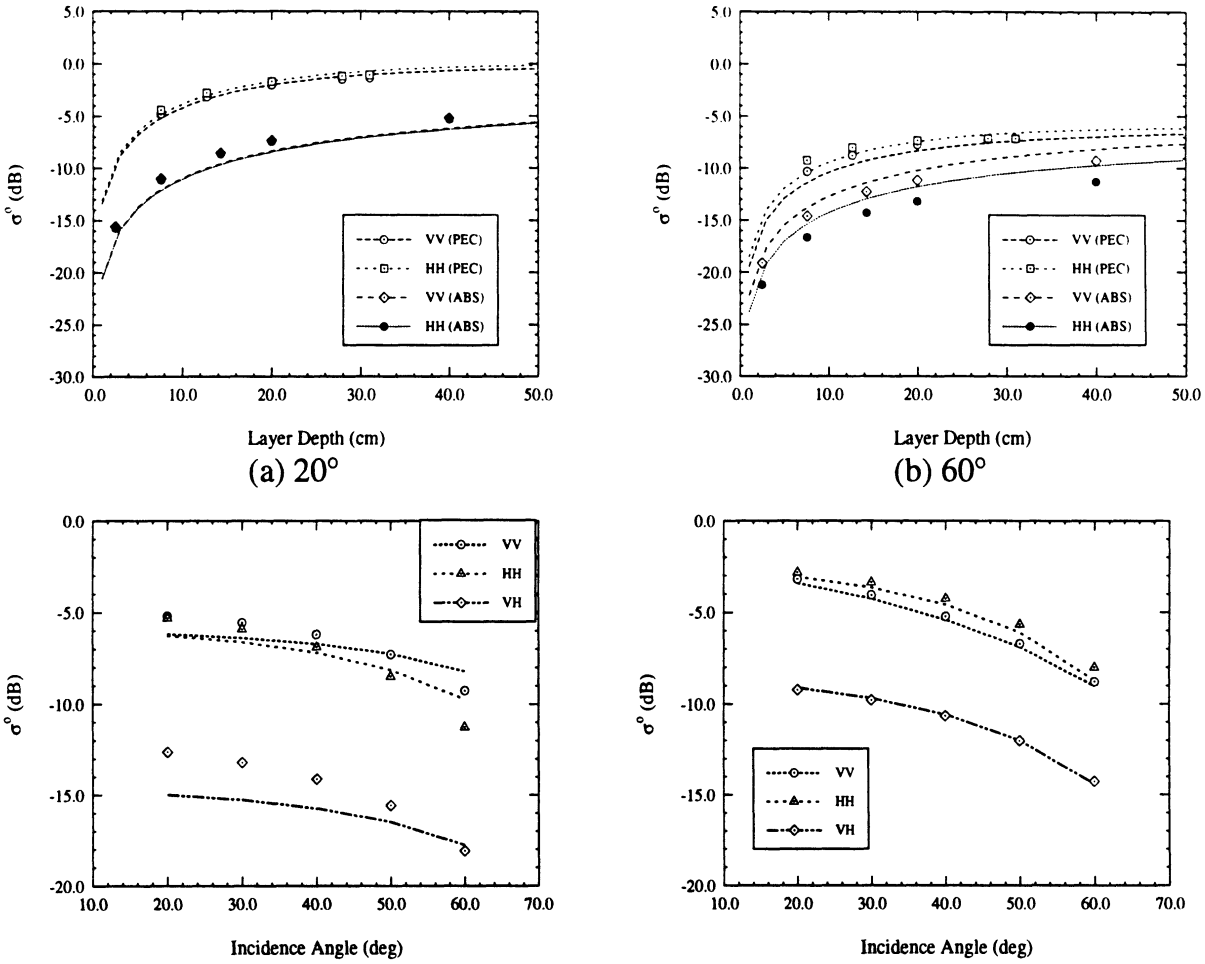

Figure 6.26: First-order *isotropic* RT Hybrid model applied to CRT simulated data. Discrete marks and continuous lines are CRT simulations and Hybrid model predictions, respectively.

of the *measured* data, for example Figures 6.12–6.14 for 8-12 Gravel and Figures 6.15–6.17

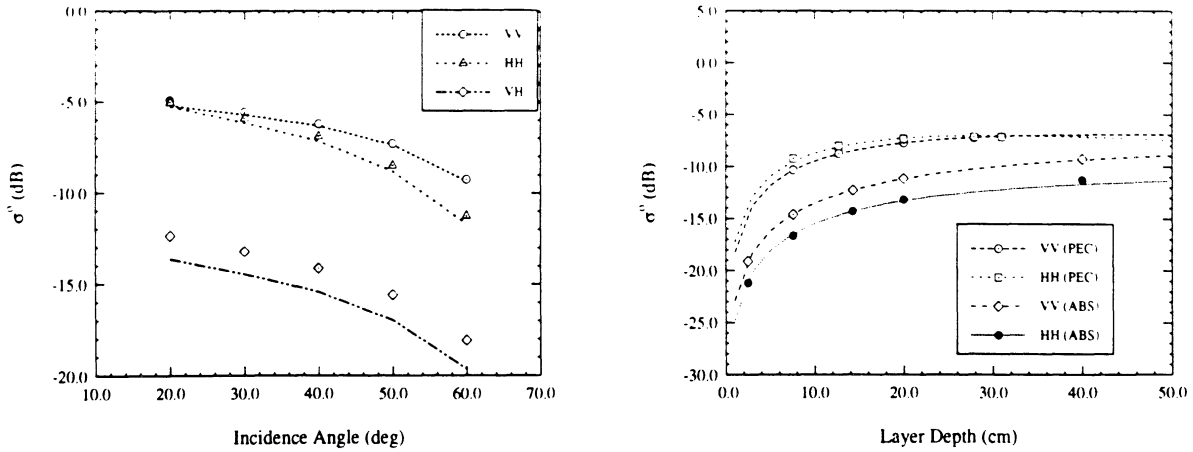

(a) 40 cm over absorber (b) 60°

Figure 6.27: First-order *non-isotropic* RT Hybrid model applied to CRT simulated data. Discrete marks and continuous lines are CRT simulations and Hybrid model predictions, respectively.

for Common sand, in which the non-isotropic model gives very close agreement generally. This result suggests that attempts to rigorously describe scattering processes within a dense media may produce effects which do not agree with heuristic explanations, which are themselves mainly compatible with real behavior.

This exercise with simulated data provides some insight into the nature of the non-isotropic approach. It was earlier suggested, in Section 5.4, that a physical departure from an isotropic state, for example, partial ordering of particles due to the force of gravity, might provide the justification for such an approach. In the CRT simulations however, there is no such condition, and yet the isotropic first-order Hybrid model is seen to be inadequate. With respect to the test materials, the one material where some non-isotropic behavior might be expected, the 8-12 gravel, shows far less departure from an isotropic description (see Figures 6.18 and 6.19) than the Common sand, for which there is little basis for an argument of particle ordering. The clear implication is that the departure from an isotropic explanation is due to the presence of multiple scattering. Where such phenomena is present, the effective quantities required by a Hybrid model have an orientation-sensitive character though the medium

itself may be completely isotropic.

What is most important for the Hybrid modeling approach is that a behavioral description is found which is valid everywhere. The use of synthesized data allows us to test the predictive capabilities of a Hybrid model. In Figure 6.28 we show the results of the Hybrid model, developed with the "over-conductor" and "over-absorber" data described in the pre-

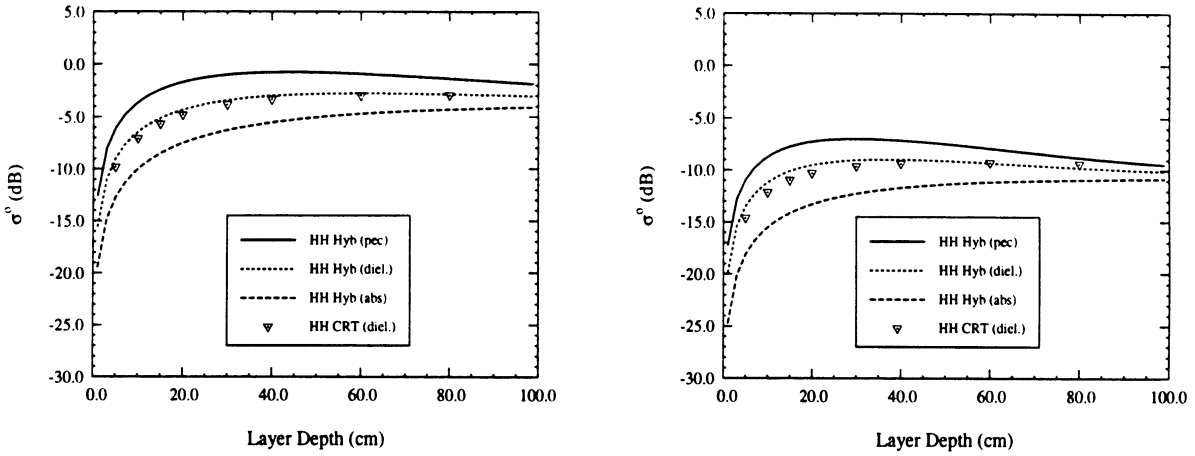

Figure 6.28: First-order *non-isotropic* RT Hybrid model developed from simulated data applied to a case of a layer over a high dielectric ($\varepsilon = 50$). Discrete marks are from CRT calculations for this case and continuous lines—which are shown also for the case of a similar layer over an absorber and over a conductor—are Hybrid model predictions.

vious paragraphs, applied to the case which was not involved in the model development, that is, layers over a halfspace having a very high dielectric, $\varepsilon = 50$. It is apparent that the behavioral description afforded by the Hybrid model closely resembles the behavior of the more complex CRT model.

CHAPTER VII

CONCLUSIONS AND RECOMMENDATIONS

In this chapter contributions to the study and practice of microwave remote sensing of snowpacks represented by this thesis are summarized. Afterwards, specific recommendations as to future directions with respect to this problem are presented.

7.1 Contributions of This Thesis

Overall, the contributions of this thesis can be considered as having taken both positive and negative forms. The "positive" contributions comprise new ideas, techniques and observations. The "negative" contributions, equally important, comprise instances where previously established findings were found to be of questionable validity. The following presents a summary of the contributions, "positive" and "negative", of this thesis.

In Chapter III the development of the Snow Probe was described. Though the initial motivation for its development was to avoid the cost of purchasing an existing device, the Snow Fork, by developing it "in house", several innovations were added which make it an original, and we believe, superior device relative to the Snow Fork. The enhanced features include a new coaxial design which affords both greater spatial resolution and improved accuracy in the estimate of the imaginary part of the dielectric constant, which is the quantity used to infer liquid water content m_v. In addition, a new mapping algorithm was developed between measured dielectric constant and snow parameters, based on field comparisons with

direct techniques, which differs considerably from that used with the Snow Fork and proposed elsewhere (Hallikainen et al. 1986). An additional finding which came out of the Snow Probe development and which constitutes a "negative" contribution, is the observation that the results of the application of the Polder-Van Santen mixing model to wet snow, and the associated claims with respect to the nature of the shape coefficients in that model, found in Hallikainen et al. (1986) and Abdelrazik (1984) are incorrect. This fact is shown through a re-analysis of their own data, the results of which are presented in Appendix C.

The development of the Snow Probe was a prerequisite to the field experiment involving radar measurements of artificial snow which was described in Chapter IV. In these experiments, steps were taken to characterize carefully all of the parameters associated with the target snowpack. The analysis of the data using discrete-particle-based theories and their failure to comprehend the observed behavior constitutes another very important "negative" contribution. An attempt to characterize the artificial snow polarimetrically using a simple RT model with empirical coefficients was described. The technique was shown to be partially successful, but the need to deal with factors such as the polarimetric character of the rough surfaces above and below the snow layer prevented a highly accurate characterization of the snow medium itself. The justification for the use of a first-order RT model with dense media was deferred to Chapter V, where it was examined intensively.

In addition to the dry snow experiments of Chapter IV, the results of diurnal experiments with accompanying wetness data provided by the Snow Probe were presented. The radar results were generally consistant with results previously published, showing a very substantial depression in the backscattering coefficient. In one of the two cases examined, this depression is momentarily arrested for a time, apparently due to an increase in the surface scattering. This argument is supported by changes in the polarimetric response during these periods, specifically in the degree of correlation and the coefficient of variation. The observation is made that these two quantities appear to supply identical information, within a simple algebraic relation. Finally, the diurnal radar and wetness data are used to evaluate

an ambitious algorithm (Shi and Dozier 1995)for the retrieval of liquid water content from polarimetric radar measurements. Despite some aspects of the basic conceptual framework which are somewhat difficult to justify, the algorithm was observed to give a very reasonable estimate of the the snow wetness levels observed in the top layer of the snowpack in the two separate diurnal data sets considered. In particular, the algorithm was able to correctly identify one snowpack as very wet at the top and the other as relatively dry.

In Chapters V and VI, a very fundamental question concerning volume scattering in dense media is posed and answered. The question, motivated by the perceived difficulty, noted in Chapter IV, of theoretical particle-based techniques to adequately explain scattering from dense media, is whether there exists a practical recourse for modeling the polarimetric behavior of such materials. In Chapter V a hybrid modeling scheme is proposed which uses the theoretical and mathematical framework of first-order vector radiative transfer (RT) but which specifies the corresponding quantities which drive its behavior, the extinction and phase matrix, through an inversion process based on backscatter measurements collected through careful laboratory experiments.

Chapter VI presents the results of the test of this assumption. The results indicate that for a relatively homogenous medium, the polarimetric scattering behavior *can* be comprehensively specified with an isotropic first-order RT model, using three quantities specific to the material: a scalar extinction, and two components of the phase matrix, a backscatter component and a bistatic component (the latter of which must be specified independantly for each incidence angle). It is shown that these polarimetric quantities can be accurately estimated based upon a limited number of polarimetric backscatter measurements. For a less homogeneous scattering medium examined, a purely isotropic model was shown to be inadequate. In this case, a non-isotropic description was obtained which also showed good agreement with the observed polarimetric behavior. From tests on simulated data, the non-isotropic behavior is shown to be a likely artifact of multiple scattering effects.

Comparisons of the measured backscatter for the 8-12 gravel (the more homogenous ma-

terial, for which scattering behavior was amenable to explanation in terms of an isotropic RT model) versus predictions of both conventional radiative transfer (CRT) and dense medium radiative transfer (DMRT) models were presented. The CRT results were relatively close, and the 3-4 dB error level could perhaps even be attributed to uncertainty in the estimate of the imaginary part of the dielectric constant of the particles. A very dramatic lack of correspondance was observed however with respect to the DMRT model, which predicts an extremely low backscatter level, 15–20 dB below the measurements.

An examination of the angular pattern of the bistatic scattering within the 8-12 gravel medium seems to confirm the existence of a fundamental scattering element considerably larger than the individual discrete particles of which the medium is composed.

7.2 Discussion & Recommendations for Future Work

In terms of the practice of microwave remote sensing of snow, it can be said that this research was confined to the "forward problem", that is, the problem of finding a suitable model for the scattering behavior of snow. The findings indicate that constructing scattering solutions from a consideration of the physical properties of the medium remains an uncertain and questionable endeavor. This was demonstrated in the case of the Brighton snow experiment (Chapter IV) and even more conclusively in the case of the 8-12 gravel. What is true for these media, composed of discrete particles, is certainly much more so for the complicated media which is natural snow. The hybrid modeling scheme provides an alternative means, at this point possibly the best and perhaps the only means available for comprehending the scattering behavior of dense materials.

The concept of a hybrid empirical/theoretical model is a very powerful one. It benefits from the strengths of each approach (empirical and theoretical) while mitigating their respective weaknesses. Like an empirical model, the model is based on the *measured* behavior of media. However, compared to a purely empirical model, the span of the parameter

space is very substantially reduced. It is only necessary to establish phase functions and extinction matrices for a representative number (which can still be quite large) of snow types, then use these in the mathematical machinery of radiative transfer to comprehend scattering from a host of problems involving assorted boundary conditions such as layers of different snow types or rough surfaces and interfaces. Like a purely theoretical model, a great deal of generality and versatility is still possible. The role of experiment here is much more than just validating theory. In that scenario, which is the common one, the results of experiment have a digital role: they bear out the predictions of the theory or they do not. In the hybrid modeling technique, the form of the model grows directly out of the experimental results. The experiments perform a role much more important than just a behavioral check; they amount to a characterization of a medium.

As to the direction of future research, I offer a general philosophy and two specific recommendations. In general, I believe an attempt should be made to simplify our view of the problem. In a sense, we have been finding that, like Heisenberg, the closer we examine the problem, down to the most minute details, the further we are finding ourselves from something which might constitute a workable solution. The hybrid model is one example of taking a simpler view. Our results indicate, as we predicted, that the behavior of the material is not so very complicated; that, even with respect to the phase statistics, the scattering behavior obeys certain fairly intuitive laws. Another example is our understanding of the dielectric constant of (dry) snow in terms of density alone (Eq. (3.13)), independant of additional physical parameters of the snow.

In the spirit of this philosophy, two recommendations are:

1. Research be performed to identify parameters by which dry (initially) snow types can be readily and unambiguously classified. If success is really dependant upon the specific geometry of particles or the exact correlation function for the permittivity, the whole enterprise is probably doomed to failure. Two suggested parameters which might be evaluated for their ability to meaningfully (i.e. correlated with scattering / extinction behavior) are density and "hardness" or resistance to crushing. The former

describes the total *amount* of material per unit volume; the latter implicitly contains information about the *structure* of that material.

2. A campaign be conducted to characterize snow types electromagnetically using the hybrid modeling technique described in Chapters V and VI. Characterization of twenty or more snow types should yield significant information as to (1) the validity of the chosen parameters as classifiers, and (2) the potential for interpolation of the scattering quantities (eg. elements of $\mathcal{P}_{bi}$) to obtain the scattering characteristics of snow types bearing intermediate physical descriptions. At the very least, assembling this sort of database will provide modelers with the ability to do realistic simulations of the scattering and extinction effects of snow.

The logistical requirements associated with the recommendation number (2) are non-trivial. As was alluded to in Section 4.3.2, the importance of the bistatic scattering terms (see Fig. 5.2) is dependent upon a number of factors, including the expected terrain type under the snow and the angular distribution of the phase matrix. The depth of the snow is another factor since these mechanisms involve a complete round trip path involving the bottom of the snowpack and will thus be subject to increasing levels of extinction with deeper snow layers. For cases where only the direct backscatter term is judged to be important, characterization of the snow medium *via* measurements over an absorbing type of material, most likely some rigid but lossy dielectric fairly well matched to snow, are all that is strictly required. Total characterization of the materials though, afforded by the addition of the experiments over a conducting sheet, allows for greater modeling flexibility (i.e. shallow snow layers over rock or wet soil) and should enhance the ability to *classify* snow types. In addition, an observation from our parameter estimation efforts, and one which can probably be demonstrated mathematically, was that, lacking data from "over-conductor" type experiments, determination of the extinction was open to considerably greater ambiguity.

APPENDICES

APPENDIX A

EVALUATION OF DILATOMETER AND FREEZING CALORIMETER

A.1 Dilatometer Evaluation

Attracted by the simplicity of the concept, apparatus, and procedure, we expended considerable effort in evaluating the dilatometer technique. As we ultimately rejected it as a result of its poor performance in determining liquid water content, we will not go into the details of the apparatus itself; a complete description is provided in (Leino et al. 1982) for those interested. Instead, we will just briefly describe the method and then present some of the drawbacks that led us to reject the method.

In the method, a weighed snow sample is placed in a cooled (0°C) jar, and then the jar is completely filled with 0°C water. A lid with a graduated tube is fixed onto the jar, and the tube itself is filled with freezing water and the level noted. The jar is placed in a warm water bath to melt the snow and then the entire system is returned to a temperature very close to 0°C. The change in the volume is related to the mass of ice present, and subtracting this from the original snow mass gives the mass of water in the snow sample.

The principal drawbacks we found were the following:

- Lack of accuracy due to non-ideal behavior of the materials. We tried the following experiment: we filled the apparatus entirely up with 0°C water (no snow or ice) and cycled the temperature up and then back down as described above. In each of several

trials, the volume of the water (which should have returned to its original value, about 1 liter) was found to have increased by about 0.1%, enough to cause a very significant error in an actual trial. In quantitative terms, if a 75 gram sample of snow having 5% water mass fraction was analyzed, it would appear that the sample had 20% water mass fraction. We believe this volume expansion effect may be caused by gases that are liberated when the cold water is warmed. Additional slight but critical volume changes may be caused by expansion or contraction of any of the parts of the dilatometer apparatus.

- Long analysis time. The snow, once added, can be melted relatively quickly by warming the system. However, to return back to 0°C (which is absolutely critical to avoid unwanted volume changes in the system) the wait required is on the order of one hour. The reason is that, unlike the warming case, for the cooling there is a relatively small temperature gradient. The bath can be no less then 0°C; so when the temperature gets down to 5 or 6°C, there is very little gradient to drive it down further.

A.2 Freezing Calorimeter Evaluation

As noted earlier, the theoretical background and the procedural details of the freezing calorimeter method are thoroughly discussed in a previous Radiation Lab report (Austin 1990). Since that report was written, there have been several major improvements made in the freezing calorimeter system:

- A second calorimeter was constructed, identical to the first, to allow for duplicate measurements to be done in parallel.

- A motorized tripod-mounted mechanical shaker was constructed which is capable of shaking both calorimeters simultaneously.

- The system has been made PC–based. Software was written which handles two calorimeter channels independent of one another. Data from each channel is collected, displayed, and reduced automatically by the computer.

The method, with these improvements, was tested for precision and accuracy. To our knowledge, it is the first time a systematic test of the method precision and accuracy has been performed.

The accuracy of the method was tested at three different levels of wetness. We prepared a sample of snow with zero wetness by placing it in a freezer at $-20°C$ for several hours. Four separated analyses were performed on the snow from this batch. To test at two other wetness levels, at the point in the procedure where the lid is removed from the calorimeter and snow added, we added—in addition to the zero-wetness snow from above—a precisely measured volume of water at exactly 0°C. In this way, we "spiked" dry snow samples at levels corresponding to 5% and 11% liquid water mass fraction. Each case was analyzed in duplicate. The results of the accuracy tests performed at these three levels are shown in Figure A.2. Shown is the degree to which the experimental results deviated from the known mass fractions. Two results, one at the 0% level and one at the 11% level, come from analyses which were noted as problematic at the time of analysis, and are marked as "suspect". From these tests, it appears that the method is accurate to a level somewhat better than $\pm 1\%$.

The precision of the method was clearly observed since all analyses were done in duplicate. From the results shown in Figure A.2 and the results which were presented in Chapter III wherein the calorimeter was compared to the Snow Probe, it seems that the precision is on the order of $\pm 0.5\%$.

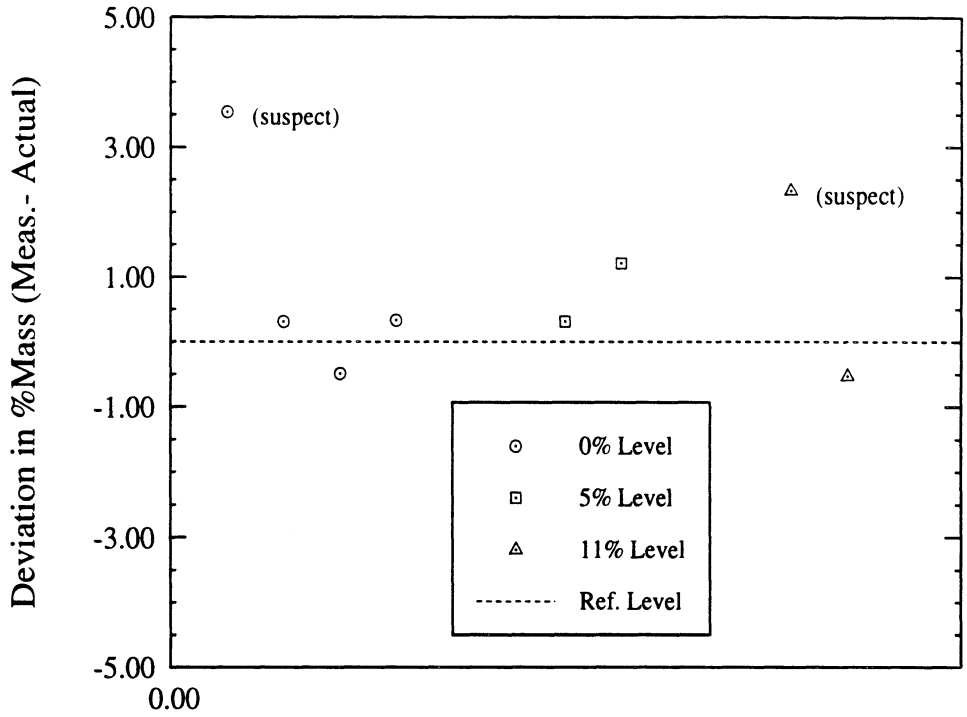

Figure A.1: Calorimeter accuracy tested at three different levels of water content. Data is normalized so all results are compared to what actual level was calculated to be in each case. The two points marked "suspect" correspond to analyses noted at the time of execution as problematic.

APPENDIX B

RESONANT CAVITY MEASUREMENTS OF DIELECTRIC CONSTANT

The L-band cavity used for the Snow Probe study (Chapter III) was a cylindrical, transmission-type resonator, with diameter 13.9 cm and depth 6.35 cm. The TM_{010} mode is resonant at 1.64618 GHz and the loaded (measured) Q for the air-filled cavity was ≈ 3750. To insure reliable, reproducible performance, the cover of the resonator was always fixed on using a torque wrench (60 ft-lbs) and following a prescribed pattern in tightening the screws.

In the most general case, the quality factor of a resonant system is given as follows:

$$\frac{1}{Q_l} = \frac{1}{Q_u} + \frac{1}{Q_{ext}} \tag{B.1}$$

where, Q_l is the *loaded* Q, Q_u is the *unloaded* Q, and Q_{ext} the *external* Q. The unloaded Q is the "real" Q of the resonator but it is possible to measure it directly. The coupling devices (loops, probes) used to couple power in and out of the resonator also contribute to power leakage out (represented by Q_{ext}) which is a source of loss not inherently related to the resonator itself or its contents. The reciprocal of Q_u may be written as the sum:

$$\frac{1}{Q_u} = \frac{1}{Q_R} + \frac{1}{Q_d} + \frac{1}{Q_m} \tag{B.2}$$

where Q_R is, as before, related to the radiated losses, Q_d to the dielectric losses, and Q_m to

the losses associated with the metal walls of the resonator having a finite conductivity. For a closed resonator, as ours is, the radiated losses are zero and we need not consider Q_R. Also, for the empty (air-filled) resonator, Q_d is not considered. Furthermore, it can be demonstrated (Nyfors and Vainikainen 1989) that for a resonator filled with a dielectric ε,

$$\frac{1}{Q_m} = \frac{\sqrt[4]{\varepsilon}}{Q_{mo}}, \tag{B.3}$$

where Q_m is associated with the metal losses in the dielectric-filled cavity, and Q_{mo} with the metal losses in the air-filled cavity. Collin (1966) has shown that,

$$\frac{1}{Q_d} = \tan\delta = \frac{\varepsilon''}{\varepsilon'}. \tag{B.4}$$

Thus the loss tangent $\tan\delta$ may be found from Q_d which may in turn be obtained if Q_u as given in (B.2) may be found and (B.3) is also used. The problem then becomes how, upon measuring Q_l (see equation (B.1)), may Q_u be determined? For the most general case of the input and output coupling networks being different, Altschuler (1963) describes a general impedance method for determining Q_u from Q_l. If it is assumed that the input and output coupling networks are equivalent, then Q_u can be directly calculated (Nyfors and Vainikainen 1989) from measurements of Q_l and the insertion loss a_r at the resonant frequency as follows:

$$Q_u = \frac{Q_l}{1 - \sqrt{a_r}}. \tag{B.5}$$

For our L-band cavity, it was found that the simple method above gave very comparable results to the general impedance method in all cases. It is noted that the general impedance method detailed in Altschuler (1963) is considerably more involved than that given by (B.5).

Based on the above discussion, the procedure for determining dielectric constants with a resonant cavity is summarized as follows:

- Real part of dielectric is found in the same way as given in equation (3.1), using the resonant frequencies of the dielectric-filled and air-filled cavity.

- Imaginary part of dielectric requires determination of Q_u. Then for the case of equivalent input and output coupling factors, equations (B.4),(B.3), and (B.5) lead to,

$$\varepsilon'' = \varepsilon' \left\{ \frac{1}{Q_l}[1 - \sqrt{a_r}] - \frac{\sqrt[4]{\varepsilon'}}{Q_{mo}} \right\} \tag{B.6}$$

where

$$\frac{1}{Q_{mo}} = \frac{1}{Q_{lo}}[1 - \sqrt{a_{ro}}] = \frac{1}{Q_{lo}} - \frac{1}{Q_{ext,o}} \tag{B.7}$$

where the "o" in the subscripts refers to quantities associated with the air-filled cavity.

APPENDIX C

RE-EXAMINATION OF THE APPLICATION OF THE POLDER-VAN SANTEN MIXING MODEL TO WET SNOW

The development of the Snow Probe (Chapter III) included the use and evaluation of certain models which have been developed relating the dielectric constant of snow, wet and dry, to snow physical parameters such as density and liquid water content. In particular, we used as a starting point the "Debye-like" models found in Hallikainen et al. (1986) for the incremental dielectric constant, $\Delta\varepsilon'_{ws}$ (Eq. (3.8)), and the dielectic loss factor ε''_{ws} (Eq. (3.9)). The results of our evaluation of the suitability of these models for the Snow Probe algorithm have been described in Chapter III.

A second important concept examined in Hallikainen et al., and the real focus of this appendix, was the degree to which the two- and three-phase Polder-Van Santen (P-VS) dielectric mixing models could be used to explain the dielectric behavior of wet snow with respect to the nature of its constituents: air, ice, and water. The two-phase model conceives of wet snow as a dry snow host with water inclusions. The mixing formula is given by (Polder and Van Santen 1946),

$$\tilde{\varepsilon}_{ws} = \varepsilon_{ds} + \frac{m_v \tilde{\varepsilon}_{ws}}{3} (\tilde{\varepsilon}_w - \varepsilon_{ds}) \sum_{j=1}^{3} [\tilde{\varepsilon}_{ws} + (\tilde{\varepsilon}_w - \tilde{\varepsilon}_{ws}) A_{wj}]^{-1}, \qquad \text{(C.1)}$$

where $\tilde{\varepsilon}_{ws}$ and $\tilde{\varepsilon}_w$ are the complex dielectric constants of wet snow and water respectively; ε_{ds} is the real part of the dielectric constant of dry snow (imaginary part constitutes a negligible contribution to ε''_{ws}), m_v is the percent volumetric liquid water content, and the factors A_{w1}, A_{w2}, and A_{w3} are the depolarization factors which describe the geometry of the water inclusions. The three-phase P-VS model conceives of wet snow as ice and water inclusions in an air background. The formula is similar to Eq. (C.1) but includes an additional summation for the ice inclusions.

Based on a comparison between measurements of the dielectric constant of wet snow (955 data points comprising ten frequencies between 3 and 37 GHz), Hallikainen et al. (1986) obtained values for the depolarization factors (for the two-phase P-VS model) which were themselves functions of the liquid water content m_v, as shown in Figure C.1. An inter-

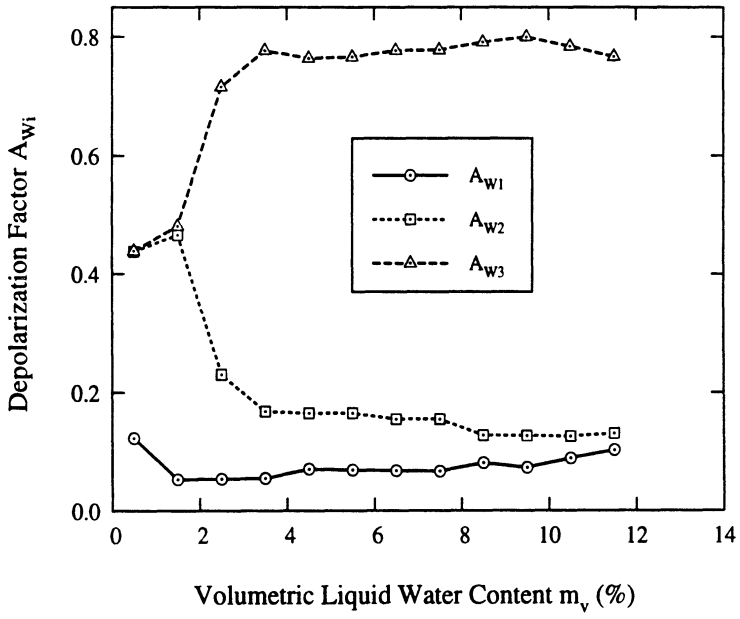

Figure C.1: Depolariztion factors A_{w1}, A_{w2}, and A_{w3} for water inclusions in snow, optimized by fitting the two-phase Polder-Van Santen model to measured values of ε''_{ws}. (From Hallikainen et al. (1986)).

esting feature is the transition in the values of the two factors A_{w2} and A_{w3} which occurs around $m_v = 2.5\%$. This feature indicates that the shape of the water inclusions changes from needle-like (for a needle, $A_{w1} = 0, A_{w2} = A_{w3} = 0.5$) to a disk (for a disk, $A_{w1} = A_{w2} =$

$0, A_{w3} = 1.0$).

In developing the Snow Probe, we discovered, as discussed in Chapter III, Section 3.3, that our experimental values of $\Delta\varepsilon'_{ws}$ did not agree with the predictions of the Debye-like equation (Eq. 3.13). In fact, it appeared as though our experimental results diverged from the predictions given by that model starting at about the point $m_v = 2.5\%$, as may be seen in Figure 3.8, essentially the same point at which a transition had been noted in the analysis with the P-VS model. This led us to examine the applicability of the P-VS model to our data.

Upon embarking upon this examination, we discovered a serious discrepancy with the curves which had purportedly—in Hallikainen et al. (1986) and, especially Abdelrazik (1984) [Appendices 27–28] where the full set appears—been generated from the two-phase P-VS model using the depolarization factors given in Figure C.1.

The curves in question are for the quantities $\Delta\varepsilon'_{ws}$ and ε''_{ws} *versus* m_v. The actual output of the P-VS model (Eq. (C.1)) is the complex quantity $\tilde{\varepsilon}_{ws} = \varepsilon'_{ws} - j\varepsilon''_{ws}$. The value of the dielectric loss factor, ε''_{ws}, used for the theoretical curves in question would then simply be the imaginary part of the complex quantity $\tilde{\varepsilon}_{ws}$. The incremental dielectric constant, $\Delta\varepsilon'_{ws}$, is obtained, for a particular m_v value, by subtracting the *dry* snow dielectric constant, ε'_{ds}, from the real part of the complex output $\tilde{\varepsilon}_{ws}$ of the P-VS model, ε'_{ws}. The dry snow dielectric, ε'_{ds}, was calculated in Hallikainen et al. (1986)[Eq. (14)] and Abdelrazik (1984)[Eq. (7.6), p. 127] using the expression,

$$\varepsilon'_{ds} = 1.0 + 1.832\rho_{ds} \tag{C.2}$$

where ρ_{ds} is the dry snow density. A value of 0.24 g-cm^{-3}, the average observed value in the study, was used for ρ_{ds} in the calculation of ε'_{ds} and hence, $\Delta\varepsilon'_{ws}$.

The complex values, $\tilde{\varepsilon}_{ws} = \varepsilon'_{ws} - j\varepsilon''_{ws}$, which are the purported outputs of the P-VS model, are assembled by taking points off the aforementioned curves of $\Delta\varepsilon'_{ws}$ and ε''_{ws} *versus*

m_v, respectively. The real part of $\tilde{\varepsilon}_{ws}$ is then formed by,

$$\varepsilon'_{ws} = \varepsilon'_{ds} + \Delta\varepsilon_{ws}, \tag{C.3}$$

with ε'_{ds} computed from Eq. (C.2) using $\rho_{ds} = 0.24$ g-cm^{-3}. Since the complex quantity $\tilde{\varepsilon}_{ws}$ appears on both sides of Eq. (C.1), this provides a means by which the solution can be directly checked. When this was done, we found that the values of $\tilde{\varepsilon}_{ws}$, obtained in the process described above, were *not* valid solutions to Eq. (C.1). The cause of this discrepancy was not discovered, but it may be the case that in the original study, the formula (Eq. (C.1)) was incorrectly applied to ε'_{ws} and ε''_{ws} *separately*, which would of course constitute a mathematically invalid treatment of complex numbers.

We decided to conduct a re-analyis of the original data. The raw measured data used in this study, some 993 data points, consisting of ε'_{ws}, ε''_{ws}, m_v, ρ_{ws}, and associated quantities for each data point are given in Appendix 1 of Abdelrazik (1984). We conducted a comprehensive re-analysis of this data, identical to that of the earlier effort. One difference in our analysis relative to that done by Hallikainen et al. was that, instead of just optimizing the agreement between the dielctric loss factor ε''_{ws} and the P-VS model, as was done in that earlier study, we simultaneously optimized both ε'_{ws} and ε''_{ws}, by choosing appropriate values for the depolarization factors A_{w1}, A_{w2}, and A_{w3} to minimize the least-squares error term E as follows:

$$E = \sum_{i=1}^{N} \left\{ (\varepsilon'_{ws} - \varepsilon'_p)^2 + (\varepsilon''_{ws} - \varepsilon''_p)^2 \right\}, \tag{C.4}$$

where N is the number of data points and $\tilde{\varepsilon}_p$ is the complex dielectric constant predicted by the P-VS model for a given choice of depolarization factors. Given a set of these factors, and values for ε_{ds} and m_v, the P-VS prediction $\tilde{\varepsilon}_p$ is obtained by finding the roots of a fourth-degree polynomial (in the most general case of three distinct depolarization factors) with complex coefficients. The root is selected for $\tilde{\varepsilon}_p$ which conforms to certain numerical

requirements which define a reasonable range for the real and imaginary parts.

Additionally, as was done in the previous study, we optimized A_{w1}, A_{w2}, and A_{w3} as a function of water content. Each water-content category was $\Delta m_v = 1\%$ in range, that is, $0 \leq m_{v1} < 1.0 \leq m_{v2} < 2.0\%$, etc. For the first water-content range, m_{v1}, we removed all of the data points for which the water content was measured to be zero, such points being irrelevent to consideration by the P-VS model of Eq. (C.1). This left 582 data points for consideration. Finally, in an extra measure beyond what was done previously, we performed the optimization once using all of the data (582 points) from 3 to 37 GHz, and then repeated the process using only the data collected between the frequencies 3 and 10 GHz (284 points).

The results of our re-analysis as pertains to the nature of the depolarization factors is given in Figure C.2, for (a) the 3–37 GHz analysis, and (b) the 3–10 GHz analysis. Both of

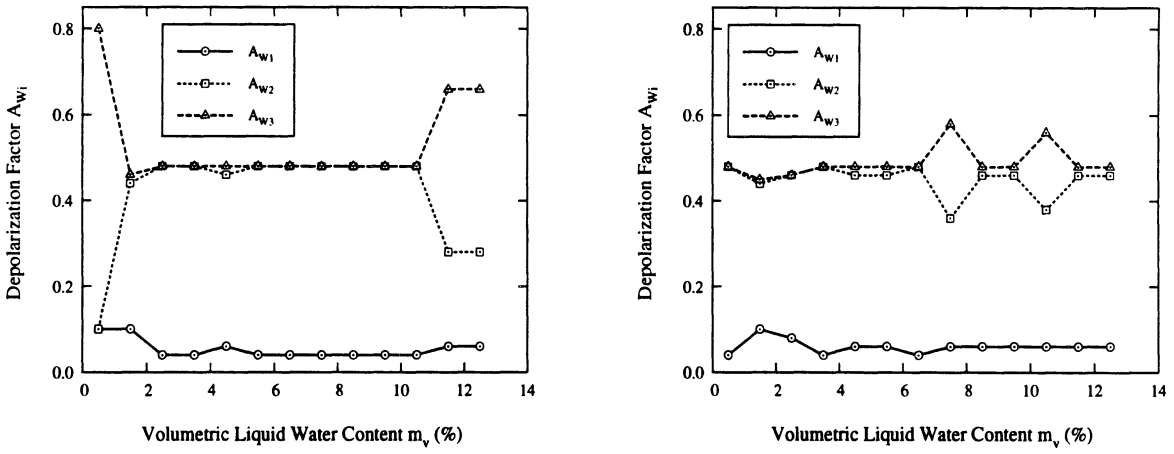

(a) 3-37 GHz analysis.

(b) 3-10 GHz analysis.

Figure C.2: Depolariztion factors A_{w1}, A_{w2}, and A_{w3} for water inclusions in snow, optimized by fitting the two-phase Polder-Van Santen model to measured values of $\tilde{\varepsilon}_{ws}$. Data in the frequency ranges indicated on each figure was used in their respective analyses.

these solutions show complex behavior for the two larger depolarization factors, including features which might be characterized as "transitions". In general, the two separate solutions are similar in that the average level of A_{w2} and A_{w3} is about 0.475 and the average level of A_{w1} is about 0.05.

In Figure C.3 we examine the performance of these new solutions for the depolarization factors in enabling the P-VS model to generate results matching the measured ones. In this figure, results from both of the new solutions (3–37 GHz and 3–10 GHz) are compared

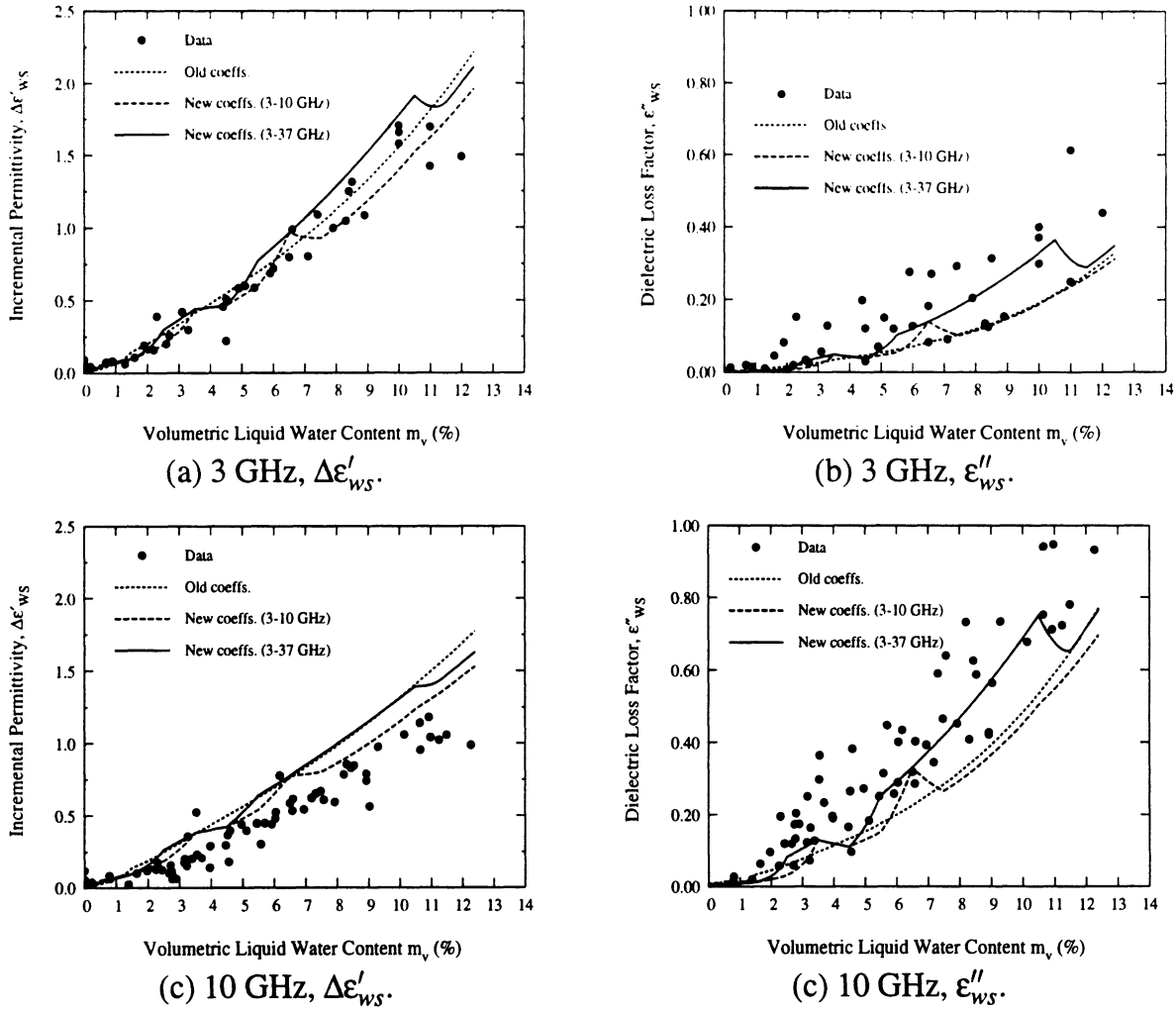

(a) 3 GHz, $\Delta\varepsilon'_{ws}$. (b) 3 GHz, ε''_{ws}.

(c) 10 GHz, $\Delta\varepsilon'_{ws}$. (c) 10 GHz, ε''_{ws}.

Figure C.3: Comparison of model predictions with measured values of incremental dielectric constant ($\Delta\varepsilon'_{ws}$) and dielectric loss factor (ε''_{ws}) at 3 and 10 GHz.

with predictions generated using the original depolarization factors (which were shown in Fig. C.1). Results are shown for 3 and 10 GHz. It is observed that due to the discontinuous nature of A_{w1}, A_{w2}, and A_{w3} as a function of m_v, (as shown in Figure C.2) the resulting P-VS predictions exhibit severe discontinuities. The severe discontinuities are actually due

to the small variations in the small shape coefficient, A_{w1} rather than the more pronounced behavior of the two larger factors. As an illustration, in Figure C.4 we show the result when

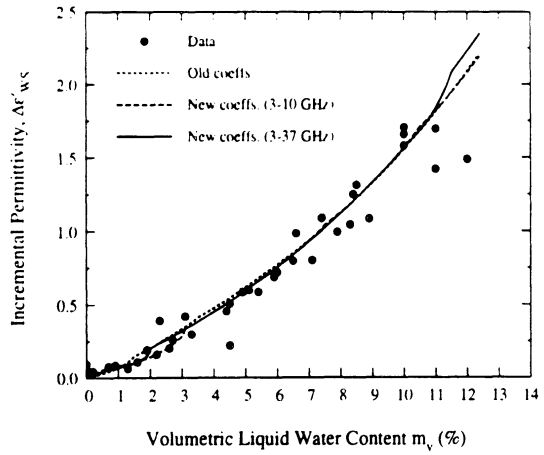

(a) 3 GHz, $\Delta\varepsilon'_{ws}$.

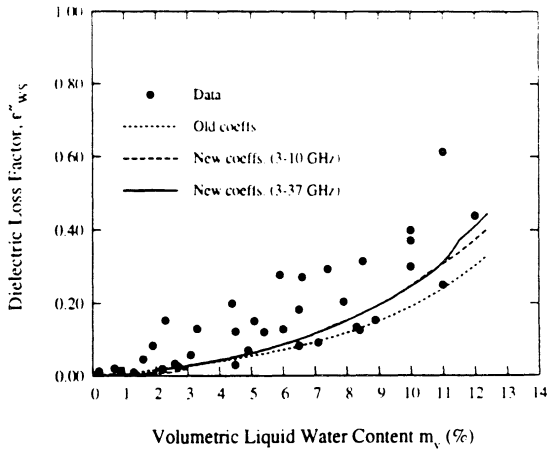

(b) 3 GHz, ε''_{ws}.

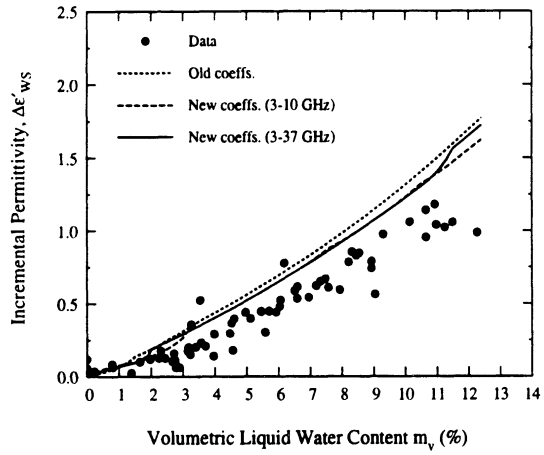

(c) 10 GHz, $\Delta\varepsilon'_{ws}$.

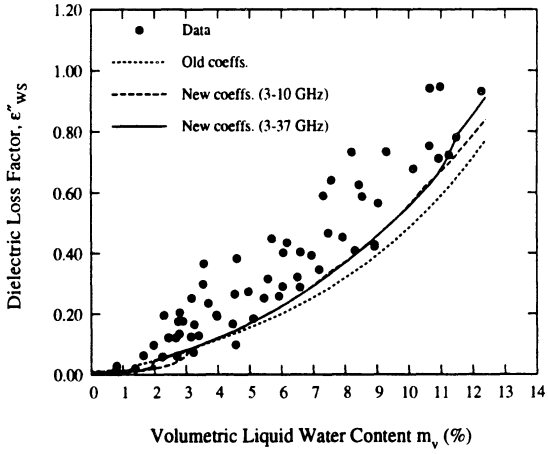

(c) 10 GHz, ε''_{ws}.

Figure C.4: Comparison of model predictions with measured values of $\Delta\varepsilon'_{ws}$ and ε''_{ws} at 3 and 10 GHz. The depolarization factor A_{w1} used for the "New coeffs." curves is a smooth function of the discontinuous lines shown for this parameter in Figures C.2(b)and(c).

an average value of the small coefficient A_{w1} is used rather than the exact values obtained in the optimization analysis. Specifically, in the case of the optimum depolarization factors obtained considering the 3–37 GHz data, shown in Figure C.2(a), beyond $m_v = 2\%$ the coefficient A_{w1} was set to 0.05. Similarly for the case of only 3–10 GHz data analyzed, for which

the shape coefficients are shown in Figure C.2(b). A_{w1} was set to be 0.05 for $m_v > 2.5\%$. As seen in Figure C.4, the severe discontinuities have disappeared despite the continued use of the very discontinuous functions A_{w2} and A_{w3}. Additionally, (1) both of the optimum solutions are seen to give essentially the same predictions, and (2) these predictions are superior to the ones which are generated using the values of the shape coefficients which are given in Abdelrazik (1984) and Hallikainen et al. (1986).

The variations as a function of m_v of the two larger depolarization factors can in fact be dispensed with altogether. In Figures C.5–C.8 we show predictions generated for seven different frequencies between 3 and 37 GHz, using the following values for the depolarization factors:

$$A_{w1} = 0.05 \tag{C.5}$$

$$A_{w2} = 0.475 \tag{C.6}$$

$$A_{w3} = 0.475 \tag{C.7}$$

It can be seen in every case that these values produce predictions which are superior to those obtained using the coefficients specified in the earlier study. In addition, it is seen that the overall quality of the agreement between the measured data and the predictions from the Polder-Van Santen mixing model is not especially high.

The "Debye-like" model predictions (produced by using Eqs. (3.13) and (3.8)) are also shown in the figures. It is seen that this model gives generally very good agreement with the data. However, there is apparently an error in the formulation of the Debye-like model as it is given in Hallikainen et al. (1986). The following expressions are reproduced from

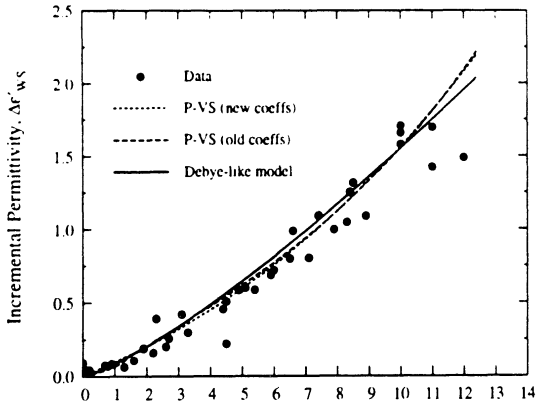

(a) 3 GHz, $\Delta\varepsilon'_{ws}$.

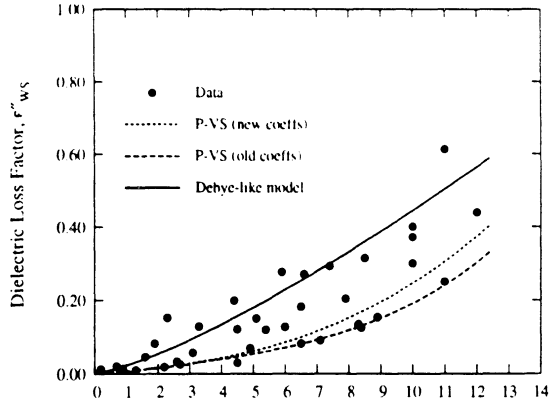

(b) 3 GHz, ε''_{ws}.

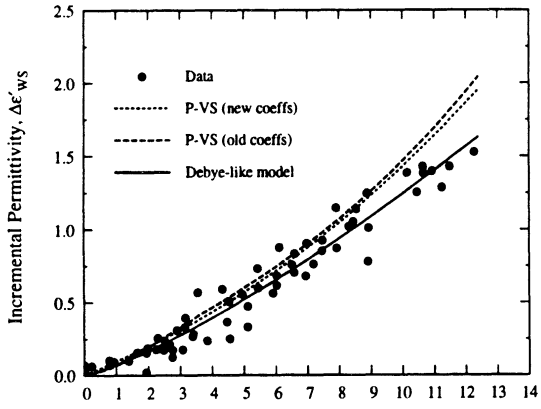

(c) 6 GHz, $\Delta\varepsilon'_{ws}$.

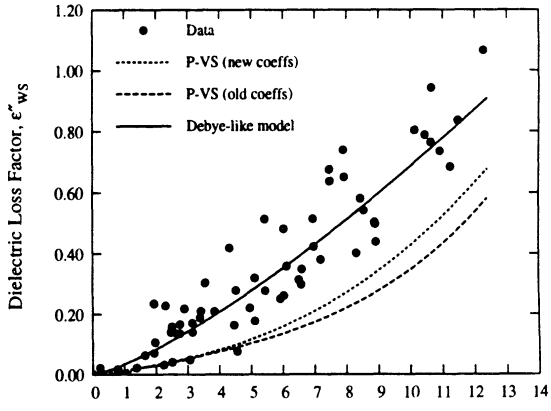

(c) 6 GHz, ε''_{ws}.

Figure C.5: Comparison of model predictions with measured values of $\Delta\varepsilon'_{ws}$ and ε''_{ws} at 3 and 6 GHz. "old coeffs." corresponds to the values for depolarization factors found in original study; "new coeffs." uses $A_{w1} = 0.05$, $A_{w2} = A_{w3} = 0.475$.

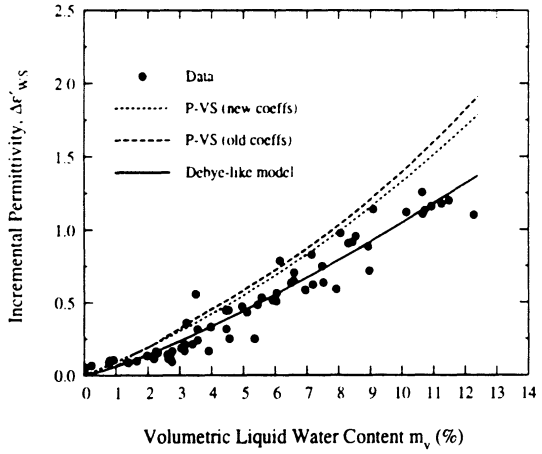

(a) 8 GHz, $\Delta\varepsilon'_{ws}$.

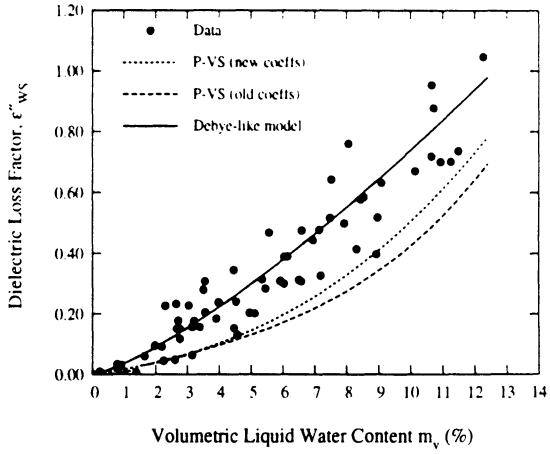

(b) 8 GHz, ε''_{ws}.

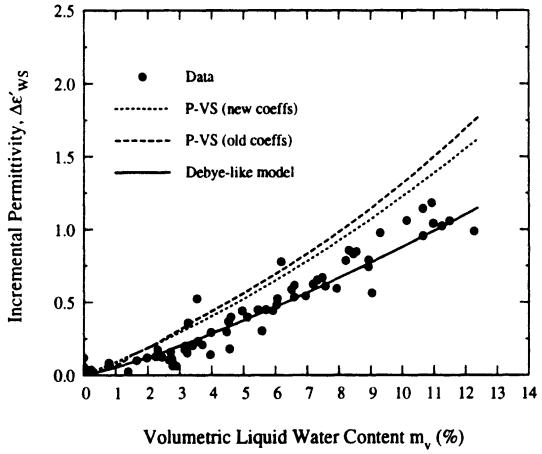

(c) 10 GHz, $\Delta\varepsilon'_{ws}$.

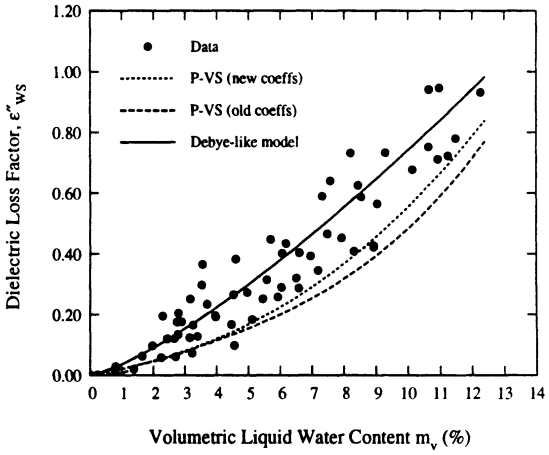

(c) 10 GHz, ε''_{ws}.

Figure C.6: Comparison of model predictions with measured values of $\Delta\varepsilon'_{ws}$ and ε''_{ws} at 8 and 10 GHz. "old coeffs." corresponds to the values for depolarization factors found in original study; "new coeffs." uses $A_{w1} = 0.05$, $A_{w2} = A_{w3} = 0.475$.

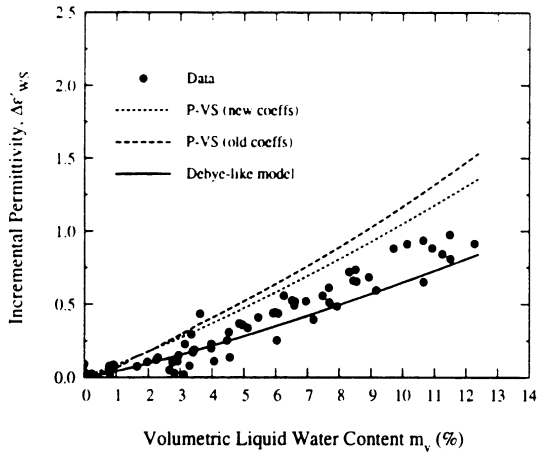

(a) 14 GHz, $\Delta\varepsilon'_{ws}$.

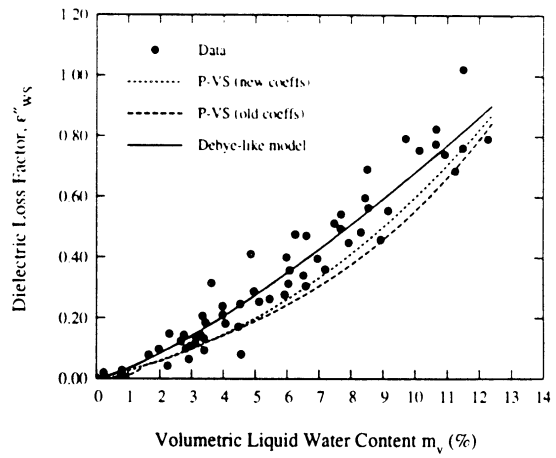

(b) 14 GHz, ε''_{ws}.

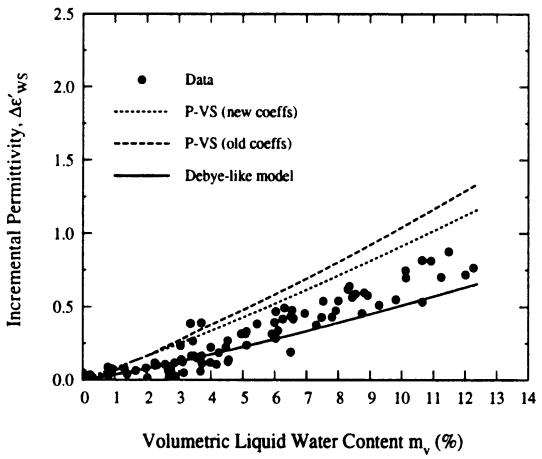

(c) 18 GHz, $\Delta\varepsilon'_{ws}$.

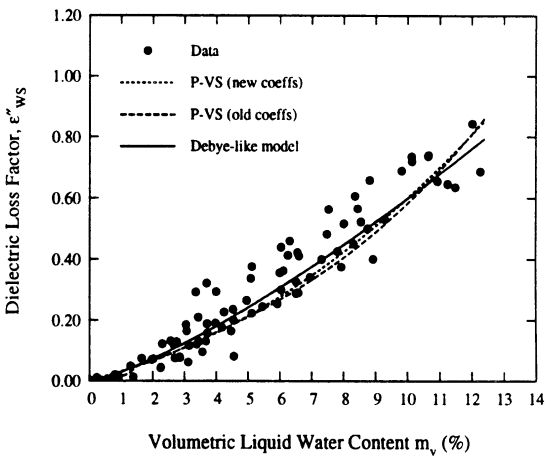

(c) 18 GHz, ε''_{ws}.

Figure C.7: Comparison of model predictions with measured values of $\Delta\varepsilon'_{ws}$ and ε''_{ws} at 14 and 18 GHz. "old coeffs." corresponds to the values for depolarization factors found in original study; "new coeffs." uses $A_{w1} = 0.05$, $A_{w2} = A_{w3} = 0.475$.

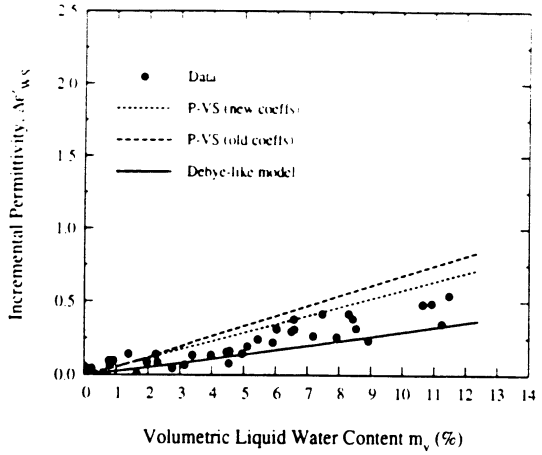

(a) 37 GHz, $\Delta\varepsilon'_{ws}$.

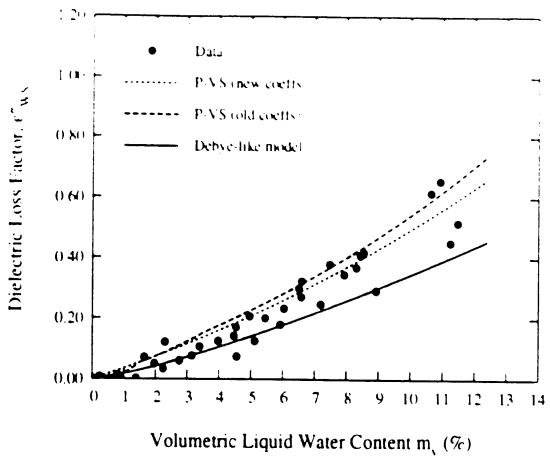

(b) 37 GHz, ε''_{ws}.

Figure C.8: Comparison of model predictions with measured values of $\Delta\varepsilon'_{ws}$ and ε''_{ws} at 37 GHz; "old coeffs." corresponds to the values for depolarization factors found in original study; "new coeffs." uses $A_{w1} = 0.05, A_{w2} = A_{w3} = 0.475$.

that paper:

$$\varepsilon'_{ws} = A + \frac{Bm_v^x}{1+(f/f_o)^2} \tag{C.8}$$

$$\varepsilon''_{ws} = \frac{C(f/f_o)m_v^x}{1+(f/f_o)^2} \tag{C.9}$$

where,

$$A = 1.0 + 1.83\rho_{ds} + 0.02A_1 m_v^{1.015} + B_1 \tag{C.10}$$

$$B = 0.073A_1 \tag{C.11}$$

$$C = 0.073A_2 \tag{C.12}$$

$$x = 1.31 \tag{C.13}$$

$$f_o = 9.07 \text{ GHz} \tag{C.14}$$

where, $A_1 = A_2 = 1.0$ and $B_1 = 0$ below 15 GHz. The following expressions are recom-

mended for use above 15 GHz:

$$A_1 = 0.78 + 0.03f - 0.58 \times 10^{-3} f^2 \tag{C.15}$$

$$A_2 = 0.97 - 0.39f \times 10^{-2} + 0.39 \times 10^{-3} f^2 \tag{C.16}$$

$$B_1 = 0.31 - 0.05f + 0.87 \times 10^{-3} f^2 \tag{C.17}$$

The error which we have detected is associated with the frequency dependent empirical factors A_1 and B_1 shown above. If the coefficients are used at 37 GHz, negative values of $\Delta\varepsilon''_{ws}$ result. An examination of the dissertation by Abdelrazik (1984)[pp. 143–145], upon which the paper by Hallikainen et al. is based, shows the correction factor A_1 (called b_1 in the dissertation) being applied to the *entire* formula given in Eq. (C.8), including the portion, $1 + 1.83\rho_{ds}$, which computes the effective dry snow dielectric constant ε'_{ds}. In Hallikainen et al. however, apparently to remain consistant with their thesis that ε'_{ws} can be explained entirely as an incremental quantity due to liquid water added to the dry snow dielectric, the correction factors are not applied to that portion of the expression for ε'_{ws} which computes the dry snow dielectric.

Unfortunately, even when the formula was implemented as described in Abdelrazik (1984) negative values were still obtained for $\Delta\varepsilon'_{ws}$ at 37 GHz. Thus, the unmodified versions, given in Eqs. (C.8) and (C.9) have been used in this presentation for all the frequencies shown.

As a final note on this issue of the effect of different shape coefficients on the predictions of the Polder-Van Santen dielectric mixing model, we present two set of plots which illustrate that the model output is primarily dependent upon the smallest coefficient of the three. In Figure C.9 we compare results generated using the P-VS model with the three depolarization factors given in Eqs. (C.5)–(C.7), with a case where the smallest factor, A_{w1} is the same as Eq. (C.5) (i.e. 0.05), but the other two are set to widely different values: $A_{w2} = 0.625$ and $A_{w3} = 0.325$. It is seen that there is very little effect produced by these changes at either 3 or 37 GHz.

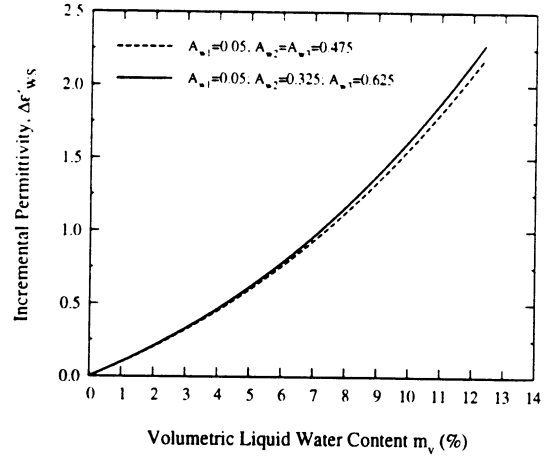

(a) 3 GHz, $\Delta\varepsilon'_{ws}$.

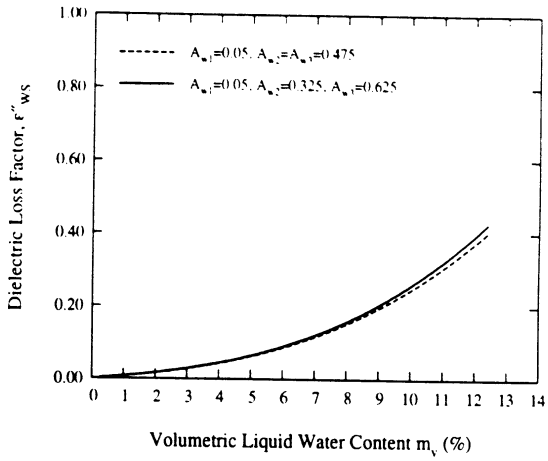

(b) 3 GHz, ε''_{ws}.

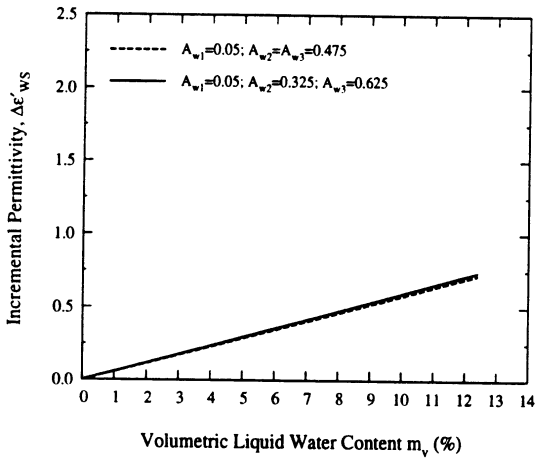

(c) 37 GHz, $\Delta\varepsilon'_{ws}$.

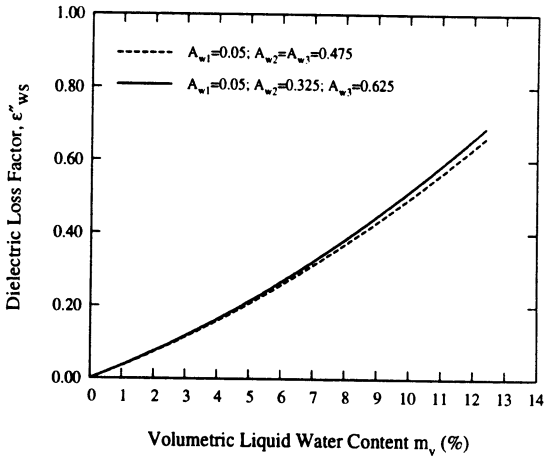

(c) 37 GHz, ε''_{ws}.

Figure C.9: Predictions of $\Delta\varepsilon'_{ws}$ and ε''_{ws} at 3 and 37 GHz, for two different sets of depolarization factors (values given on the figures). The smallest factor (A_{w1}) is identical in both cases; the values of the other two factors (A_{w2},A_{w3}) are significantly different between the two cases.

Figure C.10 presents a comparison between, again, predictions generated using factors from Eqs. (C.5)–(C.7), and those generated from a case where the smallest depolarization factor, A_{w1}, has been slightly changed from 0.05 to 0.07. The two larger coefficients are es-

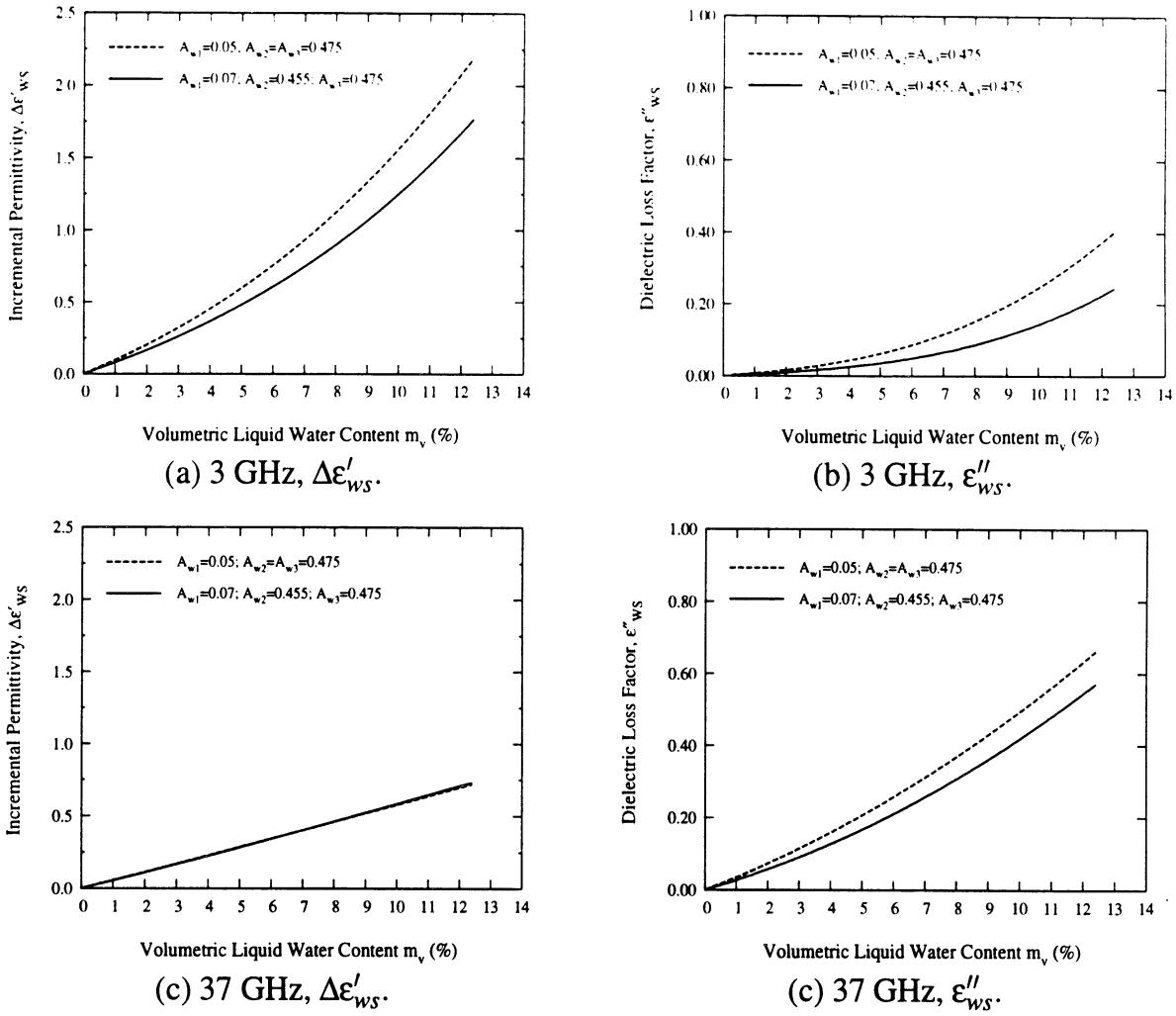

(a) 3 GHz, $\Delta\varepsilon'_{ws}$. (b) 3 GHz, ε''_{ws}.

(c) 37 GHz, $\Delta\varepsilon'_{ws}$. (c) 37 GHz, ε''_{ws}.

Figure C.10: Predictions of $\Delta\varepsilon'_{ws}$ and ε''_{ws} at 3 and 37 GHz, for two different sets of depolarization factors (values given on the figures). The smallest factor (A_{w1}) is slightly different in the two cases (0.05 *versus* 0.07); the values of the other two factors (A_{w2},A_{w3}) are nearly identical in both cases.

sentially the same as the former case except for small changes ($A_{w2} = 0.475$,$A_{w3} = 0.455$) required to satsify the constraint (required in the P-VS model (Polder and Van Santen 1946)) $A_{w1} + A_{w2} + A_{w3} = 1$. It is seen that a small adjustment in the smallest coefficient substan-

tially affects the result, with the exception of the quantity $\Delta\varepsilon'_{ws}$ at 37 GHz, is essentially unaffected.

In conclusion:

1. From a re-analysis of the original data, it has been found that the shape coefficients given for the Polder-Van Santen dielectric mixing model in Abdelrazik (1984) and Hallikainen et al. (1986) are not the values leading to the smallest error between the model predictions and the measured data.

2. A simpler set of coefficients, which are *independant of the volumetric liquid water content, m_v,* have been shown (in Figures C.5–C.8) to produce better agreement than the coefficients specified in the aforementioned references. The transition which is present in the values of the two shape coefficients A_{w1} and A_{w2} (Figure C.2), as it has already been mentioned, indicates a change in the geometry of the water inclusions from a needle-like shape to a disc-like shape. This transition was cited in Hallikainen et al. as providing evidence in support of a change in the character of snow as its wetness level increases from the *pendular regime* to the *funicular regime*. In the pendular regime, water is thought (Colbeck 1980; Denoth 1980) to exist as discrete entities in the snow with air being continuous throughout the medium; in the funicular regime, water is continuous throughout the medium and the air exists in discrete pockets. In light of the re-analysis presented here, it must be acknowledged that no support for this theory is available from the wet snow dielectric measurements which have been the subject of this appendix.

3. Even with the new coefficients, the agreement is not of a particularly high quality.

4. Examples have been presented which indicate that when one of the three shape coefficients is sufficiently small, say <0.1, the model result is very insensitive to the values of the other two coefficients.

APPENDIX D

K_U-BAND RADAR

This appendix describes the design of the K_u-band radar and also gives details important for the proper use of the instrument.

D.1 RF Circuit

For ease of reference, Figure 5.6 is reproduced below as Figure D.1. As mentioned in Chapter V, an HP Network Analyzer (NWA) (normally 8753C model was used) is an integral part of the radar system. The NWA provides the coherent IF signal in a stepped fashion over the bandwidth selected. In the present case, an IF bandwidth of 2 GHz from 1–3 GHz is stepped through in 201 frequency steps. The NWA provides coherent detection, and has time domain capability to allow isolation (gating) of the response associated with a particular time bin.

The radar box itself provides for upconversion, polarization selection, and downconverion. The schematic of the RF circuit for the radar is shown in Figure D.2. The output from a 14 GHz local oscillator is split three ways. One third of the power is mixed with the IF sent in from the NWA, and amplified. The lower mixing product is filtered out and the resulting 15–17 GHz signal is switched under computer control (*via* control lines shown in Figure D.1) to either the v- or h-port of the orthomode transducer which is attached to a horn antenna of square cross-section. The RF energy received by the antenna is directed by

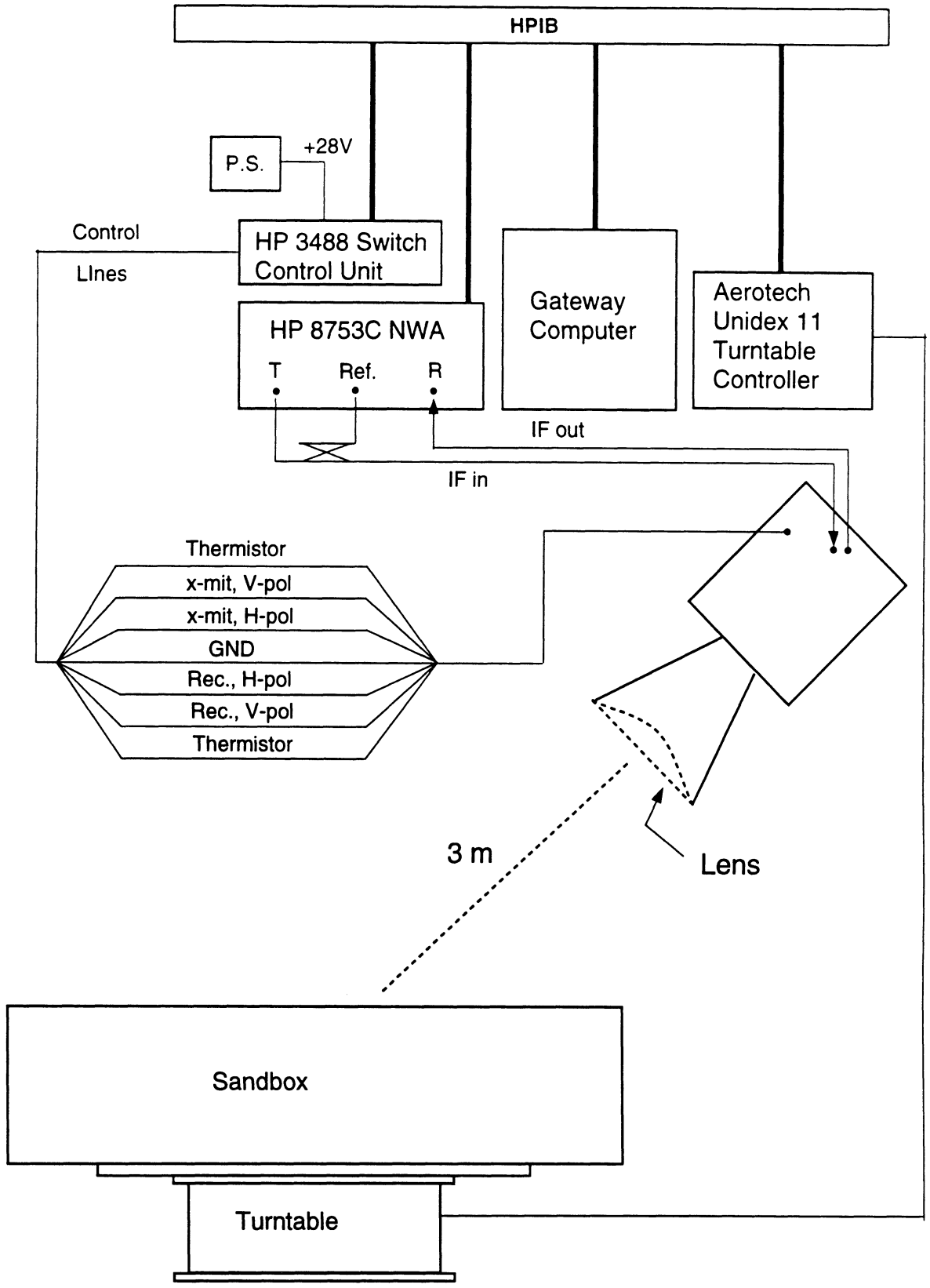

Figure D.1: Schematic of experimental setup.

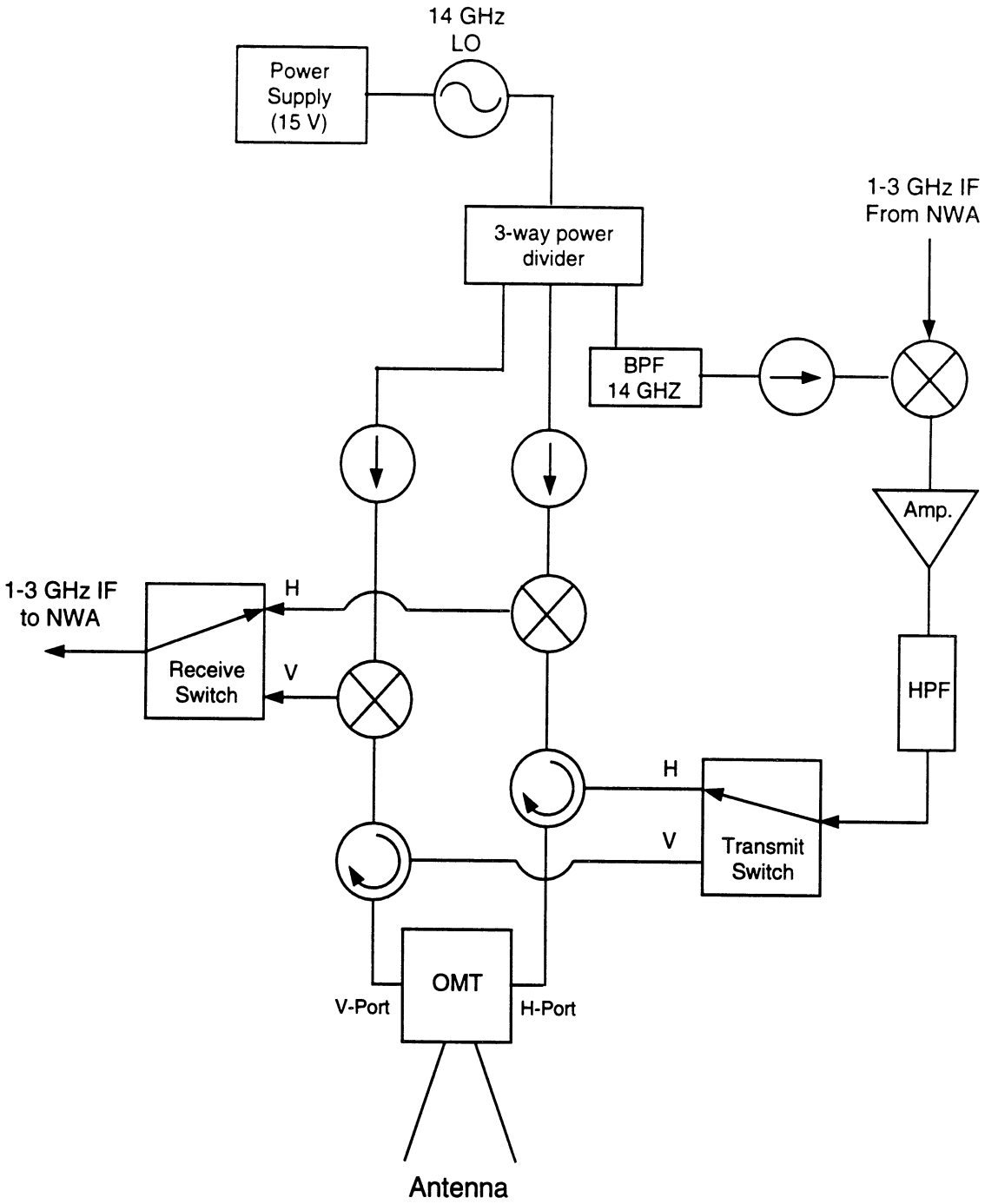

Figure D.2: Schematic of K_u-band RF circuit.

the circulators shown to mixers where they combine with the other two portions of the local oscillator output which was split three ways. The output from the mixers goes to a receive switch where the desired polarization is selected. A detailed breakdown of the components used is given in Table D.1. Photographs of the open RF box of the radar, showing the geometry of the antenna attachment and much of the RF circuit are provided in Figure D.3.

In addition to the circuit described, the radar box is equipped with means for temperature control. A rubberized flexible heating pad (Omega, model SSHB-612-180-120-P) covers the underside of the plate on which the RF components are mounted. The current to the heating pad is controlled by a heater controller (Dowty Electronics Co., Temperature Controller Model 72A) set to 40° C (104° F). To monitor the temperature, a thermistor (Omega, Linear Thermistor Composite, 44032) is glued to the top side of the RF plate. The terminals of the thermistor are accessed through the control lines (Figure D.1). The resistance-temperature function of the thermistor is given by,

$$T = \left[A + B\ln(R) + C(\ln(R))^3\right]^{-1}, \tag{D.1}$$

where T is in degrees Kelvin and R is in ohms. Finally, the entire box is lined with one inch thick styrofoam for insulation. AC power is provided to the radar box for the heater controller and for a DC power supply which provides the 15 V DC required by the LO and the amplifier.

D.2 Antenna Design and Lens Correction

A very compact design is enabled for the antenna through the use of a dielectric lens placed at the aperture to correct for phase error. The geometry of the antenna is shown in Figure D.4. A design of successive 5° flares is used to minimize the generation of cross-pol which is produced at any discontinuity. To produce the desired narrow beam, on the order of 5°, the square aperture must be the size shown in the figure, about 13λ. Unfortunately,

Component	Mfg.,Model No.	Specifications
Oscillator	Miteq, H-series -st	14 GHz, 13 dBm, 15 V, 100 mA
OMT	Atlantic Microwave, OM6203	15–17 GHz, isol. >45 dB, VSWR<1.1
Isolators	MRI, CB180I	15–17 GHz, <0.3 dB ins. loss,
Circulators	MRI, CB180C	<1.15 VSWR, >25 dB isol.
Mixer	FEI, 2200D0150-01	Duroid, conv. loss <7 dB, Isol(LO-RF)>30 dB Isol(LO-IF)>25 dB, VSWR(RF & LO)<2.5, LO Power +7–+13 dBm
Filter (high pass)	MRI, FLDP-16	15–17 GHz, 5 sections, <0.5 dB ins. loss
Filter (band pass)	MRI, FLPA-14	f_c= 14 GHz, -20 dB @ 13 & 15 GHz, 0.1 dB ripple, 1 dB ins. loss
Power Divider (3-way)	MRI, PD3W-14	<-30 dB @ 14 GHz, 0.7 dB ins. loss Ampl. Bal.=±0.4 dB, isol > 16 dB, VSWR < 1.5
Switch (stdp) (electromechanical)	Macom, 7530-6414-00	DC–18 GHz, 70 dB isol., 0.5 dB ins. loss VSRW <1.4, 28 V, 15 ms, latching
Amplifier	Miteq, AMF-5B-150170-15P	15–17 GHz, G=25-30, F(noise fig.)<7 dB, power (1 dB comp.)> 15 dBm, VSWR (in,out)<2, 15 V, 250 mA

Table D.1: K_u-Band RF unit components.

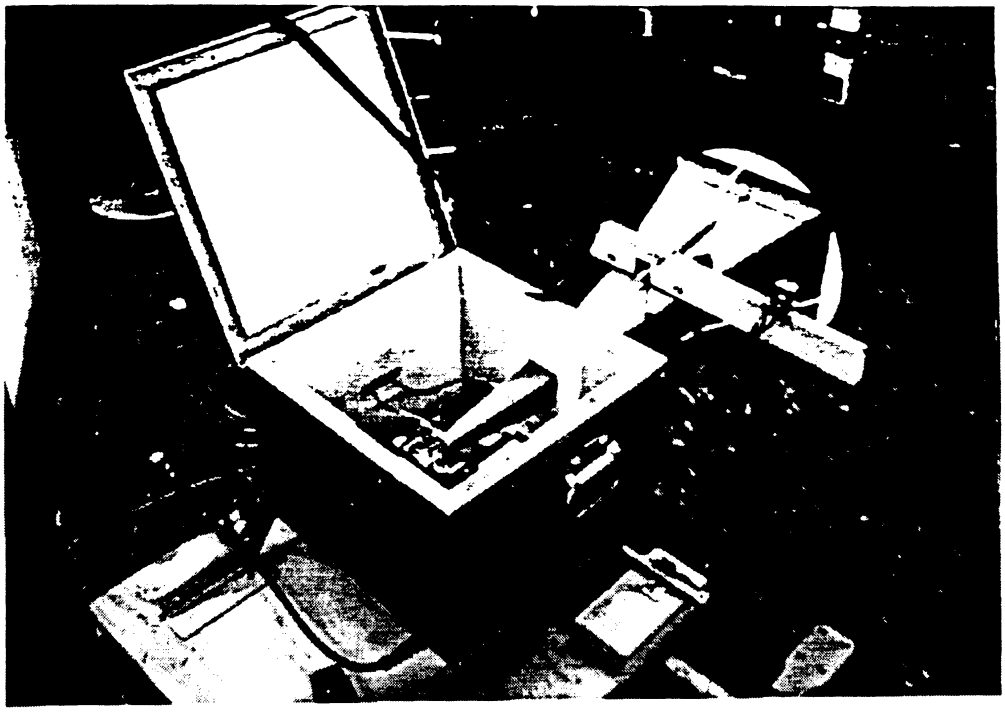

(a)

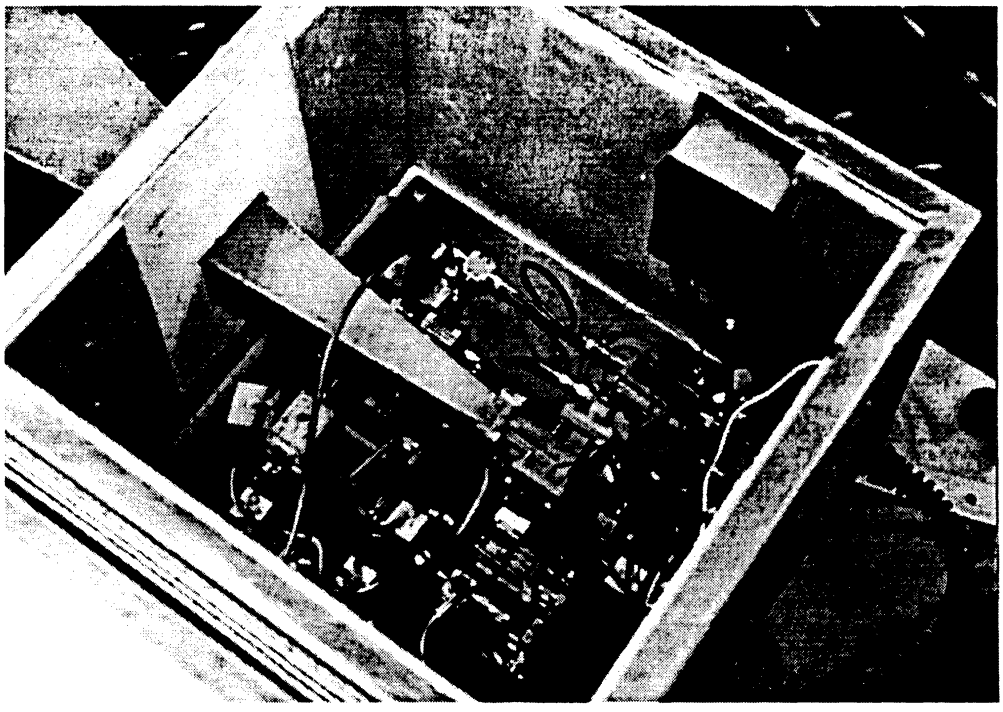

(b)

Figure D.3: Photographs of the K_u-band radar: (a) Geometry of antenna and RF box; (b) Close-up of RF-circuit.

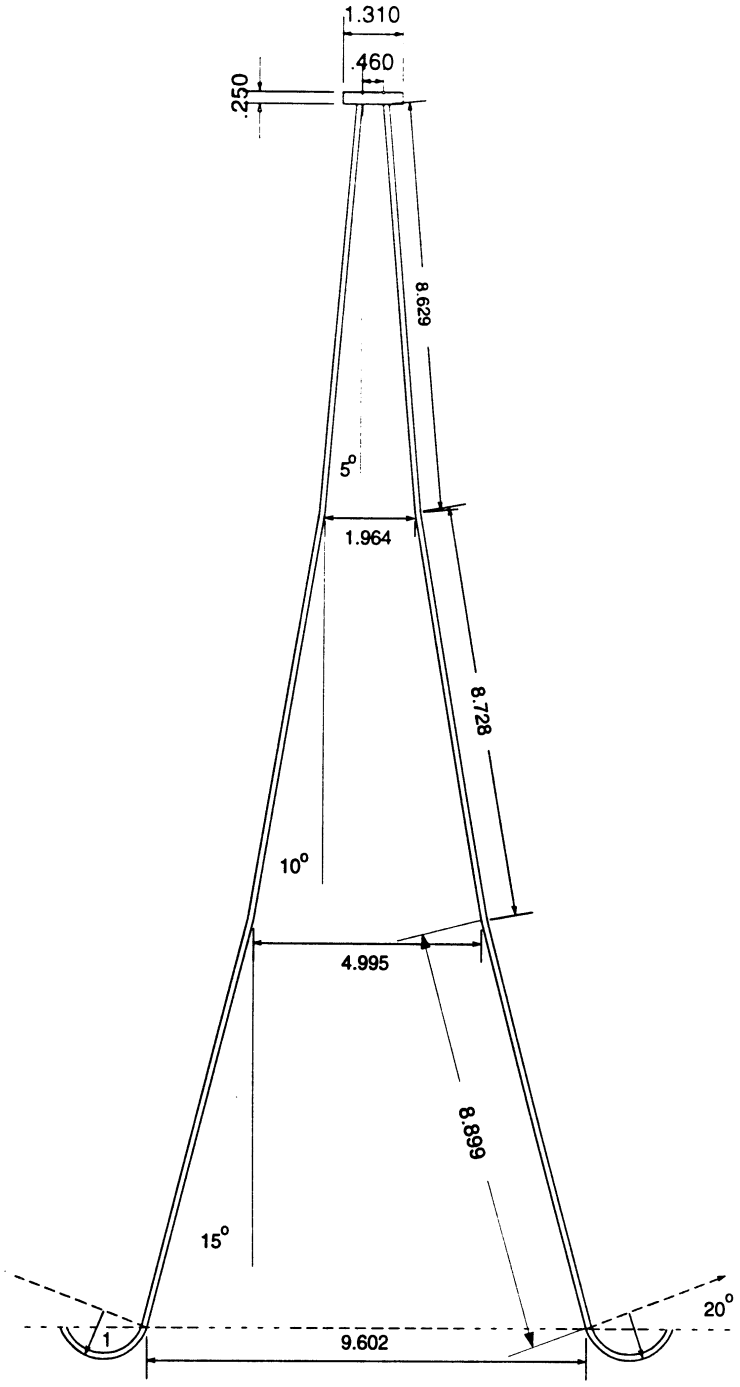

Figure D.4: Schematic of K_u-band antenna.

the antenna length which must be used in conjunction with an aperture of this size to produce an optimal pattern is about 1.6 meters. While this is comparable to the lengths of other horns used in the LCX POLARSCAT system, it is an unwieldy length for use in indoor experiments such as the present one, depicted in Figure 5.7. Using a lens, the same beamwidth was achieved while having an antenna length of only 66 cm. The following paragraphs describe the process by which the lens correction was achieved.

To optimally correct for the phase error, a mathematical description of the error should be obtained. The phase error associated with the present design, because of the system of successive flares employed cannot be simply calculated through geometrical considerations. Instead, we sought to find parameters of a standard gain square horn which would give approximately the same aperture field distribution as our horn, or equivalently, the same far-field antenna pattern. From Balanis (1982) (Chapter 12) the patterns for such horns are specified in terms of two parameters: (1) ρ which is the distance from the apex (which is approximately, but not strictly, the location of the throat of the horn) to the aperture, and (2) b which is the side dimension of the square aperture. The values which gave an antenna pattern closely resembling our uncorrected one were $\rho = 40\lambda$ and $b = 16\lambda$. For comparison, the physical dimensions of the antenna are $\rho = 35\lambda$ and $b = 13\lambda$. A comparison of the measured and theoretical far-field patterns is given in Figure D.5.

Formulas for lenses suitable for transforming the phase error associated with this horn into a uniform distribution at the aperture are expressed in terms of a focal length, F, which corresponds to the ρ obtained in the previous analysis. A lens design was chosen which employs both surfaces of the lens as refracting surfaces. In the most common type of lens with a single refracting surface, the curved refracting surface faces into the horn, and a flat surface faces out. In such a configuration reflections of the transmitted wave off the flat surface are re-focused into the apex of the antenna. The lens which was designed, with two refracting surfaces, is depicted in Figure D.6. As shown, rays undergo refraction at both surfaces. The formulas for the lens design are given in the *Antenna Handbook* (Lee 1988).

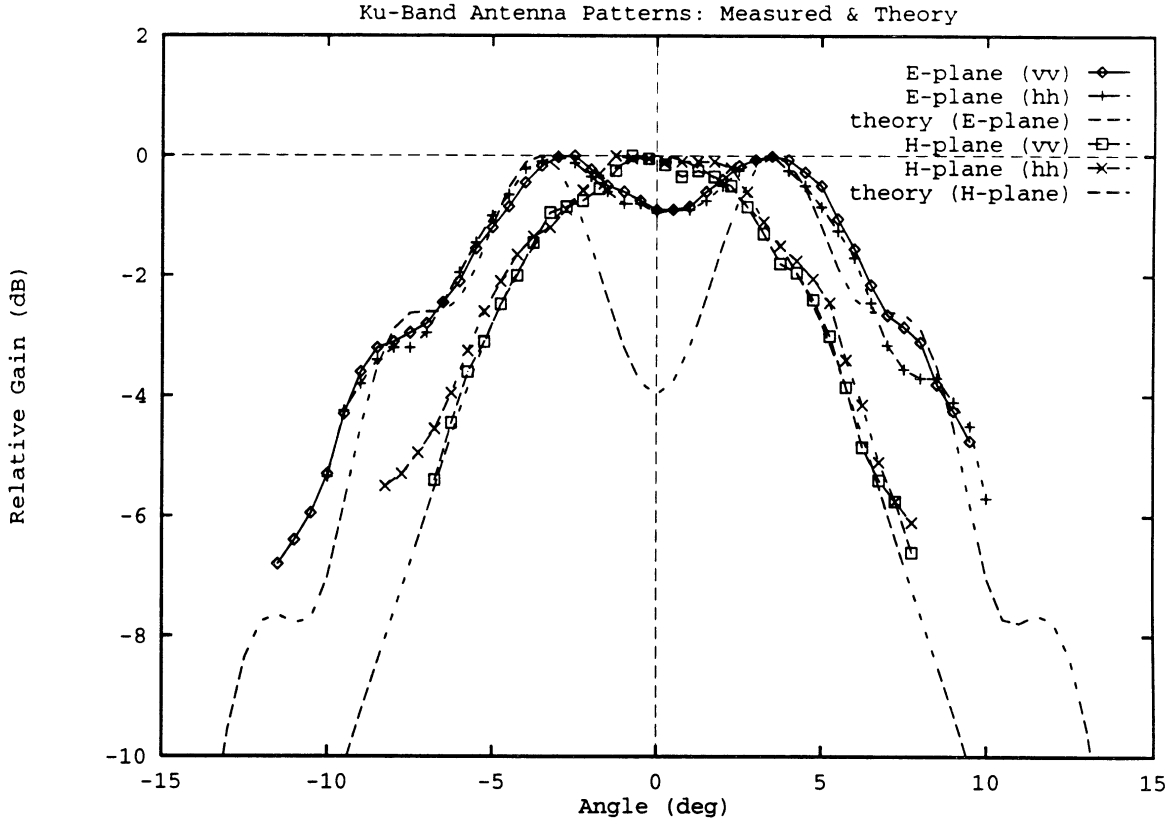

Figure D.5: Measured and theoretically predicted far-field antenna pattern for the uncorrected antenna .

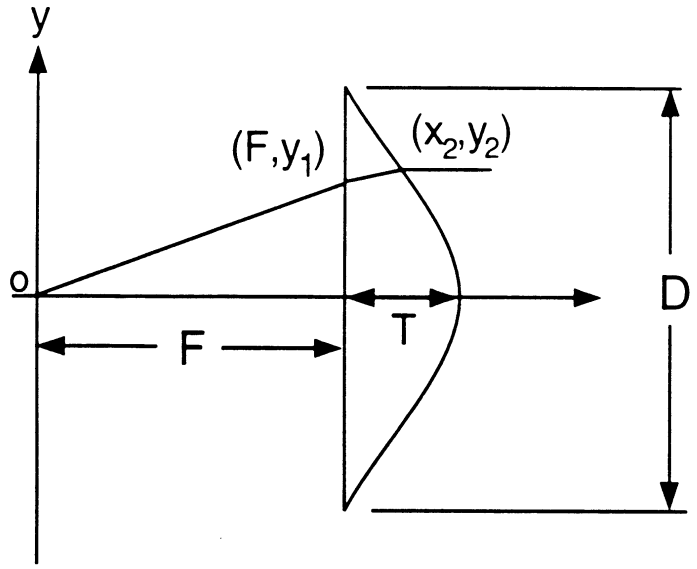

Figure D.6: Geometry of lens for design formula.

They are,

$$T = \frac{\sqrt{4F^2 + D^2} - 2F}{2(n-1)} \tag{D.2}$$

$$x_2 = \frac{\left[(n-1)T - \sqrt{F^2 + y_1^2}\right]\sqrt{(n^2-1)y_1^2 + n^2F^2} + n^2F\sqrt{F^2 + y_1^2}}{n^2\sqrt{F^2 + y_1^2} - \sqrt{(n^2-1)y_1^2 + n^2F^2}} \tag{D.3}$$

$$y_2 = y_1\left[1 + \frac{x_2 - F}{\sqrt{(n^2-1)y_1^2 + n^2F^2}}\right] \tag{D.4}$$

where the various length designations are as shown in Figure D.6. In addition, n is the index of refraction of the lens material. The material used was ultra high molecular weight (UHMW) polyethylene. The dielectric constant was measured by the same free space nadir reflection technique described in Section 5.6 with respect to slabs of absorber. It was found to be 2.3. Using coordinates obtained by the formulas given above, the lens was manufactured by the author using a lathe.

Figure D.7 shows the result of the lens correction on the on the far-field antenna pattern. The optimal pattern which could be achieved for an aperture this size (computed us-

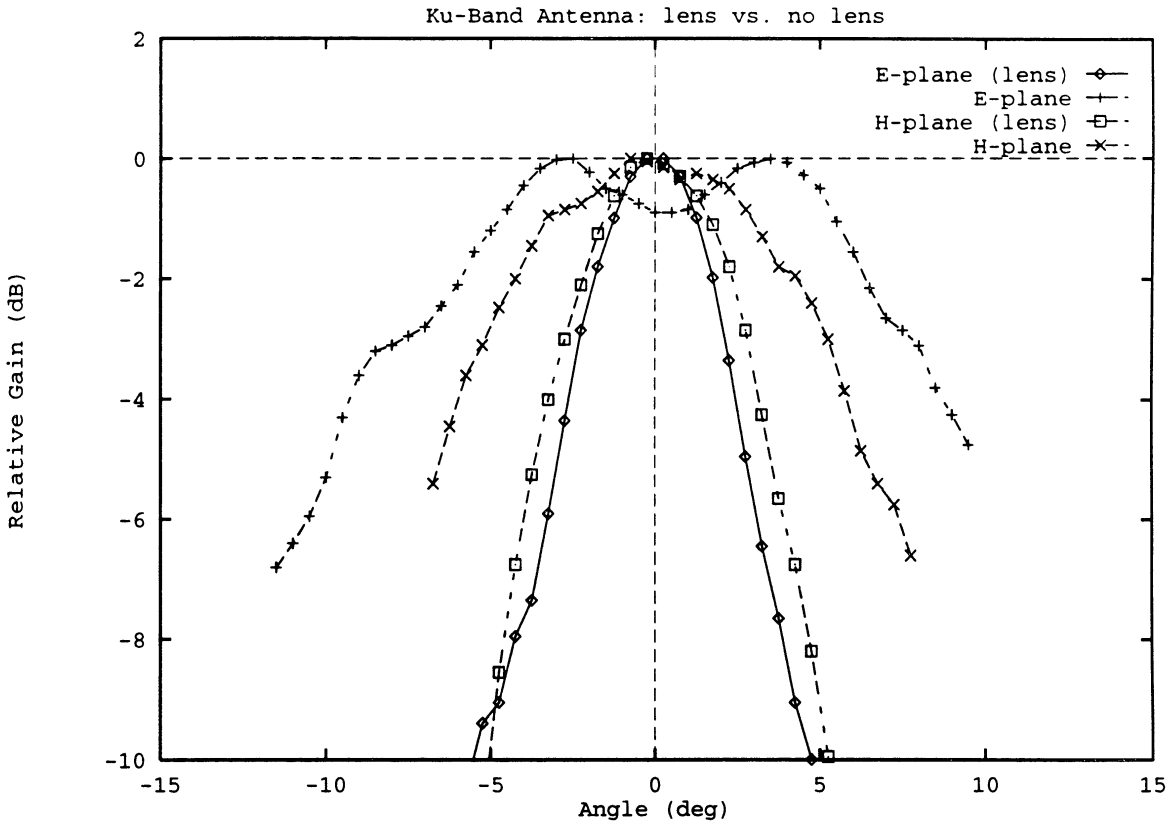

Figure D.7: Corrected (with lens) and uncorrected far-field E- and H-plane patterns of the K_u-band antenna.

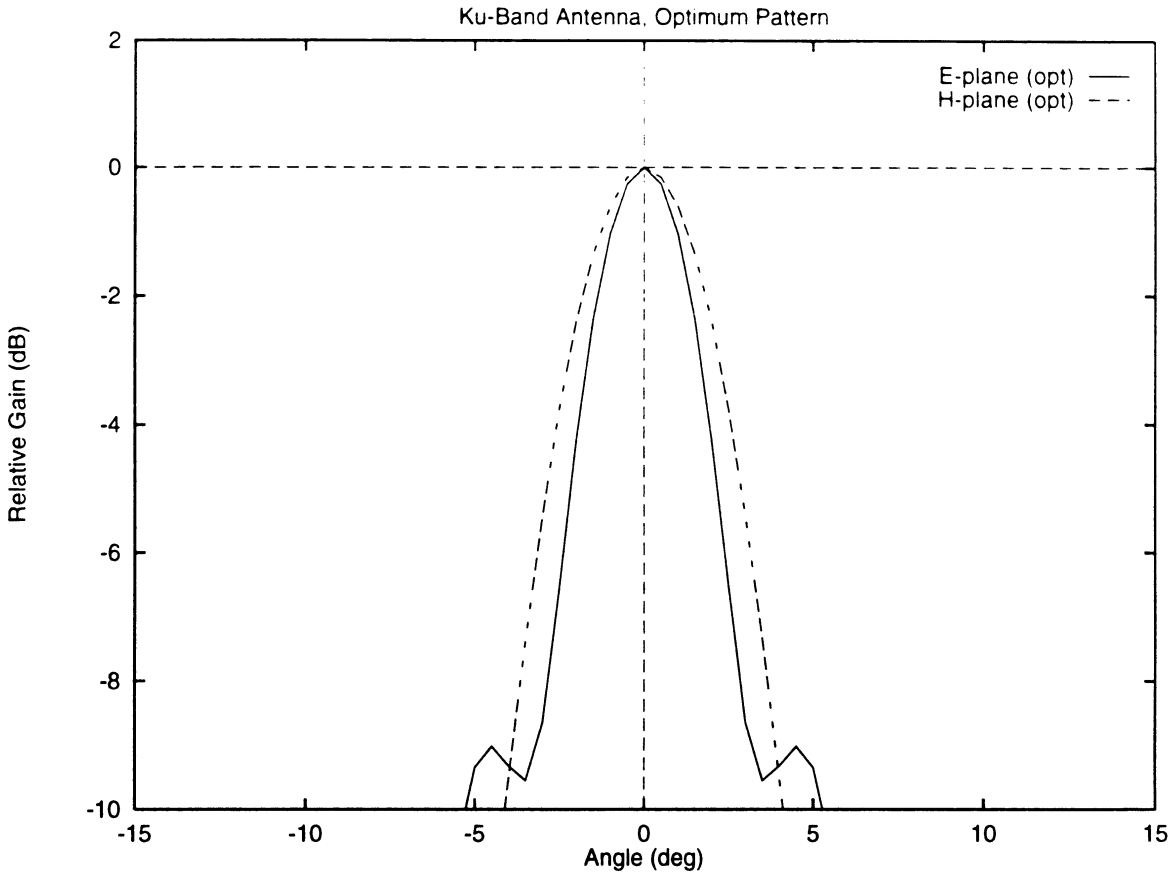

Figure D.8: Optimal E- and H-plane patterns for square horn with aperture 16λ on a side.

ing formulas from Balanis (1982))is shown in Figure D.8. The beamwidths obtained for the corrected antenna are slightly wider than those corresponding to the optimal case, but the overall improvement is quite dramatic.

The absolute gain of the antenna was not measured directly, but the theoretical gain (from Balanis (1982)) of the optimal horn is 30.8 dB. The theoretical gain of the uncorrected version was 18.8 dB. Thus, an improvement of 12 dB should have been realized by the lens correction. In Figure D.9 time domain traces corresponding to observing a 12" sphere at a distance of 11.4 m in an anechoic chamber are shown. Shown are cases with an uncorrected antenna and with a lens-corrected antenna. The sphere response (occurring at the far right of the figures) of the corrected version is seen to be approximately 20 dB higher. Since this is for a two-way, antenna pattern, it corresponds to a one-way gain improvement of about

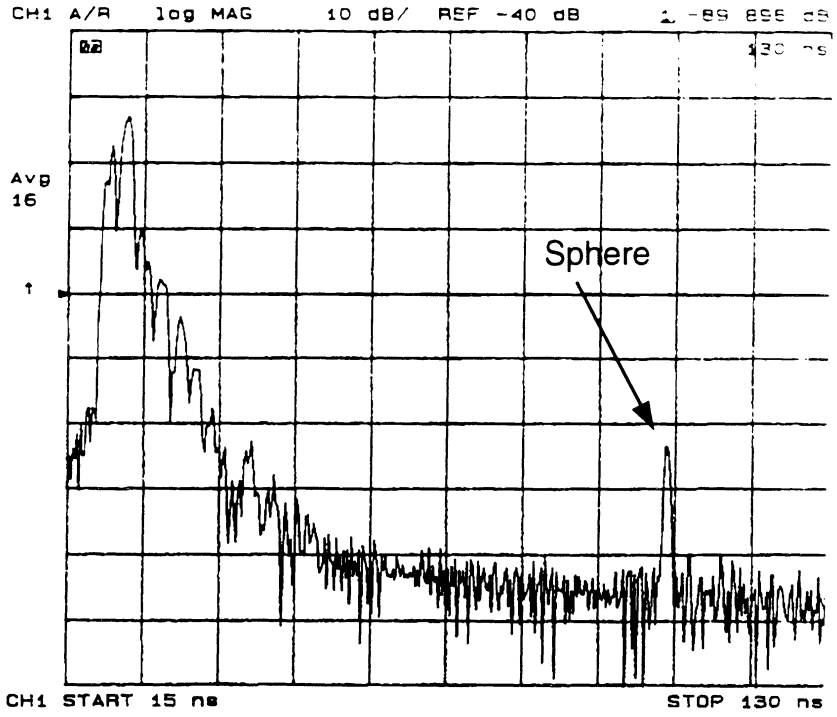

(a) 12" Sphere (no lens correction)

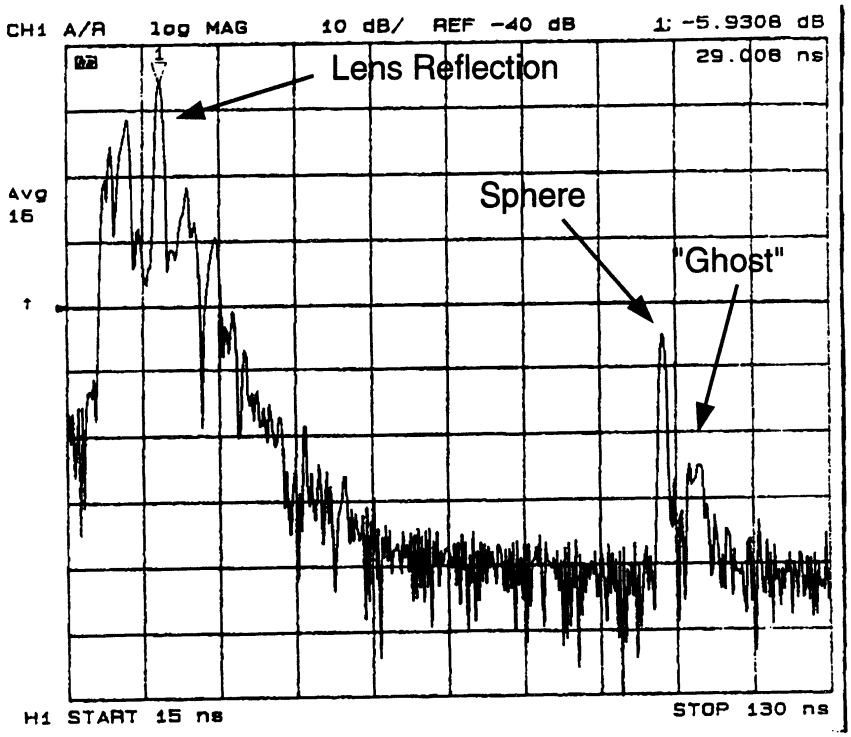

(b) 12" Sphere (lens correction)

Figure D.9: Time domain trace showing target response with (a) and without (b) lens on antenna. Response is for HH-pol at 11.4 meters.

10 dB, close to the theoretical improvement.

This Figure also shows two disadvantantages associated with the lens, one expected but the other unanticipated. The expected drawback has to to with the internal reflection the transmitted wave experiences when it encounters the lens. Referring to the schematic of the RF circuit (Figure D.2), of the energy which is transmitted (referring to the point just beyond the transmit switch), an amount reduced only by the isolation of the circulators (about 20 dB) is sent directly to the receiver. In addition, of the energy which is directed by the circulators towards the antenna, reflections due to impedance mismatches at the OMT are directed back through the circulators to the receiver with essentially no additional attenuation. These effects produce the very large responses at the far left of the plots in Figure D.9. The effect of the addition of the dielectric mismatch represented by the lens is plainly evident. These very large near-range reflections set the noise level of the system, through spectral leakage (ie. a discrete feature in the frequency domain is transformed *via* an IFFT to a feature of infinite extent in the time domain). This is one major disadvantage of single antenna systems. Thus, more severe near-range (or system) reflections result in a higher noise floor. This is also evident in the figure, the noise floor of the lens-corrected case being about 5 dB higher than the uncorrected. The large mismatch the lens presents can be partially addressed through the use of impedance matching on the lens. This will be addressed below.

The second disadvantage of the lens, which was unanticipated, is also shown in Figure D.9, is the generation of a "ghost" peak, appearing just downfield of the sphere response. In the figure, this peak is about 5 ns downfield from, and about 20 dB below the main sphere response. A time delay of 5 ns for a wave traveling at the speed of light corresponds to a distance of about 1.5 m. This is roughly twice the length of the antenna, so it seems as though the phenomenon is probably related to a double reflection mechanism that a portion of the transmitted wave undergoes between the lens and the throat of the horn or the OMT. We were unfortunately unable to get rid of this ghost peak, even by the application of impedance

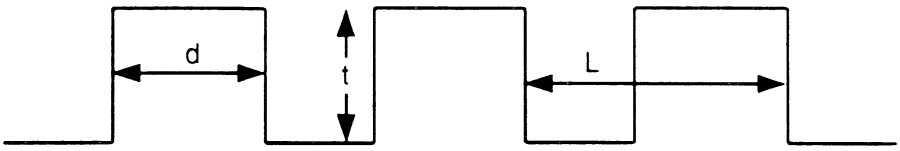

Figure D.10: Groove geometry corresponding to formulas for impedance transformer layer.

matching to the lens which is described next.

The impedance matching was accomplished by milling grooves in the flat surface of the lens to create an appropriate quarter wave transformer matching the impedance of the lens to that of air. The design formulas given in Sarabandi (1990) were used to specify a groove geometry which would produce an effective dielectric equal to $\sqrt{\varepsilon_l \varepsilon_a}$, where ε_l is the dielectric constant of the lens material (2.3) and ε_a is the dielctric constant of air (1.0). The formula is

$$\varepsilon_{eff} = 1 + (\varepsilon_l - 1)\frac{d}{L} \tag{D.5}$$

where the dimensions d and L are shown in Figure D.10. The depth of the groove is one quarter wavelength at the center frequency of operation (16 GHz). Parallel grooves were milled in the lens, and the lens was fixed onto the aperture with the grooves horizontally oriented. The result is shown for the H-pol response of the 12" sphere in Figure D.11. The lens reflection is reduced by about 8 dB, and the noise floor is lowered by a couple of dB. The ghost peak beyond the sphere response appears to be somewhat reduced, however this is actually due to another measure which was taken: the orientation of the lens was changed so that the flat side of the lens was facing *into* the antenna. Although this is not consistant with the double refracting design of the lens, it was found that this measure did offer some reduction of the ghost peak while all other attributes remained essentially unchanged. The V-pol response was unaffected with the grooves oriented horizontally. One other effect of

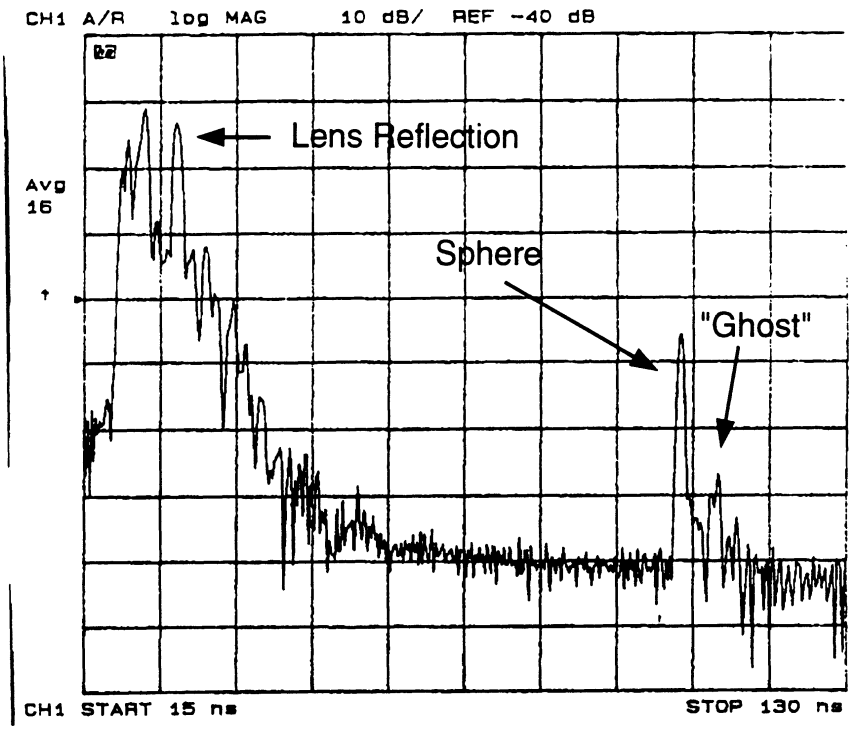

Figure D.11: Time domain trace showing target response with after an impedance matching surface has been milled onto the flat surface of the lens. In this instance, the orientation of the lens has also been changed so that the flat surface is facing into the antenna. Response is for HH-pol at 11.4 meters.

the matching grooves was a worsening of the cross-pol isolation, due apparently to the discontinuities inherent in the groove design. Given the relatively minor benefits attained by the matching grooves, compared to the threat of additional deterioration of the cross-pol isolation, it was decided to forego the application of an orthogonal set of grooves for the VV channel.

D.3 Calculation of σ° using Illumination Integral

This general expression for power received from a point target is

$$P_r = \frac{P_t G_t(\theta_t, \phi_t) G_r(\theta_r, \phi_r) \lambda^2 \sigma}{(4\pi)^3 R^4}, \tag{D.6}$$

where,

P_r = the received power

P_t = the transmitted power

θ_t, ϕ_t = target angular orientation relative to the transmit antenna

$G_t(\theta_t, \phi_t)$ = transmit antenna gain

θ_r, ϕ_r = target angular orientation relative to the receive antenna

$G_r(\theta_t, \phi_t)$ = receive antenna gain

λ = wavelength

σ = radar cross section (RCS) of target

R = range to point target.

Equation D.6 is known as the *Radar Equation*. In the backscatter direction, for a single antenna system, it becomes,

$$P_r = \frac{K_t K_r P_t g^2(\theta,\phi)\lambda^2\sigma}{(4\pi)^3 R^4} \tag{D.7}$$

where K_t and K_r are scale factors associated with the losses and gain steps involved in the transmit and receive channels of the radar, respectively. The term g now refers only to the antenna pattern.

The RCS of a target is given as,

$$\sigma_{pq} = 4\pi|S_{pq}|^2, \tag{D.8}$$

where S_{pq} is the complex scattering amplitude of the target for q-polarization transmitted and p-polarization received. For a distributed target, we consider a scattering coefficient σ° per unit area such that $\sigma = \sigma^\circ A$. Since the target is distributed, we compute the received power as follows:

$$P_r = \frac{KP_t\lambda^2\sigma^\circ}{(4\pi)^3}\int_{A_i}\frac{g^2(\theta',\phi')}{(R')^4}da' = \frac{KP_t\lambda^2\sigma^\circ}{(4\pi)^2}I, \tag{D.9}$$

where $K = K_t K_r$ and I is known as the *illumination integral*. Since we actually measure, after calibration, S_{pq}, we may compute an RCS, σ_{pq}, according to (D.8). What we are really interested in however is, for the viewing geometry involved, what value of σ°_{pq} would give the same P_r as the calculated RCS σ_{pq}?

From an examination of Equations (D.7) and (D.9), we see that for the same P_r, we must find σ° such that

$$\frac{\sigma}{R_0^4} = \sigma^\circ\int_{A_i}\frac{g^2\,da'}{(R')^4} \tag{D.10}$$

leading to,

$$\sigma^{\circ} = \frac{\sigma}{IR_{o}^{4}}. \tag{D.11}$$

so that, from (D.8),

$$\sigma^{\circ} = \frac{4\pi|S_{pq}|^{2}}{IR_{o}^{4}} \tag{D.12}$$

where R_o is the nominal distance to the target, the distance along the boresite direction.

To aid in the calibration of backscattering coefficients measured with the K_u-band radar, values for the illumination integral I have been computed for heights ranging from 3 m to 20 m, for a range of angles extending from 10° to 70°. This information is plotted in Figure D.12.

Similar calculations can be performed to determine the minimum detectable σ° that can be measured with the radar system. For this purpose, we will define the minimum detectable signal as one which is 6 dB above the noise level. To compute this quantity, we refer to Figure D.11, which shows the time domain trace of a 12" sphere measured at a range of 11.4 m. Since the RCS of a 12" sphere is known (-11.37 dB), we may easily say for this case what is the minimum detectable RCS. The sphere response is seen to be about 35 dB above the noise level. Therefore, the minimum detectable RCS is 29 dB below the RCS of the sphere, or -40.37 dB. The corresponding minimum detectable σ° may be found for this range by applying equation (D.11).

To compute the minimum detectable σ° at any other range, we consider that a for a point target, the RCS is proportional to R_o^4. Therefore, the minimum detectable RCS may be computed by considering the amount that the 12" sphere response would be above the noise

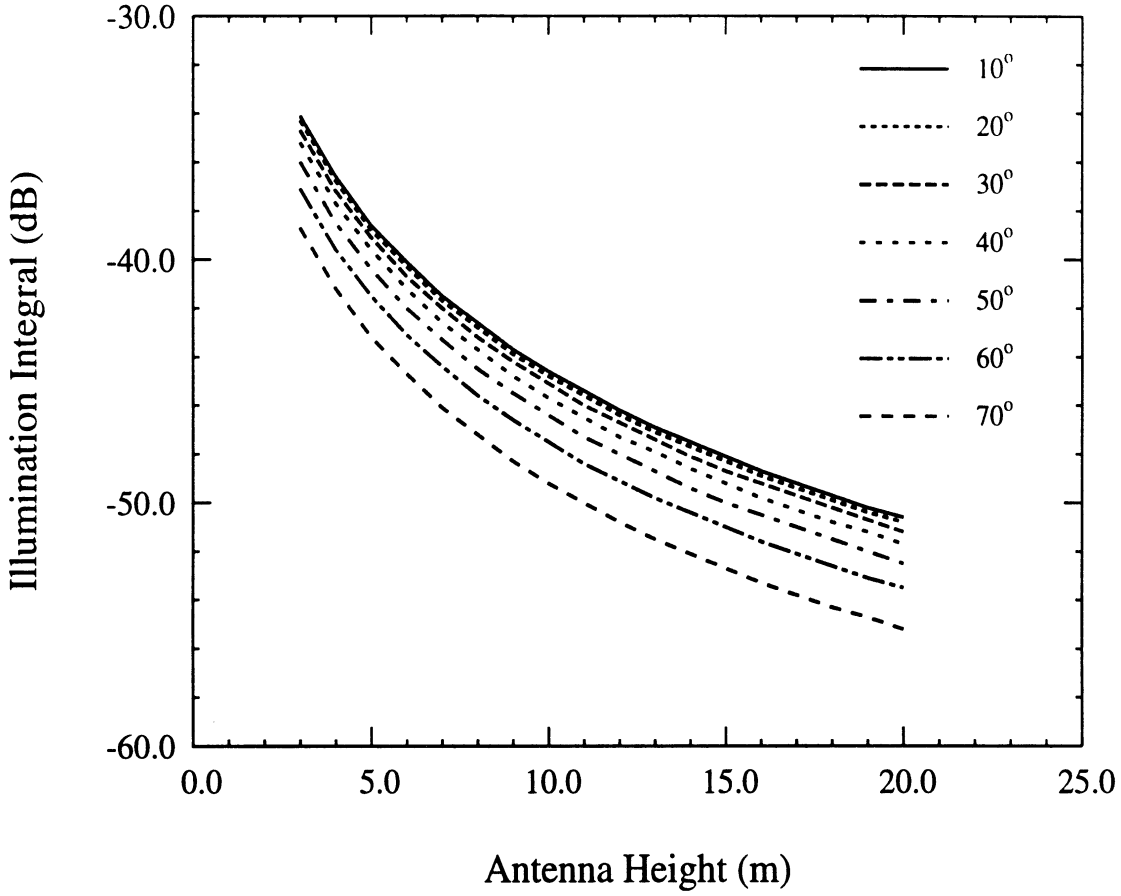

Figure D.12: Illumination integral for the K_u-band radar. Shown *versus* height with viewing angle as a parameter.

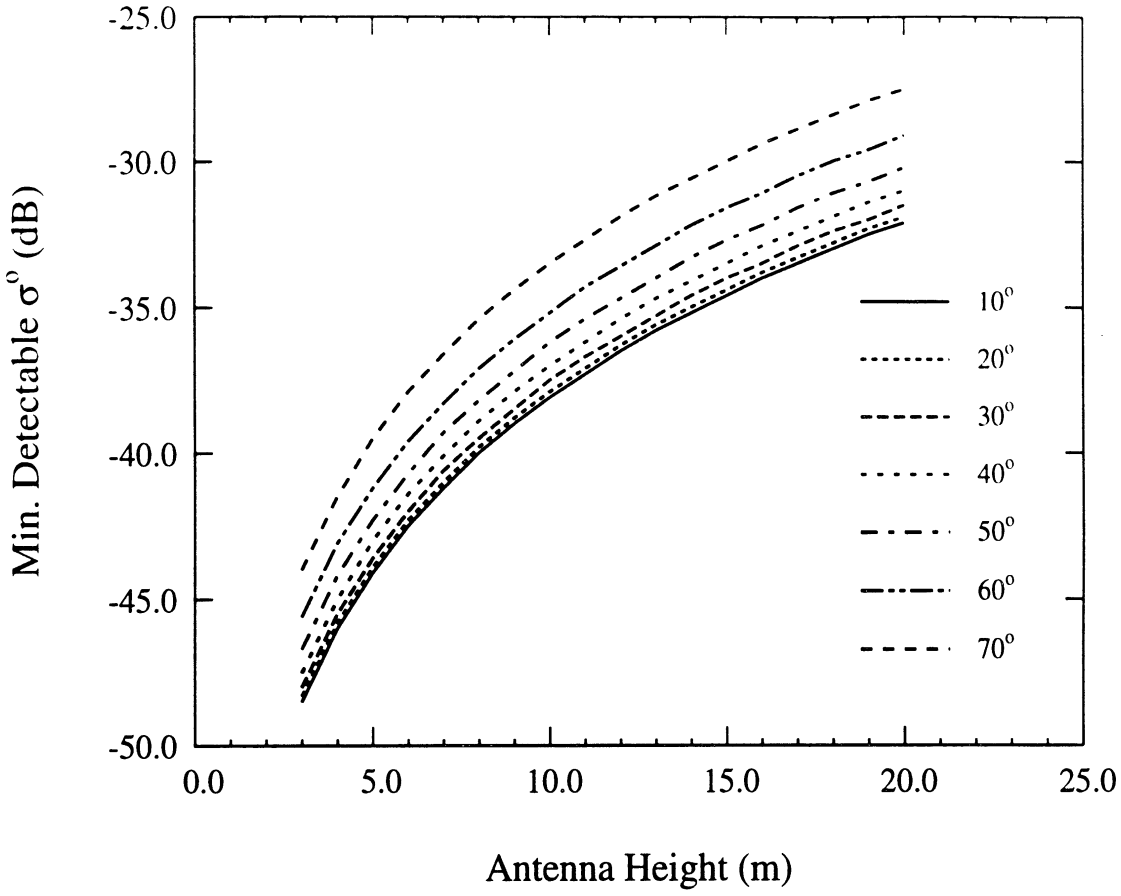

Figure D.13: Minimum detectable σ° for the K_u-band radar. Shown *versus* height with viewing angle as a parameter.

(which is considered as having a constant absolute level) at any range. This is,

$$\sigma_{min}(R) = -11.37 - 29 - 10\log(\frac{11.4}{R})^4 \tag{D.13}$$

$$= -40.4 - 40\log(\frac{11.4}{R}) \tag{D.14}$$

where $\sigma_{min}(R)$ is in dB. As before, the corresponding minimum detectable σ° may computed by applying (D.11). These values are given for ranges of heights and viewing angles in Figure D.13. It should be noted that these calculations were based upon the noise-state of the system as it appears in Figure D.11. If the noise-state is observed to be different, the values in Figure D.13 would need to be adjusted by the change in the signal to noise ratio.

Bibliography

Abdelrazik, M. (1984). *Measurements and modeling of the dielectric behavior of snow in the 1.0 to 37.0 GHz frequency range*. Ph. D. thesis, Univ. of Michigan, Ann Arbor.

Altschuler, H. M. (1963). Dielectric constant. In M. Wind and H. Rapaport (Eds.), *Handbook of Microwave Measurements*. New York: Interscience.

Attema, E. P. W., , and F. T. Ulaby (1978). Vegetation modeled as a water cloud. *Radio Science 13*, 357–364.

Austin, R. T. (1990, January). Determination of the liquid water content of snow by freezing calorimetry. Technical Report 022872–2, The University of Michigan, Radiation Laboratory.

Balanis, C. A. (1982). *Antenna Theory*. New York: NY: Wiley. Chapter 12.

Bohren, C. F. and D. R. Huffman (1983). *Absorption and scattering of light by small particles*. New York: Wiley.

Brunfeldt, D. R. (1987). Theory and design of a field-portable dielectric measurement system. In *Proc. IGARSS '87*, pp. 559–563. Vol. I.

Chandrasekhar, S. (1960). *Radiative Transfer*. New York: Dover.

Chang, A. T. C., J. L. Foster, M. Owe, and D. K. Hall (1985). Passive and active microwave studies of wet snowpack properties. *Nordic Hydrology 16*, 57–66.

Chang, P., J. Mead, R. McIntosh, R. Davis, and H. Boyne (1994). A detailed study of the backscatter characteristics of snowcover measured at 35, 95, and 225 ghz. In *Proc. IGARSS '94*, pp. 1932. Vol. IV.

Choudbury, B. J., T. J. Schmugge, A. Chang, and R. W. Newton (1979). Effect of surface roughness on the microwave emission from soils. *J. Geophys. Res. 84*, 5699–5706.

Colbeck, S. C. (1980, May). Liquid distribution and the dielectric constant of wet snow. In *Microwave Remote sensing of snowpack properties*, pp. 21–40. NASA. Conference publication 2153.

Colbeck, S. C. (1991). The layered character of snow covers. *Revs. of Geophys. 29*, 81–96.

Collin, R. E. (1966). *Foundations for Microwave Engineering*. New York: McGraw-Hill.

Cumming, W. (1952). The dielectric properties of ice and snow at 3.2 cm. *J. Appl. Phys. 23*, 768–773.

Davis, D. T., Z. Chen, L. Tsang, J. N. Hwang, and A. T. C. Chang (1993). Retrieval of snow parameters by iterative inversion of a neural network. *IEEE Trans. Geosci. Rem. Sens. 31*(4).

Denoth, A. (1980). The pendular-funicular transition in snow. *J. Glaciology 25*(91), 93–97.

Denoth, A. (1984). A comparative study of instruments for measuring the liquid water content of snow. *J. Appl. Phys. 56*(7).

Denoth, A. (1989). Snow dielectric measurements. *Adv. Space Res. 9*(1), 233–243.

Ellerbruch, D. A. and H. S. Boyne (1980). Snow stratigraphy and water equivalence measured with an active microwave system. *J. Glaciol. 26*, 225–233.

Evans, D. L., T. G. Farr, J. J. van Zyl, and H. A. Zebker (1988). Radar polarimetry: Analysis tools and applications. *IEEE Trans. Geosci. Rem. Sens. 26*(6).

Fung, A. K. and K. S. Chen (1991). Dependence of the surface backscattering coefficients on roughness, frequency, and polarization states. *Int. J. Remote Sensing 13*(9), 1663–1680.

Fung, A. K. and H. J. Eom (1985). A study of backscattering and emission from closely packed inhomogeneous media. *IEEE Trans. Geosci. Rem. Sens. 23*, 761–767.

Gibbs, D. and A. K. Fung (1990). Measurement of optical transmission and backscatter from a dense distribution of particles. In *Proc. IGARSS '90*, pp. 1029–1032.

Hallikainen, M. (1984). Retrieval of snow water equivalent from nimbous-7 smmr data: Effect of land-cover categroies and weather conditions. *IEEE J. Oceanic Eng. 9*, 372–376.

Hallikainen, M., F. T. Ulaby, and M. Abdelrazik (1986). Dielectric properties of snow in the 3 to 37 ghz range. *IEEE Trans. Antennas Propagat. AP–34*, 1329–1339.

Hallikainen, M. T., F. T. Ulaby, M. C. Dobson, M. A. El-Rayes, and L. Wu (1985). Microwave dielectric behavior of wet soil —part i: Empirical models and experimental observations. *IEEE Trans. Geosci. Rem. Sens. GE-23*, 25–34.

Hallikainen, M. T., F. T. Ulaby, and T. E. Van Deventer (1987). Extinction behavior of dry snow in the 18- to 90-ghz range. *IEEE Trans. Geosci. Rem. Sens. GE-25*(6).

IEEE (1979). *Standard Test Procedures for Antennas*. New York: IEEE. IEEE Press.

Ishimaru, A. (1978). *Wave Propagation and Scattering in Random Media*, Volume I and II. New York, NY: Academic Press.

Ishimaru, A. and R. L.-T. Cheung (1980). Multiple scattering effects on wave propagation due to rain. *Ann. Telecommunication 35*, 373–379.

Ishimaru, A. and Y. Kuga (1982). Attenuation constant of a coherent field in a dense distribution of particles. *J. Opt. Soc. Am. 72*, 1317–1320.

Jones, E. B., A. Rango, and S. M. Howell (1983). Snowpack liquid water determinations using freezing calorimetry. *Nordic Hydrol. 14*, 113–126.

Kendra, J. R., F. T. Ulaby, and K. Sarabandi (1994). Snow probe for *in situ* determination of wetness and density. *IEEE Trans. Geosci. Rem. Sens. 32*(6).

Kleinman, R. E. and T. B. A. Senior (1986). Rayleigh scattering. In V. K. Vardan and V. V. Varadan (Eds.), *Low and High Frequency Asymtotics*, Chapter 1. Amsterdam: North-Holland.

Koh, G. and R. E. Davis (1994). Effect of snow stereology on millimeter wave extinction. In *Proc. IGARSS '94*, pp. 1929. Vol. IV.

Kong, J. A. (1975). *Theory of Electromagnetic Waves*. New York, NY: Wiley.

Koskinen, J., L. Kurvonen, V. Jääskeläinen, and M. Hallikainen (1994). Capability of radar and microwave radiometer to classify snow types in forested areas. In *Proc. IGARSS '94*, pp. 1283. Vol. II.

Kuga, Y., F. T. Ulaby, T. F. Haddock, and R. D. DeRoo (1991). Millimeter-wave radar scattering from snow: 1. radiative transfer model. *Radio Science 26*(2), 329–341.

Lee, J. J. (1988). Lens antennas. In Y. T. Lo and S. W. Lee (Eds.), *Antenna Handbook*, Chapter 16, pp. 10–11. New York: VNR Co.

Leino, M. A. H., P. Pihkala, and E. Spring (1982). A device for practical determination of the free water content of snow. *Acta Polytechnica Scandinavica 135*. Applied Physics Series.

Mandt, C. E. (1987). Microwave propagation and scattering in a dense distribution of spherical particles. Master's thesis, Univ. of Washington, Seattle.

Mätzler, C., H. Aebischer, and E. Schanda (1984). Microwave dielectric properties of surface snow. *IEEE J. Oceanic Eng. 9*(5).

Mätzler, C. and E. Schanda (1984). Snow mapping with active microwave sensors. *Int. J. Rem. Sens. 5*(2), 409–422.

Mätzler, C., E. Schanda, and W. Good (1982). Towards the definition of optimum sensor specifications for microwave remote sensing of snow. *IEEE Trans. Geosci. Rem. Sens. GE-20*(1).

Mätzler, C. and U. Wegmüller (1987). Dielectric properties of fresh water ice at microwave frequencies. *J. Phys. D: Applied Physics 20*, 1623–1630.

Mead, J. B., P. S. Chang, S. P. Lohmeier, P. M. Langlois, and R. McIntosh (1993). Polarimetric observations and theory of millimeter-wave backscatter from snow cover. *IEEE Trans. Antennas Propagat. 41*(1).

Narayanan, R. M. and S. R. Jackson (1994). Snow cover classification using millimeter-wave radar imagery. In *Proc. IGARSS '94*. Vol. IV.

NASA, Goddard Space Flight Center (1982). *Plan of Research for Snowpack Properties Remote Sensing—(PRS)*^{2}. Greenbelt, Md.: NASA, Goddard Space Flight Center. Proposal issued through Goddard Space Flight Center.

Nyfors, E. (1982). On the dielectric properties of dry snow in the 800 mhz to 13 ghz range. Technical Report S135, Helsinki University of Technology, Radio Laboratory.

Nyfors, E. and P. Vainikainen (1989). *Industrial Microwave Sensors*. Norwood, MA: Artech House.

Oh, Y., K. Sarabandi, and F. T. Ulaby (1992). An empirical model and an inversion technique for radar scattering from bare soil surfaces. *IEEE Trans. Geosci. Rem. Sens. 30*(2).

Oh, Y., K. Sarabandi, and F. T. Ulaby (1993). An empirical model for phase difference statistics of rough surfaces. In *Proc. IGARSS '93*.

Polder, D. and J. H. Van Santen (1946). The effective permeability of mixtures of solids. *Physica 12*, 257–271.

Sarabandi, K. (1990, Nov.). Simulation of a periodic dielectric corrugation with an equivalent anisotropic layer. *Int. J. of Infrared and Millimeter Waves 11*(11), 1303–1321.

Sarabandi, K. (1992). Derivation of phase statistics from the mueller matrix. *Radio Science 27*(5), 553–560.

Sarabandi, K., Y. Oh, and F. T. Ulaby (1992, Dec.). Measurement and calibration of differential mueller matrix of distributed targets. *IEEE Trans. Antennas Propagat. 40*(12), 1524–1532.

Sarabandi, K. and F. T. Ulaby (1990). A convenient technique for polarimetric calibration of single-antenna radar systems. *IEEE Trans. Geosci. Rem. Sens. 28*(6).

Sarabandi, K., F. T. Ulaby, and M. A. Tassoudji (1990). Calibration of polarimetric radar systems with good polarization isolation. *IEEE Trans. Geosci. Rem. Sens. 28*(1).

Shi, J. and J. Dozier (1992). Radar backscattering response to wet snow. In *Proc. IGARSS '92*, pp. 927. Vol. II.

Shi, J. C. and J. Dozier (1995). Inferring snow wetness using c-band data from sir-c's polarimetric synthetic aperture radar. *IEEE Trans. Geosci. Rem. Sens. 33*(4), 905–914.

Sihvola, A. and M. Tiuri (1986). Snow fork for field determination of the density and wetness profiles of a snow pack. *IEEE Trans. Geosci. Remote Sensing GE–24*, 717–721.

Siqueira, P. R. and K. Sarabandi (1995). Numerical evaluation of the two-dimensional quasi-crystalline approximation. *IEEE Trans. Antennas Propagat.*. accepted for publication.

Siqueira, P. R., K. Sarabandi, and F. T. Ulaby (1995). Numerical simulation of scatterer positions in a very dense medium with an application to the two-dimensional born approximation. *Radio Science*. accepted for publication.

Stiles, W. H. and F. T. Ulaby (1980a). The active and passive microwave response to snow parameters 1. wetness. *J. Geophys. Res. 85*(C2), 1037–1044.

Stiles, W. H. and F. T. Ulaby (1980b, June). Microwave remote sensing of snowpacks. NASA Contractor Report 3263, The University of Michigan, Radiation Lab.

Tassoudji, M. A., K. Sarabandi, and F. T. Ulaby (1989). Design consideration and implementation of the lcx polarimetric scatterometer (polarscat). Technical Report Rep. 022486-T-2, The University of Michigan, Radiation Lab.

Tiuri, M. E., A. H. Sihvola, E. G. Nyfors, and M. T. Hallikainen (1984). The complex dielectric constant of snow at microwave frequencies. *IEEE J. Oceanic Engr. 9*, 377–382.

Tsang, L. and A. Ishimaru (1987). Radiative wave equations for vector electromagnetic propagation in dense nontenuous media. *J. Electromagnetic Waves and Applications 1*(1), 59–72.

Tsang, L. and J. A. Kong (1992). Scattering of electromagnetic waves from a dense medium consisting of correlated mie scatterers with size distributions and applications to dry snow. *Journal of Electromagnetic Waves and Applications 6*(3), 265–296.

Tsang, L., J. A. Kong, and R. T. Shin (1985). *Theory of Microwave Remote Sensing*. New York, NY: Wiley Interscience.

Ulaby, F. T., T. H. Bengal, M. C. Dobson, J. R. East, J. B. Garvin, and D. L. Evans (1990). Microwave dielectric properties of dry rocks. *IEEE Trans. Geosci. Rem. Sens. 28*(3).

Ulaby, F. T. and C. Elachi (Eds.) (1990). *Radar Polarimetry for Geoscience Applications*. Dedham, MA: Artech House, Inc.

Ulaby, F. T., T. F. Haddock, R. T. Austin, and Y. Kuga (1991). Millimeter-wave radar scattering from snow: 2. comparison of theory with experimental observations. *Radio Science 26*(2), 343–351.

Ulaby, F. T., R. K. Moore, and A. K. Fung (1986). *Microwave Remote Sensing, Active and Passive*, Volume 1–3. Dedham, MA: Artech House, Inc.

Ulaby, F. T., P. Siqueira, and K. Sarabandi (1993). A hybrid electromagnetic-statistical approach for characterizing mmw scattering by terrain. In *AGARD Conf. Proc. 501*.

Ulaby, F. T. and W. H. Stiles (1980). The active and passive microwave response to snow parameters 2. water equivalent of dry snow. *J. Geophys. Res. 85*(C2), 1045–1049.

Vallese, F. and J. A. Kong (1981, Aug.). Correlation function studies for snow and ice. *J. Appl. Phys. 52*(8).

Van de Hulst, H. C. (1981). *Light scattering by small particles*. New York: Dover. pp. 28-42.

van Zyl, J. J. (1989). Unsupervised classification of scattering behavior using radar polarimetry data. *IEEE Trans. Geosci. Rem. Sens. 27*(1).

van Zyl, J. J., H. A. Zebker, and C. Elachi (1987). Imaging radar polarization signatures: Theory and observation. *Radio Science 22*(4), 529–543.

Wen, B., L. Tsang, D. P. Winebrenner, and A. Ishimaru (1990, Jan.). Dense medium radiative transfer theory: comparison with experiment and application to microwave remote sensing and polarimetry. *IEEE Trans. Geosci. Rem. Sens. 28*(1).

West, R., L. Tsang, and D. P. Winebrenner (1993, Mar). Dense medium radiative transfer theory for two scattering layers with a rayleigh distribution of particle sizes. *IEEE Trans. Geosci. Rem. Sens. 31*(2), 426–437.

Whitt, M. W. (1991). *Microwave scattering from periodic row-structured vegetation*. Ph. D. thesis, The University of Michigan, Ann Arbor, MI.

Zhou, J. L. and A. L. Tits (1993, September). User's guide for fsqp version 3.3b: A fortran code for solving constrained nonlinear (minimax) optimization problems, generating iterates satisfying all inequality and linear constraints. Technical Report TR-92-107r3, Systems Research Center, The University of Maryland.

Zhu, P. Y., A. K. Fung, and K. W. Wong (1987). Effective propagation constants in dense random media under effective medium approximation. *Radio Science 22*(2), 234–250.

Zuniga, M. A. and J. A. Kong (1980). Active remote sensing of random media. *J. Appl. Phys. 51*(1), 74–79.

Zurk, L. M., K. H. Ding, L. Tsang, and D. P. Winebrenner (1994). Monte carlo simulations of the extinction rate of densely packed spheres with clustered and non-clustered geometries. In *Proc. IGARSS '94*, pp. Vol. I, p. 535.